(81)

THE DEFORMATION OF LARGE TELESCOPE MIRRORS AND OPTICAL QUALITY

by

James P. Weldon, Jr.

S.M., Management, Massachusetts Institute of Technology (1987)

B.S., Business Administration, University of New Hampshire (1978)

Submitted to the Department of Physics in Partial Fulfillment of the Requirements for the Degree of

Science

MASSACHUSETTS INSTITUTE OF TECHNOLOGY

JUN 05 1996

LIBRARIES

Master of Science in Physics

at the

Massachusetts Institute of Technology

June, 1996

The author hereby grants to MIT permission to reproduce and to distribute publicly paper and electronic copies of this thesis document in whole or in part.

Signature of Author _____
Department of Physics
Date

Certified by _____
John Tonry
Professor of Physics
Thesis Supervisor

Certified by _____
Wit Busza
Professor of Physics
Thesis Reader

Accepted by _____
George Koster
Professor of Physics
Chairman, Departmental Committee

V.1

THE DEFORMATION OF LARGE TELESCOPE MIRRORS AND OPTICAL QUALITY

by

James P. Weldon, Jr.

Submitted to the Department of Physics in Partial Fulfillment of the Requirements for the Degree of Master of Science in Physics

Abstract

The 2.4 meter primary mirror of the MDM/Hiltner Telescope is modeled using the finite element method and analyzed for structural deformations caused by gravity acting on the mirror and its primary support systems. The finite element data is applied in two separate optical codes in order to analyze the effects of mirror surface deformation on image quality.

A series of point loads is applied to the mirror, and the resulting structural and optical perturbations are measured in order to ascertain the relationship between applied forces and deformation of mirror optical quality.

Finally, an active optics support system is proposed for the primary mirror. The design includes a linear optimization routine that acts to minimize reflected wavefront distortions by adjusting pressures in the new axial supports. The results of the active system predict that it is possible to achieve a diffraction limited image with the MDM/Hiltner Telescope.

In preparation for the finite element and optical analysis, and the design of an active optics system, the thesis introduces the theory of bending of thin plates, the methods of finite element and optical analysis, and the astronomical optics and wavefront aberrations appropriate to this subject.

Thesis Supervisor: John L. Tonry
Professor of Physics

Reader: Wit Busza
Professor of Physics

ACKNOWLEDGMENTS

First and foremost, I would like to thank Professor John Tonry for inviting me to join him in this project, for his supervision, guidance, and ongoing help. Professor Tonry's insight and skill are matched only by his patience, his willingness to instruct, and his love of astronomy.

I would like to extend a special thank you to Dr. Martinus Van Schoor of MIT's Department of Aeronautics and Astronautics. Dr. Van Schoor generously spent many hours teaching me the methods of engineering mechanics and finite element analysis, and provided me with the facilities to complete the structural and optimization research.

I would like to also thank Professor Wit Busza for our discussions and his advice.

I am especially grateful to Keith Doyle of Lincoln Laboratories. Keith exhibited unlimited generosity in helping to verify the accuracy of the finite element model, answer questions, and generally supply moral and technical support. Special thanks to Lorenzo Williams, also of Lincoln Laboratories, for introducing me to Keith and making available my access to the Laboratories.

I would also like to thank all the people who work with Dr. Van Schoor at the Space Engineering Research Center of MIT's Department of Aeronautics and Astronautics for their support. SERC Director Professor Edward F. Crawley, Dr. David Miller, and SERC Administrator Sharon Leah Brown were very generous in allowing me the use of their computers, and granting me unfettered access to faculty, staff and graduate students.

Finally, I would like to thank my parents, Mr. and Mrs. James P. Weldon, and my grandmother, Mrs. J.D. Cahill Sr., for their unending moral and financial support.

Table of Contents

Chapter 1 Introduction 7
1.1 Background & Motivation 8
1.2 MDM and the Old School 12
1.3 Objectives and Approach 13

Chapter 2 The Beam Equation 15
2.1 Linear Relation Between Stress and Strain 16
2.1.1 Properties of Stress 16
2.1.2 Displacements and Displacement Functions 18
.1.3 Hooke's Law & The Extension of a Beam 23
2.2 Pure Bending of Beams 25
2.3 A "Technical Theory" of Bending 29

Chapter 3 The Plate Equation 36
3.1 Plate Equation From Stress-Strain Relations 37
3.1.1 Thin Plate Stress-Strain Relations 37
3.1.2 The Plate Eqn From Equilibrium Conditions 39
3.2 Plate Equation for a Circular Plate 45

Chapter 4 Analytical Solutions 46
4.1 Analytical Solutions to the Beam Equation 47
4.1.1 Cantilever Beam with a Point Load 47
4.1.2 Cantilever Beam With Uniform Load 48
4.1.3 Cantilever Beam, Distributed & Point Loads 49
4.1.4 Simply Supported Beam & Distributed Force 50
4.1.5 Simply Supported Beam W. Point Load 51
4.1.6 Simply Supported, Gravity & Point Load 53
4.2 Radial Plate Analytical Solutions 54
4.3.1 Solution to a Plate Clamped at the Edges 55
4.3.2 Solution for a Simply Supported Plate 57

Chapter 5 Finite Element Analysis 59
5.1 Conceptual Finite Element Analysis 60
5.1.1 Introduction to The Finite Element Method 60
5.1.2 Explicit Plane Truss 62
5.1.3 Utility of Direct Physical Argument 64
5.2 Energy Methods 65
5.2.1 Energy Method Definitions 65
5.2.2 The Principle of Minimum Potential Energy 66
5.2.3 Developing the Total Potential Energy 68
5.3 Rayleigh-Ritz 70
5.4 Analytic and FEA Methods Compared 73
5.4.1 Cantilever Beam Numerics 73
5.4.2 Simply-Supported Beam Numerics 76
5.4.3 Plate Numerics 78

Chapter 6 Introduction to Astronomical Optics....81
6.1 Geometrical Optics and Image Formation....82
6.1.1 How MDM Forms an Image....82
6.1.2 Conic Sections of Revolution....85
6.1.3 Focal Length and Radius of Curvature....87
6.2 Physical Optics & Diffraction....90
6.2.1 The Diffraction Integral....91
6.2.2 Diffraction Limit & Point Spread Function....95

Chapter 7 Basic Aberration Theory....98
7.1 The Aberration-Free Wavefront....99
7.2 OPD, Defocus and Lateral Shift....100
7.2.1 Defocus....101
7.2.2 Lateral Shift and Tilt....102
7.3 Angular, Transverse, Longitudinal Aberrations....104
7.4 Seidel Aberrations....106
7.4.1 Spherical Aberration....108
7.4.2 Coma....110
7.4.3 Astigmatism....111
7.4.4 Distortion....114
7.4.5 Field Curvature....114

Chapter 8 Optical Analysis and Zernike Polynomials....115
8.1 Zernike Polynomials and Wavefront Fitting....116
8.2 Table of Zernike Polynomials....120
8.3 PCFRINGE....122

Chapter 9 The Mirror, the Model & Model Verification....123
9.1 The MDM/Hiltner Primary Mirror,....124
9.2 FEA Model Description....127
9.2.1 Model Objectives....127
9.2.2 Model Assumptions....128
9.2.3 Building The Basic Mesh....129
9.2.4 FE Model of the Axial Support System....132
9.2.5 Modeling the Radial Support System....133
9.3 Model Verification....135

Chapter 10 Structural and Optical Analysis of MDM....141
10.1 Analysis of the MDM Primary Mirror....142
10.1.1 Mirror Structural Response....142
10.1.2 Optical Results For the Nominal Mirror....147
10.2 Mirror Resting on Hard Points....152
10.3 Single Point Load Perturbations....158
10.3.1 Structural Response to A Point Load....158
10.3.2 Optical Response to A Point Load....165
10.4 Perturbations From Two Point Loads....172
10.4.1 Structural Response, Pair of Point Loads....172
10.4.2 Optical Response, Pair of Point Loads....180
10.5 Perturbations From Two Pair....187
10.5.1 Structural Response , Four Point Loads....188
10.5.2 Optical Response to Four Point Loads....195

Chapter 11 Active Optics 202
11.1 Active Optics System Theory 203
11.2 Description of the Active Optics System 206
11.3 Explanation of Design Configuration 212
11.4 Nominal Mirror Active Control 213
11.4.1 Active Control of Perturbed Mirror 213
11.4.2 Optical Results 218
11.5 Correcting Gravity and Point Load 221
11.5.1 Active Control of Perturbed Mirror 221
11.5.2 Optical Results of Active Control 226
11.6 Active Control of 100 Pound Point Load 229
11.6.1 The 100 Pound Perturbation 229
11.6.2 Optical Results, 100 Pound Point Load 234
11.7 Correcting Perturbations From Gravity 238
11.7.1 Active Control of Four 20 lb. Point Loads 238
11.7.2 Optical Results of Active Control 243
11.8 Correcting Two Pair of 100 lb. Loads 247
11.8.1 Active Control of Four 100 lb. Point Loads 247
11.8.2 Optical Results of Active Control 251

Chapter 12 Conclusions and Recommendations 254

References 257

Bibliography 261

Chapter 1

Introduction

The goals of this thesis are to accurately model the primary mirror of the Michigan, Dartmouth, MIT 2.4 meter Hiltner Telescope (MDM), to produce a detailed structural and optical analysis of the mirror's performance, and to re-design the primary mirror's axial support system in order to minimize optical aberrations caused by gravity induced mirror deformation.

Two preliminary goals will serve to prepare for the finite element and optical analysis and axial support re-design. The first preliminary goal is to investigate the mechanics that explains the how the mirror responds to applied force. This is done by deriving the equations that describe bending of beams and plates, and applying those equations to analytical examples that share some commonalty with the MDM mirror.

The second preliminary goal is to describe the behavior of light as it enters and travels through a reflecting telescope. Of particular interest are the nature of wavefront aberrations, the wave equations that describe these aberrations, and the specific optical testing methods that have been selected to quantify the aberrations in the MDM model.

1.1 Background & Motivation

The ability to collect light and to resolve images are the two primary performance criteria for a telescope. Aperture size determines a telescope's ability to collect light and contributes to the telescope's ability to see very faint objects. The other primary criteria, image resolution, is a measure of a telescope's ability to resolve small objects, or to resolve small, far away objects that lie in close proximity to one another. Resolution is a function of light collection ability, the quality of the incoming wavefront, and the quality of the telescope's optics.

Anything that detracts from a perfectly formed image constitutes a problem for astronomers and for telescope designers. Historically, the two most persistent sources of imaging problems have been atmospheric turbulence and telescope mechanics.

Atmospheric turbulence is associated with temperature variations that cause changes in air density. These density changes cause some parts of an incoming astronomical wavefront to be slowed relative to other parts. The result is a spatial and temporal wavefront perturbation that can be defined as a complex phase aberration. The real part of the complex phase aberration is a phase shift of the wavefront - this is called "the seeing". The imaginary part of the phase aberration is a measure of intensity fluctuations known to astronomers as scintillation. Poets call it the "twinkling" of the stars.

Imperfect telescope optics are another major cause of blurred images. A perfectly formed incoming wavefront (no atmospheric turbulence or any other sort of interference) that reflects from a telescope's primary mirror will form a less than optimal image if any part of the reflecting surface suffers from deformation. Deformations typically are caused by gravity acting on the mirror's mass, externally induced vibrations that affect telescope structure, or temperature variations acting across the mirror. The result is that the mirror structure bends or deforms, and the optical surface loses its shape.

Until very recently, designers and astronomers have been limited in their attempts to correct the effects of either the atmospheric turbulence or

the telescope structure problems. Though the physics of turbulence has long been well understood, the technology for correcting a turbulence-degraded wavefront did not exist. And for a very long time, the best answer to gravity, thermal and wind induced distortions in the optical surfaces was to build a very rigid optic.

Overview of Telescope Technology Evolution

The very first telescopes were relatively primitive refracting instruments of small light gathering and limited resolving capability. The pace of early post-Galileo telescope development was limited by the difficulties encountered grinding and polishing large surface area lens. Another challenge was the requirement to properly suspend the optic within the telescope tube so that the optical axis was properly aligned, and in such a way that the optic did not deform.

A major early innovation that addressed the problems of light gathering ability and optical and tubular support was the reflecting telescope. Isaac Newton, Guillaume Cassegrain and James Gregory in the early 17th century independently designed compact, reflecting telescopes that utilized secondary mirrors to redirect the reflected wavefront to a position acceptable for observing. Newton (using a folding flat mirror) , Cassegrain (using a small convex mirror), and Gregory (using a small concave secondary) defined the basic configurations of the reflecting telescope only fifty years after Galileo's first refractor.

For several centuries following the Newton era refracting and reflecting telescope designs competed with each other for astronomical primacy. Technology development followed an irregular path. While advances helped both designs, the early years favored the refractors. Innovations included advances in grinding, polishing and manufacturing lenses, the development of counterweights to improve tube suspension, and a discovery that some astronomical objects show a well defined, measurable parallax, which contributed a strong boost to the refractor's ability to render precise measurements. Refractors continued to be the telescope of choice through the end of the 19th century.

The optic suspension handicap proved to be an acute and persistent problem for the refractor community. Engineers could not support massive lenses while adequately maintaining lens figure and optical quality. This inability placed an upper bound on lens mass and aperture size. The Yerkes Observatory 40" refractor and the Lick 36" refracting telescope of the late 19th century represented the pinnacle of refracting technology.

A breakthrough innovation in the late 19th century was the development of the ability to deposit silver on glass. This made possible the manufacture of large area, precisely figured astronomical mirrors. The high quality of the reflecting surface made with the silver deposition technology gave reflectors optical and structural advantage over refractors. This advantage, combined with the problems inherent in peripherally supported massive glass lenses, effectively made the refractor obsolete. The reflector became the instrument of choice.

The reflecting telescope breakthrough did not address the problems of telescope-optic support. As the primary mirrors grew very large, so did the challenges of building support systems that could maintain the mirror's designed optical figure. Increases in mirror size came at the price of increased weight, unwanted mirror flexure and the associated loss of optical figure and resolution. The traditional answer to the unwanted bending of the mirror brought on by the mirror's own mass and the action of gravity was to make very rigid mirrors. The thinking was that a stiff mirror made out of a material with a very low coefficient of thermal expansion would act, due to its own stiffness, to resist structural deformation.

Active and Adaptive Optics

This thinking began to change as early as 1953 with an idea by Horace W. Babcock, who proposed that a mirror's surface could be adapted in order to correct for errors in the phase of the incoming wavefront. Though Babcock lacked the resources to develop his idea, his bold vision initiated the innovations that would address not only the mechanical difficulties of astronomical optics, but the atmospheric difficulties as well.

The Strategic Defense Initiative, the 1980's era anti-missile effort of the US Department of Defense, adopted and developed Babcock's idea in order to develop a capability to optically identify Soviet satellites from ground-based sites. The SDI's success with deformable optics, now called active and adaptive optics, became available to civilian astronomical applications in the 1980's.

Active optics is a method for correcting the structural deformations commonly found in large astronomical mirrors due to the effects of gravity and thermal forces acting on the mirror's structure. The system bends the mirror back into shape and restores the required optical figure to the reflecting surface.

The active optics concept utilizes a deformable mirror, a set of actuators, and an information set. The actuators mounted on the back side of the mirror replace the traditional passive axial support system found in older telescope designs. The information set describes the mirror's known response to force inputs, as well as the differences between the mirror's optimal surface figure and the figure that actually exists as a result of mirror orientation and ambient conditions. This data is used in the actuator control system to adjust the mirror surface and correct structural deformations.

Adaptive optics is a much more ambitious technology. The adaptive concept is to rapidly alter the mirror surface by using a closed loop control system to compensate for phase changes in the incident wavefront caused by atmospheric turbulence. Adaptive optics systems include segmented, highly deformable thin mirrors, actuators and actuator control systems, wavefront sensors and data processors.

An adaptive optics system measures the relative phases of the components of the incident wavefront. This is done by segmenting the mirror surface, and measuring wavefront tilt in each zone. This information is fed to a control system which is responsible for positioning the actuators that drive each of the mirror segments. Given wavefront data, the control system adjusts the individual segments of the mirror's surface in such a way that any wave component arriving later than another actually travels a shorter distance to the focal point. A collateral benefit of adaptive optics is that the technology

inherently compensates for any mirror deformation problems that arise due to gravity, thermal forces or vibration.

The differences between the two types of systems is best seen by looking at their respective speeds. Few active systems work faster than 1 Hz - the mechanical causes of mirror system deformation addressed by active optics, gravity and heat, proceed on a relatively long time scale. Adaptive optics, on the other hand, compensates for rapidly varying atmospheric wavefront distortions. Some adaptive systems use bandwidths of 100 to 1000 Hz.

1.2 MDM and the Old School

The MDM /Hiltner Telescope located at Kitt Peak, Arizona is a member of the older school of reflecting telescopes. In the hierarchy of telescope evolution, MDM falls into the stage that just predates the onset of active/adaptive optics. The primary mirror, not considered deformable, is designed to rely on its own stiffness and support system in order to maintain correct optical figure.

The MDM primary mirror is 2.4 meters in diameter, and weighs approximately 1990 kg. The mirror is made of Cervit, a glass-composite material that is very stiff (Elasticity ≈ 9.2 E10 N/m2) and that exhibits a very low coefficient of thermal expansion (approximately zero). The mirror rests in a mirror cell, supported by an axial and a radial support system.

Primary axial support is provided by a set of three neoprene air bladders. The air bladders are controlled to provide a constant pressure across the mirror's back surface. Also providing axial support is a set of three hard points located at radius = .825 meters, at intervals of 120°. The neoprene air bladders are adjusted by a control system so that the hard points support a load of no more than 30 pounds (≈ 135 Newtons) in the axial direction. The hard points effectively constrain the mirror from moving in the radial plane. The pressure control that maintains a constant and uniform set of reaction forces on the hard points is the only active control component. Hence, MDM might be called a semi-passive, or tilt-active control system.

Radial support is provided by a neoprene mercury belt located along the mirror periphery at the axial center of mass. The mercury inside the belt acts an analog computer, feeding down to provide support as the mirror is rotated away from the zenith, or pure vertical orientation. The belt acts as a buffer between the mirror and the mirror cell. If the mirror is rotated to the horizontal, the mercury belt is sufficient to support all the mirror's mass.

The MDM/Hiltner telescope exhibits many of the problems common to heavy, rigid mirrors. Most of these problems are directly related to the mirror's mass, its primary axial support, and the lack of active control over the primary mirror's surface. This thesis endeavors to solve these problems.

1.3 Objectives and Approach

The principal objectives of this research are academic. If MIT continues its association with the MDM consortium, it is possible that the axial support re-design developed in this thesis will be implemented. Otherwise, it is hoped that the analysis contained in this study will help to improve the quality of information delivered by MDM/Hiltner. Academic objectives are as follows:

(1) Develop an accurate model of the MDM primary mirror and its support system to determine the nature of the structural and optical distortions that are induced by the action of gravity.

(2) Determine the mirror's reaction to force inputs, and develop a correlation between the mirror's reaction to force (Newtons) and its optical performance.

(3) Design a new axial support system that minimizes gravity induced deformations. Investigate the feasibility of an active axial support system.

Finite element analysis is the primary structural analysis tool. An optical analysis package that utilizes the method of Zernike polynomials, and a spot-diagram/contour-diagram code written by Professor John Tonry (MIT, 1995) serve as the optical analysis tools. The axial support redesign was accomplished with the aid of a least squares optimization code written by Dr. Martinus Van Schoor (MIT, 1995). The thesis is composed of three parts:

Part 1: Chapters 2, 3 , 4 and 5.

Chapters 2 and 3 investigate the mechanics of the bending of plates and beams and serve as a theoretical guideline for investigating the methods of structural analysis and finite elements. Chapter 4 is an exercise in fitting numbers to bending theory. Deflection solutions are found for a series of beams and plates under various load and support conditions. Chapter 5 introduces the method of finite element analysis.

Part 2: Chapters 6, 7 and 8.

Chapter 6 is a limited investigation of geometric and physical optics. Ideal wavefront behavior in a telescope system is discussed. Chapter 7 develops basic optical aberration theory. Chapter 8 describes the method of Zernike polynomials in optical analysis. Zernike polynomials are a set of orthogonal polynomials that act to decompose an aberrant wavefront. The individual polynomial coefficients are used to evaluate the relationship between measured optical surface distortions and active support changes.

Part 3: Chapter 9, 10 , 11 and 12.

Chapter 9 describes the finite element model of the MDM 2.4 meter mirror and support system. The model is verified by a real world experiment done at Kitt Peak. With the telescope in a purely vertical orientation, a telescope technician drained the air from the axial air bladders, which put the mirror to rest on the three hard points. A star image was taken. The same procedure was accomplished with the model, and the optical results are compared to the actual results.

Chapter 10 presents the results of finite element and optical analysis for the mirror under various load conditions. Both finite element and optical data are presented. Chapter 11 proposes and tests a new active axial support design based on unit load response and a least squares optimization. Chapter 12 offers lessons learned and recommendations.

Chapter 2

The Beam Equation

This chapter introduces the mechanics of bending of rigid bodies and develops an equation that describes bending in solid beams. This derivation follows the presentation of classic mechanics in Housner (Ref. 1) and Timoshenko (Ref. 2). In combination with the next chapter's treatment of the plate equation, this chapter will serve as a prelude to the analytical and numerical study of the mechanical behavior of the MDM/Hiltner Telescope's 2.4 meter primary mirror.

Linear stress-strain relations, displacement functions and Hooke's Law form the basis for both the theory of elasticity and the beam equation. The beam equation,

$$EI_x \frac{d^4 v}{dx^4} = p.$$

describes a solid beam's response to applied force. The equation assumes a linear stress-strain relations to calculate the deformation of a solid body under the influence of stress.

2.1 Linear Relation Between Stress and Strain

A linear stress-strain relationship means that a solid body (a wooden beam or a telescope mirror) will deform in proportion to the applied force. These changes in geometry can be predicted with a high degree of accuracy if the applied stress is within that material's elastic limits. When stressed beyond elastic limits, the material becomes plastic and will not recover its shape.

2.1.1 Properties of Stress

Stress is defined as force per unit area:

$$stress = \lim_{A \to 0} \frac{force}{area}.$$

The stress vector has two components, the normal stress vector and the tangential stress vector, as shown in Figure 2.1. The normal stress vector is denoted by the symbol σ, and is defined as the force per unit area that acts normally to the face of a solid. The three components of normal stress are σ_x, σ_y, and σ_z, such that σ_x is a stress normal to the x-face on which it is acting. The stress that acts tangentially to the face of the solid is called the shear stress. Shear stress is denoted by τ; τ_{xy} means that τ acts on the x-face in a direction parallel to the y-axis.

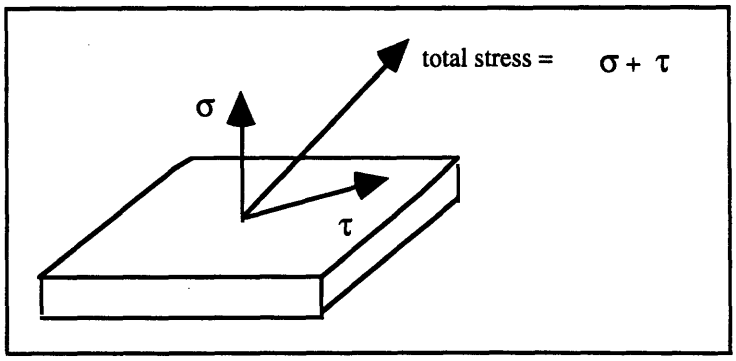

Figure 2.1: Total stress vector is a combination of normal and shear stress.

A complete description of the state of stress of a body requires that the stress at every infinitesimal point in the body be known. For any given point in a body, the total stress is a linear sum of normal and tangential stress.

$$\text{stress}_x = \sigma_x \hat{x} + \tau_{xy}\hat{y} + \tau_{xz}\hat{z}$$

$$\text{stress}_y = \tau_{yx}\hat{x} + \sigma_y \hat{y} + \tau_{yz}\hat{z} \qquad (2.1)$$

$$\text{stress}_z = \tau_{zx}\hat{x} + \tau_{zy}\hat{y} + \sigma_z\hat{z}\ .$$

From equations (2.1), the state of stress experienced by a body at any point can be represented by a matrix of nine scalar stress components:

$$\begin{vmatrix} \sigma_x & \tau_{xy} & \tau_{xz} \\ \tau_{yx} & \sigma_y & \tau_{yz} \\ \tau_{zx} & \tau_{zy} & \sigma_z \end{vmatrix} = \textit{stress}.$$

For a small body element to be in static equilibrium, the vector sum of all forces acting on that element must be zero. Equilibrium also requires that the sum of all moments be zero. In the case of a three dimensional solid element, the stress τ_{yx} multiplied by the area on which it works equals a force τ_{yx} dx dz. This force multiplied by a radius dy gives a moment τ_{yx} dx dy dz. Equilibrium requires that the sum of the moments be zero, therefore

$$\tau_{yx}\ dx\ dy\ dz = \tau_{xy}\ dx\ dy\ dz.$$

Since the areas are equal, in an equilibrium state opposing shear stresses are equal and indistinguishable:

$$\tau_{xy} = \tau_{yx}\ ,$$

and for any element in equilibrium, the two in-plane components of shear stress are equal.

2.1.2 Displacements and Displacement Functions

The deformation of a solid body can be described in terms of displacements of any point within that body. For a continuous body that exhibits a linear response to stress, these displacements are functions of position. The displacement functions u(x, y, z), v(x, y, z) and z(x, y, z) describe the displacement of a small element of a continuous body under stress from some original position P(x, y, z) to a new position P'(x, y, z).

For a body to be considered continuous, all physical properties must be specified at every point and be continuous throughout the body. This definition effectively states that the average properties of a small element of a material may be used to characterize the entire material's volume.

Displacement of a point within a continuous body may result from rotation, deformation, or translation. (This paper will not address translation.)

Rotation

Figure 1.2 shows the rotation of a small unit element about a point. This rotation produces displacements that can be defined in terms of position. In the figure, a small angle rigid body rotation occurs at a point "A" about the z-axis. The rotation "ω_z" of the square element displaces corner "B" .

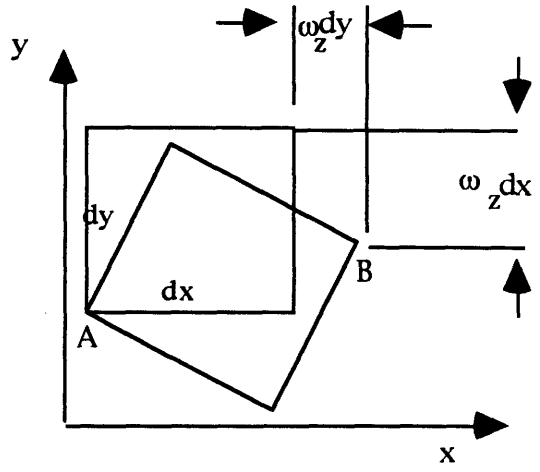

Figure 2.2: A small body rotation about a point "A".

The displacement relative to "A" due solely to rotation are

$$(du)_{rotation} = \omega_y\, dz - \omega_z\, dy$$
$$(dv)_{rotation} = \omega_z\, dx - \omega_x\, dz \qquad (2.2)$$
$$(dw)_{rotation} = \omega_x dy - \omega_y\, dx.$$

The components of rotation can be generalized (eqn (2.3) below):

$$\omega_x = \frac{1}{2}\left(\frac{\partial w}{\partial y} - \frac{\partial v}{\partial z}\right) \qquad \omega_x = \frac{1}{2}\left(\frac{\partial u}{\partial z} - \frac{\partial w}{\partial x}\right) \qquad \omega_x = \frac{1}{2}\left(\frac{\partial u}{\partial z} - \frac{\partial w}{\partial x}\right).$$

Normal Strain

Normal strain of an element is defined as an incremental change in the element's length divided by the element's original length. Extension is positive strain, while contraction is negative strain. Figure 2.3 (below) shows positive strains experienced by a small element as the result of normal stress.

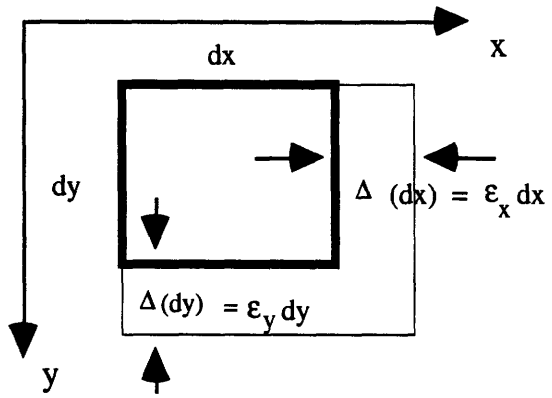

Figure 2.3: An element showing normal strain. Each side has of the element has been extended a small fraction of its original length.

Positive strains shown in Figure 2.3 are defined by "ε":

$$\varepsilon_x = \frac{\Delta(dx)}{dx}, \quad \varepsilon_y = \frac{\Delta(dy)}{dy}, \quad \varepsilon_z = \frac{\Delta(dz)}{dz} \qquad (2.4)$$

Figure 2.4. (below) shows the positive strains of the element in terms of displacements. The x and y coordinates of the corners of the element have been displaced in the x- and y-directions as a result of a stretching of the material in the element.

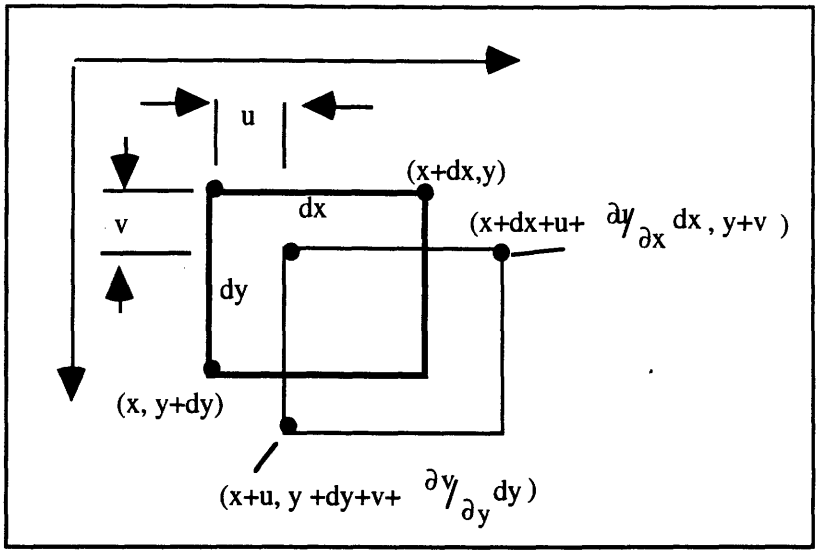

Figure 2.4: Positive strains in terms of displacement functions.

The element has been stretched in the x-direction by an amount

$$(du)_{\text{normal strain}} = \Delta\,(dx) = \left(x + dx + u + \frac{\partial u}{\partial x}dx\right) - (x + dx + u).$$

The x-, y-, and z-direction displacements are found by canceling terms:

$$\begin{aligned}(du)_{\text{normal strain}} &= \Delta\,(dx) = \frac{\partial u}{\partial x}dx.\\ (dv)_{\text{normal strain}} &= \Delta\,(dy) = \frac{\partial v}{\partial y}dy,\\ (dw)_{\text{normal strain}} &= \Delta\,(dz) = \frac{\partial w}{\partial z}dz.\end{aligned} \tag{2.5}$$

Normal strains (from eqn 2.4) are defined in terms of displacements by

$$\varepsilon_x = \frac{\partial u}{\partial x}, \quad \varepsilon_y = \frac{\partial v}{\partial y}, \quad \varepsilon_z = \frac{\partial w}{\partial z}. \tag{2.6}$$

Shearing Strain

An element can deform without changing the length of its sides. In this "shear strain" case, called distortion or pure shear, neither rigid body displacement, normal strain nor rotation are involved. The element experiences a change in its geometry that is best characterized as an angular deformation, as shown in Figure 2.5:

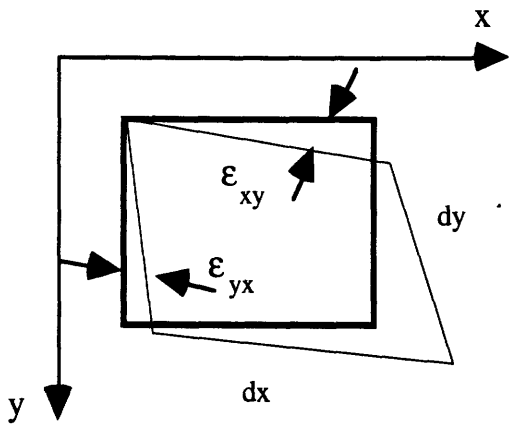

Figure 2.5: Shearing strain as two simple shearing deformations.

The total shearing strain in Figure 2.5 is

$$\gamma_{xy} = \varepsilon_{xy} + \varepsilon_{yx}$$

where the terms ε_{xy} and ε_{yx} describe angular deformations of the sides "dx" and "dy" and are called the xy-components of shearing strain of the element. If there is no rotation involved in the displacements, $\varepsilon_{xy} = \varepsilon_{yx}$.

The shearing strains can be expressed in terms of displacements. As can be seen in the Figure 2.6, the rate of change of displacement with respect to the x- and y-axis define the total shearing strain.

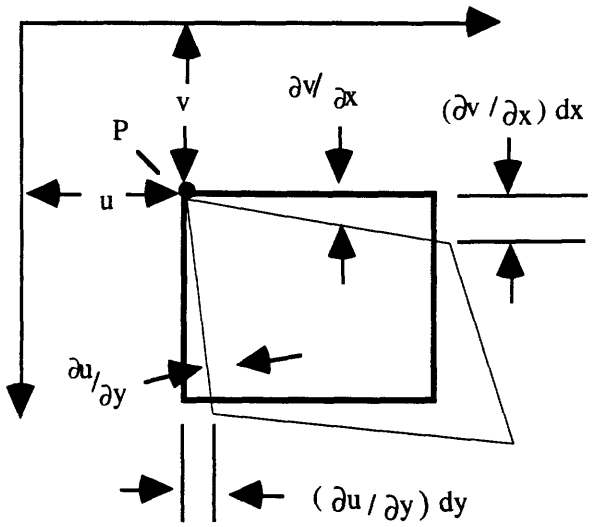

Figure 2.6: Shear strain as rates of change of displacement functions.

Shearing strains are defined in terms of displacements:

$$\gamma_{xy} = \frac{\partial v}{\partial x} + \frac{\partial u}{\partial y} \qquad \gamma_{yz} = \frac{\partial v}{\partial z} + \frac{\partial w}{\partial y} \qquad \gamma_{xz} = \frac{\partial u}{\partial z} + \frac{\partial w}{\partial x}. \tag{2.7}$$

Summary

The state of strain at any point in a continuous body can be specified by examining the variations in displacements. Displacements are functions of position and result from rotation, normal strain and shearing strain. The total differential of the displacement functions is:

$$du = \frac{\partial u}{\partial x}dx + \frac{\partial u}{\partial y}dy + \frac{\partial u}{\partial z}dz$$

$$dv = \frac{\partial v}{\partial x}dx + \frac{\partial v}{\partial y}dy + \frac{\partial v}{\partial z}dz \tag{2.8}$$

$$dw = \frac{\partial w}{\partial x}dx + \frac{\partial w}{\partial y}dy + \frac{\partial w}{\partial z}dz.$$

2.1.3 Hooke's Law & The Extension of a Beam

Hooke's Law states that a solid material will deform in proportion to the applied force. Hooke formalizes the linear relationship that exists between stress and strain in many materials. Strains from normal x-axis stress are

$$\varepsilon_x \equiv -\frac{1}{E}\sigma_x, \qquad \varepsilon_y \equiv -\frac{\nu}{E}\sigma_x, \qquad \varepsilon_z \equiv -\frac{\nu}{E}\sigma_x . \tag{2.9}$$

Figure 2.7 illustrates the meaning of the constants E and "ν". The elasticity "E" is defined as the ratio of longitudinal stress/strain, $E = \sigma / \varepsilon$.. The ratio of contractive strains ε_y and ε_z to the tensile strain ε_x is the Poisson ratio (ratio of contraction in y and z for stretching in x).

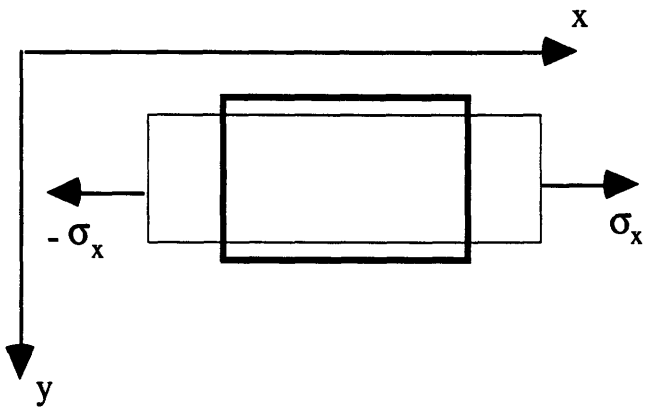

Figure 2.7: Normal stress acting on a beam element showing contraction in y and z for stretching in x.

Equations analogous to equation (2.9) define a body's response (strain) to force (stress) applied in the y and z directions.

$$\varepsilon_x = -\frac{\nu}{E}\sigma_y \qquad \varepsilon_y = \frac{1}{E}\sigma_y \qquad \varepsilon_z = -\frac{\nu}{E}\sigma_y . \tag{2.10}$$

For a z-direction linear the force, the stress-strain relations are

$$\varepsilon_x = -\frac{\nu}{E}\sigma_z, \qquad \varepsilon_y = -\frac{\nu}{E}\sigma_z \qquad \varepsilon_z = \frac{1}{E}\sigma_z . \tag{2.11}$$

The linear relation between shearing stress and shearing strain is

$$\gamma_{xy} = \frac{\tau_{xy}}{G}$$

where the term "G" is the shearing modulus. The complete description of linear deformation includes terms for thermal expansion, normal and shearing stress. For an isotropic material, Hooke's Law is:

$$\varepsilon_x = \frac{1}{E}\left(\sigma_x - \nu\sigma_y - \nu\sigma_z\right) \qquad \gamma_{xy} = \frac{\tau_{xy}}{G}$$

$$\varepsilon_y = \frac{1}{E}\left(\sigma_y - \nu\sigma_x - \nu\sigma_z\right) \qquad \gamma_{yz} = \frac{\tau_{yz}}{G} \qquad (2.12)$$

$$\varepsilon_z = \frac{1}{E}\left(\sigma_z - \nu\sigma_x - \nu\sigma_y\right) \qquad \gamma_{xz} = \frac{\tau_{xz}}{G}.$$

Beam Extension

Figure 2.7 shows a solid beam of known material under a constant x-direction stress. If all other stresses equal to zero:

$$F = (\sigma_x)(Area), \quad \Rightarrow \quad \sigma_x = \sigma_0, \quad \sigma_y = \sigma_z = \tau_{xy} = \tau_{xz} = \tau_{yz}. \qquad (2.13)$$

The resulting linear strains are

$$\varepsilon_x \equiv \frac{1}{E}\sigma_0 \qquad \varepsilon_y \equiv -\frac{\nu}{E}\sigma_0 \qquad \varepsilon_z \equiv -\frac{\nu}{E}\sigma_0. \qquad (2.14)$$

There is zero shearing stress: $\gamma_{xz} = \gamma_{xy} = \gamma_{yz} = 0$ (2.15)

The length of the beam increases by an amount proportional to the force, if it remains within the elastic limits of the material. The measured increase in length is

$$\Delta L_x = \varepsilon_x L = \frac{\sigma_x}{E} L = \frac{sL}{E}.$$

2.2 Pure Bending of Beams

A beam bends in reaction to an applied load. The load may be due to gravity or to a point loading somewhere along the beam's length. Consider a cantilever beam that experiences a vertical force at its free end. Assume that the applied load, represented by a delta function, bends the beam slightly, but not enough to induce any shearing strain.

The beam experiences both compression and tension as it bends. For a downward force (please see Figure 2.8) the material at the top of the beam along the long axis will be pulled slightly apart, while the material along the bottom of the beam will be compressed. The crunching together of the lower part and the pulling apart of the top part are manifestations of horizontal stress induced by the action of the point load acting at the beam's end.

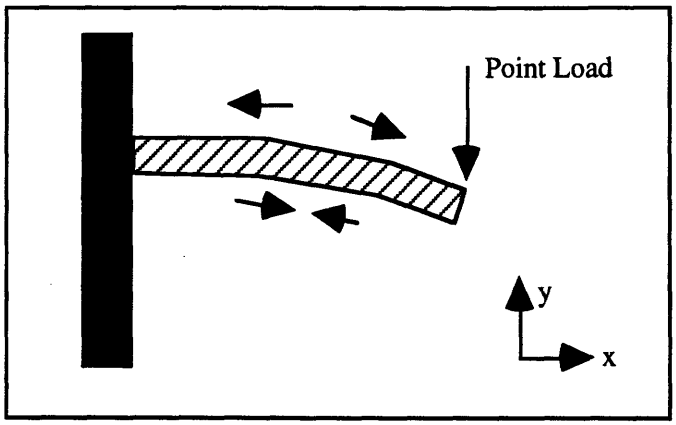

Figure 2.8: Cantilever beam with point load showing both compression and tension. The neutral axis runs between the top and bottom of the beam and experiences no strain.

If the applied force in Figure 2.8 is constant, the beam reaches a point of static equilibrium where sum of all forces acting on the beam equals zero:

$$\frac{\partial \sigma_x}{\partial x} + \frac{\partial \tau_{xy}}{\partial y} + F_x(gravity) = 0 \qquad (2.16a)$$

$$\frac{\partial \sigma_y}{\partial y} + \frac{\partial \tau_{xy}}{\partial x} + F_y(gravity) = 0 \qquad (2.16b)$$

From the diagram, σ_x is solely a function of "y", where "y" is a measure of disyance from th neutral axis. The point load creates a smoothly varying horizontal stress that is a linear function of y-axis position:

$$\hat{\sigma}_x = \frac{\sigma_0}{y_0}\hat{y} = c_1 y. \tag{2.17}$$

The total stress in the x-direction is the integral sum of the incremental stresses over the entire face of the beam. The total force experienced by the beam is the integral sum of linear stress multiplied by incremental area:

$$F_x = \int \sigma_x dA = \int cy dA, \text{ and } \quad c_1 = \frac{\sigma_0}{y_0}.$$

The linear stress described in equation (2.17) acts incrementally and at a distance from the beam's neutral longitudinal axis giving rise to a bending moment. Each stress increment acts at some small distance from the neutral axis, creating a little unit of torque. The total moment is the integral sum of these cross products. Since the applied stress is oriented in the x-direction and varies linearly with y, the moment acts about the z-axis in the y-direction:

$$M_{xz} = \int y \sigma_x dA \, . \tag{2.18}$$

The subscript "x" denotes the direction of the applied force, and the subscript z denotes the axis around which the beam bends. From the definition of the stress in equation (2.17), the moment equation can be expanded

$$M_{xz} = \int y \sigma_x dA = \int c y^2 \, dA = c I_z \tag{2.19}$$

where "I", the second moment of area, is defined

$$I_z = \int y^2 \, dA = \int y^2 \, dx \, dy \, . \tag{2.20}$$

The stress can now be defined in terms of the bending moment, the second moment of area, and the radius from the neutral axis:

$$\sigma_x = cy = \frac{M_{xz}}{I_z} y, \qquad \Rightarrow \qquad c = \frac{M_{xz}}{I_z}. \tag{2.21}$$

Hooke's Law thus relates stress to strain, and strain to bending moment,

$$\varepsilon_x = \frac{1}{E}\sigma_x \qquad \varepsilon_x = \frac{1}{E}\sigma_x = \frac{M_{xz}}{EI_z} y. \tag{2.22}$$

Radius of Curvature and the Beam Equation.

Strain and bending moment are related to the beam's radius of curvature. The radius of curvature is defined by the displacement of the beam's neutral axis. This relationship establishes a differential equation for displacement which is known as the beam equation.

The angle between the undisplaced and the displaced neutral axis in Figure 2.8 is equivalent to tan θ =dv/dx. For a very small angle, tan θ is approximately equal to θ:

$$\tan\theta = dv/dx \qquad \Rightarrow \qquad \theta \approx \tan\theta = dv/dx.$$

The radius of curvature of bending is defined as (Ref 3)

$$R_x = \frac{\left[1+(dv_0/dx)^2\right]^{\frac{3}{2}}}{d^2v_0/dx^2} = a\ constant \tag{2.23}$$

where v_0 is a displacement in the y-direction. In the limit of small deflections, $(dv_0/dx)^2$ approaches zero and the curvature can be defined as a second order condition of the deflection:

$$\frac{1}{R_x} = d^2v_0/dx^2. \tag{2.24}$$

Arc length ds is defined: R dθ = ds. Therefore, (dθ / ds) = $\frac{1}{R_x} = d^2v_0/dx^2$.

The trick, at this point, is to relate the strain ε_x to the radius of curvature, and thereby derive a second order differential equation of bending. This is done in Housner (Ref. 4) by examining a beam element under horizontal (x-direction) stress that bends around the z-axis in the y-direction.

In the Housner relation, the neutral axis defines the coordinate system, so that "y" is a measure of vertical distance from the undisplaced neutral axis. The geometry of the beam element shows that the displaced beam's radius of curvature, the angle $d\theta$ between the displaced and undisplaced neutral axis, the arc length ds of the element's displaced neutral axis, and the x-direction strain are related by the equation

$$y\, d\theta = \varepsilon_x\, ds.$$

From the above relation,

$$1/R = \varepsilon_x/y\ .$$

Therefore, the curvature is related to the second derivative of the deflection, and the moment:

$$\frac{1}{R_x} = \frac{M_{xz}}{EI_z} = \frac{d^2v}{dx^2}. \tag{2.25}$$

This produces a second order equation for displacement and moment:

$$EI\frac{d^2v}{dx^2} = M_{xz}\ . \tag{2.26}$$

Combining (2.25) and (2.26) establishes a second order equation which can be integrated to obtain a function for the y-axis displacement of the beam:

$$\frac{d^2v_0}{dx^2} = \frac{d\theta}{ds} = \frac{M_{xz}}{EI_z}\ . \tag{2.27}$$

2.3 A "Technical Theory" of Bending

The methodology of "pure bending", described in Section 2.2 , requires an exact stress function. Since exact stress functions are rarely available, it is possible to construct approximate displacement functions by using equilibrium conditions as long as beam deflections remain small and the forces acting upon the beam cause little or no shearing strain. In the language of beam theory, the idea of small deflections translates to "plane sections remain plane", so that any cross section of the beam that is planar before bending will be planar after bending. Practically speaking, the criteria for applying this approximation technique is to use beams that experience little or no shearing stress and that exhibit a ratio of beam depth to length that is much less than one.

This section develops the "Technical Theory of Bending" for a beam of continuous and isotropic construction and symmetric cross section. The assumptions are summarized below:

$$\varepsilon_x = \frac{\sigma_x}{E} \tag{2.28}$$

$$\varepsilon_y = 0 \tag{2.29}$$

$$\gamma_{xy} = \gamma_{xz} = \gamma_{yz} = \varepsilon_z = 0 \tag{2.30}$$

$$\left(\frac{dv}{dx}\right)^2 << 1. \tag{2.31}$$

The first equation is Hooke's relation between stress and strain for materials operating within the limits of their elasticity. The second equation specifies that the beam experiences no y-direction strain. The deformation of the beam is limited to expansion and contraction in the x-direction. The third equation is the condition that there is no shearing strain. Lastly, the fourth equation explicitly limits beam deformation to small angles, thus completing a small scale, no shear, bending-only scenario.

Under the assumptions given, the y-direction strain is zero, so the displacement function v is solely a function of x:

$$v = f_1(x). \tag{2.32}$$

Shearing strain is also zero,

$$\frac{\partial u}{\partial y} = -\frac{\partial v}{\partial x} \tag{2.33}$$

and the displacement u is a function of both x and y:

$$u = -y\frac{dv}{dx}. \tag{2.34}$$

Since x-direction strain is given by

$$\frac{\partial u}{\partial x} = \varepsilon_x, \quad \text{then} \quad \varepsilon_x = -y\frac{d^2v}{dx^2} \quad \text{and} \quad \sigma_x = E\varepsilon_x = -Ey\frac{d^2v}{dx^2}.$$

The bending moment is the integral sum of the applied force multiplied by the radius of action:

$$M_{xz} = -\int y\sigma_x dA = \int Ey^2 \frac{d^2v}{dx^2} dA. \tag{2.35}$$

Since "dA" is equal to (dy dz), the integral is an expression for the moment of inertia of the cross-sectional area about the z-axis:

$$M_{xz} = E\frac{d^2v}{dx^2}\int y^2 dA = EI_z\frac{d^2v}{dx^2} \quad \Rightarrow \quad M_{xz} = EI_z\frac{d^2v}{dx^2} \tag{2.36}$$

Equation (2.36) describes a beam experiencing small bending deflections.

The Beam Equation From the Applied Loads

The equations of equilibrium are of three types: forces parallel to the beam axis, forces normal to the beam axis, and moments. A differential relationship exists between the bending moment and the beam's equilibrium condition. The figures below depict a beam under a point load, and a free body diagram of a beam element.

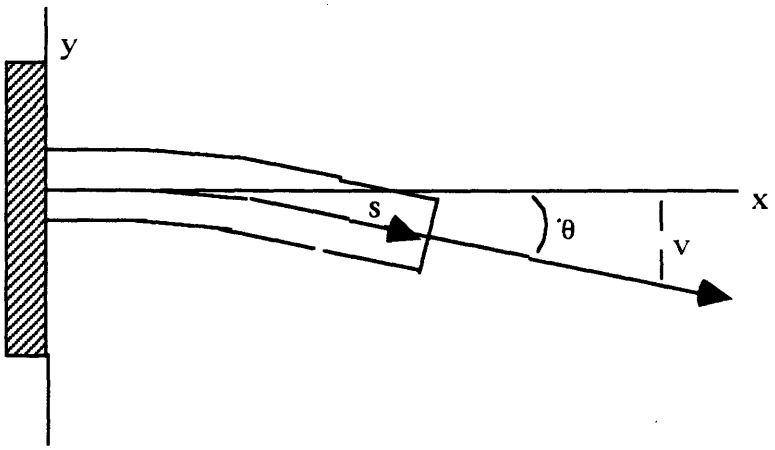

Figure 2.9: A cantilever beam under a distributed load, showing x-direction stress and displacement function v(x,y).

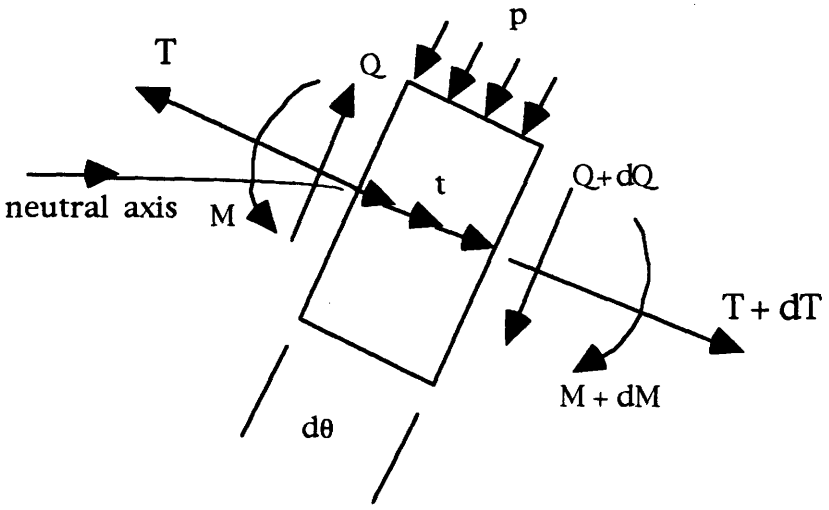

Figure 2.10: Free body diagram of a beam element in static equilibrium.

In Figures 2.9 and 2.10, "t" is a distributed force per unit length along the beam's neutral axis, "Q" is the shearing force, "T" is the tension resulting from x-direction stress, and "M": is the moment. Element length is "ds". Forces parallel to the axis and in equilibrium are:

$$tds + dT - Qd\theta = 0, \quad \frac{dT}{ds} = -t + Q\frac{d\theta}{ds}. \tag{2.37}$$

Forces in equilibrium normal to the beam axis are:

$$dQ + pds + T\sin\frac{d\theta}{2} + (T + dT)\sin\frac{d\theta}{2} = 0. \tag{2.38}$$

Moments in equilibrium are:

$$dM + Qds = 0 \qquad \text{or} \qquad \frac{dM}{ds} = -Q. \tag{2.39}$$

The small angle approximation $\sin\theta = \theta$, drops the second order term:

$$\frac{dQ}{ds} = -p - T\frac{d\theta}{ds}. \tag{2.40}$$

The second derivative of M can then be related to the derivative of Q:

$$\frac{d^2M}{ds^2} = -\frac{dQ}{ds} = p + T\frac{d\theta}{ds}. \tag{2.41}$$

The basic beam equation-moment identity (2.36) is substituted:

$$M_{xz} = EI_z\frac{d^2v}{dx^2}, \quad \Rightarrow \quad \frac{d^2M}{ds^2} = EI_z\frac{d^2}{dx^2}\left(\frac{d^2v}{dx^2}\right) = p + T\frac{d\theta}{ds} \tag{2.42}$$

For a situation where T = 0, the equation is fourth order in terms of the applied load. The beam equation becomes

$$EI_x\frac{d^4v}{dx^4} = p. \tag{2.43}$$

Dimensional Analysis of the Beam Equation

A brief dimensional analysis of displacement functions and their derivatives will shed some light on the fourth order equation that describes action in terms of force per unit length. The displacement functions u(x,y) and v(x) are in units of length:

$$v(x) \Rightarrow meters.$$

The first derivative w.r.t. space is the slope, and is dimensionless:

$$\frac{dv}{dx} = \theta.$$

The second derivative has units of inverse length. When multiplied by the elasticity and second moment of area, units of torque result:

$$\frac{d^2v}{dx^2} = \frac{d\theta}{ds} = \left(meters^{-1}\right), \quad E \equiv \frac{N}{m^2} \equiv \frac{kg}{s^2 m}, \qquad I = \int y^2 dydz \Rightarrow m^4$$

$$EI\frac{d^2v}{dx^2} = M \quad \Rightarrow \quad \frac{N}{m^2} m^4 \frac{1}{m} \quad \Rightarrow \quad \frac{kg \bullet m^2}{s^2}.$$

The first derivative of the moment (which is the third derivative of the displacement function) is the shear force:

$$\frac{dM}{dx} = Q \quad \Rightarrow \quad \frac{kg \bullet m}{s^2}.$$

Finally, the second derivative of the moment (which is the fourth derivative of the displacement) gives force per unit length:

$$\frac{d^2M}{dx^2} = \frac{dQ}{dx} = EI\frac{d^2}{dx^2}\left(\frac{d^2v}{dx^2}\right) \Rightarrow \frac{N}{m}.$$

Delta Functions and Half-Range Functions

A likely place to apply the technical theory of bending is to a beam that experiences forces of known magnitude, position and direction, but whose exact stress distribution is unknown or is not continuous. These forces may be distributed along the length of the beam, or be concentrated in certain positions. An example of a distributed force is the body force generated by the beam's mass acted on by a gravity field. Examples of concentrated forces are end supports of a simply supported beam, or point loads that are applied at some position along the length of the beam.

The point load at the center of a simply supported beam represents not only a concentrated force, but a serious discontinuity problem. The solution to this potential conundrum is the "half-range" function, which is a member of the family to which Dirac delta functions belong.

One of the defining properties of delta functions that makes them so appropriate for this type of work is the fact that a delta function has value only at one spot. Everywhere else, it has zero magnitude.

$$\delta(x-a)=0 \quad for \quad x \neq a$$

The other property of the delta function that makes it appropriate is that the delta spikes to infinity, but the area under the curve is equal to unity. It therefore acts as the perfect modifier to a point load of arbitrary magnitude:

$$\int_{-\infty}^{+\infty} \delta(x) = 1.$$

It is useful to view the delta function as a member of a set of functions called half-range functions. By definition, half-range functions produce a value only when the argument is positive:

$$\{x-a\}=0 \qquad for\,all \quad (x-a)<0,$$

$$\{x-a\}=(x-a) \quad for\,all \quad (x-a)>0.$$

The half-range functions are denoted by brackets. The delta function, considered as a member of the larger set of half-range functions, is defined as

$$\delta(a) = \{x-a\}^{-1}.$$

The general differential forms of the half range functions are :

$$\frac{d}{dx}\{x-a\}^{n} = n\{x-a\}^{n-1} \quad for \quad n \neq 0$$

$$\frac{d}{dx}\{x-a\}^{1} = \{x-a\}^{0} = 0 \quad for \quad x < a$$

$$= 1 \quad for \quad x > a$$

$$\frac{d}{dx}\{x-a\}^{0} = \{x-a\}^{-1} = 0 \quad for \quad x < a \quad and \quad x > a$$

$$= \infty \quad for \quad x = a$$

$$\frac{d}{dx}\{x-a\}^{-1} = -\{x-a\}^{-2} = 0 \quad for \quad x < a \quad and \quad x > a$$

$$= \pm\infty \quad for \quad x = a$$

The half-range functions can be shown in integral form. Note that the integral of the delta function generates a step function.

$$\int_0^x \{x-a\}^{n-1}\,dx = \frac{1}{n}\{x-a\}^{n} \qquad for \quad n \neq 0.$$

$$\int_0^x \{x-a\}^{-1}\,dx = \{x-a\}^{0}.$$

$$\int_0^x \{x-a\}^{0}\,dx = \{x-a\}^{1}.$$

$$\int_0^x \{x-a\}^{1}\,dx = \{x-a\}^{2}$$

Chapter 3

The Plate Equation

This chapter derives the radial plate equation,

$$\nabla^4 w(r) = \frac{q}{D} .$$

Stress-strain relations, equilibrium equations and deformation conditions are used to develop the equation of bending of a thin plate which experiences a force perpendicular to the plate's horizontal plane. The motivation for this derivation is found in the classic mechanics texts written by Timoskenko (Ref. 5) and Housner (Ref. 6).

The plate equation in conjunction with appropriate boundary conditions will be used to approximate the mechanical behavior of the MDM primary mirror and provide an analytical check for results obtained with the NASTRAN finite element model.

3.1 Plate Equation From Stress-Strain Relations

This derivation of the plate equation uses the example of a thin, isotropic plate built of uniform material which experiences a relatively small vertical stress and zero vertical shear. The plate deforms in such a way as to produce no stretching or contraction of the middle surface.

These initial conditions allow deformation of the plate only by horizontal bending strain. This means that the middle axis or "neutral axis" of the plate *will be displaced, but not deformed.* This eliminates the possibility of middle surface z-direction strain. Any load that is applied to the plate will contribute zero shearing stress to the plate's middle surface.

3.1.1 Thin Plate Stress-Strain Relations

The thin plate shown in the diagram below exhibits a depth that is much less than its length or width. The plate's middle surface lies in the x-y plane. The depth is measured in "h" units. The top surface is located at coordinates (x, y, z = h/2), while the bottom surface is located at (x, y, z = -h/2).

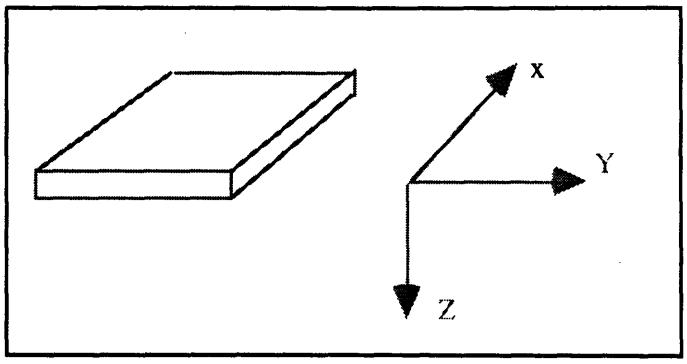

Figure 3.1: A thin rectangular plate with middle surface in the x-y plane.

The conditions described above are those that were used to justify the technical theory of bending of beams in Chapter 2. The technical theory of bending of a thin plate uses deformation and stress-strain conditions to develop a function w(x,y) that describes the transverse displacements of the middle surface of the plate. (Please see Table 3.1.)

Deformation Conditions		Stress-Strain Relations	
$\varepsilon_z = \frac{\partial w}{\partial z} = 0$	(3.1.a)	$\varepsilon_x = \frac{1}{E}\left(\sigma_x - \nu\sigma_y\right)$	(3.1.d)
$\gamma_{xz} = \frac{\partial w}{\partial x} + \frac{\partial u}{\partial z} = 0$	(3.1.b)	$\varepsilon_y = \frac{1}{E}\left(\sigma_y - \nu\sigma_x\right)$	(3.1.e)
$\gamma_{yz} = \frac{\partial w}{\partial y} + \frac{\partial v}{\partial z} = 0$	(3.1.c)	$\gamma_{xy} = \frac{1}{G}\tau_{xy}$	(3.1.f)

Table 3.1: Assumptions for technical theory of bending of a thin plate.

Equation (3.1.a) states that "w" is independent of "z", so that the displacement of the middle surface is a function of only x and y. In other words, all points through the thickness of the plate that share the same x and y coordinates are displaced from their equilibrium positions relative to the middle surface by the same amount. There is no pure z-direction strain. Equations (3.1.b) and (3.1.c) state that there is zero middle surface shearing strain. Equations 3.1.d-f describe the x- and y- direction bending strain.

The displacement functions in the x, y and z-directions are:

$$\frac{\partial w}{\partial x} + \frac{\partial u}{\partial z} = 0 \qquad (3.2.a) \qquad\qquad \frac{\partial w}{\partial x} + \frac{\partial u}{\partial z} = 0 \qquad (3.2.d)$$

$$\frac{\partial u}{\partial z} = -\frac{\partial w}{\partial x} \qquad (3.2.b) \qquad\qquad \frac{\partial v}{\partial z} = -\frac{\partial w}{\partial y} \qquad (3.2.d)$$

$$u = -z\frac{\partial w}{\partial x} + f_1(x,y) \qquad (3.2.c) \qquad\qquad v = -z\frac{\partial w}{\partial y} + f_2(x,y) \qquad (3.2.e)$$

From Chapter 2, normal strain is defined as the rate of change of displacement with respect to position:

$$\varepsilon_x = \frac{\partial u}{\partial x} \qquad (3.3) \qquad\qquad \varepsilon_y = \frac{\partial v}{\partial y}. \qquad (3.4)$$

Substituting equations (3.3) and (3.4) into (3.2) yields a relation between normal strain and the displacement functions u(x,y) and v(x,y):

$$\varepsilon_x = \frac{\partial u}{\partial x} = -z\frac{\partial^2 w}{\partial x^2} \qquad (3.5) \qquad\qquad \varepsilon_y = \frac{\partial v}{\partial y} = -z\frac{\partial^2 w}{\partial y^2}. \qquad (3.6)$$

Horizontal shear stress deforms the plate through the angle γ. Shear strain is the rate of change of "u" and "v" with respect to "y", and "x".

$$\gamma_{xy} = \frac{1}{G}\tau_{xy} = \frac{\partial u}{\partial y} + \frac{\partial v}{\partial x} \qquad (3.7)$$

Substituting equation (3.2.c) and (3.2.e) into (3.7) leads to a second derivative of "w" with respect to both x and y:

$$\frac{\partial u}{\partial y} = -z\frac{\partial^2 w}{\partial x \partial y} \qquad (3.10) \qquad\qquad \frac{\partial v}{\partial x} = -z\frac{\partial^2 w}{\partial y \partial x} \qquad (3.8)$$

The resulting strain-displacement relations between normal and shear x- y- direction strain and the displacement function w(x,y) are:

$$\varepsilon_x = \frac{\partial u}{\partial x} = -z\frac{\partial^2 w}{\partial x^2} \qquad \varepsilon_y = \frac{\partial v}{\partial y} = -z\frac{\partial^2 w}{\partial y^2} \qquad \gamma_{xy} = -2z\frac{\partial^2 w}{\partial x \partial y} \qquad (3.9)$$

3.1.2 The Plate Equation From Equilibrium Conditions

The plate equation is derived by relating the strain-displacement conditions of equation (3.9) to the applied load. The trick is to isolate the z-direction normal stress as a function of middle surface displacement. Unfortunately, the z-direction normal stress appears in the equilibrium equations only in a relation with τ_{yz} and τ_{xz}. So there is some work to do.

The first step in deriving the fourth order plate equation is to list the general equilibrium equations for a plate under stress. The next step will be to invert the stress-strain relations in Table 3.1. The most tedious chore is to substitute the inverted stress-strain relations into the general equilibrium equations, and then determine by integration the shear and normal stresses.

The actual equation will result from equating the normal stresses to the intensity of the applied load at the upper surface of the plate.

Step 1: The General Equilibrium Equations

For a rigid body in equilibrium the sum of all forces and torques (moments) that act on the body must be zero:

$$\sum_i Forces = 0 \qquad \sum_i Moments = 0.$$

The general equilibrium equations that describe the plate at rest are:

$$\frac{\partial \sigma_x}{\partial x} + \frac{\partial \tau_{xy}}{\partial y} + \frac{\partial \tau_{xz}}{\partial z} = 0$$

$$\frac{\partial \sigma_y}{\partial y} + \frac{\partial \tau_{yz}}{\partial z} + \frac{\partial \tau_{xy}}{\partial x} = 0 \qquad \text{(eqns 3.10)}$$

$$\frac{\partial \sigma_y}{\partial y} + \frac{\partial \tau_{yz}}{\partial z} + \frac{\partial \tau_{xy}}{\partial x} = 0.$$

Step 2: Invert the Stress-Strain Relations

Inverting these relations expresses the plate's stresses in terms of strains, Poisson ratio, elasticity and shearing modulus.

Stress-Strain Relations	The Inversions
$\varepsilon_x = \frac{1}{E}(\sigma_x - \nu\sigma_y)$	$\sigma_x = \frac{E}{1-\nu^2}(\varepsilon_x + \nu\varepsilon_y)$
$\varepsilon_y = \frac{1}{E}(\sigma_y - \nu\sigma_x)$	$\sigma_y = \frac{E}{1-\nu^2}(\varepsilon_y + \nu\varepsilon_x)$
$\gamma_{xy} = \frac{1}{G} = \tau_{xy}$	$\tau_{xy} = G\gamma_{xy}$

Table 3.1: Inverted stress in a thin plate as a linear function of strain.

In terms of the curvature of the middle surface, the inverted relations are:

$$\sigma_x = -z\frac{E}{1-\nu^2}\left(\frac{\partial^2 w}{\partial x^2} + \nu\frac{\partial^2 w}{\partial y^2}\right) \tag{3.12}$$

$$\sigma_x = -z\frac{E}{1-\nu^2}\left(\frac{\partial^2 w}{\partial x^2} + \nu\frac{\partial^2 w}{\partial y^2}\right) \tag{3.13}$$

$$\tau_{xy} = -z\frac{E}{1-\nu^2}(1-\nu)\frac{\partial}{\partial x}\left(\frac{\partial w}{\partial y}\right) \tag{3.14}$$

The next steps will integrate the equilibrium equations, and expand the tangential shear stress and normal stress functions.

Step 3: Shear and Normal Stresses From Equilibrium Equations

The equilibrium equation can be re-written as

$$\frac{\partial \tau_{xz}}{\partial z} = -\left(\frac{\partial \sigma_x}{\partial x} + \frac{\partial \tau_{xy}}{\partial y}\right) \tag{3.15}$$

and then integrated to create equation (3.21) below:

$$\int_{\frac{h}{2}}^{z}\frac{\partial \tau_{xz}}{\partial z} = -\int_{\frac{h}{2}}^{z}\left(\frac{\partial \sigma_x}{\partial x} + \frac{\partial \tau_{xy}}{\partial y}\right) = \int_{z}^{\frac{h}{2}}\left(\frac{\partial \sigma_x}{\partial x} + \frac{\partial \tau_{xy}}{\partial y}\right) \quad \Rightarrow \quad \tau_{xz} = \int_{z}^{\frac{h}{2}}\left(\frac{\partial \sigma_x}{\partial x} + \frac{\partial \tau_{xy}}{\partial y}\right)dz \tag{3.16}$$

In order to integrate equation (3.16), the normal and shear stresses must be differentiated. The stress normal to the x-face (equation 3.12) is written in equation (3.12) as a function of middle surface displacement. Its rate of change in the x-direction is (equation (3.17)):

$$\frac{\partial \sigma_x}{\partial x} = \frac{\partial}{\partial x}\left(-z\frac{E}{1-\nu^2}\left(\frac{\partial^2 w}{\partial x^2} + \nu\frac{\partial^2 w}{\partial y^2}\right)\right) = -z\frac{E}{1-\nu^2}\frac{\partial}{\partial x}\left(\frac{\partial^2 w}{\partial x^2} + \nu\frac{\partial^2 w}{\partial y^2}\right)$$

The derivative with respect to the y-axis of the shear stress that is tangential to the x-face in the y-direction is:

$$\frac{\partial \tau_{xy}}{\partial y} = \frac{\partial}{\partial y}\left(-z\frac{E}{1-\nu^2}(1-\nu)\left(\frac{\partial}{\partial x}\frac{\partial w}{\partial y}\right)\right) \tag{3.18}$$

Substituting equations (3.16) and (3.17) into (3.18) defines τ_{xz}

$$\tau_{xz} = \int_z^{\frac{h}{2}}\left(\frac{\partial}{\partial x}\left(-z\frac{E}{1-\nu^2}\left(\frac{\partial^2 w}{\partial x^2}+\nu\frac{\partial^2 w}{\partial y^2}\right)\right)+\frac{\partial}{\partial y}\left(-z\frac{E}{1-\nu^2}(1-\nu)\left(\frac{\partial}{\partial x}\frac{\partial w}{\partial y}\right)\right)\right)dz$$

$$\tau_{xz} = -\frac{E}{(1-\nu^2)}\left[\frac{\partial}{\partial x}\left(\frac{\partial^2 w}{\partial y^2}+\frac{\partial^2 w}{\partial x^2}\right)\right]\int_z^{\frac{h}{2}} z dz.$$

The final result is:

$$\tau_{xz} = -\frac{E}{2(1-\nu^2)}\left(\frac{h^2}{4}-z^2\right)\left[\frac{\partial}{\partial x}\left(\frac{\partial^2 w}{\partial y^2}+\frac{\partial^2 w}{\partial x^2}\right)\right]. \tag{3.19}$$

The process for obtaining τ_{yz} is exactly analogous to the above development of τ_{xz}. Shearing stress acting on the y-face in the z-direction is:

$$\tau_{yz} = -\frac{E}{2(1-\nu^2)}\left(\frac{h^2}{4}-z^2\right)\left[\frac{\partial}{\partial y}\left(\frac{\partial^2 w}{\partial y^2}+\frac{\partial^2 w}{\partial x^2}\right)\right]. \tag{3.20}$$

Normal stresses that result from a z-direction load applied to the surface of the thin plate are found by using the third of the equations of equilibrium:

$$\frac{\partial \sigma_z}{\partial z}+\frac{\partial \tau_{xz}}{\partial x}+\frac{\partial \tau_{yz}}{\partial y} = 0. \tag{3.10}$$

$$\sigma_z = \int_z^{h/2}\left(\frac{\partial \tau_{xz}}{\partial x}+\frac{\partial \tau_{yz}}{\partial y}\right)dz. \tag{3.21}$$

Integrating the above equation develops a fourth-order, partial differential equation that defines bending in a thin plate. To do this integration it is necessary to first differentiate the z-direction shear stresses. While this protracted derivation may be causing a loss of any intuitive feel, the development of the plate equation from this point onward is straight forward. All that remains is to differentiate the shear stresses that constitute, along with the z-face normal stress, one of the general equations of equilibrium of a plate at rest. Differentiating the shear stress (equations (3.19) and (3.20) above) that acts on the x-face in the z-direction yields:

$$\frac{\partial \tau_{xz}}{\partial x} = -\frac{E}{2(1-\nu^2)}\left(\frac{h^2}{4} - z^2\right)\left[\frac{\partial^2}{\partial x^2}\left(\frac{\partial^2 w}{\partial y^2} + \frac{\partial^2 w}{\partial x^2}\right)\right]. \tag{3.22}$$

Differentiating the stress that acts on the y-face in the z-direction produces:

$$\frac{\partial \tau_{yz}}{\partial y} = -\frac{E}{2(1-\nu^2)}\left(\frac{h^2}{4} - z^2\right)\left[\frac{\partial^2}{\partial y^2}\left(\frac{\partial^2 w}{\partial y^2} + \frac{\partial^2 w}{\partial x^2}\right)\right]. \tag{3.23}$$

From (3.21), the vertical normal stress σ_z is:

$$\sigma_z = \int_z^{h/2}\left(\frac{\partial \tau_{xz}}{\partial x} + \frac{\partial \tau_{yz}}{\partial y}\right)dz.$$

Substituting the results of equations (3.22) and (3.23) into (3.21) produces z-axis normal stress:

$$\sigma_z = \int_z^{\frac{h}{2}} dz\left[-\frac{E}{2(1-\nu^2)}\left(\frac{h^2}{4} - z^2\right)\right]\left[\left[\frac{\partial^2}{\partial x^2}\left(\frac{\partial^2 w}{\partial y^2} + \frac{\partial^2 w}{\partial x^2}\right)\right] + \left[\frac{\partial^2}{\partial y^2}\left(\frac{\partial^2 w}{\partial y^2} + \frac{\partial^2 w}{\partial x^2}\right)\right]\right]$$

$$\sigma_z = \int_z^{\frac{h}{2}} dz\left[-\frac{E}{2(1-\nu^2)}\left(\frac{h^2}{4} - z^2\right)\right]\left[\left(\frac{\partial^2}{\partial x^2} + \frac{\partial^2}{\partial y^2}\right)\left(\frac{\partial^2 w}{\partial y^2} + \frac{\partial^2 w}{\partial x^2}\right)\right]$$

$$\sigma_z = \int_z^{\frac{h}{2}} dz\left[-\frac{E}{2(1-\nu^2)}\left(\frac{h^2}{4} - z^2\right)\right]\left[\nabla^4 w\right]. \tag{3.24}$$

The operators ∇^2 and ∇^4 are defined to be:

$$\nabla^2 w = \left(\frac{\partial^2}{\partial x^2} + \frac{\partial^2}{\partial y^2}\right) w \qquad \text{and} \qquad \nabla^4 w = \left(\frac{\partial^2}{\partial x^2} + \frac{\partial^2}{\partial y^2}\right)^2 w \ .$$

Completing the integral using the del operator yields:

$$\sigma_z = -\frac{E}{2(1-\nu^2)} \nabla^4 w \int_z^{\frac{h}{2}} \left(\frac{h^2}{4} - z^2\right) dz$$

$$\sigma_z = -\frac{E}{2(1-\nu^2)} \nabla^4 w \left[\frac{h^2}{12} - \frac{h^2}{4} z + \frac{z^3}{3}\right]. \tag{3.25}$$

This equation shows that the normal stress applied to the surface of the thin plate is a parabolic function of distance in the z-direction. The stress varies proportionately with the cube of the depth of the plate.

Note that according to these definitions, z=-h/2 represents the upper surface of the plate. By setting z=-h/2 in the above stress equation, the intensity of the applied load is:

$$\sigma_z\left(z = -\frac{h}{2}\right) \Rightarrow q = \frac{E}{(1-\nu^2)} \frac{h^3}{12} \nabla^4 w.$$

The elasticity, Poisson ratio and vertical-position constants can be combined into a quantity called the "flexural rigidity", or D.

$$D = \frac{E}{(1-\nu^2)} \frac{h^3}{12}$$

The final form of the equation is a fourth order equation that describes a plate's surface deflections in terms of load per unit area.

$$q = D\left(\frac{\partial^4 w}{\partial x^4} + 2\frac{\partial^4 w}{\partial x^2 \partial y^2} + \frac{\partial^4 w}{\partial y^4}\right) = D\nabla^4 w. \tag{3.26}$$

3.2 Plate Equation for a Circular Plate

The expeditious way to develop the equation that describes deflections in circular plates is to assume a symmetric load distribution centered at the middle (r=0) of the of the circular plate. This assumption grants the use of θ symmetry and allows a clean transformation of the Bi-Laplacian (eqn 3.26) from Cartesian to polar coordinates. The result is

$$\frac{d^2}{d^2r}\left(r\frac{d^2w}{dr^2}\right)-\frac{d}{dr}\left(\frac{1}{r}\frac{dw}{dr}\right)=\frac{rq}{D}. \tag{3.27}$$

Here, "r" is the radius of the plate, "w" is the deflection function, "q" is the load per unit area, and "D" is the flexural rigidity. Equation (3.26) is re-written as

$$\nabla^4 w(r)=\frac{q}{D}. \tag{3.28}$$

A more useful form of the above equation allows a simplified integration. The final radial plate equation is:

$$\frac{1}{r}\frac{d}{dr}\left\{r\frac{d}{dr}\left[\frac{1}{r}\frac{d}{dr}\left(r\frac{dw}{dr}\right)\right]\right\}=\frac{q}{D} \tag{3.29}$$

The solution functions to the radial plate equation rely heavily on the equilibrium boundary conditions for shear forces and moments. The simple coordinate transformation provides no additional insight into the physics of the plate's deflections, but additional insight is not necessarily needed. The effort to work through a physical derivation of the equation based on conditions of static equilibrium is both redundant and extremely time consuming. Instead, this paper will look at certain analytical examples in order to verify the accuracy of the finite element modeling of the MDM/Hiltner 2.4 meter primary mirror.

Chapter 4

Beam and Plate

Analytical Solutions

This chapter solves six beam and two plate problems using the technical theory of bending. These analytical solutions provide a bench-mark for testing the veracity of the numerical techniques of finite element modeling.

All beam solutions assume that there is zero y- and z-direction strain. The plate problems assume zero z-direction strain. It is also assumed that the beams and plates are thin - length is much greater than depth.

4.1 Analytical Solutions to the Beam Equation

The following series of examples solves the beam equation for the cases of cantilever and simply supported beams under point and uniform loads.

4.1.1 Cantilever Beam with a Point Load

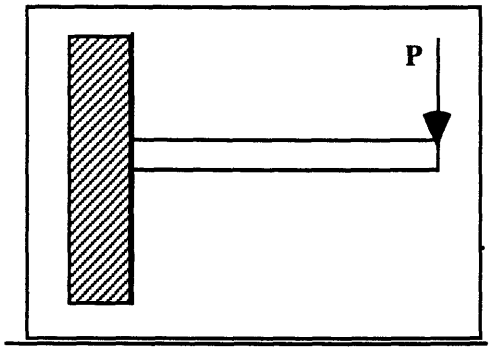

Figure 4.1: Cantilever beam with a point load at beam's end.

The bending moment generated by a point load at the beam's end is

$$EI\frac{d^2v}{dx^2} = -P(x-l). \qquad \Rightarrow \qquad EI\frac{dv}{dx} = \frac{-Px^2}{2} + Plx + c_1 .$$

The slope at the point where the beam meets the wall (x=0) is zero, so, $c_1 = 0$:

$$EIv(x) = \frac{-Px^3}{6} + \frac{Plx^2}{2} + c_2.$$

Deflection at x = 0 is also zero: $v(x=0) = 0,$ *and* $c_2 = 0,$ The final results are,

$$v(x) = \frac{P}{EI}\left(\frac{-x^3}{6} + \frac{lx^2}{2}\right)$$

$$v(x=l) = \frac{Pl^3}{3EI}$$

$$v\left(x = \frac{l}{2}\right) = \frac{5Pl^3}{48EI}.$$

4.1.2 Cantilever Beam With Uniform Load

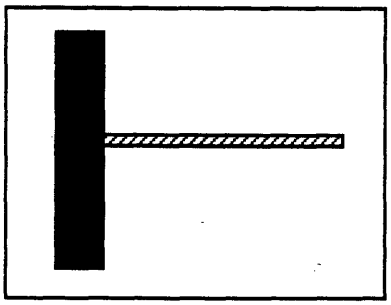

Figure 4.2: Cantilever beam under the influence of gravity, a uniform load distribution.

This example is most easily solved by applying the fourth order beam equation. The fourth order beam equation is in units of force per unit length:

$$EI\frac{d^4v}{dx^4} = p_0.$$

The first integration yields shearing force, which equals zero at the free end:

$$EI\frac{d^3v}{dx^3} = p_0x + c_1, \qquad v'''(x=l) = 0 \qquad \Rightarrow \qquad c_1 = -p_0l.$$

The second integration yields the moment, which is also zero at the free end:

$$EI\frac{d^2v}{dx^2} = p_0\frac{x^2}{2} - p_0lx + c_2, \quad v''(x=l) = 0 \Rightarrow \qquad c_2 = \frac{p_0}{2}l^2.$$

The moment for the uniformly loaded beam is

$$EI\frac{d^2v}{dx^2} = \frac{p_0x^2}{2} - p_0lx + \frac{p_0l^2}{2}.$$

The boundary conditions at x=0 ensure that the last two constants of integration are zero: $v'(x=0) = v(x=0) = 0$ The final integrations yield:

$$EI\frac{dv}{dx} = \frac{p_0x^3}{6} - \frac{p_0lx^2}{2} + \frac{p_0l^2x}{2}, \qquad EIv(x) = \frac{p_0x^4}{24} - \frac{p_0lx^3}{6} + \frac{p_0l^2x^2}{4},$$

$$EIv(x) = p_0\left(\frac{x^4}{24} - \frac{lx^3}{6} + \frac{l^2x^2}{4}\right).$$

At the free end the deflection is

$$v(x=l) = \frac{p_0}{EI}\left(\frac{x^4}{24} - \frac{lx^3}{6} + \frac{l^2x^2}{4}\right) = \frac{p_0 l^4}{8EI}.$$

At the beam's center the deflection is

$$v(x=l/2) = \frac{p_0 l^4}{24EI}\left(\frac{17}{16}\right).$$

4.1.3 Cantilever Beam, Distributed and Point Loads

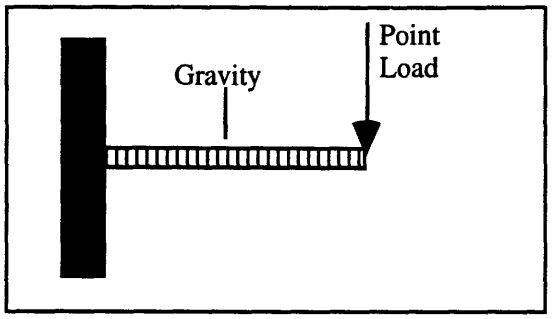

Figure 4.3: Cantilever beam under point and gravity loads.

This case is solved using superposition. From Sections 4.1.1 and 4.1.2,

$$v(x)_I = \frac{P}{EI}\left(\frac{-x^3}{6} + \frac{lx^2}{2}\right), \qquad v(x)_{II} = \frac{p_0}{EI}\left(\frac{x^4}{24} - \frac{lx^3}{6} + \frac{l^2x^2}{4}\right).$$

The superposition of the two equations yields a result for the combined case:

$$v(x)_{III} = \frac{P}{EI}\left(\frac{-x^3}{6} + \frac{lx^2}{2}\right) + \frac{p_0}{EI}\left(\frac{x^4}{24} - \frac{lx^3}{6} + \frac{l^2x^2}{4}\right).$$

4.1.4 Simply Supported Beam & A Distributed Force

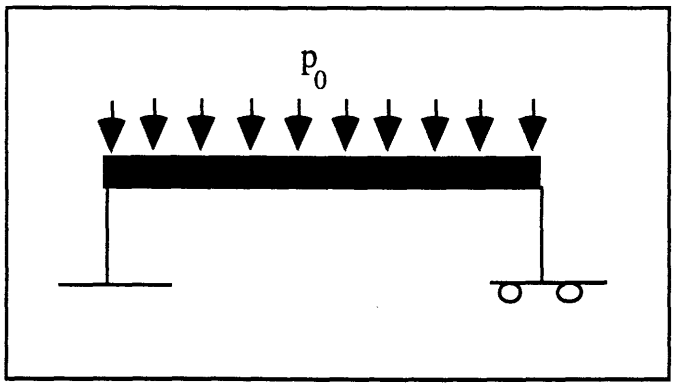

Figure 4.4: Simply supported beam under a uniform (gravity) load p_0.

The above diagram depicts a straight beam composed of uniform material that is simply supported at both its ends. The support at the right end is on wheels which allows the right end of the beam to move slightly to the left as the beam bends. Without these wheels the x-direction stress induced by the uniform load would cause a lateral force that would pull on the supports. The bending moments about the z axis that result from stress in the x-direction are:

$$M_{xz} = EI_z \frac{d^2v}{dx^2}.$$

The moment has two components. One results from the left support, or

$$torque = radius\, x\, force = x \times \left(\frac{-pl}{2}\right).$$

The other component results from the cumulative effect of incremental mass acting at a distance "x", or

$$torque = radius\, x\, force = (x)\int_0^x pdx = \frac{px^2}{2}.$$

Total bending moment at the point "x" is the sum of the component torques:

$$M_{xz} = \frac{-plx}{2} + \frac{px^2}{2}.$$

Solving through integration yields:

$$EI_z \frac{d^2v}{dx^2} = \frac{-plx}{2} + \frac{px^2}{2}, \quad \Rightarrow \quad EI_z \frac{dv}{dx} = \frac{-plx^2}{4} + \frac{px^3}{6} + C_1,$$

$$EI_z v(x) = \frac{-plx^3}{12} + \frac{px^4}{24} + C_1 x + C_2.$$

Constants are determined by applying boundary conditions at the beam's ends:

$$v(x=0) = 0, \quad \therefore \quad C_2 = 0 \qquad v(x=l) = 0, \quad \therefore \quad \frac{-pl^4}{12} + \frac{pl^4}{24} + C_1 l = 0$$

$$\frac{-pl^3}{12} + \frac{pl^3}{24} + C_1 = 0, \quad \Rightarrow \quad C_1 = \frac{pl^3}{24}.$$

The final equation for this simply supported beam under a uniform load is:

$$EI_z v(x) = \frac{-2plx^3}{24} + \frac{px^4}{24} + \frac{pl^3}{24}x \quad \Rightarrow \quad EI_z v(x) = \frac{-2plx^3}{24} + \frac{px^4}{24} + \frac{pl^3}{24}x.$$

4.1.5 Simply Supported Beam With Center Point Load

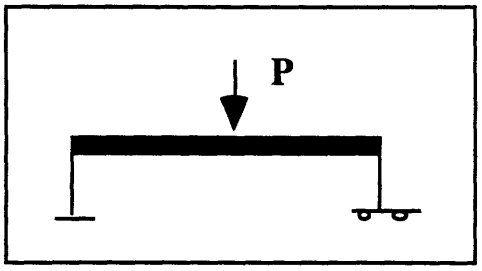

Figure 4.5 Simply supported beam under a point load at $x = l/2$.

The above diagram depicts a simply supported beam under the stress of a delta function point load at its mid-point. It is important to note that in this example, the only force experienced by the beam is this delta force applied at the beam's mid-point. There is no distributed, or "body" force. Hence, when setting up the delta functions in the fourth order equation, the only force supported by the simple supports is the delta force at the beam's mid-point.

The beam equation equates displacement to force per unit length:

$$EI\frac{d^4v}{dx^4}=\frac{P}{2}\{x\}^{-1}+P\left\{x-\frac{l}{2}\right\}^{-1}.$$

The integration gives

$$EI\frac{d^3v}{dx^3}=\frac{P}{2}\{x\}^{0}+P\left\{x-\frac{l}{2}\right\}^{0}+c_1. \qquad EI\frac{d^2v}{dx^2}=\frac{P}{2}\{x\}^{1}+P\left\{x-\frac{l}{2}\right\}^{1}+c_1x+c_2.$$

The boundary conditions show that there is no moment at x=0, so c_2=0. Also, there is no moment at the right hand side, or at $x=l$. Therefore,

$$v''(x=l)=0=\frac{P}{2}(l)+P\left(\frac{l}{2}\right)+c_1l$$

and $c_1=-P$. The second and first order equations become

$$EI\frac{d^2v}{dx^2}=\frac{P}{2}\{x\}^{1}+P\left\{x-\frac{l}{2}\right\}^{1}-Px \qquad EI\frac{dv}{dx}=\frac{P}{4}\{x\}^{2}+\frac{P}{2}\left\{x-\frac{l}{2}\right\}^{2}-P\frac{x^2}{2}+c_3$$

and, finally, $$EIv(x)=\frac{P}{12}\{x\}^{3}+\frac{P}{6}\left\{x-\frac{l}{2}\right\}^{3}-P\frac{x^3}{6}+c_3x+c_4.$$

At x = 0 and x = 1 the beam's deflection is zero. Therefore, $c_4=0$.

$$v(x=l)=0=\frac{P}{12}l^3+\frac{P}{6}\left(\frac{l}{2}\right)^3-\frac{Pl^3}{6}+c_3l \quad \Rightarrow \quad c_3=\frac{3Pl^2}{48}.$$

The final deflection is:

$$EIv(x)=\frac{P}{12}\{x\}^{3}+\frac{P}{6}\left\{x-\frac{l}{2}\right\}^{3}-\frac{Px^3}{6}+\frac{3Pl^2}{48}x.$$

Maximum deflection is at the point where the first derivative is equal to zero.

$$EIv(x)=\frac{P}{12}\{x\}^{3}+\frac{P}{6}\left\{x-\frac{l}{2}\right\}^{3}-\frac{Px^3}{6}+\frac{3Pl^2}{48}x.$$

4.1.6 Simply Supported Beam, Gravity & Point Load

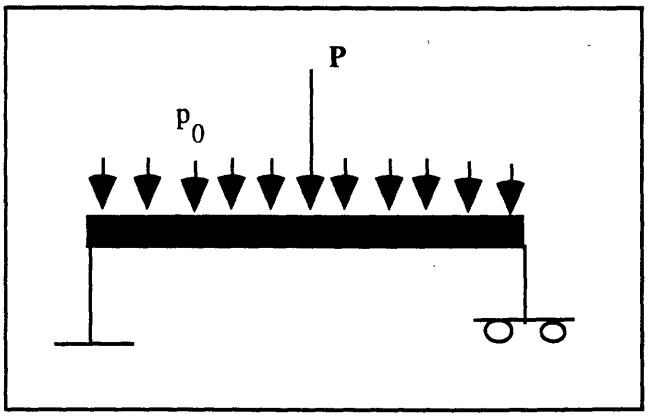

Figure 4.6: Simply supported beam under the influence of a point load (P) and gravity (p_0 = force/unit length).

Total deflection of the simply supported beam under both point and distributed loads can be determined through the superposition of the two previously solved cases. The two independent deflection equations are

$$EI_z v(x) = \frac{plx}{24}\left(\frac{x^3}{l} - 2x^2 + l^2\right)$$

$$EIv(x) = \frac{P}{12}\{x\}^3 + \frac{P}{6}\left\{x - \frac{l}{2}\right\}^3 - \frac{Px^3}{6} + \frac{3Pl^2}{48}x$$

Superposition produces the result:

$$v(x) = \frac{plx}{24EI_z}\left(\frac{x^3}{l} - 2x^2 + l^2\right) + \frac{P}{EI_z}\left(\frac{1}{12}\{x\}^3 + \frac{1}{6}\left\{x - \frac{l}{2}\right\}^3 - \frac{x^3}{6} + \frac{3l^2x}{48}\right)$$

At the beam's mid-point, $x = \frac{l}{2}$, the equation simplifies to

$$EI_z v\left(x = \frac{l}{2}\right) = \frac{pl^2}{96}\left(l^2 + 1\right) + \frac{Pl^3}{48}.$$

4.2 Radial Plate Analytical Solutions

The radial plate equation is a bi-Laplacian:

$$\nabla^4 w(r,\theta) = \frac{q}{D}.$$

For cases of axial symmetry, the plate equation can be grouped into a more easily integrated form:

$$\frac{1}{r}\frac{d}{dr}\left\{r\frac{d}{dr}\left[\frac{1}{r}\frac{d}{dr}\left(r\frac{dw}{dr}\right)\right]\right\} = \frac{q}{D}.$$

The first and second integrations yield

$$r\frac{d}{dr}\left[\frac{1}{r}\frac{d}{dr}\left(r\frac{dw}{dr}\right)\right] = \frac{q}{D}\int r dr = \frac{q}{D}\left(\frac{r^2}{2} + c_1\right),$$

$$\frac{1}{r}\frac{d}{dr}\left(r\frac{dw}{dr}\right) = \frac{q}{D}\int\frac{1}{r}\left(\frac{r^2}{2} + c_1\right)dr = \frac{q}{D}\int\left(\frac{r}{2} + \frac{c_1}{r}\right)dr = \frac{q}{D}\left(\frac{r^2}{4} + c_1\ln r + c_2\right).$$

The second result is simply

$$\frac{1}{r}\frac{d}{dr}\left(r\frac{dw}{dr}\right) = \frac{q}{D}\left(\frac{r^2}{4} + c_1\ln r + c_2\right).$$

Integrating again,

$$r\frac{dw}{dr} = \frac{q}{D}\int\left(\frac{r^3}{4} + c_1 r\ln r + c_2 r\right)dr$$

which becomes

$$r\frac{dw}{dr} = \frac{q}{D}\left(\frac{r^4}{16} + c_1\frac{r^2}{2}\left(\ln r - \frac{1}{2}\right) + c_2\frac{r^2}{2} + c_3\right).$$

This gives the function's slope:

$$\frac{dw}{dr} = \frac{qr}{D}\left(\frac{r^4}{16} + c_1\frac{r^2}{2}\left(\ln r - \frac{1}{2}\right) + c_2\frac{r^2}{2} + c_3\right).$$

The slope integrates to the displacement function:

$$w(r) = \frac{q}{D}\left(\frac{r^4}{64} + \frac{c_1 r^2}{4}\ln r - \frac{c_1 r^2}{4} + c_2\frac{r^2}{4} + c_3 \ln r + c_4\right).$$

4.3.1 Solution to a Plate Clamped at the Edges

If a plate is clamped at its edges, it will have no linear or rotational motion at any point along its outer radius, r = R. Therefore the displacement at the plate's edge is zero, w(r = R) = 0, and the slope at the plate's edge is zero, w'(r = R) = 0.

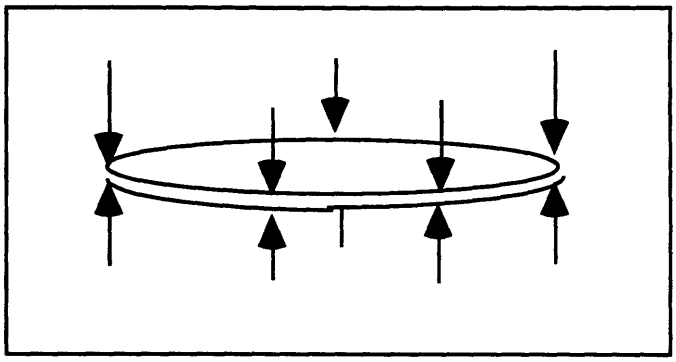

Figure 4.8: Plate clamped around its edges.

Knowing that both slope and displacement are zero at the plate's edge greatly simplifies the plate equation. Since, at r = 0, ln r = ln 0, and since ln 0 = ∞, then C_1 and C_3 both must equal zero. This simplifies the equation for a clamped plate:

$$w(r) = \frac{q}{D}\left(\frac{r^4}{64} + c_2\frac{r^2}{4} + c_4\right).$$

The boundary condition that determines the coefficient c_2 is the fact that at the edge (where r = R), the slope is zero:

$$\frac{dw}{dr} = 0 = \frac{q}{D}\left(\frac{R^3}{16} + c_2\frac{R}{2}\right), \qquad c_2 = -\frac{R^2}{8}.$$

The displacement is zero at the edge:

$$w(r = R) = 0 = \frac{q}{D}\left(\frac{R^4}{64} - \frac{R^2}{8}\frac{R^2}{4} + c_4\right).$$

This makes it possible to isolate the remaining coefficient:

$$0 = \frac{R^4}{64} - \frac{R^4}{32} + c_4, \qquad c_4 = \frac{R^4}{64}.$$

The displacement function for a clamped axi-symmetric plate is:

$$w(r) = \frac{q}{64D}\left(\frac{r^4}{64} - \frac{R^2r^2}{32} + \frac{R^4}{64}\right)$$

$$w(r) = \frac{q}{64D}\left(r^2 - R^2\right)^2.$$

The clamped plate will attain its maximum deflection at its center (r = 0):

$$w(r = 0) = \frac{qR^4}{64D}.$$

4.3.2 Solution for a Simply Supported Plate

The simply supported plate offers several boundary conditions that expedite finding an analytical solution. At the plates edge, (r = R), the plate will have zero deflection. The plate will have a moment of zero at the edge because there is no restriction on the edge's rotational freedom. And, finally, slope is zero at r = 0 in the case of a symmetrically loaded, thin circular plate.

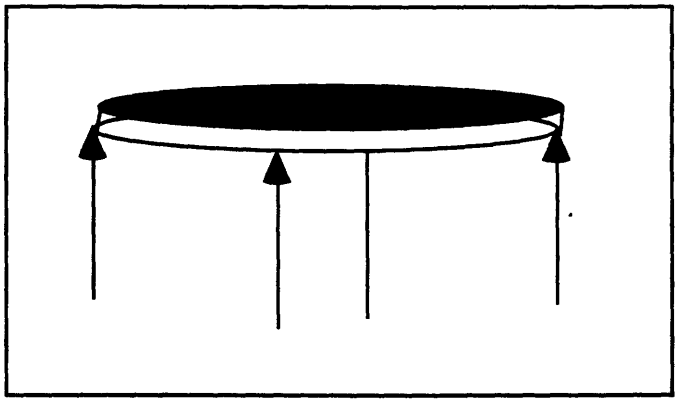

Figure 4.9: Simply supported plate under its own weight.

The general solution to the plate equation is

$$w(r)=\frac{q}{D}\left(\frac{r^4}{64}+\frac{c_1 r^2}{4}\ln r-\frac{c_1 r^2}{4}+c_2\frac{r^2}{4}+c_3\ln r+c_4\right).$$

As in the case of the clamped plate, the coefficients c_1 *and* c_3 are zero because ln r cannot equal infinity. This simplifies the general solution:

$$w(r)=\frac{q}{D}\left(\frac{r^4}{64}+\frac{c_2 r^2}{4}+c_4\right)$$

The moment at the plate's edge is:

$$M_r=-D\left(\frac{dw}{dr}+\frac{\nu}{r}\frac{dw}{dr}\right).$$

Using the above equation for w(r), the moment is written

$$M_r = -D\left(\frac{q}{D}\left(\frac{3r^2}{16}+\frac{c_2}{2}\right)+\frac{\nu}{r}\frac{q}{D}\left(\frac{r^3}{16}+\frac{c_2}{2}\right)\right).$$

Evaluated at r = R, the moment is zero:

$$M_r\big|_{r=R} = 0 = \frac{3R^2}{16}+\frac{c_2}{2}+\frac{\nu R^2}{16}+\frac{\nu c_2}{2}.$$

$$0 = \frac{R^2}{8}(3+\nu)+c_2(1+\nu).$$

It is possible to isolate the second coefficient:

$$\frac{-R^2}{8}\frac{(3+\nu)}{(1+\nu)} = \frac{-\beta R^2}{8} = c_2, \qquad \text{where} \qquad \beta = \frac{(3+\nu)}{(1+\nu)}.$$

At r = R, the displacement is zero:

$$w(r=R) = 0 = \frac{q}{D}\left(\frac{R^4}{64}-\frac{2R^4\beta}{64}+c_4\right).$$

The result for the final coefficient is: $-\frac{R^4}{64}(1-2\beta) = c_4.$

An analytical solution for the simply supported circular plate is:

$$w(r) = \frac{q}{64D}\left(r^4-2\beta R^2 r^2+2R^4\beta-R^4\right).$$

For the maximum deflection at r = 0, the deflection equation is

$$w(r=0) = \frac{q}{64D}\left(-R^4+2\beta R^4\right) = \frac{qR^4}{64D}(2\beta-1).$$

Chapter 5

Finite Element Analysis

The analytical methods developed in the previous sections on structural mechanics describe stress and displacement in terms of partial differential equations. For problems of beams and plates under asymmetric loads, analytical methods quickly become cumbersome.

The MDM primary mirror, while homogeneous and continuous, creates a challenging analytical problem. The mirror varies in thickness as a result of its hyperbolic figure and thus exhibits a non-uniform mass distribution. The mirror's axial support system includes three hard point supports that anchor the mirror's translational movement and produce local point loads on the mirror's back surface. The combination of non-uniform mass distribution, hard point axial supports, and a desire to test the mirror with asymmetric loads makes closed form mathematical treatment difficult. The alternative is a numerical technique called finite element analysis.

This chapter describes the basic concepts of the finite element method and briefly introduces the NASTRAN code before applying FEA and NASTRAN to the same beam and plate examples previously solved analytically.

5.1 Conceptual Finite Element Analysis

Finite element analysis is a numerical procedure for solving continuum mechanics problems that is commonly used by engineers. The essence of the finite element method is a series of linear equations that create a piece-wise approximation of a mechanical structure that, together with boundary conditions, are solved to find displacements and stress fields. The primary tool used in this thesis for analyzing the MDM primary mirror's structural properties is the NASTRAN finite element code.

The finite element model's linear equations include information about model geometry, applied forces, and material properties such as stiffness, density, and Poisson ratio. The FEA method breaks a structure down into many small subregions, or elements. The elements are defined and interconnected by nodes. The nodes are exercised by the linear equations and simulate a structure's response to force. The sum of the nodal displacements determines the model's structural behavior.

5.1.1 Introduction to The Finite Element Method

Section (5.1.1) introduces FEA using a plane truss model. The section demonstrates how a structure can be modeled as an assembly of small elements, how the so-called "stiffness" matrix is produced, and how such a matrix is used to solve structural problems.

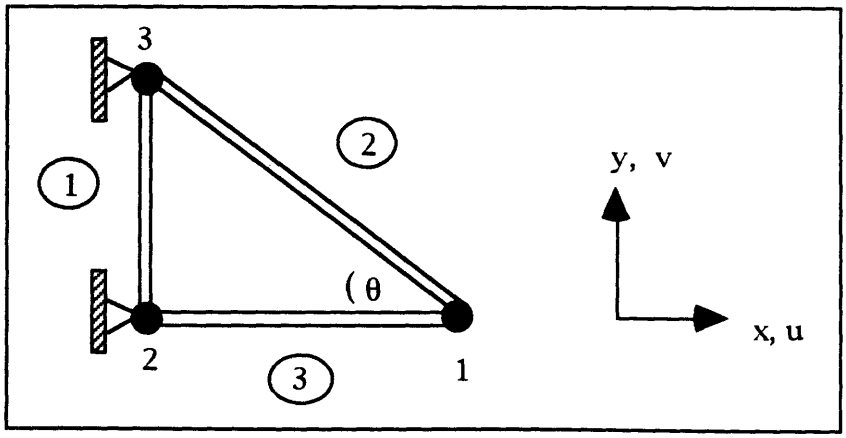

Figure 5.1: Plane truss. Nodes and elements numbered arbitrarily.

Figure 5.1 is an example of a direct physical argument that illustrates the finite element method. (Ref 7) For any node "i" (i = 1, 2, 3) in Figure 5.1, the x-axis displacement is labeled "u_i", and the y-axis displacement is labeled "v_i". For any bar element "i", A_i = cross-sectional area, E_i = elasticity, and L_i= length. The axial force F_i and change in length e_i of any of the three bars are related by the expression

$$e_i = \frac{F_i L_i}{A_i E_i}, \tag{5.1}$$

Equation (5.1) is derived from the stress-strain relation:

$$\frac{e_i}{L_i} = strain = \frac{1}{E_i} stress.$$

Stiffness is defined as the ratio of force to displacement and is assigned the symbol "k_i". For the bar element "i", the stiffness is

$$k_i = \frac{F_i}{e_i}. \tag{5.2}$$

A degree of freedom (d.o.f.) is defined as the displacement or rotation of a node. Then for any element "i" in a set of "m" elements, where each node has "n" degrees of freedom, and each node suffers a general displacement "d", the following equations hold:

$$\begin{aligned}
&k_{11}d_1 + k_{12}d_2 + \ldots\ldots + k_{1n}d_n = \bar{r}_1 \\
&k_{21}d_1 + k_{22}d_2 + \ldots\ldots + k_{2n}d_n = \bar{r}_2 \\
&\quad\bullet \quad\quad \bullet \quad\quad \bullet \quad \bullet \\
&\quad\bullet \quad\quad \bullet \quad\quad \bullet \quad \bullet \\
&k_{i1}d_1 + k_{i2}d_2 + \ldots\ldots + k_{in}d_n = \bar{r}_i \\
&\quad\bullet \quad\quad \bullet \quad\quad \bullet \quad \bullet \\
&\quad\bullet \quad\quad \bullet \quad\quad \bullet \quad \bullet \\
&k_{m1}d_1 + k_{m2}d_2 + \ldots\ldots + k_{mn}d_n = \bar{r}_m .
\end{aligned} \tag{5.3}$$

Equations (5.3) can be summarized in matrix form

$$[\mathbf{K}]\{\mathbf{d}\} = \{\mathbf{r}\} \tag{5.4}$$

where $[\mathrm{K}]$ is the element stiffness matrix, $\{\mathbf{d}\}$ is the element nodal displacement vector, and $\{\mathbf{r}\}$ is the vector of element nodal loads. Equation (5.4) can be solved for the displacement vector $\{\mathbf{d}\}$. This is a solution for all nodal displacements and element deformations. From the deformations, it is possible to compute the stresses, and a complete structural solution is obtained.

5.1.2 Explicit Plane Truss and the Stiffness Method

Figure 5.1 is a two-dimensional truss, each node with two translational degrees of freedom. If a force of unit magnitude is applied in the positive x-direction to node 1, four other force applications will be required to maintain truss static equilibrium. The goal of this example is to set up the calculation of forces that must be applied to maintain static equilibrium given the stiffness and displacement matrices that describe the three bar truss.

Force is equal to the bar element stiffness constant "k" multiplied by the associated element displacement. The applied force moves node 1 to the right, stretching bar element 3 by an amount

$$e_3 = u_1$$

and stretching bar element 2 by an amount

$$e_2 = u_1 \cos\theta.$$

The forces along the two individual bar axis are thus

$$F_3 = k_3 e_3 = k_3 u_1$$

$$F_2 = k_2 e_2 = k_2 u_1 \cos\theta \ .$$

The force required to stretch bar element 2 can be broken down into horizontal and vertical components:

$$F_{2x} = k_2 u_1 \cos^2\theta \qquad \text{(horizontal)}$$

$$F_{2y} = k_2 u_1 \cos\theta \sin\theta. \qquad \text{(vertical)}$$

These component forces are summarized graphically in Figure 5.2.

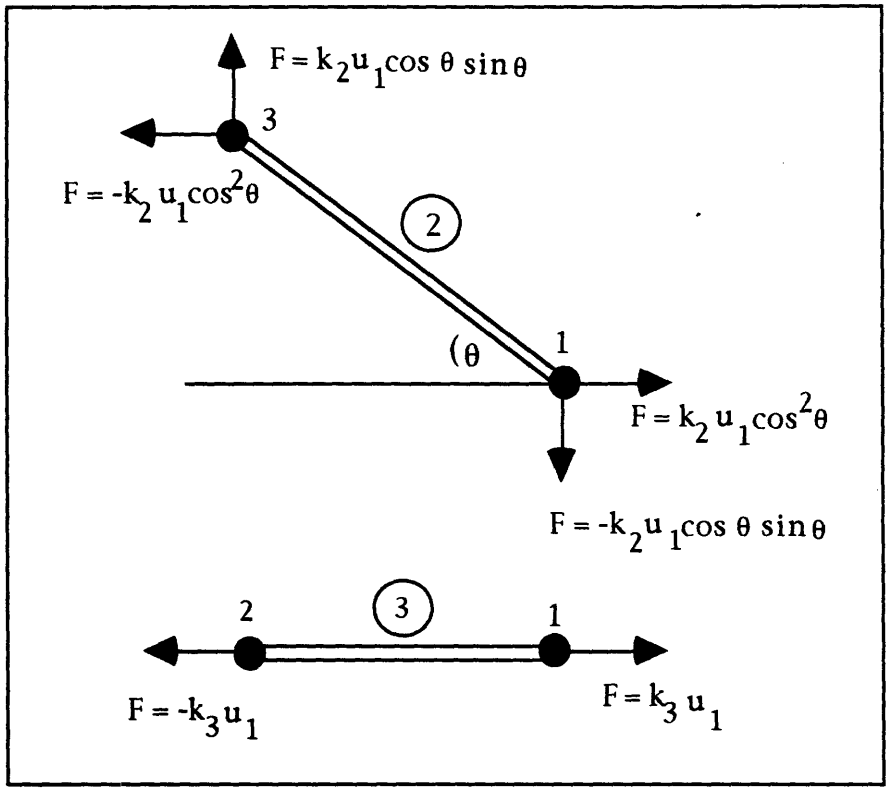

Figure 5.2: Forces required to maintain static equilibrium in the displacement state $\{\mathbf{D}\} = \{\mathbf{u_1\ 0\ 0\ 0\ 0}\}$.

If $[\mathbf{K}_1]$ represent the stiffness matrix for displacement u_1, the forces acting to maintain static equilibrium for the unit displacement are :

$$[\mathbf{K}_1]u_1 = \begin{bmatrix} k_3 + k_2\cos^2 q & -k_2\cos q\sin q & -k_3 \\ 0 & -k_2\cos^2 q & k_2\cos q\sin q \end{bmatrix} u_1$$

Given three nodes, each with two d.o.f., there are six unit displacement possibilities. Let the force vectors for those six displacements be

$$[\mathbf{K}_2], [\mathbf{K}_3], [\mathbf{K}_4], [\mathbf{K}_5], \text{ and } [\mathbf{K}_6].$$

Nodal forces are the sum of the six cases:

$$[\mathbf{K}_1\ \mathbf{K}_2\ \mathbf{K}_3\ \mathbf{K}_4\ \mathbf{K}_5\ \mathbf{K}_6]\begin{Bmatrix} u_1 \\ v_1 \\ u_2 \\ v_2 \\ u_3 \\ v_3 \end{Bmatrix} = \begin{Bmatrix} p_1 \\ q_1 \\ p_2 \\ q_2 \\ p_3 \\ q_3 \end{Bmatrix}. \tag{5.5}$$

In a standard abbreviation, the structure stiffness equation is

$$[\mathbf{K}]\{\mathbf{D}\} = \{\mathbf{R}\}. \tag{5.6}$$

If the applied forces are known, it is possible to obtain the nodal displacements by inverting the stiffness matrix.

5.1.3 Utility of Direct Physical Argument

The trouble with the method of direct physical argument is that the stiffness matrix is generated by analyzing the structure in its entirety. This is a brute force approach.

A more theoretical and general approach to describing finite element methodology uses the system's total potential energy. The next section addresses total potential energy and its application within the FEA method. The operational details of building the finite element matrices and solving the ensuing equations are not trivial. The numerical method is best suited to digital computers, pre-processors and FEA codes such as NASTRAN.

5.2 Energy Methods

The use of direct physical arguments for constructing finite element models is effective only for such simple systems as beams and bars. To model more complex systems one must be able to reduce the continuum problem to one with a finite number of d.o.f.'s.

The alternative to direct physical argument is an energy form of the Raleigh-Ritz method. (Ref 8) The energy method expresses the total potential energy of a mechanical system as a function of displacements, and then works to minimize the total potential energy with respect to a set of general coordinates in order to approximate displacements and stress fields. The finite element Rayleigh-Ritz method uses interpolation to express the displacements of each point in a continuum in terms of a finite number of degrees of freedom. This combination of energy method and interpolation has the advantage of not requiring a particular geometry or a specific number of degrees of freedom.

5.2.1 Energy Method Definitions

A "system" is defined to include a structure and all the forces acting on that structure. The system is "conservative" if, when displaced and then returned to the initial configuration, the forces involved do zero net work.

The "compatibility condition" is the condition that a displacement field is continuous and single valued. No cracks appear in stretching, no kinks appear in bending, and no parts overlap one another.

The concept of "current potential energy" describes the system's current energy state and disregards any prior or future state.

A configuration or a displacement field is "admissible" if it violates neither internal compatibility nor essential boundary conditions.

5.2.2 The Principle of Minimum Potential Energy

The Principle of Minimum Potential Energy states that "among all admissible configurations of a conservative system, those that satisfy the equations of equilibrium make the potential energy stationary with respect to small variations in displacement. If the stationary condition is a minimum, the equilibrium state is stable." (Ref. 9) Minimum potential energy is best explained with an example. Consider the system in Figure 5.4:

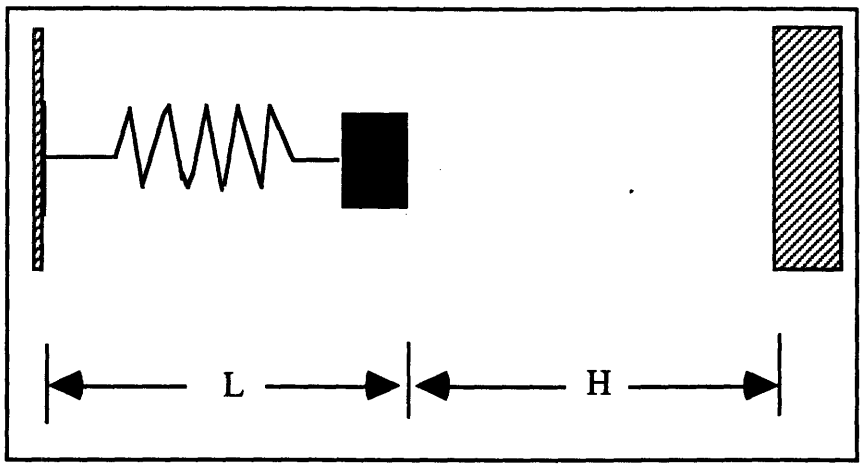

Fig 5.4 A: Unstretched linear spring of stiffness "k".

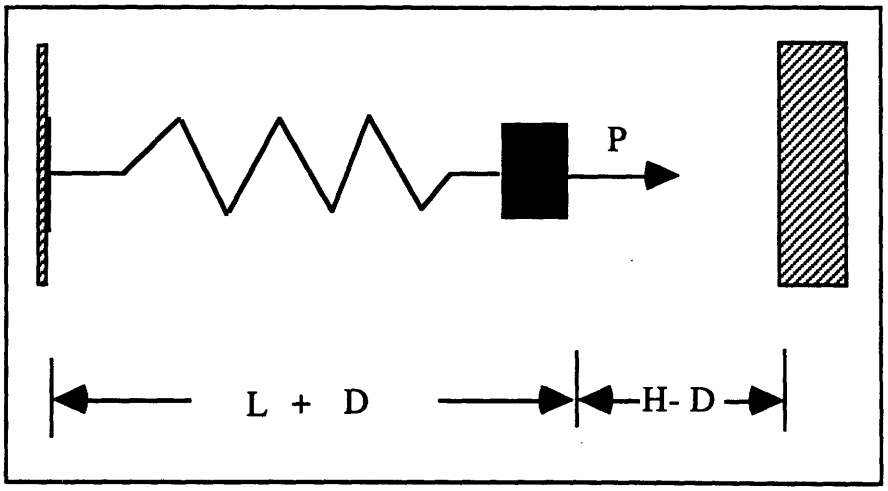

Fig 5.4 B: Stretched linear spring of stiffness "k".

The system in Figure 5.4 is conservative: it will do zero net work in the course of moving back and forth. Its one degree of freedom defines all admissible configurations. The potential energy of the stretched spring is

$$\Pi_p = \frac{1}{2}kD^2 + P(H-D), \tag{5.7}$$

where Π_p is the symbol for potential energy, $\frac{1}{2}kD^2$ is the work done and the strain energy stored in stretching the spring D units, while P (H - D) is the potential energy available for load P. If the potential energy is stationary (invariant) with respect to small displacements, then the equilibrium condition is stable. Equilibrium equations (eqn 5.8) and conditions (eqn 5.9) are generated by differentiating the potential energy (5.7) and setting the differentiation equal to zero:

$$\frac{d\Pi_p}{dD} = 0 = kD - P. \tag{5.8}$$

$$D_{eq} = \frac{P}{k}. \tag{5.9}$$

This balance of energy argument is a result of the virtual work principle. The virtual work principle states that zero net work is done during an infinitesimal displacement dD from an equilibrium configuration. Stated mathematically, the virtual change in potential energy is

$$d\Pi_p = (kD - P)dD, \tag{5.10}$$

where

$$d\Pi_p = \frac{\partial \Pi_p}{\partial D_1}dD_1 + \frac{\partial \Pi_p}{\partial D_2}dD_2 + \ldots + \frac{\partial \Pi_p}{\partial D_n}dD_n \tag{5.11}$$

is the total differential if the potential energy is a function of position:

$$\Pi_p = \Pi_p(D_1, D_2, D_3, \ldots, D_n).$$

5.2.3 Developing the Total Potential Energy

A body accrues potential energy from three sources: internal stresses (strain energy), body forces (gravity) and point loads. A general expression for Π_p is generated by integrating over the body's volume the potential energy states of individual elements.

Strain Energy

Strain energy results from an elastic material undergoing stress and changing shape. The work done by stress as it acts on an element of infinitesimal volume can be calculated by integrating the sum of the products of all infinitesimal stresses multiplied by the associated displacements.

The stress acting on each x-face of an element is $(\pm \sigma_x dydz)$. If the element is not rigid, it displaces. The work done by the displacing stress is

$$work = \int_0^{\varepsilon_x} (\sigma_x dydz)(d\varepsilon_x dx) = \int_0^{\varepsilon_x} \sigma_x d\varepsilon_x (dxdydz). \tag{5.12}$$

The stress $\{\sigma\}$ and strain $\{\varepsilon\}$ vectors for any element are:

$$\{s\} = \{\sigma_x, \sigma_y, \sigma_z, \tau_{xy}, \tau_{yz}, \tau_{zx}\}$$

$$\{e\} = \{\varepsilon_x, \varepsilon_y, \varepsilon_z, \gamma_{xy}, \gamma_{yz}, \gamma_{zx}\}.$$

The stress-strain relation, including initial conditions, is then

$$\{s\} = [E]\{e\} - [E]\{e_0\} + \{s_0\}. \tag{5.13}$$

Let U_0 be defined as strain energy per unit volume. On a unit cube, the strain energy per unit volume is equal to

$$dU_0 = \sigma_x d\varepsilon_x + \sigma_y d\varepsilon_y + \ldots + \tau_{zx} d\gamma_{zx} = \{s\}^T \{de\}. \tag{5.14}$$

The rate of change of potential energy with respect to displacements is

$$\frac{\partial U_0}{\partial \varepsilon_x} = \sigma_x, \quad \frac{\partial U_0}{\partial \varepsilon_y} = \sigma_y, \quad \ldots, \quad \frac{\partial U_0}{\partial \gamma_{zx}} = \tau_{zx} \tag{5.15}$$

which, in matrix form and using equation (5.12), is

$$\left\{\frac{\partial U_0}{\partial e}\right\} = \{s\} = [E]\{e\} - [E]\{e_0\} + \{s_0\}. \tag{5.16}$$

Integrating equation (5.16) yields potential energy per unit volume:

$$U_0 = \frac{1}{2}\{e\}^T[E]\{e\} - \{e\}^T[E]\{e_0\} + \{e\}^T\{s_0\}. \tag{5.17}$$

Body Forces and Point Loads

Body forces, defined as $\{F\}$, cause a loss of potential energy when displacing elements. In a unit volume, the potential change for an element experiencing a deformation due to gravity is the work produced by the product of the body forces $\{F\}$ and the associated displacements $\{f\} = \{u\ v\ w\}$:

$$\textit{Potential Change} = -F_x u - F_y v - F_z w. \tag{5.18}$$

Concentrated forces (here defined as $\{P\}$) and their displacements (defined as $\{D\}$) usually act on individual nodes:

$$\{D\}^T\{P\} = D_1 P_1 + D_2 P_2 + \ldots. \tag{5.19}$$

Total Potential Energy

A body of volume has total potential energy contributions from strain energy, body forces and point load forces:

$$\Pi_p = \int_V U_0\, dV - \int_V \{f\}^T\{F\} - \{D\}^T\{P\}. \tag{5.20}$$

5.3 Rayleigh-Ritz

The Rayleigh-Ritz method uses interpolation to describe displacements within a continuum in terms of a finite number of degrees of freedom. (Ref. 10) The method, as used in finite element analysis, is an iterative process that begins by establishing an assumed displacement field, generates a set of trial solutions, and then applies a test criterion to the set of trial solutions in order to select the final answer. The test criterion used in this paper is that the total potential energy be stationary.

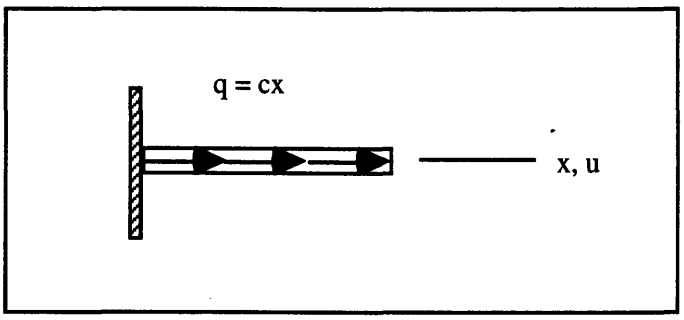

Figure 5.5: An elastic cantilever beam of cross-sectional area A, elasticity E, with a uniformly distributed axial load q = cx.

The total potential energy equation for the beam in Figure 5.5 is

$$\Pi_p = \int_0^L \frac{E}{2}\left(\frac{\partial u}{\partial x}\right)^2 A\,dx - \int_0^L \frac{q}{A} u A\,dx, \tag{5.21}$$

where q/A = Force. The assumed displacement field and uniaxial stress are

$$u = u(x) \qquad \text{(Assumed Displacement Field)} \tag{5.22}$$

$$\sigma_x = E\varepsilon_x \qquad \text{(Uniaxial Stress).} \tag{5.23}$$

The most simple "admissible" assumption that conforms to the boundary condition u = 0 at x = 0, is

$$u = a_1 x. \qquad \text{(First Attempt at Solution)} \tag{5.24}$$

The Rayleigh-Ritz solution is found by testing the first attempted solution. This is done by inserting the equation (5.24) into the potential energy equation (5.21), differentiating and finding the unknowns:

$$\Pi_p = \frac{AEL}{2} a_1^2 - \frac{cL^3}{3} a_1 \qquad \Rightarrow \qquad \frac{d\Pi_p}{da_1} = 0$$

$$a_1 = \frac{cL^2}{3AE}, \; u = \frac{cL^2}{3AE} x, \; \sigma_x = \frac{cL^2}{3A}.$$

A second solution attempt is the expanded admissible:

$$u = a_1 x + a_2 x^2. \tag{5.26}$$

Again, the Rayleigh-Ritz assumed solution is tested using the new trial solution in the potential energy equation (5.21), and then differentiated:

$$\Pi_p = \int_0^L \frac{E}{2} \left(a_1 + 2a_2 x\right) A dx - \int_0^L \frac{cx}{A} \left(a_1 x + a_2 x^2\right) A dx \tag{5.27}$$

$$\Pi_p = \frac{EA}{2} \left(a_1^2 L + 2a_1 a_2 L^2 + \frac{4}{3} a_2^2 L^3 \right) - c\frac{a_1 L^3}{2} - c\frac{a_2 L^4}{4}$$

$$\frac{\partial \Pi_p}{\partial a_1} = \frac{\partial \Pi_p}{\partial a_2} = 0.$$

The matrix form of the solution is equation (5.28):

$$AEL \begin{bmatrix} 1 & L \\ L & 4L^2/3 \end{bmatrix} \begin{Bmatrix} a_1 \\ a_2 \end{Bmatrix} = \frac{cL^3}{12} \begin{Bmatrix} 4 \\ 3L \end{Bmatrix} \quad \Rightarrow \quad \begin{Bmatrix} a_1 \\ a_2 \end{Bmatrix} = \frac{cL}{12AE} \begin{Bmatrix} 7L \\ -3 \end{Bmatrix},$$

which determines the displacement and the stress:

$$u = \frac{cL}{12AE} \left(7Lx - 3x^2\right) \quad \sigma_x = \frac{cL}{12A} (7L - 6x). \tag{5.28}$$

The next solution attempt is a cubic. The general polynomial assumption for this elastic cantilever beam is

$$u = a_1 x + a_2 x^2 + a_3 x^3 + \ldots + a_n x^n. \tag{5.29}$$

The exact solution for this problem the cubic solution,

$$u = \frac{c}{6AE}\left(3L^2 x - x^3\right). \tag{5.30}$$

Continuing to test the general solution will produce results until a convergence with the exact solution is found. This convergence is achieved through the iterative application of an assumed field function. Completeness means exactness, and is achieved only if there are sufficient terms in the trial field to match actual displacements. Enough terms must be used so that the model can displace into shapes that correctly describe the actual structure's deformation. Otherwise, the actual deformations can only be modeled by superposing terms of the assumed displacement field.

The Rayleigh-Ritz method is a finite element solution technique because of this piece wise approach to fitting exact shapes and slopes. In FEA codes, Raleigh-Ritz is applied to define a simple polynomial over a small portion of the structure. This then becomes piece-wise polynomial interpolation as the code sums the polynomials in order to build assumed displacement fields representative of the structure.

5.4 Analytic and FEA Methods Compared

This section compares analytical and numerical solutions for a series of beam and plate examples in order to validate the FEA technique and the NASTRAN code, calibrate finite element method accuracy, and investigate the material properties of Cervit. (The MDM primary mirror is made of homogeneous Cervit.)

Distributed loads in the MDM finite element model (as well as in the actual telescope) are a result of gravity pulling the mirror against the air-bag axial support and the mercury belt radial support systems. Point loads are created by the action of the three hard points pushing up against the back of the mirror. Solving for the deflection of a beam under the influence of both point and distributed loads, and looking at the behavior of a thin, circular, simply supported plate will provide a rough estimate of what should be expected in the MDM model.

5.4.1 Cantilever Beam Numerics

A single beam geometry and set of material properties is selected for both cantilever and simply supported beam models.

Structural Dimensions	Material Properties
length = 2.4 meters	Elasticity = $9.18E10\ N/m^2$
height = .1 meters	Density = $2.5\ kg/m^3$
width = .1 meters	Poisson Ratio = .22

Table 5.1: Properties of the beam used in the trial FE analysis.

The other common inputs are inertia and point load magnitudes:

$$I = \int_{\frac{-h}{2}}^{\frac{+h}{2}} \int_{\frac{-w}{2}}^{\frac{+w}{2}} y^2\,dy\,dz = \frac{y^3 z}{12} = 8.33E-6\ m^4$$

P = point load magnitude = 25 N

Model 1: Cantilever Beam, Point Load at Beam's End

The cantilever beam is modeled in NASTRAN as a single element. Support schemes are created in NASTRAN by specifying nodal degrees of freedom and by applying point and distributed loads. The condition that the beam have zero deflection at x = 0 (where the beam meets the wall) is specified by constraining "node 1" to zero translational and rotational degrees of freedom. The point load is obtained by directing a down vector of magnitude 25 N at the end node. The single element model proves sufficient to generate an exact solution for deflection at the end point. From Section 4.1.1,

$$v(x=l) = \frac{P}{EI}\left(\frac{l^3}{3}\right) \quad , \qquad v\left(x=\frac{l}{2}\right) = \frac{5Pl^3}{48EI} \quad .$$

Analytical Results	Numerical Results
v (x=L) = -1.5059 meters	v (x=L) = -1.5065
mass = 60 kg	mass = 60 kg

Table 5.2: Analytical vs. finite element y-axis deflections in a cantilever beam.

Model 2: Cantilever Beam, Uniformly Distributed Load

The distributed load cantilever beam is modeled using ten beam elements. In the previous point load example, a single element is sufficient to model the point load because NASTRAN assigns point loads to single nodes.

The distributed load example requires multiple elements so that it may simulate the effects of a broadly distributed force application. NASTRAN applies gravity loads by looking at the mass represented by each individual element, multiplying the element mass by the gravitational acceleration (9.81 m/s2), dividing this total force by the number of nodes that define the element, and then distributing the force amongst those defining elements. Hence, more elements lead to a better approximation of a distributed force.

Model 2: Cantilever Beam, Distributed Load (cont.)

Section 4.1.2 develops the equations of bending for a cantilever beam under z-axis gravity, showing deflections at the beam's middle and end points. Table 5.3 compares analytical and numerical results for a cantilever example:

$$v(x=l)=\frac{p_0 l^4}{8EI} \quad , \qquad v(x=l/2)=\frac{p_0 l^4}{24EI}\left(\frac{17}{16}\right).$$

Analytical Results	Numerical Results
$v(x=l)=-1.3295488E-3$ meters	$v(x=l) = -1.334509E-3$ meter
$v(x=l/2) = -4.7088E-4$ meters	$v(x=l/2) = -4.721769E-4$ meters
mass = 60 kg	mass = 60 kg

Table 5.3: Deflections in a cantilever beam under a uniformly distributed load.

The analytical and numerical results are nearly identical. In both the $v(x=l/2)$ and the $v(x=l)$ computations, NASTRAN deflections are slightly larger than analytical results. The difference is within 1%.

Model 3: Cantilever Beam With Point and Gravity Loads

The cantilever beam deflections that result from the combined action of a uniformly distributed and point loads are the superposition of the two separate cases. Deflections at middle and end points, from Section 4.1.3, are

$$v(x)=\frac{p_0}{EI}\left(\frac{x^4}{24}-\frac{lx^3}{6}+\frac{l^2x^2}{4}\right)+\frac{P}{EI}\left(\frac{-x^3}{6}+\frac{lx^2}{2}\right)+\frac{P}{EI}\{x-l\}^3$$

$$v(x=l)=\frac{p_0 l^4}{8EI}+\frac{Pl^3}{3EI} \qquad v(x=l/2)=\frac{p_0 l^4}{24EI}\left(\frac{17}{16}\right)+\frac{Pl^3}{EI}\left(\frac{5}{48}\right).$$

Analytical Results	Numerical Results
$v(x=l)=$ -.14801488 meters	$v(x=l)=$ -.14851575 meters
$v(x=l/2)=$ -.04752997788 meters	$v(x=l/2)=$ -.04754983 meters

Table 5.4: Cantilever beam under point and gravity loads, y-axis deflections.

5.4.2 Simply-Supported Beam Numerics

The simply supported beam series uses the same geometry and materials constants as the cantilever beam FE models. Changes were in the use of boundary conditions to simulate the action of simple supports at beam's end.

Node 1, the left hand side boundary, is constrained for zero translational motion in x, y, or z, and zero rotational motion about the x or z axis. Zero translational motion provided NASTRAN with its required single point constraint, anchoring on point of the beam. Node 11, at the right hand boundary. is constrained from movement in z, as any support will preclude a vertical deflection at the support point location. Node 11, and all other nodes 2-10, were allowed to move in the x-direction, as any beam that deflects downward must be allowed to travel slightly in x. These nodes were also constrained from lateral motion and from rotation about the x- or z-axis.

Model 4: Simple Supports, Uniformly Distributed Load

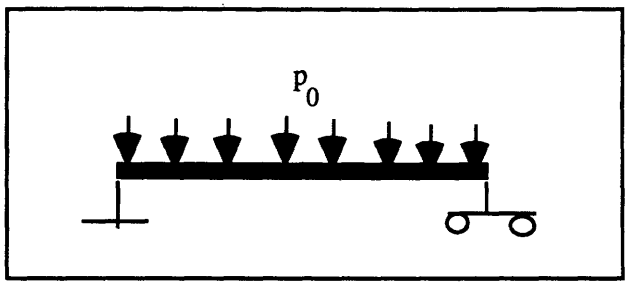

Figure 5.6: Simply supported beam with a uniformly distributed load.

This model also uses 10 elements in order to simulate the action of the uniformly distributed gravity load p_0. From Section 4.1.4,

$$EI_z v(x) = \frac{plx}{24}\left(\frac{x^3}{l} - 2x^2 + l^2\right) \qquad v_{max} \Rightarrow v\left(x = \frac{l}{2}\right) = \frac{pl^2}{EI_z 96}\left(l^2 + 1\right)$$

Analytical Results	Numerical Results
$v_{max}\left(x = \frac{l}{2}\right) = 1.3011E-4$ meters	$v_{max}\left(x = \frac{l}{2}\right) = 1.374411E-4$ meters

Table 5.5: Deflections for a simply supported beam, uniform load.

Model 5: Simply Supported Beam With a Point Load

The equation of bending for a simply supported beam under the influence of a point load is found in section 4.1.5. Maximum deflection is attained at the middle point:

$$EIv\left(x=\frac{l}{2}\right)=\frac{P}{12}\left\{\frac{l}{2}\right\}^3+\frac{P}{6}\{0\}^3-\frac{P}{6}\left(\frac{l}{2}\right)^3+\frac{3Pl^2}{48}\frac{l}{2}=\frac{Pl^3}{48}.$$

Analytical Results	Numerical Results
$v_{\max}\left(x=\frac{l}{2}\right)=-9.4121E-6$ meters	$v_{\max}\left(x=\frac{l}{2}\right)=-9.4155E-6$ meters

Table 5.5: Simply supported beam with a point load.

Numerical and analytical results are the same for the point load case (Model 5), while the distributed load case (Model 4) shows a slight variance. The difference is explained by the FE model's piece-wise approximation of the distributed load as FE uses ten elements, with a measure of force applied to each element, in order to approximate the load distribution.

Model 6: Simply Supports With Distributed and Point Loads

The combination of the point and distributed load cases is proven (Section 4.1.6) to be the superposition of the individual case results.

$$EI_z v\left(x=\frac{l}{2}\right)=\frac{pl^2}{96}\left(l^2+1\right)+\frac{Pl^3}{48}$$

Analytical Results	Numerical Results
$v_{\max}\left(x=\frac{l}{2}\right)=-9.5456E-6$ meters	$v_{\max}\left(x=\frac{l}{2}\right)=-9.27809E-6$ meters

Table 5.6: Deflections for a simply supported beam with both distributed and point loads.

5.4.3 Plate Numerics

The next two models analyze the behavior of circular plates that deflect under gravity loads. The first of the two models is clamped along the plate's circumference. The second is simply supported.

Deflections in circular plates of constant thickness can be found using classical small deflection theory, as developed by Timoshenko and Housner and addressed in Chapter Three of this thesis. Analysis of the boundary conditions that create the simple and clamped supports is found in Chapter Four.

The two circular plate models are designed to incorporate some features of the MDM/Hiltner primary mirror. The plates are 2.4 meters in diameter, and use the material constants of Cervit. The plates differ from the actual mirror in both overall figure and thickness. MDM/Hiltner has a parabolic surface figure, and a thickness ranging from .162 meters at the inner radius to .234 meters at the outer radius. The plates are of constant .02 m thickness.

Structural Dimensions	Material Properties
radius = 1.2 meters	Elasticity = $9.18E10\ N/m^2$
thickness = .02 meters	Density = $2.5\ kg/m^3$
mass = 234 kg	Poisson Ratio = .22

Table 5.7: Properties of the circular plates that deflect under gravity

The plate models were constructed on the LapCAD preprocessor by sweeping a simple, two dimensional multi-element rectangle through 360° in 30° increments. Each 30° "slice" contains six elements. The elements are all .02 meters thick, but vary in surface area and volume in relation to their radial position. There is a central hole of radius .02 meters.

The general circular plate deflection equation is:

$$\nabla^4 w(r) = \frac{q}{D}, \qquad \text{where} \qquad D = \frac{E}{\left(1-\nu^2\right)}\frac{h^3}{12}.$$

In the case of the plate model, D is exactly

$$D = \frac{9.18E+10}{\left(1-(.225)^2\right)}\frac{(.02)^3}{12} = 64,463.4628$$

The plate examples are under gravity loads. The analytical and numerical mass calculations show slightly different results. (NASTRAN uses a piece-wise continuous circular geometry.)

$$Volume = \pi\left(r_{outed}^2 - r_{inner}^2\right)*height = .0905\ m^3$$

$$analytical\ mass = \rho_{cervit} * Volume = 226.3kg$$

$$q = \frac{mass * 9.81}{Surface\ Area}, \qquad q = \frac{(2.5E+3)*(.0905)*9.81}{4.5226} = 490.76\frac{N}{m^2}$$

Model 7: Circular Plate, Clamped, Under Z-Axis Gravity

The equation for a clamped circular plate under a uniform load is

$$w(r) = \frac{q}{64D}\left(r^2 - R^2\right)^2, \quad \text{where} \quad \frac{q}{64D} = \frac{490.76}{64*64,463.4628} = 1.19E-4.$$

Deflections are uniform for points of equal radius. Table 5.8 (below) shows analytical and FEA deflections for the radial arm along the positive x-axis.

Radius	.02	.2	.4	.6	.8	1.0
Analytic	2.47E-4	2.33E-4	1.95E-4	1.39E-4	7.61E-5	2.30E-5
FEA	2.35E-4	2.16E-4	1.81E-4	1.29E-4	7.01E-5	1.99E-5

Table 5.8: Deflections of a clamped circular plate under gravity, in meters.

The finite element calculations match the analytical calculations within an average of 5% for the clamped circular plate model.

Model 8: Circular Plate, Simply Supported, Under Gravity

The general solution for a simply supported plate under uniform load is

$$w(r) = \frac{q}{64D}\left(r^4 - 2\beta R^2 r^2 + 2R^4\beta - R^4\right).$$

Deflections are:

Radius	.02	.2	.4	.6	.8	1.0
Analytic	1.03E-3	9.73E-4	8.59E-4	6.99E-4	4.99E-5	2.64E-5
FEA	8.99E-4	8.58E-4	7.76E-4	6.43E-4	4.56E-5	2.34E-5

Table 5.9: Deflections for a simply supported circular plate under gravity. Units are meters.

Summary

The finite element calculations produce 90 - 99% of the maximum deflections predicted by the plate equation. This is an inexact result and could be caused by modeling the plates with an insufficient number of elements, and thereby an insufficient number of degree of freedom.

Chapter 6

Introduction to Astronomical Optics

This chapter introduces geometrical and physical optics techniques for modeling light behavior and quantifying the quality of images produced by optical systems.

Physical optics treats light as a transverse electromagnetic wave. Diffraction theory is a subset of physical optics that applies the principle of superposition to study wave behavior in optical systems. Diffraction theory considers each point on the wavefront as the source for another, secondary wavefront. These secondary wavefronts, or "wavelets", iteratively reproduce, modeling the wavefront as a superposition of a large number of wavelets. The "diffraction integral", the sum of these superposed wavelets, describes the characteristics of the image of a point source object, and established the diffraction limit.

Geometrical optics ignores the wave nature of light, instead treating light as a ray that behaves vectorially. What wave theory describes as a "spherical wavefront", geometrical optics labels a "fan of rays". What wave theory calls a "planar wavefront", geometrical optics calls a "bundle of parallel rays". Geometrical optics models the behavior of light as a set of vectors that strikes reflective and refractive surfaces and forms an image when the vectors assemble along what is known as the system's optical axis.

6.1 Geometrical Optics and Image Formation

Stars emit light in the form of expanding spherical waves. Earth-bound observers perceive the portion of the spreading stellar wavefront to be almost exactly flat, since the radius of curvature of the emitted spherical wavefront is the semi-infinite distance from the star to the observer and the angle between the incoming rays is infinitesimally small. The combination of infinite radius and very small angle allows the use of the geometric optics model.

6.1.1 How MDM Forms an Image

A reflecting telescope is designed to collect the (virtually) parallel rays of the incident stellar wavefront, and through the coordinated action of primary and secondary mirrors to focus these rays to a single point so that they may be collected by instrumentation. The surface of the primary mirror is designed so that reflected star light is transformed from a bundle of parallel rays (the planar wavefront) into a fan of converging rays. The surface cross-section that enables a mirror to convert a plane wave into a converging wave is that of a conic section.

The MDM/Hiltner 2.4 meter telescope is a two-mirror system, and belongs to the family of Cassegrain telescopes. The primary and secondary mirror surfaces are hyperboloids. In order to expeditiously link the concepts of image formation, aberration theory, and mechanical deformations of optical surfaces, this paper will make the simplifying approximation that the MDM mirror can be treated as a paraboloid. The parabola is the correct surface form to convert a plane wave into a spherical wave, and focus the light to a point. This simplification eliminates the modeling complications of dealing with a second mirror, allowing the analysis to concentrate on a single reflected wavefront.

An ellipse is defined (Ref. 11) as *"the set of points in a plane whose distances from two fixed points (the foci) in the plane have a constant sum"*. (Please see the figure, below.)

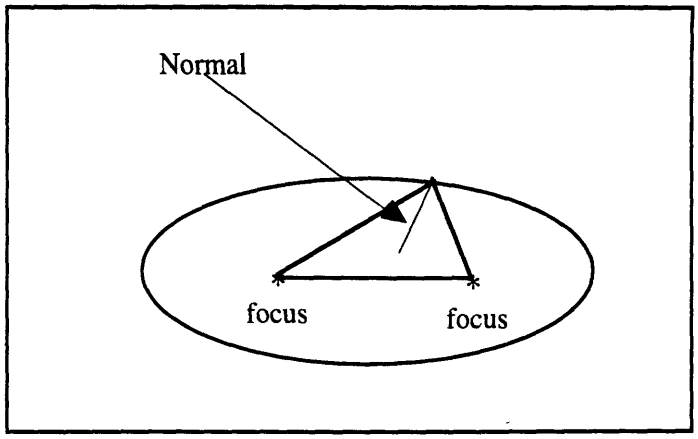

Figure 6.1: An ellipse, its foci, and an internally oriented normal.

Figure 6.1 shows a vector that emanates from one foci of the ellipse, "reflects" from the locus of elliptical points and "arrives" at the other focus. The definition of the ellipse requires that no matter what the initial direction of the vector's propagation, the resulting internal reflection will cross the other foci. The *key concept* is that, by definition, inside an ellipse, *the distance traveled from the first focus to the periphery and back to the second focus, is a constant sum.*

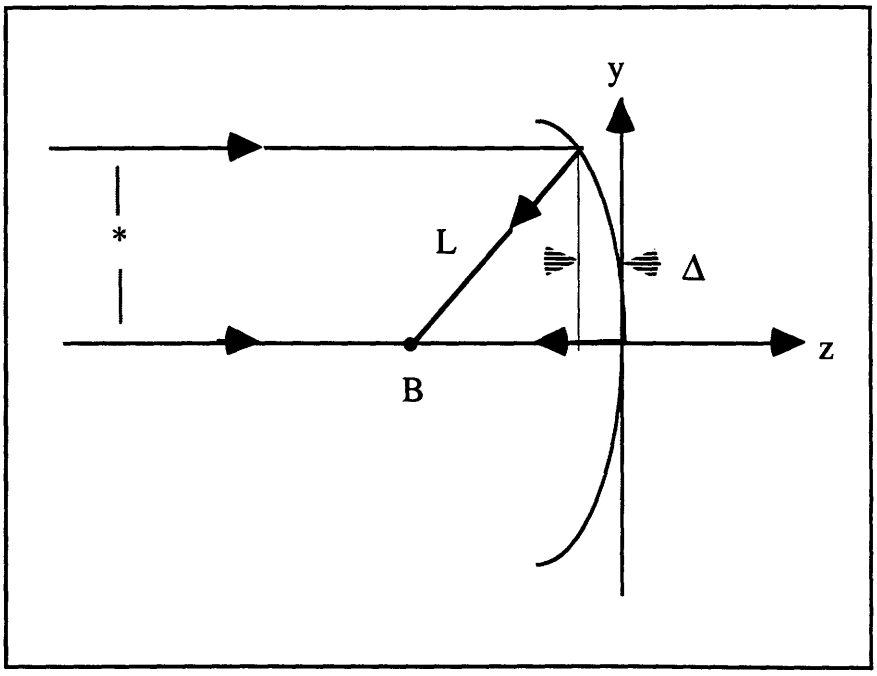

Figure 6.2: Conic surface reflecting parallel rays. Rays parallel to the optical axis will be reflected to a common focal point by a parabolic surface.

In Figure 6.2 (Ref. 12), the incident planar wavefront propagates from left to right parallel to the mirror's optical axis. Two arbitrarily selected rays reflect from the curved surface; one reflects at height "y", and travels down to the "z" (optical) axis. The other ray travels along the "z" (optical) axis both before and after reflection. The goal of this example is to show that the surface that brings these rays to a common focus is a parabola.

In order that all rays arrive at the same point, all optical path lengths are required to be equal. The optical path length is defined as the distance traveled from the point of emission (the star) to the focal point (B). Since both rays travel the same distance from the star to the immediate area of the optical system, it is possible to neglect the majority of this semi-infinite distance and consider only the portion of the total path length from just outside the system. From this point (labeled with an *) to a common focus, equal OPL's require

$$2f = l + (f - \Delta).$$

From the geometry in Figure 6.2,

$$l^2 = y^2 + (f - \Delta)^2.$$

From the requirement that all OPL's be equal, it must be true that

$$l = (f + \Delta).$$

Therefore, $$(f+\Delta)^2 = y^2 + (f-\Delta)^2$$

which is equivalent to saying

$$y^2 = 4f\Delta \quad or, \quad y^2 = -4fz \tag{6.1}$$

This is the equation of a parabola with vertex at (0,0). The complete equation of a paraboloid of revolution where f is defined as the focal length, is

$$x^2 + y^2 = -4fz\ . \tag{6.2}$$

6.1.2 Conic Sections of Revolution

The goal of this section is to form a general equation for conic sections in order to develop the relationship between focal length and radius of curvature for a parabolic mirror. (Ref. 13) Figure 6.2 depicts an optical system composed of a concave mirror with a light source a distance "s" from the mirror vertex, and a light collector at distance "s'". All rays have equal total OPL from the source to the mirror and on to absorption at the collector.

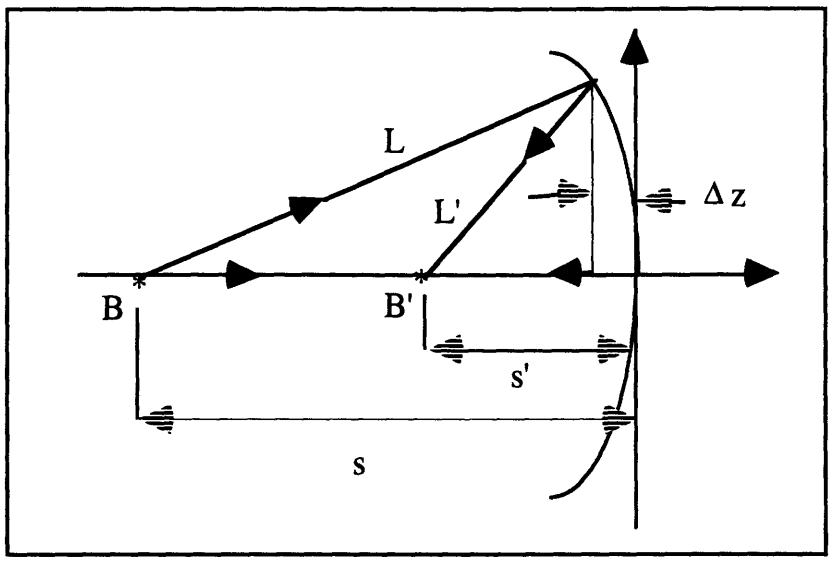

Figure 6.2 Rays reflecting from an elliptical surface between conjugates.

In Figure 6.2, one ray travels from the point source "B" up to the mirror surface at height "y" and then back down to the optical axis at point "B' ". The other travels along the optical axis from "B" to the mirror vertex and back to the collector at point " B' ". From equal optical path lengths,

$$L + L' = -(s + s'). \tag{6.3}$$

The lengths L and L' are defined as:

$$L^2 = y^2 + (-s - \Delta)^2 \qquad \& \qquad L'^2 = y^2 + (-s' - \Delta)^2.$$

It is possible to eliminate L and L' from equation (6.3) , as shown in Schroeder. (Ref. 14) If Δ = -z , then

$$y^2 - 4z\frac{ss'}{s+s'} + 4z^2\frac{ss'}{(s+s')^2} = 0, \tag{6.4}$$

which is the equation for an ellipse with center at x = 0, y = a . To develop a general equation for a conic section, Schroeder chooses

$$2a = s+s' \qquad \text{and} \qquad b^2 = ss', \tag{6.5}$$

and defines the eccentricity of the ellipse as $e=\frac{c}{a}$, where "c" is the distance from one of the foci to the center of the ellipse and $c^2 = a^2 - b^2$. Schroeder substitutes s and s' values in equation (6.5) for a and b,

$$\frac{2b^2}{a} = \frac{2ss'}{s+s'} \tag{6.6}$$

and defines the variable "R" as the ratio $\frac{ss'}{(s+s')} = \frac{R}{2}$. (6.7)

Schroeder substitutes equations (6.5), (6.6) and (6.7) into equation (6.4), and then rotates the result to obtain an equation for a conic surface of revolution:

$$r^2 - 2Rz + z^2(1+K) = 0. \tag{6.8}$$

The "conic constant" is $K=-e^2$ and $\rho^2 = x^2 + y^2$. A table of conic equations in terms of "K" is presented below:

Prolate ellipsoid	$e^2 < 0$	K > 0
Sphere	e = 0	K = 0
Oblate ellipsoid	0 < e < 1	-1 < K < 0
Paraboloid	e = 1	K = -1
Hyperboloid	e > 1	K < -1

Table 6.1: Conic constants and eccentricity.

6.1.3 Focal Length and Radius of Curvature

Radius of curvature and focal length provide measures of a mirror's figure and performance. In the case of a flawed mirror, it is possible to measure image aberration by comparing actual and intended focal points. The example of an incoming ray that travels parallel to the mirror's optical axis at a height "y" above the mirror's vertex will be used to develop the relationship between a parabolic mirror's radius of curvature and its focal length.

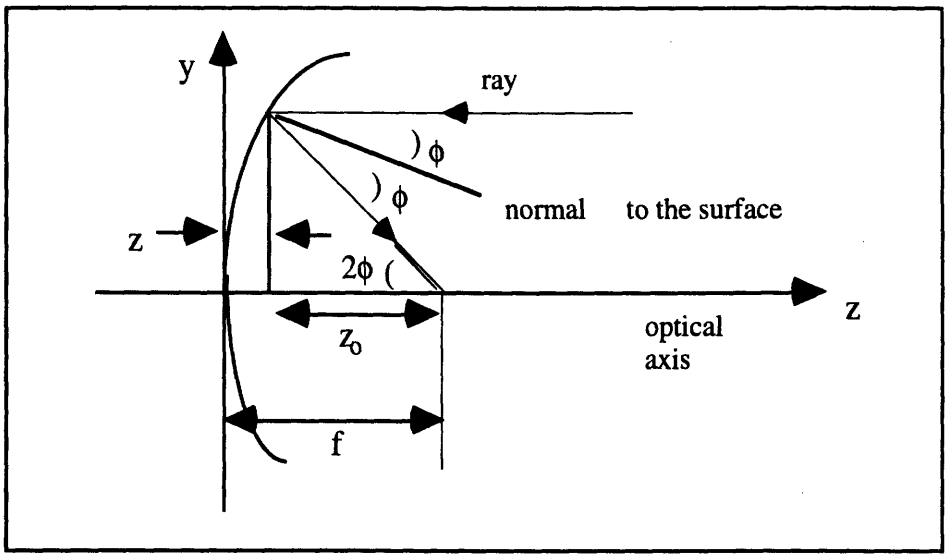

Figure 6.4: Parabolic surface with normal to the surface at height "y".

For a perfect paraboloid and parallel incoming rays, equal optical path lengths require that the rays reflect from the mirror surface and strike the optical axis at a common focal point. The diagram shows the focal length "f" is

$$f = z + z_0. \tag{6.9}$$

From the geometry, the length z_0 is related to the height "y" by

$$z_0 = \frac{y}{\tan 2\phi}$$

From the double angle formula,

$$z_0 = \frac{y}{\tan 2\phi} = \frac{y\left(1-\tan^2\phi\right)}{2\tan\phi}. \tag{6.10}$$

Basic calculus defines the slope of the normal to a curve as the inverse of the slope of the curve at the point of tangency. Since the slope of the curve in the diagram is dy/dz, the slope of its normal is dz/dy. From the diagram, the slope of the normal is $\tan\phi$. Therefore,

$$\frac{dz}{dy} = \tan\phi. \tag{6.11}$$

The general expression for a conic section derived in Section 6.1.2 is

$$\rho^2 - 2Rz + z^2(1+K) = 0 \tag{6.12}$$

where "R" is the ratio defined in equation (6.7). From equation (6.12),

$$\frac{dz}{dy} = \frac{y}{\left[R-(1+K)z\right]}. \tag{6.13}$$

Substituting equation (6.11) into equation (6.10) yields:

$$z_0 = \frac{y\left(1-\tan^2\phi\right)}{2\tan\phi} = \frac{y}{2}\left[\frac{1}{\tan\phi} - \tan\phi\right]$$

$$z_0 = \frac{y}{2}\left[\frac{\left[R-(1+K)z\right]}{y} - \frac{y}{\left[R-(1+K)z\right]}\right]$$

$$z_0 = \frac{R}{2} - \frac{(1+K)z}{2} - \frac{y^2}{2\left[R-(1+K)z\right]}. \tag{6.14}$$

To finally put "R" and "f" into the same expression, z_0 can be substituted into the equation that describes focal length, $f = z + z_0$. First, an expression for "z" is obtained by re-arranging equation (6.8) in terms of "z":

$$z = \frac{R}{1+K}\left[1-\left(1-\frac{y^2}{R^2}(1+K)^{\frac{1}{2}}\right)\right]. \tag{6.15}$$

Expanding this expression for "z" in a power series produces

$$z = \frac{y^2}{2R} + (1+K)\frac{y^4}{8R^3} + (1+K)^2\frac{y^6}{16R^5} + \ldots\ldots \tag{6.16}$$

Adding z *and* z_0 (equations 6.14 & 6.16) determines the focal length:

$$f = z_0 + z \tag{6.9}$$

$$f = \frac{R}{2} - \frac{(1+K)y^2}{4R} - \frac{(1+K)(3+K)y^4}{16\,R^3} - \ldots\ldots \tag{6.17}$$

For a parabolic mirror of perfect figure, K = -1, and r = R, so that the relation between focal length and curvature for a parabolic dish is

$$f = \frac{R}{2}. \tag{6.18}$$

For any other conic section, the change in focal length as a function of ρ (where $\rho^2 = x^2 + y^2$) is

$$\Delta f = f(actual) - f(perfect\ paraboloid)$$

$$\Delta f = -\frac{(1+K)\rho^2}{4R} - \frac{(1+K)(3+K)\rho^4}{16\,R^3} - \ldots.$$

6.2 Physical Optics & Diffraction

The previous two sections employed the concepts of geometric optics to describe the behavior of light as it passes through an optical system. Geometric optics predicts that any system governed by Fermat's principle can produce, in the absence of aberrations, a true point image. In the physical world, this prediction is inaccurate. True "point" images do not occur - the wave nature of light sets a minimum image size. In an otherwise perfect optical system, this limit on the minimum image size is known as the "diffraction limit".

"Diffraction" is a term coined by the 17th century scientist Francesco Grimaldi to describe what he saw as the deviation of light from rectilinear propagation. (Ref. 15) The diffraction effect can most easily be understood as a characteristic of wave phenomena that occurs whenever a portion of a wavefront is in some way obstructed. If an opaque screen is placed between a point source of light and a white screen, the shadow cast on the screen will not be perfectly sharp. Dark fringes will appear around the edges of the screen, lending a "smearing" effect to the edges of the image.

Edge-effects and dark and bright fringes are the result of constructive and destructive interference between waves. In fact, there is no physical distinction between interference and diffraction. It is a convention that the term "diffraction" is used to describe the wave-related behavior of light in certain situations, usually in regard to wave propagation around obstructions and edges.

The earliest attempt to quantify the diffraction phenomena was by Christiaan Huygens who, in 1690, asserted that every point on a primary wavefront serves as the source of spherical secondary wavelets. Huygens' considered the primary wave to be an envelope of secondary wavelets - but he did not account for the action of the many ensuing wavelets, nor for the differences in behavior between waves of very small and very large wavelengths.

Fresnel modified the Huygens model by incorporating the concept of interference. Fresnel asserted that the amplitude of the electric wave at any point beyond the primary wave is a superposition of wavelet amplitudes and relative phases.

Kirchhoff enhanced the Fresnel-Huygens model, introducing a more rigorous approach that employed differential equations. Yet neither Kirchoff nor any succeeding approach satisfactorily models the edge-effects of propagating light. Exact solutions to the differential equations of rigorous diffraction theory are rare. Given the mathematical complexity, Chapter 9 will use Huygens' concept of the diffraction integral as a sum of wavelets across the face of an aperture.

6.2.1 The Diffraction Integral

Each point on a wavefront can be envisioned as the source of a spherical wavelet. The electromagnetic result at a distant point is the cumulative effect of constructive and destructive interference of all these little Huygens wavelets. The face of the aperture in an optical system such as a reflecting telescope is the source of a primary wavefront which is, in turn, the source for an infinite number of tiny Huygens wavelets. Each wavelet can be considered to be the source for an infinite number of tiny sub-wavelets.

This iterative process repeats itself along the entire focal length until, finally, the propagating wavelets reach the image plane. The diffraction integral, taken at the image plane, is the incremental sum of all these propagating wavelets.

This derivation of the diffraction integral begins with the divergence theorem and its corollary, Green's Theorem. Green's theorem is used to develop the Kirchhoff integral theorem. The Kirchhoff integral theorem is useful because it relates the value of any scalar wave function at any point *inside* an arbitrary closed surface to the value of that wave function *at* the surface.

The geometry of the electromagnetic field reflected by a telescope mirror can be modeled by Kirchoff in a Gaussian sense, despite the fact that the integral theorem is a scalar quantity. The Fresnel-Kirchoff integral formula considers the beam of wavelets reflecting from the mirror to be a scalar volume, while the image formation on the image plane is considered to be a scalar surface value. (Ref. 16)

The divergence theorem states that there exists a connection between surface and volume integrals.

$$\iint_{surface} \hat{n} \bullet \overline{F}\, ds = \iiint_{volume} \nabla \bullet \overline{F}\, d\tau. \tag{6.19}$$

This relationship can loosely be described by saying that the rate of change of the amount of "stuff" inside some volume is equal to the rate at which that "stuff" is flowing through the enclosed surface. By setting

$$F = U\nabla V - V\nabla U$$

and then using the vector identity,

$$\nabla \bullet (U\nabla V) = U\nabla^2 V + (\nabla U) \bullet (\nabla V), \tag{6.20}$$

the divergence relation (eqn 6.19) becomes a form of Green's theorem.

Green's theorem states that if two functions U and V are any two scalar point functions that satisfy conditions of continuity and integrability, then

$$\iint_{surface} \hat{n} \bullet (V\nabla U - U\nabla V) ds = \iiint_{volume} (V\nabla^2 U - U\nabla^2 V) d\tau. \tag{6.21}$$

If the two functions "U" and "V" satisfy the wave equations

$$\nabla^2 U = \frac{1}{c^2}\frac{\partial^2 U}{\partial t^2} \quad \text{and} \quad \nabla^2 V = \frac{1}{c^2}\frac{\partial^2 V}{\partial t^2}$$

and also have a time dependence of the form $e^{\pm i\omega t}$, the volume integral in equation (6.21) is equal to zero:

$$\iint_{surface} \hat{n} \bullet \left(V \frac{\partial}{\partial r} U - U \frac{\partial}{\partial r} V \right) ds = 0. \tag{6.22}$$

The wave theory of light considers the reflection of a plane wave from a parabolic dish to be a converging spherical wave. In this instance it is logical to choose "V" to be a spherical wave of the form

$$V = V_0 \frac{e^{i(kr-\omega t)}}{r}. \tag{6.23}$$

Any solution that describes the convergence of a wave to a particular focal point must consider the case where the radius "r" of the spherical wave goes to zero. At the point "P" where r → 0, the function "V" becomes infinite. The answer to the little challenge of infinite "V" at r = 0 is to exclude the small point "P" from the integration. This can be accomplished by subtracting an integral over a small sphere of radius "ρ" centered at P. Equation (6.22) becomes

$$\iint \left(\frac{e^{ikr}}{r} \frac{\partial}{\partial r} U - U \frac{\partial}{\partial r} \frac{e^{ikr}}{r} \right) ds - \iint \left(\frac{e^{ikr}}{r} \frac{\partial}{\partial r} U - U \frac{\partial}{\partial r} \frac{e^{ikr}}{r} \right)_{r=\rho} \rho^2 \, d\Omega = 0 \tag{6.24}$$

where $d\Omega$ is an element of solid angle centered at P. The corresponding element of area is $\rho^2 \, d\Omega$. The terms V_0 *and* $e^{i\omega t}$ are canceled as common factors.

As the radius of the small sphere approaches zero, the integral on the right hand side approaches the value that the original function "U" has at point "P". Equation (6.24) thus becomes

$$U_P = \iint \left(\frac{e^{ikr}}{r} \frac{\partial}{\partial r} U - U \frac{\partial}{\partial r} \frac{e^{ikr}}{r} \right) ds, \tag{6.25}$$

which is the Kirchhoff integral theorem linking the value of any scalar wave function at any point "P" *inside* an arbitrary surface to the wave function value *at* the surface. A function of the form

$$U = U_0 \frac{e^{i(kr-\omega t)}}{r},$$

when used in equation (6.22), produces a result of the form

$$U_P = U_0 e^{-i\omega t} \iint \left(\frac{e^{ikr}}{r} \frac{\partial}{\partial r} U - U \frac{\partial}{\partial r} \frac{e^{ikr}}{r} \right) ds, \tag{6.25}$$

where the integration is applied only to the area of the aperture.

Equation (6.26) can be further simplified by assuming that any variation in the factor e^{ikr}/r is generated primarily by the exponential term. This assumption allows the 1/r term to be replaced by its mean value and thus taken out of the integral. (Ref. 17). Using this assumption, equation (6.25) reduces to

$$U_P = C \iint e^{ikr}\, ds, \tag{6.27}$$

which is the Fresnel-Kirchhoff diffraction integral. Equation (6.27) obtains the distribution of diffracted light simply by integrating the phase factor e^{ikr} over the area of the aperture. This result is the sum of all amplitude contributions "dU" from each little incremental area of wavefront "ds" .

Equation (6.27) is thus a simple scalar sum, and represents the amplitude at the imaging surface from all aperture-related sources.

6.2.2 Diffraction Limit and the Point Spread Function

One of the very practical advantages of diffraction theory is that it provides a reality check for geometric optics.

One example where geometric optics needs a reality check is the case of the spot diagram. A spot diagram is produced by geometrically tracing a number of rays through an optical system from the object plane to the image plane. The spot can be computed numerically by using Snell's law to calculate the angle of reflection and multiplying by the focal length. This is useful as long as significant aberrations exist in either incident or reflected wavefronts. Caution should be used when calculating a geometric spot diagram for a wavefront that exhibits little or no aberration - the geometrically generated spot diagram will live up to its name and produce a spot on the image plane, and thereby defy the wave nature of light.

The reality check for the spot diagram comes in the form of a Point Spread Function. The Point Spread Function (PSF) is a ratio of intensities derived from diffraction analysis, and is often used to measure the imaging performance of an optical system.

Diffraction integrals in general and PSF's in particular are cumbersome when the wave in question exhibits significant aberrations. In the absence of aberrations, the PSF can be determined in closed form by evaluating the diffraction integral, and calculating the normalized intensity.

The amplitude distribution given by the diffraction integral in the previous section is

$$U_P = C\iint e^{ikr}\, ds. \tag{6.27}$$

To calculate the diffraction pattern of a circular aperture, (Ref. 18) choose "R" as the radius of the aperture, and "y" as the variable of integration, so that an arbitrary radial distance from the center of the aperture is defined

$$r = r_0 + y\sin\theta.$$

Then the element of area "ds" is the product of a strip of width "dy" and a length

$$2\sqrt{R^2 - y^2}.$$

The amplitude distribution of the diffraction pattern can then be given, according to (Ref. 19),

$$U_P = Ce^{ikr_0}\iint e^{iky\sin\theta}\, 2\sqrt{R^2 - y^2}\, dy. \tag{6.28}$$

If the substitutions

$$u = \frac{y}{R} \qquad \text{and} \qquad \rho = kR\sin\theta$$

are made, the amplitude distribution becomes

$$U(\rho) = \int_{-1}^{+1} e^{i\rho u}\sqrt{1 - u^2}\, du. \tag{6.29}$$

The intensity at some point "P" is the absolute square of the time-averaged amplitude of the electro-magnetic wave at that point "P":

$$I = \left|U_P\right|^2.$$

That intensity, normalized to unity at the point where the intensity is a maximum, is called the Point Spread Function (PSF). (Ref. 20) Changed into a standard Bessel function integral, the PSF is

$$\frac{I}{I_0} = \left[\frac{2J_1(\rho)}{\rho}\right]^2, \tag{6.30}$$

where J_1 is the Bessel function of the first kind.

A plot of the intensity function is the Airy disk pattern, which consists of a bright central disk surrounded by concentric circular bands of rapidly diminishing intensity. The bright central area of the Airy disk is the best that a wave-related phenomenon can do to create a true "spot diagram". The radius of the first dark ring is given by the first zero of the Bessel function, at ρ = 3.832. The angular radius of this first dark ring is thus

$$\sin\theta = \frac{3.832}{kR} = \frac{1.22\lambda}{D} \approx \theta, \tag{6.31}$$

where $\lambda = \frac{2\pi}{k}$, $D = 2R$, and θ is small.

This is the diffraction limit, the approximate minimum angular separation between two equal point sources such that they can just barely be resolved. It is a direct function of the wave nature of light, and throws cold water on the measures of image radius offered by geometric ray tracing spot diagrams.

Chapter 7

Basic Aberration Theory

A perfectly formed optical surface will produce in its exit pupil a distortion-free wave. If the optical surface under study is a parabolic mirror, and if the incident wave is planar, then the reflected wave will be perfectly spherical and will converge into a diffraction limited image at the focal point.

If the reflecting mirror is not perfectly shaped, that is, if there are small imperfections or distortions in the mirror surface, the reflected wave will also be imperfect and will form a blurred image. The blurred image is said to result from certain wavefront aberrations.

This chapter introduces wavefront aberration theory using the methods of geometrical optics as described by Creath. (Ref. 21) The chapter begins by writing an equation for an unaberrated wavefront, and then addresses how the equation might change in a series of aberration scenarios. In these aberrations, parts of the wave reach the image plane outside the area described by the diffraction limit, or away from the geometrical focal point. The method goes on to describe standard first and third order aberration patterns, the relation between these aberration patterns and Zernike polynomials, and the use of Zernike polynomials as numerical tools.

7.1 The Aberration-Free Wavefront

The aberration-free wavefront equation describes wavefront distribution, and acts as a basis for quantifying wavefront aberrations.

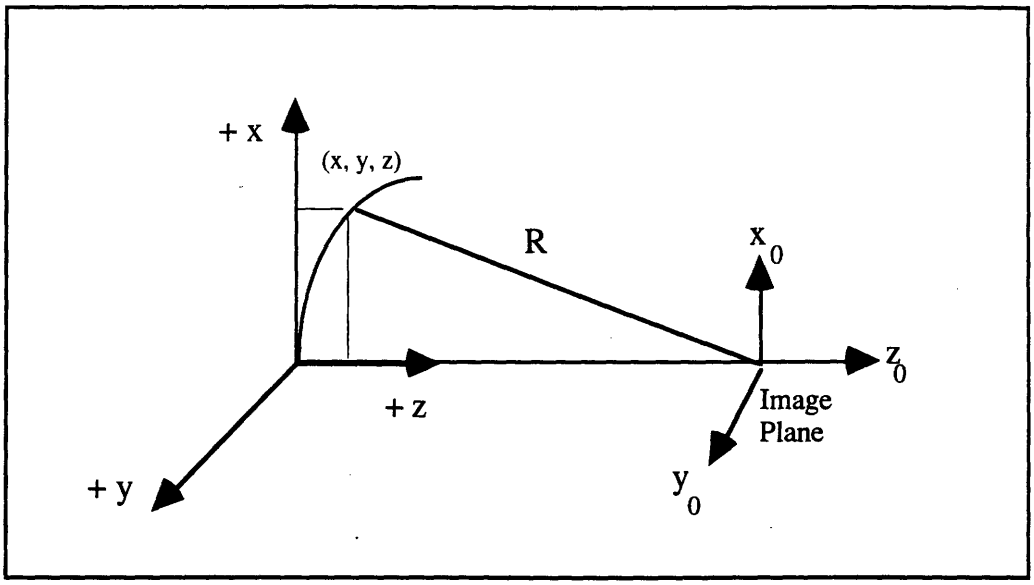

Fig. 7.1: Relation between image and exit pupil coordinates.

The origin in Figure 7.1 is the center of the exit pupil (vertex of the mirror). "R" is the radius of curvature of the spherical wavefront. The z-axis is the optical axis, the x-axis the "meridianal" axis, and the y-axis is the "tangential" axis. The unaberrated spherical wavefront equation is

$$x^2 + y^2 + (z - R)^2 = R^2. \tag{7.1}$$

If "x" and "y" are small compared to "R", and if "z" is small so that z^2 can be ignored, then equation (7.1) can be written as

$$z = \frac{x^2 + y^2}{2R}. \tag{7.2}$$

The spherical wavefront distribution in the exit pupil converging to the point (x_0, y_0, z_0) at a distance "R" is $W(x,y) = \frac{x^2 + y^2}{2R}$. (7.3)

7.2 OPD, Defocus and Lateral Shift

The optical path difference (OPD) is the path difference between the aberrated and the ideal unaberrated wavefront. The OPD is positive if the aberrated wave leads the unaberrated wave. (See Figure 7.2.)

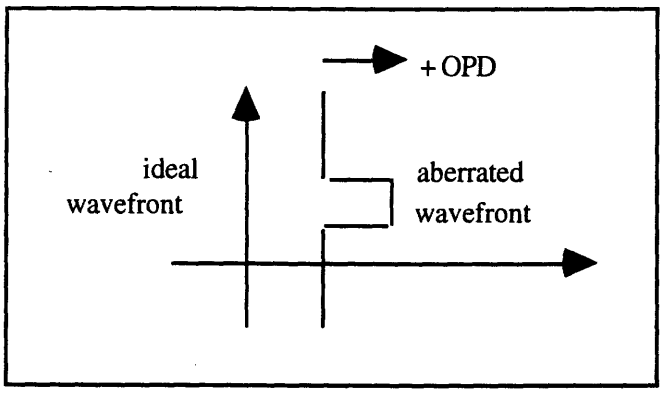

Fig. 7.2: Definition of Optical Path Difference.

Another way to visualize OPD is to consider a parabolic mirror that suffers from a warping action that has turned the edges of the mirror inward, beyond the normally parabolic curvature.

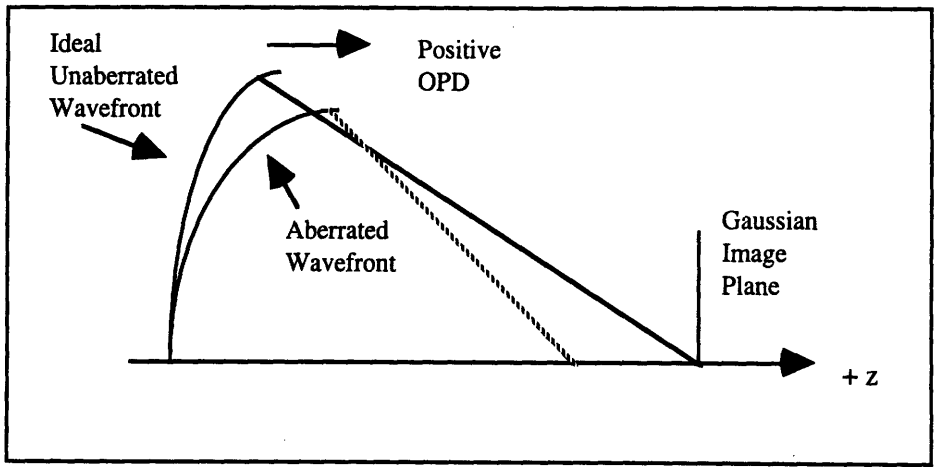

Fig. 7.3: Ideal and deformed wavefronts and the OPD between the two.

The OPD produced by the warped mirror in Figure 7.3 is a measure of the distance between the actual, flawed wavefront and the ideal wavefront that would exist if the optic were correctly figured.

7.2.1 Defocus

The OPD can be used to describe the nature of an aberration, as can be seen in the next figure where an OPD is actually equivalent to a defocus term in the wave equation. Figure (Fig. 7.4) shows an observation plane that has been interposed in front of the Gaussian image plane. The observation plane is thus effectively an image plane that has been shifted along the optical axis toward the exit pupil by a small amount (ε_z).

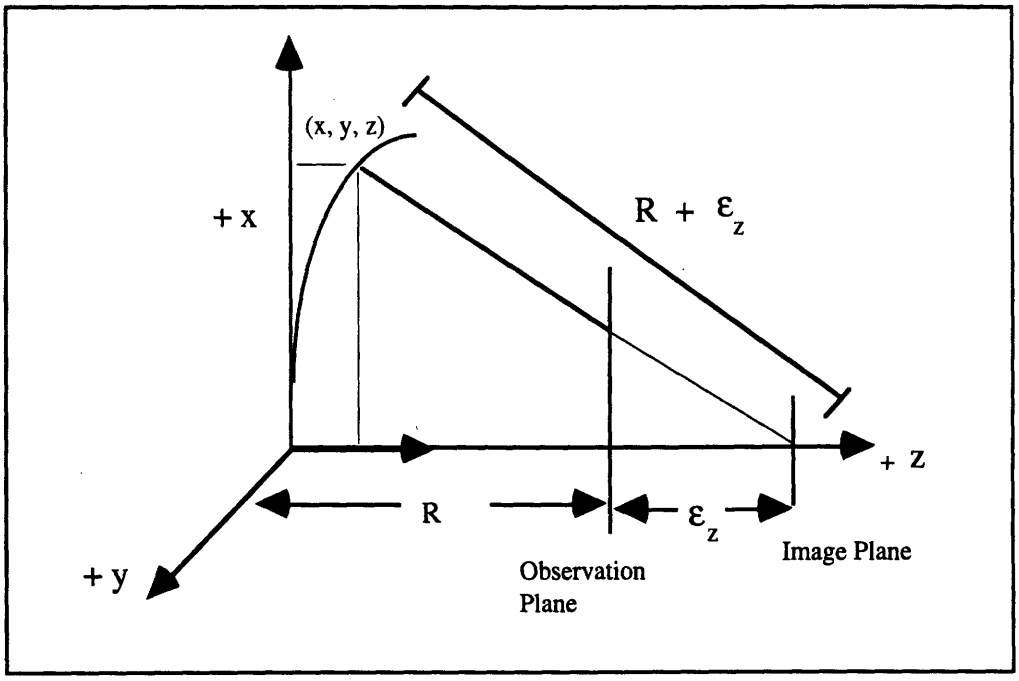

Fig. 7.4: Defocus in a spherical wavefront from a focus shift .

The original wavefront has a radius of curvature of $\left(R+\varepsilon_z\right)$, while the observation plane lies at a radius of "R" from the exit pupil vertex. In this scenario, the original wavefront has a distribution

$$W(x,y)=\frac{x^2+y^2}{2\left(R+\varepsilon_z\right)}=\left(\frac{x^2+y^2}{2R}\right)\left(\frac{1}{1+\varepsilon_z/R}\right). \tag{7.4}$$

For an "ε_z" much smaller than R, equation (7.4) reduces to

$$W(x,y)=\left(\frac{x^2+y^2}{2R}\right)-\varepsilon_z\left(\frac{x^2+y^2}{2R^2}\right). \tag{7.5}$$

The second term of the RHS of equation (7.5) is a defocus term, and is the optical path difference between the two wavefronts. This wavefront aberration known as defocus effectively shifts the focal point of the wavefront along the optical axis.

7.2.2 Lateral Shift and Tilt

Now consider a system that exhibits a vertical shift of the converging wavefront's focal point, so that it moves the focal point a small distance in the positive direction along the x_0 axis.

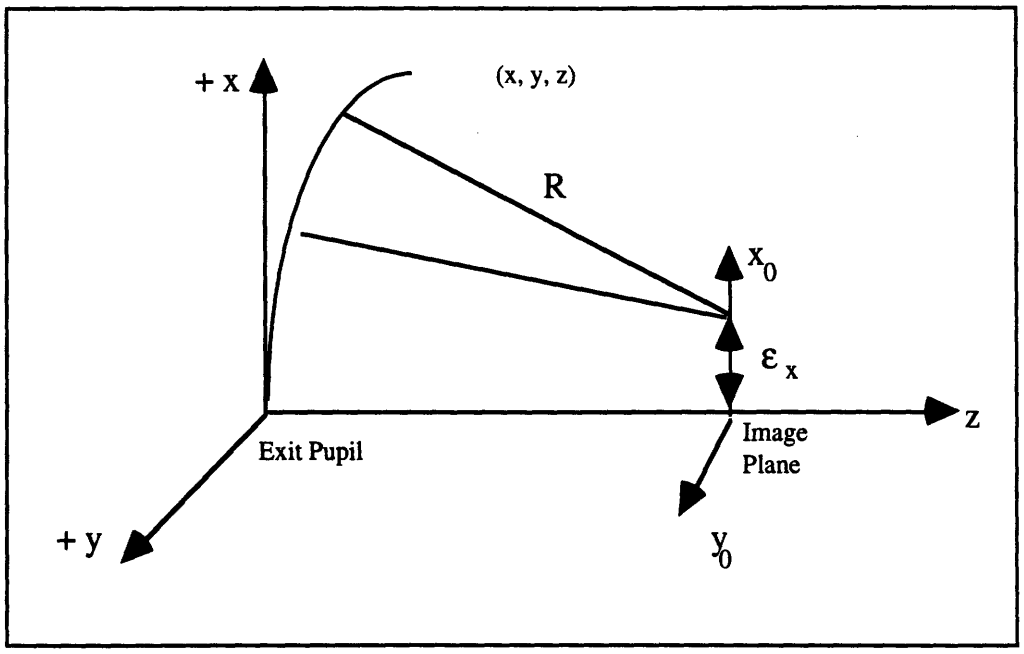

Fig. 7.5: A lateral shift of the image position along the x_0 - axis.

The equation of the wavefront in Figure 7.5 can be written

$$y^2+\left(x-\varepsilon_z\right)^2+\left(z-R\right)^2=R^2. \tag{7.6}$$

As in Section 7.2.2, the change in focal position is small so that

$$\varepsilon_z << R,$$

thus ε_z^2 and z^2 can be neglected. The resulting wavefront distribution is

$$W(x,y) = \left(\frac{x^2+y^2}{2R}\right) - x\frac{\varepsilon_x}{R}. \tag{7.7}$$

The OPD found in equation (7.7) is

$$\Delta W(x,y) = -x\frac{\varepsilon_x}{R}, \tag{7.8}$$

which is a lateral shift in the position of the focus. An analogous argument quantifies a transverse shift of the focus along the y_0 axis, with an OPD of

$$\Delta W(x,y) = -y\frac{\varepsilon_y}{R}. \tag{7.9}$$

This transverse shift of the center of the wavefront is commonly called "tilt".

The combination of the OPD's from equations (7.5), (7.8) and (7.9) is

$$W(x,y) = \left(\frac{x^2+y^2}{2R}\right) - \varepsilon_z\left(\frac{x^2+y^2}{2R^2}\right) - x\frac{\varepsilon_x}{R} - y\frac{\varepsilon_y}{R} \tag{7.10}$$

and describes a wavefront with center of curvature at the point $(\varepsilon_x, \varepsilon_x, \varepsilon_z)$ which lies in an image plane coordinate system (x_0, y_0, z_0), where the coordinate system's origin is a distance R from the exit pupil vertex.

7.3 Angular, Transverse, Longitudinal Aberrations

The wavefront of equation (7.10) is aberrated. Ray theory describes the aberrated wave as producing rays that cross the image plane in different places - creating something other than a perfect focus. Diffraction theory shows the aberrated wave as creating an imperfect pattern on the image plane, irregular in shape and contour with an energy distribution larger than the minimum prescribed by the diffraction limit.

Figure 7.6 depicts two wavefronts. The ideal, unaberrated reference wavefront exits the pupil as a spherical wave, converging to a point focus at the image plane's origin. The aberrated wavefront's rays intersect the image plane along a length of distance "ε".

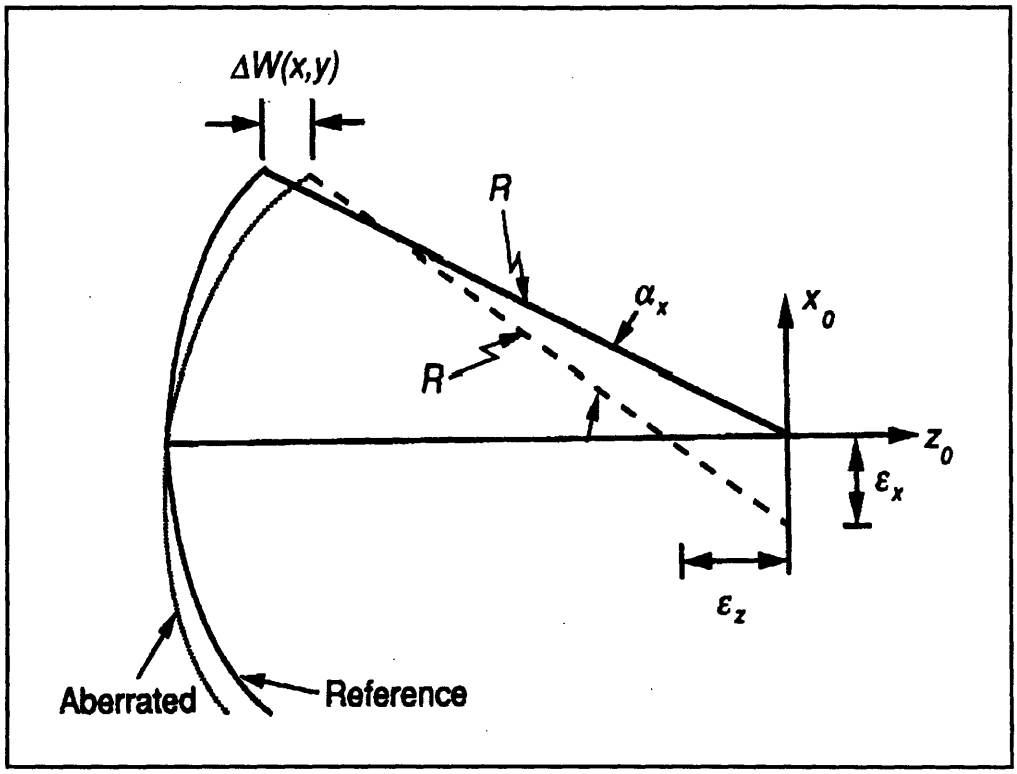

Figure 7.6: Transverse, Longitudinal and Angular Aberrations

The OPD in the Figure 7.6 is exaggerated - theory states that the OPD between aberrated and unaberrated wavefronts is very small, so that the sine of the angle "α" equals the angle itself. This angle between the ideal ray and the aberrated ray is called the "angular aberration", and is defined as

$$\alpha_x = -\frac{\partial \Delta W(x,y)}{n \partial x}. \tag{7.11}$$

"n" is the refractive index, and will be set equal to one. The distance "ε" along the x- and y-axis of the image plane is a measure of "transverse aberration". The x-axis transverse aberration is

$$\varepsilon_x = R\alpha_x = -R\frac{\partial \Delta W(x,y)}{n \partial x}. \tag{7.12}$$

The y-axis transverse aberration is

$$\varepsilon_y = R\alpha_y = -R\frac{\partial \Delta W(x,y)}{n \partial y}. \tag{7.13}$$

A third measure of aberration is the longitudinal distance between the image plane and the point along the optical axis where the aberrated ray crosses. It is the "longitudinal aberration". From Figure 7.6,

$$\frac{\varepsilon_z}{\varepsilon_x} \approx \frac{R}{x - \varepsilon_x}, \tag{7.14}$$

so that the longitudinal aberration, in a small angle approximation, is

$$\varepsilon_z \approx \frac{R}{x}\varepsilon_x = -\frac{R^2}{x}\frac{\partial \Delta W(x,y)}{n \partial x}. \tag{7.15}$$

The wavefront OPD in normalized coordinates is

$$\Delta W = -\frac{h^2}{R^2}\int_0^{x'} x\varepsilon_z \, dx \tag{7.16}$$

or

$$\Delta W = -\frac{h}{R}\int_0^{x'} \varepsilon_x \, dx. \tag{7.17}$$

7.4 Seidel Aberrations

In section 7.2, the wavefront distribution

$$W(x,y) = \left(\frac{x^2+y^2}{2R}\right) - \varepsilon_z\left(\frac{x^2+y^2}{2R^2}\right) - x\frac{\varepsilon_x}{R} - y\frac{\varepsilon_y}{R} \qquad (7.10)$$

is used to describe a spherical wavefront with center of curvature at the point $(\varepsilon_x, \varepsilon_x, \varepsilon_z)$. This point lies in an image plane coordinate system (x_0, y_0, z_0), where the origin is a distance R from the exit pupil vertex. (Please see Fig 7.1)

W. T. Welford (Ref. 22), in his development of the aberration types of Sir William Hamilton, drew the coordinate system in Figure 7.1 in such a way that the image point forms in a plane defined by the x and z axes. This makes y_0 equal to zero, and allows $W(x,y)$ to be written as a power series expansion:

$$\begin{aligned} W(x, y, x_0) &= W(x^2+y^2,\, x x_0,\, x_0^2) \\ &= a_1(x^2+y^2) + a_2 x x_0 + a_3 x_0^2 + b_1(x^2+y^2)^2 \\ &\quad + b_2 x x_0(x^2+y^2) + b_3 x^2 x_0^2 + b_4 x_0^2(x^2+y^2) \\ &\quad + b_5 x x_0^3 + b_6 x_0^4 + \ldots\ldots \end{aligned} \qquad (7.11)$$

It turns out that imperfect optical surfaces often exhibit certain common design/manufacturing errors that give rise to well defined test patterns. The infinite series in equation (7.11) is a decomposition of the errors that are often seen in waveforms passing through various aberrated optical surfaces. The first three terms in equation (7.11) give rise to the tilt and defocus. aberrations described in Section 7.2..

The terms with coefficients b_1 to b_6 are fourth degree polynomials, and reduce to third order when expressed as transverse ray aberrations. Expressing the aberrations in polar coordinate form,

$$x = \rho\cos\theta \qquad y = \rho\sin\theta,$$

and the polar expansion is

$$W(x_0, \rho, \theta) = \sum_{j,m,n} W_{klm}\, x_0^k \rho^l \cos^m\theta$$

$$\textit{where} \qquad k = 2j + m, \qquad \textit{and} \qquad l = 2n + m,$$

$$\begin{aligned} W(x_0, \rho, \theta) &= W_{200}\, x_0^2 + W_{111}\, x_0 \rho\cos\theta + W_{020}\,\rho^2 \\ &+ W_{040}\,\rho^4 + W_{131}\, x_0 \rho^3\cos\theta + W_{222}\, x_0^2 \rho^2\cos^2\theta \\ &+ W_{220}\, x_0^2\rho^2 + W_{311}\, x_0^3 \rho\cos\theta. \end{aligned} \tag{7.12}$$

Aberration Coefficient	Functional Form	Aberration Name
W_{200}	x_0^2	piston
W_{111}	$x_0\rho\cos\theta$	tilt
W_{020}	ρ^2	focus
W_{040}	ρ^4	spherical
W_{131}	$x_0\rho^3\cos\theta$	coma
W_{222}	$x_0^2\rho^2\cos^2$	astigmatism
W_{220}	$x_0^2\rho^2$	field curvature
W_{311}	$x_0^3\rho\cos\theta$	distortion

Table 7.1: Associating the functional form with the aberration name.

Spherical aberration, coma, astigmatism, field curvature and distortion are sometimes called the Seidel aberrations, after Ludwig von Seidel (1821-1896), who pioneered the study of the monochromatic third order aberrations.

7.4.1 Spherical Aberration

Spherical aberration is represented by the term

$$\Delta W = W_{040}\,\rho^4 = W_{040}\left(x^2 + y^2\right)^2.$$

In spherical aberration, the marginal rays (the rays reflected from the edge of the mirror) cross the optical axis at some point other than the paraxial focus. This can be caused by symmetric wavefront distortion characterized by concentric contour lines at the outer radii of the wavefront.

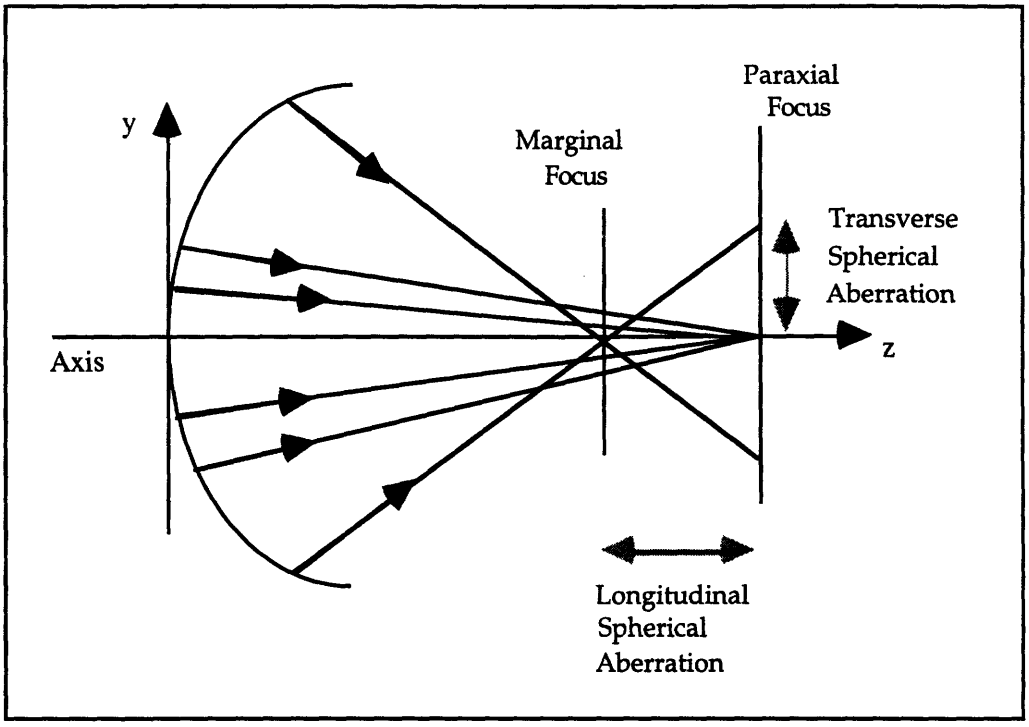

Figure 7.7: A deformed parabolic mirror forcing the marginal rays to an aberrant focus, showing Spherical Aberration (SA).

Figure 7.7 shows the SA described by concentric contours. It can be imagined that the outer portions of the optic have been bent inward so that the designed parabolic figure more closely resembles a spherical figure. This forces the marginal rays to cross the optical axis short of the paraxial focus. Had the outer portions of the optic been deformed outwards, the marginal focus would have been beyond the paraxial focus along the optical axis.

Figure 7.8 shows the uniform contour intervals of the wavefront that along the outer radii that so characterizes the aberration.

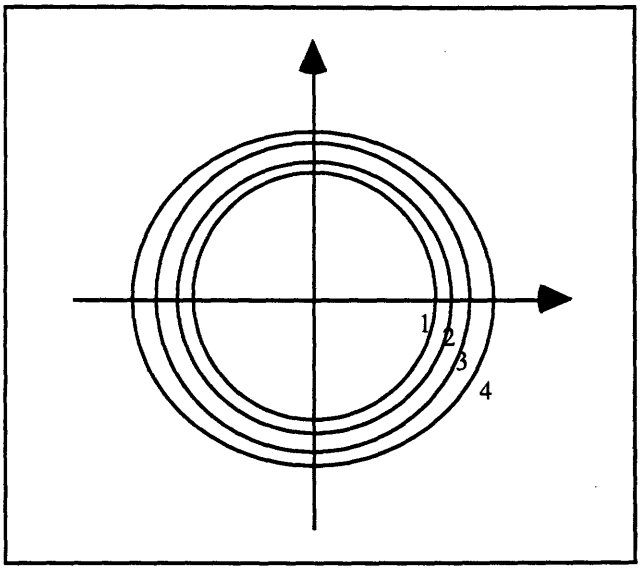

Figure 7.8 Contours of constant spherical aberration.

The visual effect of spherical aberration is to soften the contrast of the image with the background, and to blur image details.

Transverse Spherical Aberration

Transverse spherical aberration (TSA) measures the distance from the optical axis to the point where the marginal rays strike the image plane. From the definition of a transverse aberration in Section 7.3 ,

$$\varepsilon_x = -\frac{R}{h}\frac{\partial \Delta W}{\partial x} \quad \Rightarrow \quad \varepsilon_x = -\frac{4RW_{040}}{h}x\left(x^2+y^2\right)$$

$$\varepsilon_y = -\frac{R}{h}\frac{\partial \Delta W}{\partial y} \quad \Rightarrow \quad \varepsilon_y = -\frac{4RW_{040}}{h}y\left(x^2+y^2\right)$$

where "h" is the geometrical pupil radius. The aberration is symmetric about the principal ray, and the transverse variant can be written

$$\varepsilon_x = \varepsilon_y = -\frac{4RW_{040}}{h}\rho^3.$$

7.4.2 Coma

The name "coma" originates from the visual similarity some observers perceive between the elongated comatic image and the sight of a comet streaking across the night sky. Coma is described by the term

$$\Delta W = W_{131} x_0 \rho^3 \cos\theta = W_{131} x_0 x\left(x^2 + y^2\right). \tag{7.13}$$

The presence of the single field term "x_0" in equation (7.13) ensures that coma lacks the uniformly symmetric distortion contour pattern of spherical aberration. The coma pattern is one of asymmetric contour lines.

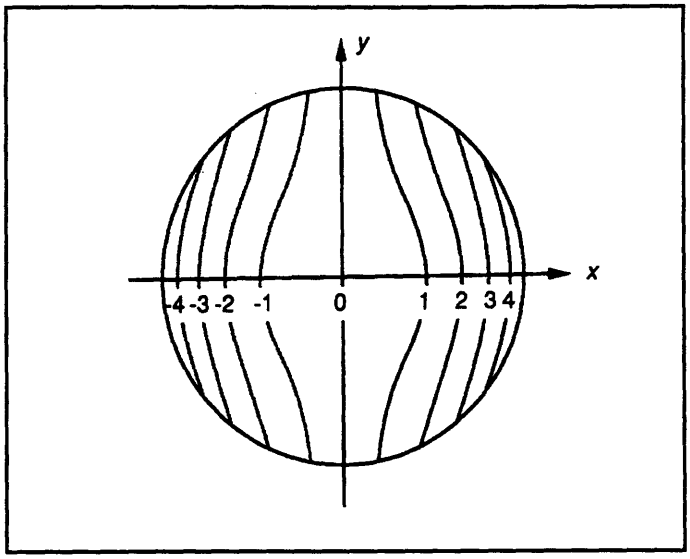

Figure 7.9: Contours of aberration for coma, from Shannon (Ref. 23).

The transverse aberration components of coma are

$$\varepsilon_x = -\frac{R}{h} W_{131} x_0 \left(3x^2 + y^2\right) = -\frac{R}{h} W_{131} x_0 \rho^2 (2 + \cos 2\theta)$$

$$\varepsilon_y = -\frac{2R}{h} W_{131} x_0 xy = -\frac{R}{h} W_{131} x_0 \rho^2 \sin 2\theta.$$

Where this thesis utilizes Creath's (Ref. 24) wave equation "W(x,y)" to describe wavefronts and aberrations, Schroeder (Ref. 25) uses a more geometric method that emphasizes optical path lengths. Schroeder emphasizes

that an aberration can be defined as being either an "on-axis" or "off-axis" object. An on-axis object lies on the mirror's optical axis, and an "off-axis" object's incoming rays make an angle "ϕ" with the optical axis. Schroeder describes coma as an off-axis aberration, and defines transverse coma as

$$TCA_y \propto \frac{y^2}{R^2}\phi s'$$

where "y" is the height of the point of the ray's reflection from the mirror, "R" is the mirror's radius of curvature, s' is the focal length, "f" is the angle the incoming ray makes with a line parallel to the mirror's optical axis. TCA stands for "transverse comatic aberration". This approach shows coma as being linearly proportional to the optical-axis angle ϕ, with a heavy " y^2 " dependence that drives the aberration's geometry. This " y^2 " dependence means that rays incident on the outer portion of the mirror will focus at a different height than rays reflecting from the center of the mirror. This creates an elongated image.

7.4.3 Astigmatism

The word "astigmatism" derives from the Greek; "a" means not, and "stigma" means spot or point. Hence, the word "astigmatic" suggests an aberration that is not circularly symmetric. This is quite accurate, as the extreme condition of astigmatism is a line image. Astigmatic images, like comatic images, are members of the "off-axis" class of optical faults. The term in the Creath/Wolford wave equation that describes astigmatism is

$$\Delta W = W_{222} x_0^2 \rho^2 \cos^2\theta = W_{222} x_0^2 x^2 \ .$$

Figure 7.5 below shows the propagation of an astigmatic wavefront. The tangential plane is defined as any plane through the optical axis. The sagital plane contains the chief ray and is perpendicular to the tangential plane. (Ref. 26)

An ideal, unaberrated converging spherical wave takes on the appearance of a propagating cone converging toward a point. In the case of astigmatism, the cross section of this developing cone deforms as it progresses away from the mirror. It starts its reflective life as a perfectly circular cross-section, then grows progressively more elliptical as the wave propagates toward its focus. It finally reaches an extreme of eccentricity at the "tangential focus", where this ever more eccentric cone collapses into a two-dimensional line. This line, exactly aligned with the sagital plane, is called the tangential line image, and is a distance from the mirror that is defined as the tangential focus length.

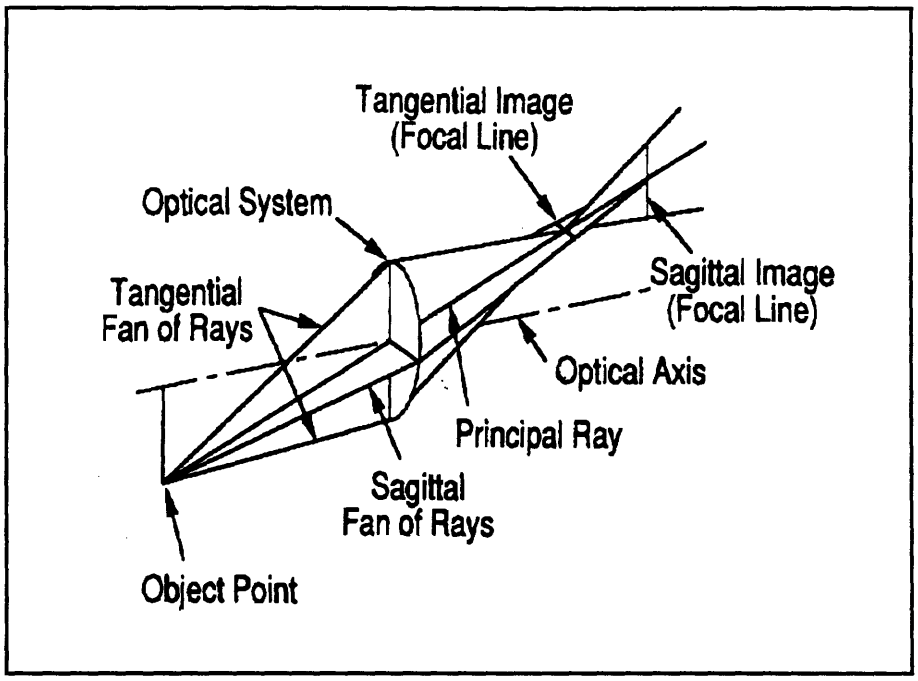

Figure 7.10: Astigmatic cone of rays leaving the optic becomes elliptical, forming a line image at tangential focus. The line image grows open, before again becoming elliptical, and forming a sagital line image.

As the wave continues to propagate it grows again, regaining a cone-type geometry and rapidly exhibiting, once again, nearly circular symmetry. This reborn circular symmetry is soon lost to another eccentric, elliptical deformation. The extreme of this second elliptic is a two-dimensional line image that forms in the tangential plane and is known as the "sagital line image". This sagital line image is oriented at 90° to the tangential line image at a distance from the vertex known as the sagital focal length.

The components of transverse astigmatism in the meridional plane are

$$\varepsilon_y = 0,$$

$$\varepsilon_x = -\frac{2R}{h} W_{222} x_0^2 x = -\frac{2R}{h} W_{222} x_0^2 \rho \cos\theta.$$

These components will form a line image of length

$2\varepsilon_x$ or, equivalently $\frac{4R}{h} W_{222} x_0^2$.

If the wavefront aberration is compounded by a focal shift of length

$$\frac{\varepsilon_z h^2}{2R^2}\left(x^2+y^2\right),$$

then the wave front aberration becomes

$$\Delta W = W_{222} x_0^2 x^2 + \frac{\varepsilon_z h^2}{2R^2}\left(x^2+y^2\right)$$

and the resulting transverse aberration becomes

$$\varepsilon_y = -\left(\frac{\varepsilon_z h}{R}\right) y, \qquad \text{or} \qquad \varepsilon_x = -\left(\frac{2R}{h} W_{222} x_0^2 + \frac{\varepsilon_z h}{R}\right) x.$$

7.4.4 Distortion

Distortion has the effect of distorting the image. The image of any straight line that meets the origin is a straight line, while the image of any other straight line is curved. The wave function term and the length of transverse image shift associated with distortion are

$$\Delta W = W_{311}\, x_0^3 \rho \cos\theta = W_{311}\, x_0^3\, x \qquad\qquad \varepsilon_x = -\frac{R}{h} W_{311}\, x_0^3.$$

7.4.5 Field Curvature

Field curvature is described by the wave function term

$$\Delta W = W_{220}\, x_0^2 \rho^2 = W_{220}\, x_0^2 \left(x^2 + y^2\right).$$

The aberration has the same ρ^2 dependence as a focal shift, and is proportional to the square of the field height x_0^2. The visual appearance of field curvature (please see Figure 7.11, (Ref. 27)) is that of a true point image on a curved surface. The imaginary surface on which the image appears is called the Petzval Surface.

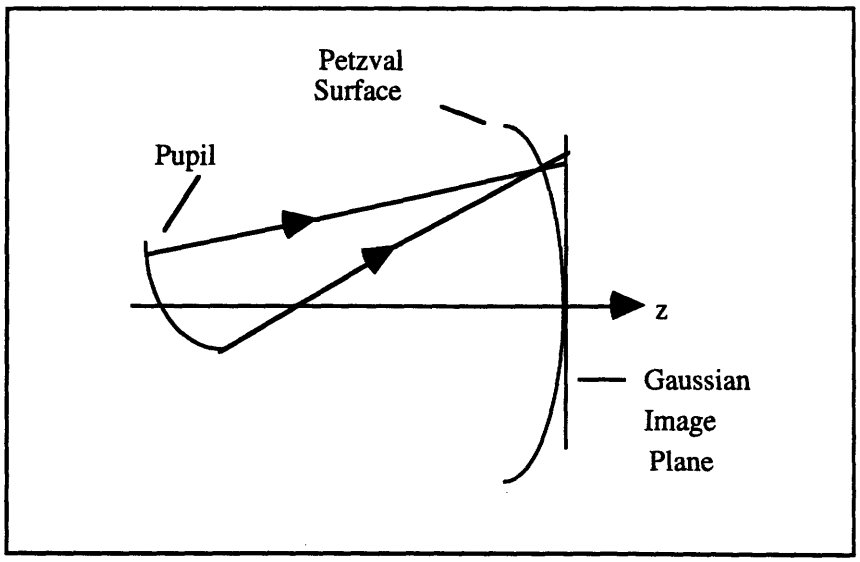

Figure 7.11: Field Curvature and the Petzval Surface.

Chapter 8

Optical Analysis: "SURFACE", "PCFRINGE", and the Method of Zernike Polynomials

The optical performance of the MDM/Hiltner primary mirror is analyzed with the help of two optical analysis codes. Both codes numerically calculate the form of the reflected wavefront by using the surface deflection data generated by the NASTRAN finite element analysis.

"SURFACE", written by Professor John Tonry (MIT, 1996), uses NASTRAN deflection data to map the mirror surface and then simulates a reflected wavefront by tracing a large number of individual rays from the point of reflection at the mirror surface toward the ray's intersection with the image plane. The code's image plane can be moved forward and backward along the optical axis so that a spot diagram can be made at any point along the reflected wavefront's path. This valuable option makes possible a sequential view of the wavefront's propagation on either side of the nominal focal point.

In addition to creating the spot diagrams, SURFACE provides a measure of spot diagram quality by quantifying the density of the rays that constitute the spots. This ray density is used to produce spot diagram RMS, Peak to Valley,

and encircled energy measurements. RMS, P-V, and encircled energy are given in units of microns.

SURFACE also produces a wavefront contour plot that shows the reflected wave (and hence, the mirror surface) as it travels through the exit pupil. RMS and Peak-Valley measurements are calculated for this contour plot.

Another set of optical tests is accomplished with a code called PCFRINGE, which quantifies reflected wavefront aberrations by fitting the series of Zernike polynomials to the NASTRAN mirror surface deflection data.

The Zernike polynomials used in PCFRINGE are a set of orthogonal polynomials that can be used as basis functions to describe the composition of a wavefront. Zernike polynomials are commonly used to interpret optical test results. The coefficients associated with these polynomials provide a measure of higher order wavefront aberrations. These coefficients are used in this thesis both as an analytical tool and as a control component in a least squares optimization process that services a prospective active optics system.

8.1 Zernike Polynomials and Wavefront Fitting

Frits Zernike in the 1930's endeavored to devise a set of polynomials that would bring algebraic order to certain problems associated with his studies of optical image formation. The resulting polynomial series that bares Zernike's name expresses wavefront data in polynomial form.

Zernike polynomials are a set of orthogonal polynomials within a unit circle that act to decompose an aberrant wavefront. The individual polynomials describe types of aberration normally seen in optical analysis. The polynomials of the Zernike series decompose the aberrant wave by fitting the optical path difference (OPD) between an ideal, unaberrated wave and that of a deformed, aberrated wave in component form. The individual components of the Zernike series, as modified by their coefficients, characterize specific optical aberrations. Each of the polynomial terms are of the same form as a type of aberration commonly observed in optical tests.

The Zernike polynomials are one of an infinite number of complete sets of polynomials in two real variables, ρ and θ, that are orthogonal and continuous over a unit circle. Several properties (described below) distinguish Zernike polynomials from other sets of orthogonal polynomials and make them usable for fitting wavefront data. (Ref. 28):

The first defining property of the Zernike polynomials is that they exhibit a simple rotational symmetry. They form a product of the form

$$R(\rho)G(\theta)$$

where $G(\theta)$ is a continuous function that repeats itself every 2π radians.

The second property is that the above polynomial must satisfy a requirement that a rotation of the coordinate system by an angle "α" will not change the polynomial's form, so that:

$$G(\theta+\alpha) = G(\theta)G(\alpha).$$

The set of trigonometric functions that meets this requirement is

$$G(\theta) = e^{\pm im\theta},$$

where "m" is any positive integer or zero.

The third defining property is that the radial function must be a polynomial in "ρ" of degree "n" and contain no power of "ρ" less than "m".

The fourth defining property is that $R(\rho)$ must be even if "m" is even, and odd if "m" is odd.

The radial component of Zernike polynomials can be derived from Jacobi polynomials. Orthogonality and normalization properties are (Ref. 29)

$$\int_0^1 R_n^m(\rho)\, R_{n'}^m(\rho)\, \rho\, d\rho = \frac{1}{2(n+1)}\delta_{nn'} \qquad \text{and} \qquad R(1) = 1.$$

The radial polynomial can be factored into $R_{2n-m}^m(\rho) = Q_n^m(\rho)\,\rho^m$

where the polynomial $Q_n^m(\rho)$ is of order $2(n-m)$. $Q_n^m(\rho)$ can be written

$$Q_n^m(\rho) = \sum_{s=0}^{n-m}(-1)^s \frac{(2n-m-s)!}{s!(n-s)!(n-ms)!}\rho^{2(n-m-s)}.$$

The practical application of the radial polynomial uses sines and cosines. The series can be defined as a sum of OPD components

$$\Delta W = \overline{\Delta W} + \sum_{n=1}^{\infty}\left[A_n Q_n^0(\rho) + \sum_{m=1}^{n} Q_n^m(\rho)\rho^m\left(B_{nm}\cos m\theta + C_{nm}\sin m\theta\right)\right]$$

where $\overline{\Delta W}$ is the mean wavefront optical path difference.

In order to see the Zernike series as directly equivalent to the wavefront distribution developed in Section 7.4, it is necessary to group like terms and then equate the like terms with the wavefront aberration coefficients. (Ref. 30) The wavefront distribution, using the first nine Zernike terms, before regrouping is:

$$\begin{aligned} W(\rho,\theta') = {} & Z_0 + Z_1\rho\cos\theta' + Z_2\rho\sin\theta' + Z_3(2\rho^2-1) \\ & + Z_4\rho^2\cos 2\theta' + Z_5\rho^2\sin 2\theta' \\ & + Z_6(3\rho^2-2)\rho\cos\theta' + Z_7(3\rho^2-2)\rho\sin\theta' \\ & + Z_8(6\rho^4-6\rho^2-1). \end{aligned}$$

Regrouping the first nine terms and equating them with aberrations yields:

$$W(\rho,\theta') = Z_0 - Z_3 - Z_8 \qquad \text{Piston}$$

$$+\left(Z_1 - 2Z_6\right)\rho\cos\theta' + \left(Z_2 - 2Z_7\right)\rho\sin\theta' \qquad \text{Tilt}$$

$$+\left(2Z_3 - 6Z_8 + Z_4\cos 2\theta' + Z_5\sin 2\theta'\right)\rho^2 \qquad \text{Focus \& Astigmatism}$$

$$+ 3\left(Z_6\cos\theta' + Z_7\sin\theta'\right)\rho^3 \qquad \text{Coma}$$

$$+ Z_8\,\rho^4. \qquad \text{Spherical}$$

The above equation can be rewritten using the identity

$$a\cos\alpha + b\sin\alpha = \sqrt{a^2+b^2}\,\cos\left[\alpha - \tan^{-1}\left(\frac{b}{a}\right)\right].$$

The result is a wavefront equation that isolates the aberration coefficients:

$$W(\rho,\theta') = Z_0 - Z_3 - Z_8 + \qquad \text{Piston}$$

$$\rho\sqrt{\left(Z_1-2Z_6\right)^2+\left(Z_2-2Z_7\right)^2}\;\times\;\cos\left[\theta-\tan^{-1}\left(\frac{Z_2-2Z_7}{Z_1-2Z_6}\right)\right] \qquad \text{Tilt}$$

$$+\;\rho^2\left(2Z_3-6Z_8\pm\sqrt{Z_4^2+Z_5^2}\right) \qquad \text{Focus}$$

$$+\;2\rho^2\sqrt{Z_4^2+Z_5^2}\,\cos^2\left[\theta-\frac{1}{2}\tan^{-1}\left(Z_5/Z_4\right)\right] \qquad \text{Astigmatism}$$

$$+\;3\rho^3\sqrt{Z_6^2+Z_7^2}\,\cos\left[\theta-\tan^{-1}\left(Z_7/Z_6\right)\right] \qquad \text{Coma}$$

$$+\;6\rho^4 Z_8. \qquad \text{Spherical}$$

The next sections list the first thirty-six Zernike terms, and show a pictorial view of the aberrations they represent.

8.2 Table of Zernike Polynomials

n	*m*	*No.*	*Polynomial*	
0	0	0	1	
1	1	1	$\rho\cos\theta$	*x tilt*
		2	$\rho\sin\theta$	*y tilt*
	0	3	$2\rho^2-1$	*focus*
2	2	4	$\rho^2\cos 2\theta$	*astigmatism @ 0°*
		5	$\rho^2\sin 2\theta$	*astigmatism @ 45°*
	1	6	$(3\rho^2-2)\rho\cos\theta$	*coma and x−tilt*
		7	$(3\rho^2-2)\rho\sin\theta$	*coma and y−tilt*
	0	8	$6\rho^4-\rho^2+1$	*spherical and defocus*
3	3	9	$\rho^3\cos 3\theta$	
		10	$\rho^3\sin 3\theta$	
	2	11	$(4\rho^2-3)\rho^2\cos 2\theta$	
		12	$(4\rho^2-3)\rho^2\sin 2\theta$	
	1	13	$(10\rho^4-12\rho^2+3)\rho\cos\theta$	
		14	$(10\rho^4-12\rho^2+3)\rho\sin\theta$	
	0	15	$20\rho^6-30\rho^4+12\rho^2+1$	

4	4	16	$\rho^4 \cos 4\theta$
		17	$\rho^4 \sin 4\theta$
	3	18	$(5\rho^2 - 4)\rho^3 \cos 3\theta$
		19	$(5\rho^2 - 4)\rho^3 \sin 3\theta$
	2	20	$(15\rho^4 - 20\rho^2 + 6)\rho^2 \cos 2\theta$
		21	$(15\rho^4 - 20\rho^2 + 6)\rho^2 \sin 2\theta$
	1	22	$(35\rho^6 - 60\rho^4 + 30\rho^2 - 4)\rho \cos\theta$
		23	$(35\rho^6 - 60\rho^4 + 30\rho^2 - 4)\rho \sin\theta$
	0	24	$70\rho^8 - 140\rho^6 + 90\rho^4 - 20\rho^2 + 1$
5	5	25	$\rho^5 \cos 5\theta$
		26	$\rho^5 \sin 5\theta$
	4	27	$(6\rho^2 - 5)\rho^4 \cos 4\theta$
		28	$(6\rho^2 - 5)\rho^4 \sin 4\theta$
	3	29	$(21\rho^4 - 30\rho^2 + 10)\rho^3 \cos 3\theta$
		30	$(21\rho^4 - 30\rho^2 + 10)\rho^3 \sin 3\theta$
	2	31	$(56\rho^6 - 105\rho^4 + 60\rho^2 - 10)\rho^2 \cos 2\theta$
		32	$(56\rho^6 - 105\rho^4 + 60\rho^2 - 10)\rho^2 \sin 2\theta$
	1	33	$(126\rho^8 - 280\rho^6 + 210\rho^4 - 60\rho^2 + 10)\rho \cos\theta$
		34	$(126\rho^8 - 280\rho^6 + 210\rho^4 - 60\rho^2 + 10)\rho \sin\theta$
	0	35	$252\rho^{10} - 630\rho^8 + 560\rho^6 - 210\rho^4 + 30\rho^2 - 1$
6	0	36	$924\rho^{12} - 2772\rho^{10} + 3150\rho^8 - 1680\rho^6 + 420\rho^4 - 42\rho^2 + 1$

8.3 PCFRINGE

PCFRINGE (abbreviated as PCF) is the IBM-PC compatible version of a FORTRAN program written by James D. Rancourt and John S. Loomis at the University of Arizona's Optical Science Center. PCF takes its input data from a finite element model and produces both ray tracing and diffraction analysis. PCF is this thesis' primary optical-analysis tool for the MDM mirror model .

PCFRINGE accepts two basic inputs from a finite element model. The first is a "geometry" file that contains information describing the identity and location of all nodes and elements in the FE model. The second is a "displacement" file that contains information describing all nodal displacements that occur as a result of load conditions imposed in the running of the finite element model.

From the FE geometry and displacement information and user-supplied command and control files, PCF knows the mirror's radius of curvature and the identity of the nodes that constitute the surface of the mirror model. (Focal length is equal to 1/2 the radius of curvature.) PCF constructs an "ideal", or "reference" wavefront using the geometry and radius of curvature information. The code acts to compute displacements normal to the surface at each nodepoint using the displacement data, and thus creates an "actual" or "aberrated" wavefront.

The primary analytical tool of PCF is the Zernike polynomial fit. The code fits the Zernike polynomials to the optical path length difference between the reference and aberrated wavefronts. This fitting of Zernike polynomials transforms information on mirror surface structure into an algebraic measure of wavefront distortion.

PCF performs its optical analysis by manipulating the Zernike coefficients. The coefficients state explicitly how much of any particular aberration (coma, astigmatism, etc.) exists in the subject wavefront. The Zernike manipulation produces contour maps, spot diagrams, radial energy distributions and RMS data. Diffraction analysis based on a fast Fourier transform yields a point spread function and a modulation transfer function.

Chapter 9

The Mirror, the Model, and Model Verification

Chapter 9 presents a detailed description of the Michigan Dartmouth MIT/Hiltner telescope's 2.4 meter primary mirror and its axial and radial support systems. This chapter also describes the finite element model that is used to analyze the mirror and its support systems. Finally, the chapter describes the structural experiment that was conducted on the MDM/Hiltner telescope at Kitt Peak to test the finite element model's accuracy. The experiment's optical results are presented.

The finite element model described and verified here is used in Chapter 10 for an examination of the mirror's structural and optical response to applied force. In Chapter 11 the model is used to design an active optics system for the MDM/Hiltner primary mirror.

9.1 The MDM/Hiltner Primary Mirror, and Axial and Radial Support Systems

The Michigan, Dartmouth, MIT/Hiltner Telescope is a Cassegrain-type reflecting telescope located on the southwest ridge of Kitt Peak, near Tucson, Arizona, about two miles from the site of the National Optical Astronomical Observatories. The telescope's primary mirror, the subject of this thesis' research, is 2.4 meters in diameter, weighs approximately 1990 kg, and has a focal length of 4.82 meters.

The primary mirror structure is continuous and homogeneous, and is made of Cervit, a glass-composite material produced by Owens-Illinois, Inc. Cervit is a relatively stiff material (Elasticity $\approx$ 9.2 E10 N/m^2) that exhibits a very low coefficient of thermal expansion. Cervit is a member of a family of micro crystalline-polycrystalline materials called glass-ceramics. (Ref. 31)

At the time of its introduction, Cervit represented a significant advancement in optical mirror materials. Cervit showed advantages in polishability, expansion coefficient, stiffness, microcreep and stability. In other words, it was the stiffest stuff that would take a good polish that anyone could make, and was a great material for the mirror design philosophy that called for stiff, rigid mirrors as the best way to ensure a good optical figure. Table 9.1 compares the material properties of Cervit to other, more well known substances. (Ref. 31)

Material	Density	Elasticity	Poisson Ratio	α*
Cer-Vit C-101	2.5E3 Kg/m^3	9.18E10 N/m^2	.25	≈ 0
Pine	417 Kg/m^3	8.0 E9 N/m^2		
Glass	2.5E3 Kg/m^3	5.51E10 N/m^2		9
Aluminum	2.62E3 Kg/m^3	6.90E10 N/m^2	.33	23
Steel	7.9E3 Kg/m^3	20.67E10 N/m^2	.33	11

Table 9.1: *The thermal expansion coefficient α is a dimensionless constant that satisfies the relation $\alpha = (\Delta L/L)/\Delta T$.)

The mirror's reflecting surface has a hyperbolic figure, while its back surface is flat. This gives the mirror a variable thickness. The central hole defines the inner radius, which is .1524 meters. The mirror's thickness at this inner radius is .1622 meters. Calculation of the mirror's thickness at the outer radius is complicated by the "knob" that protrudes from the mirror body at the outer edge of the reflecting surface. The vertical height of the mirror's front surface at the outside radius is .2334 meters above the plane of the mirror's back surface. Figure 9.1 is a conceptual cross-section.

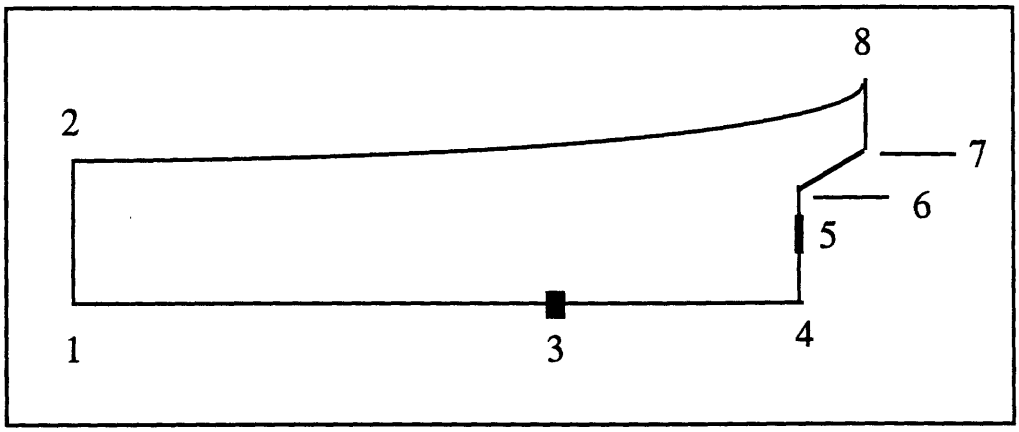

Figure 9.1: Conceptual radial profile (r, z) of a slice of the MDM primary mirror.

Key node definitions in Figure 9.1 give the mirror's exact dimensions. These dimensions were extracted from the G.L. Barnes finite element analysis of August, 1990 (Ref. 32), and confirmed by the telescope blueprints (Ref. 33).

Pt. 1 defines the radius of the inner hole at the mirror's bottom surface (r = .1524 m, z = 0).

Pt. 2 defines the radius of the inner hole at the mirror's top surface (r = 1524 m, z =.1622 m).

Pt. 3 defines the exact radius of the hard points (r = .8255 m, z = 0). The three hard points are spaced at 120° intervals across the bottom surface.

Pt. 4 defines the outer radius along the mirror's bottom (r = 1.143 m, z = 0).

Pt. 5 defines center of mass. This is also the center of the mercury belt. The lower boundary of the mercury belt is at (r = 1.143 m, z = .0845 m). The upper Hg belt boundary is at (r = 1.143 m, z = .1163 m).

Pt. 6 defines the node at which the mirror's outside wall drives laterally upward, creating "the notch". (r = 1143.0 m, z = 170.18 m).

Pt. 7 defines the node at which the mirror's outer wall is again perpendicular to the back surface. (r = 1.181 m, z =.2083 m) Note that the scale of the notch is exaggerated in Figure 9.2.

Pt. 8 defines the mirror's outer rim, the outside radius of the reflecting surface. (r = 1.181 m, z = .2334 m). Points 1-8 define the hyperbolic reflecting surface, which has a primary conic constant of -1.050145. The radius of curvature is 9.6327 meters, the focal length is 4.82 meters.

The mirror rests in a mirror cell, supported by axial and radial support systems. Primary axial support is a set of three neoprene air bladders which provide a constant pressure across the mirror's back surface. Also providing axial support is a set of three hard points located at r = .825 meters, at intervals of 120°. The hard points effectively constrain the mirror from moving in the radial plane. Hard point locations are shown in Figure 9.2.

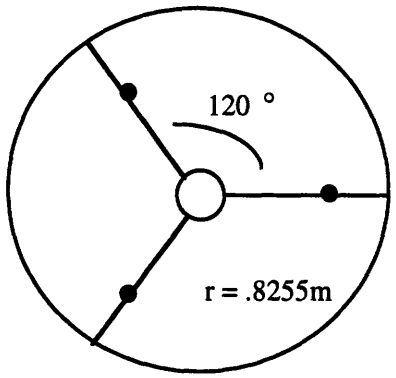

Figure 9.2: Hard points in relation to central hole and mirror outer radius. Radius at SPC's = .8255 meters.

An air pressure controller maintains a specified hard point loading by regulating pressure in the three neoprene air bags. When the mirror is oriented in the purely vertical direction, the three hard points exert a uniform reaction force of 30 pounds (≈ 135 Newtons). This effectively gives the axial support system one degree of freedom and control over mirror tilt. The axial support system can thus be considered tilt-active.

Radial support is provided by a neoprene bladder filled with mercury belt that runs along the mirror periphery at the axial center of mass. The mercury acts as its own analog computer, feeding along the mirror's radial center of mass as the mirror is rotated away from the pure vertical. The mercury exerts a pressure that is proportional to the angle between the optical axis and the pure vertical. The belt acts to support all the mirror's mass if the mirror is rotated to a horizontal orientation. The mercury belt acts as a tangential buffer between the mirror and the mirror cell.

9.2 FEA Model Description

This section describes the finite element model of the 2.4 meter primary mirror and its support systems. This FE model serves as the basis for all subsequent structural and optical analysis.

9.2.1 Model Objectives

The primary objective in building this finite element model is to make an accurate numerical tool for investigating the mechanical and optical behavior of the 2.4 meter mirror and its support system. Specific objectives for the model include the desire to investigate gravity induced deflections in the primary mirror, mirror response to the hard point reaction forces, and mirror reaction to externally applied force inputs.

In a later chapter, the model will be used to design and test an active axial support system so that gravity induced degradations in the mirror may be corrected.

9.2.2 Model Assumptions

Certain assumptions were made about the mirror and the finite element techniques that are used in modeling the mirror. The more significant assumptions are:

- It is assumed that the mirror experiences only small deflections. In other words, the ratio of z-axis deflection to the radius of the deflection point from the center of the mirror's central hole is small.

- The finite element model's nodes require no rotational degrees of freedom. This assumption is a corollary to the small deflection assumption.

- The mirror's hyperbolic figure can be approximated as a parabolic figure without causing a loss of accuracy in modeling the mirror's mechanical or optical response. The ratio of the parabolic conic constant to the primary mirror's conic constant is 1/1.050145 = .95225.

- The supporting action of the axial neoprene airbags and the radial neoprene mercury belt can be simulated by using the pressure functions available in the NASTRAN finite element code.

- It is assumed that single point constraints (zero degrees of translational and rotational freedom) are sufficient to model the action of the three hard points. This assumption proved to be less than wholly accurate in a model verification experiment conducted at Kit Peak. In that experiment, all air pressure was released from the axial support airbags, placing the full weight of the mirror on the hard points. The hard points compressed under the load of the 1990 kg mirror by approximately .10 mm. It was decided that in the absence of unlimited time and funding, the use of single point constraints to represent the compressible hard points would be a workable approximation.

9.2.3 Building The Basic Mesh

The model mesh was built on the Macintosh LapCAD finite element preprocessor. The method chosen was to draw a two-dimensional profile of a slice of the mirror in the x-z plane. The information described in Section 9.1 was used to define the critical nodes. The two dimensional slice was segmented into a mesh, and the 2-D mesh was then extruded around a center point through 360° to create the basic mirror mesh. The extrusions were done in steps of 15°. This produced a three dimensional mirror mesh that has the appearance of a home-baked pie sliced into twenty four pieces.

A primary concern in building the finite element model was to limit the number of elements and thus the total number of degrees of freedom and overall model complexity. This was done with the understanding that a limit on the number of elements might translate into a limit on the model's sensitivity and hence a loss of model accuracy.

Two steps were taken to limit model complexity. First, the elements in the 2-dimensional mesh were created with an aspect ratio greater than 1:1. A larger elemental aspect ratio means that fewer elements and fewer degrees of freedom are required to span the space in the mirror's radial profile.

The second simplifying design consideration was to limit the number of steps in the 360° extrusion of the 2-dimensional mesh to 24 sections of 15°. Several model variations were initially made that effectively tested the sensitivity and complexity of meshes made of 12, 24 and 36 extrusion steps. The results showed that 12 steps of 30° per step were insufficient to accurately model mirror edge deflections. The added sensitivity gained in the 36 step model came at the cost of adding many more degrees of freedom and significantly increasing required CPU time. The compromise between sensitivity and simplicity was made by deciding on a model built in 24 extrusion steps of 15° per step.

Figures 9.3 and 9.4 on the following two pages illustrate the basic three-dimensional mirror mesh.

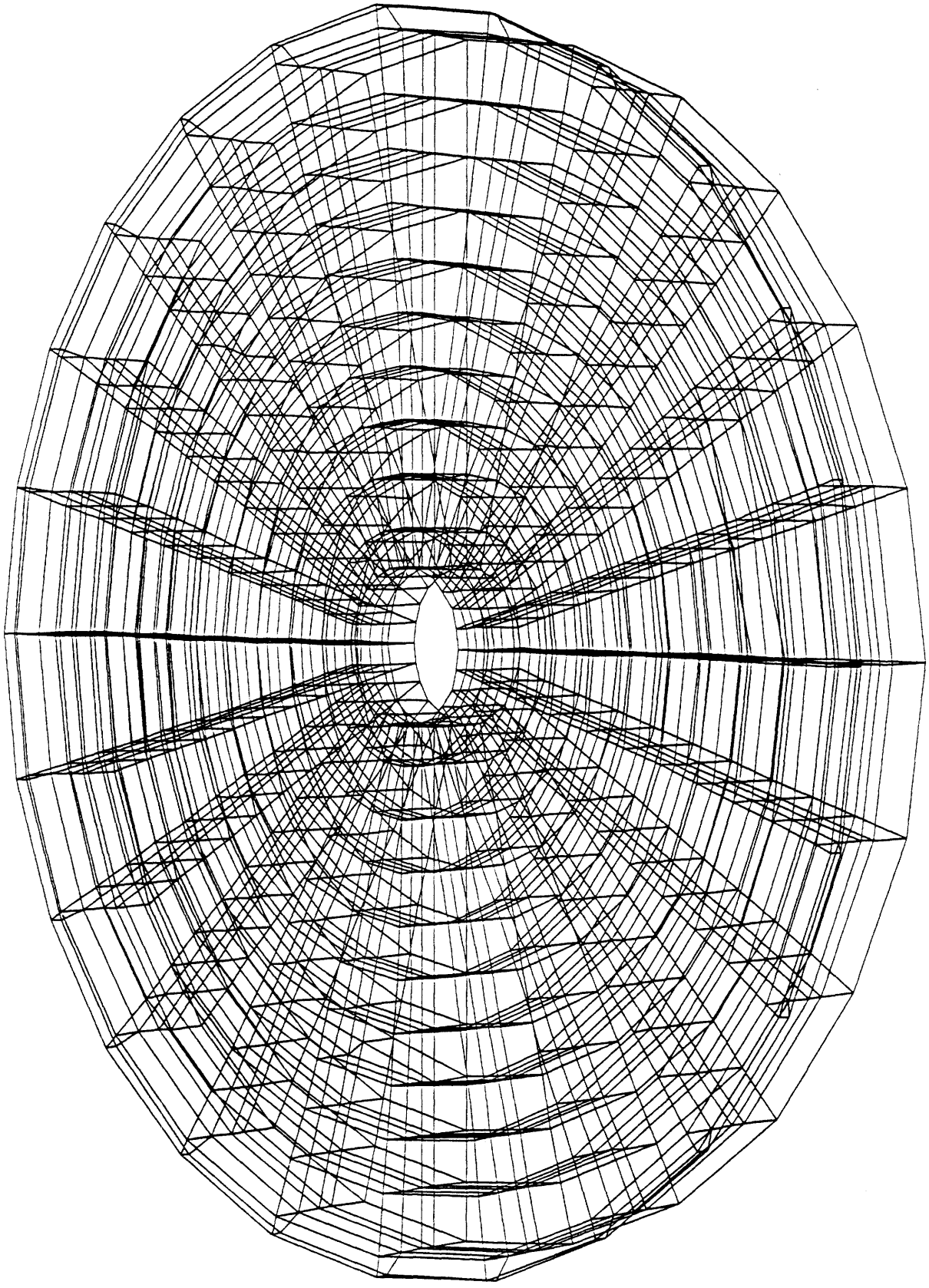

Figure 9.3 Horizontal view of the finite element mesh for the MDM primary mirror model.

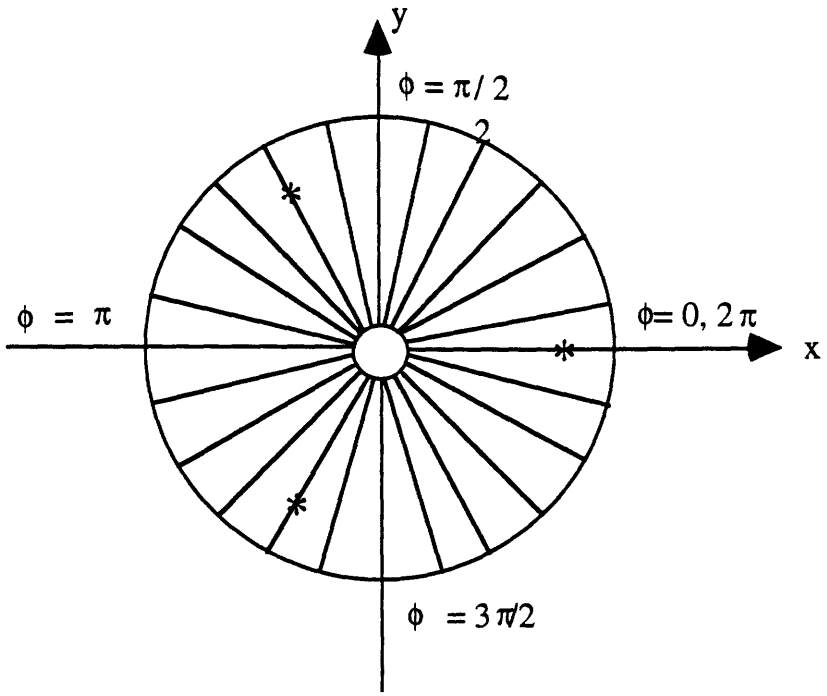

Figure 9.4A: Distribution of 15° extrusion steps and location of SPC's (hard points) in relation to the model's x and y-axis.

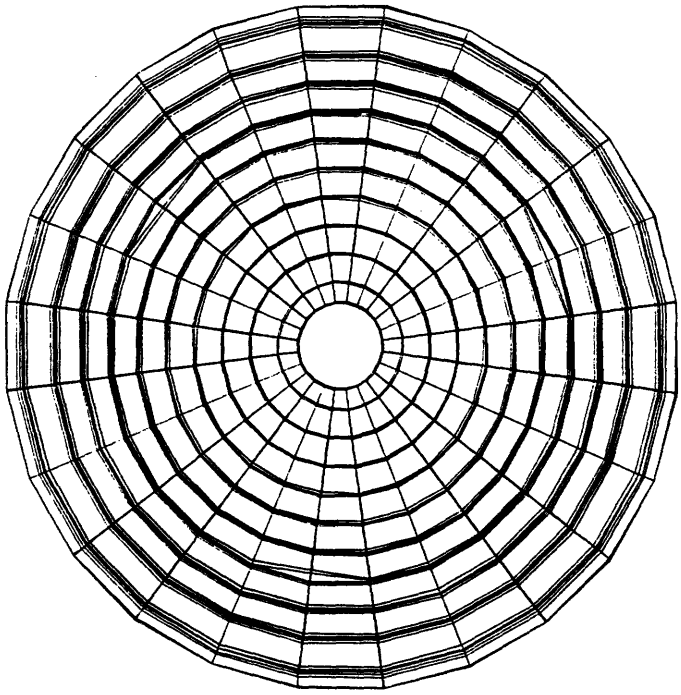

Figure 9.4B Vertical view of the finite element mesh for the MDM primary mirror model.

9.2.4 FE Model of the Axial Support System

The actual mirror is supported in the z-axis by three neoprene air bags and three hard points. When the optical axis of the mirror is oriented to the vertical, the air bags that support the bottom mirror surface are controlled so as to maintain a constant residual thirty pound (133 N) reaction load on each of the hard points. In this vertical orientation, approximately half of the mass of the mercury radial support belt rests on the mirror's perimeter. This adds 15 kg to total mirror mass.

Total mirror mass ≈ 1990 kg.
Total mercury mass supported by the mirror = 15 kg.
Total mass to be supported = 2005 kg.
Force = mg = 2005 kg* 9.81 m/s^2 = 19669.05 N.

The FE model uses a NASTRAN pressure function to simulate axial airbag pressure support. Pressure applied to the mesh's bottom surface elements is calculated as a function of total mirror mass, bottom surface area, gravity orientation and hard point loading. The hard points are modeled as single point constraints (SPC's). The model's SPC's support a residual load of approximately 30 pounds (133 N) each. The SPC nodes constrain all translational and rotational motion.

The residual reaction load of 30 pounds per hard point (133 N/hard point) reduces the total load supported by the axial air bags by approximately 400 N. The calculation for simulating the axial airbag pressure is:

Total Force = 19669 N (mirror mass) - 400 N (Hard Points) = 19229 N.
Bottom Surface Area = $\pi\left(r_{outer}^2 - r_{inner}^2\right)$ = 4.0314 m^2.
Pressure = Force/Area = 4779.8 N/m^2 .

When the mirror is rotated away from a purely vertical orientation, the effective gravity load changes according to the sine of the angle formed by the optical axis and the pure vertical axis. As the angle increases, the load is transferred from the axial to the radial support system.

9.2.5 Modeling the Radial Support System

The mercury belt radial support system applies pressure in proportion to the mirror's vertical orientation. The system is comprised of a neoprene rubber tube which contains approximately 15 kg of mercury. The neoprene bladder has inner and outer flanges. The inner flange fits into an indentation in the mirror that runs along the mirror's outer circumference at the vertical center of mass. The outer flange is supported by the mirror cell. These flanges hold the mercury belt in place.

The model simplifies the belt/mirror interface by using a series of 24 smooth sidewall elements in place of the more complicated flange/indentation structure. Each sidewall element is 32 mm in height and of length .2994 m. The action of the mercury is modeled by applying pressure directly across the face of these exterior sidewall elements. The radial pressures are calculated on the basis of Archimedes principle. The pressure calculation is

$$\text{Pressure} = \rho(\text{density})*g(\text{acceleration})*h(\text{height}) \tag{9.1}$$

where h is the height of a vertical column of mercury. The total force exerted across any element by mercury pressure is

$$F = \int_A^B \rho g(h\sin\theta)(r+r\cos\phi)\,r\,h'\,d\phi. \tag{9.2}$$

where θ is the angle between the optical axis and the horizontal, h' is the width of the mercury belt, and ϕ measures tangential angle. The $(r + r\cos\phi)$ term is a measure of "vertical" diameter for calculating effective mercury column height. The point where $\phi = 0$ is the lowest point of the mercury belt as the mirror's optical axis is rotated toward the horizon. The area of a mercury element, $(r\,h'd\phi)$ is a constant. The calculation is

$$P = F/A = \rho g(h\sin\theta)r^2h'\int_A^B(1+\cos\phi)\,d\phi \Big/ .0095 \tag{9.3}$$

where (.0095) is the surface area of each the model's mercury belt elements.

Table 9.2 presents incrementally averaged pressures for the FE model mercury belt. Column 1 lists the elements' location. Columns 2 - 5 list the pressures for each element at certain mirror orientations. The angle θ is the angle between the optical axis and the pure vertical. At "00" the optical axis is straight up; at "90" the optical axis is parallel to the horizontal. Please see Figure 9.4A for the ϕ orientations. $\phi = 0$ is always the mirror's low point.

$\Delta\ \phi$	$\theta = 00$	$\theta = 30$	$\theta = 45$	$\theta = 90$
$0 - \pi/12$	2534.90	151637.15	214445.25	303274.29
$\pi/12 - 2\pi/12$	2534.90	146499.82	207180.05	292999.64
$2\pi/12 - 3\pi/12$	2534.90	136575.27	193144.75	273150.54
$3\pi/12 - 4\pi/12$	2534.90	122539.83	173295.83	245079.67
$4\pi/12 - 5\pi/12$	2534.90	105350.01	148985.98	210700.01
$5\pi/12 - 6\pi/12$	2534.90	86177.25	121871.86	172354.49
$6\pi/12 - 7\pi/12$	2534.90	66328.14	93801.26	132656.29
$7\pi/12 - 8\pi/12$	2534.90	47155.38	66687.14	94310.76
$8\pi/12 - 9\pi/12$	2534.90	29965.55	42377.29	59931.11
$9\pi/12 - 10\pi/12$	2534.90	15930.12	22528.38	31860.24
$10\pi/12 - 11\pi/12$	2534.90	6005.57	8493.07	12011.14
$11\pi/12 - 12\pi/12$	2534.90	868.24	1227.87	1736.48
$12\pi/12 - 13\pi/12$	2534.90	868.24	1227.87	1736.48
$13\pi/12 - 14\pi/12$	2534.90	6005.57	8493.07	12011.14
$14\pi/12 - 15\pi/12$	2534.90	15930.12	22528.38	31860.24
$15\pi/12 - 16\pi/12$	2534.90	29965.55	42377.29	59931.11
$16\pi/12 - 17\pi/12$	2534.90	47155.38	66687.14	94310.76
$17\pi/12 - 18\pi/12$	2534.90	66328.14	93801.26	132656.29
$18\pi/12 - 19\pi/12$	2534.90	86177.25	121871.86	172354.49
$19\pi/12 - 20\pi/12$	2534.90	105350.01	148985.98	210700.01
$20\pi/12 - 21\pi/12$	2534.90	122539.83	173295.83	245079.67
$21\pi/12 - 22\pi/12$	2534.90	136575.27	193144.75	273150.54
$22\pi/12 - 23\pi/12$	2534.90	146499.82	207180.05	292999.64
$23\pi/12 - 24\pi/12$	2534.90	151637.15	214445.25	303274.29

Chart 9.2: Pressures are in Pascals. The density of mercury is 1.36E4 kg/m^3. The height of the mercury elements is .032m. Column two uses an average h'.

9.3 Model Verification

An experiment was conducted on the MDM/Hiltner telescope at Kitt Peak to test the finite element model's ability to replicate actual results. The telescope was oriented with the optical axis pointing in the vertical, the telescope was focused on a star, and all air pressure was released from the air bag axial supports. The resulting star image made by the deformed primary mirror was recorded electronically using the telescope's "Charlotte" CCD.

To make the comparison between telescope reality and finite element model, the model was exercised under the same support conditions. The NASTRAN pressure function applied to the mesh bottom surface elements was set to zero. The model assigned all of the mirror's weight to the three SPC's (hard points). The deformation produced in both the actual mirror and the model, as demonstrated by spot images and contour diagrams, is dramatic.

The image created by the actual MDM mirror sitting on its three hard points resembles a snowflake, and is termed the "Starflake". This "Starflake" image, shown in Figures 9.3.1, 9.3.3 and 9.3.4, exhibits a six-fold symmetry. An extreme astigmatism is present, with three well defined line images forming, each moved off-center by an equal distance. The image radius (for approximately 100% encircled energy) measures 2.85 arc seconds.

Figure 9.3.6 is a series of nine spot diagrams taken at increments of .05 mm showing the model's attempt to duplicate the starflake image. Spot #5 is taken at the model's nominal focal. Spot #1 is taken at the model's nominal focal plane minus .20 mm. Spot #9 is at the nominal plane plus .20 mm.

The spot diagram series shows the tortured propagation of the starflake wave front as it twists through space. The model's best representation of the Starflake occurs at .10 mm beyond the nominal focal plane. The model's starflake shape and size is very similar to the actual starflake. This similarity is enhanced by slightly blurring the model's starflake image in order to approximate the seeing conditions experienced at MDM the evening of the test.

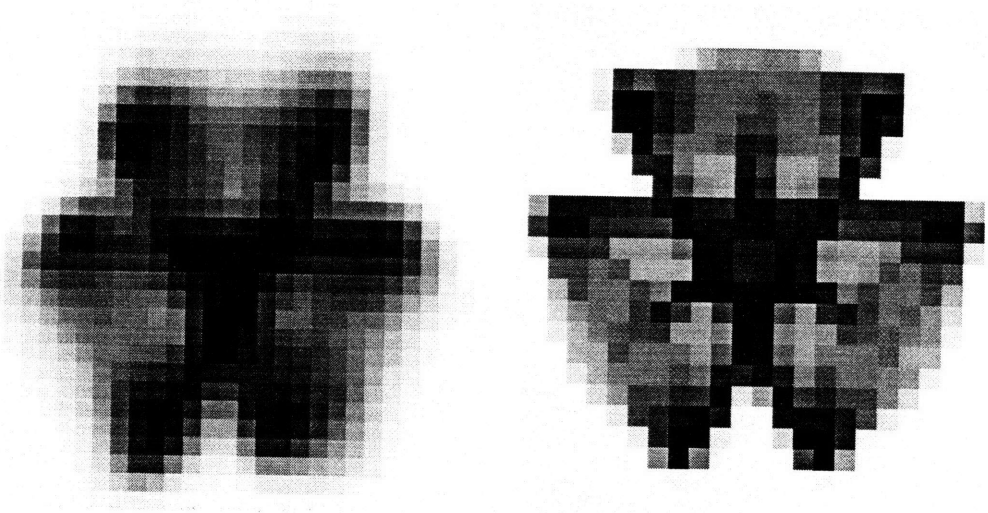

Figure 9.3.1: The left hand picture is the actual starflake image taken by the MDM/Hiltner telescope with the primary mirror resting on the hard point supports. The image on the right is made by the finite element model, with a certain amount of blurring introduced so as to match the seeing conditions that existed at Kitt Peak the night of the verification experiment.

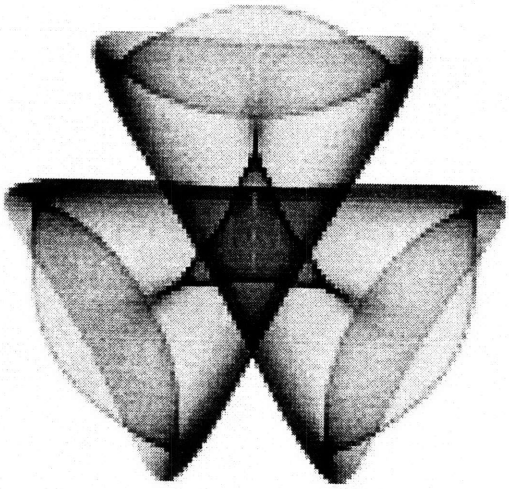

Figure 9.3.2: The model's starflake image without blurring., and rotated 90° counterclockwise.

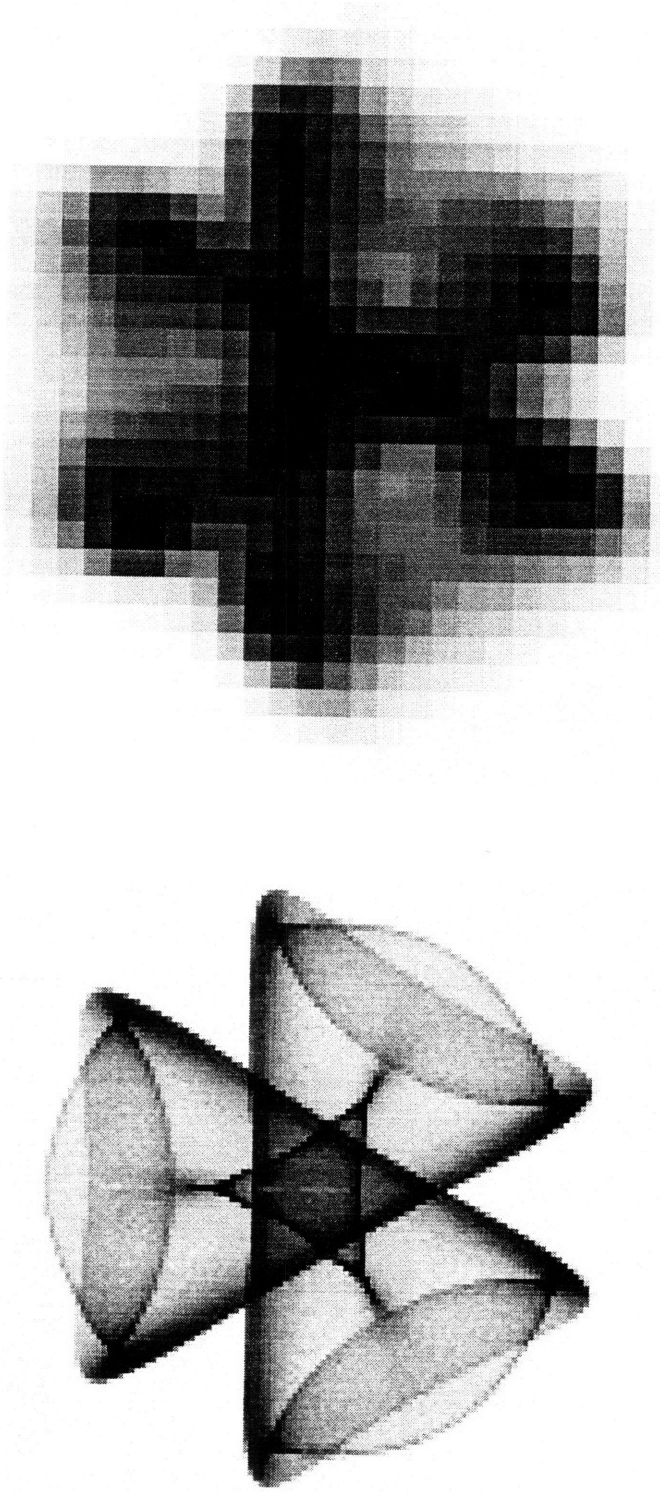

Figure 9.3.3: Comparison of actual "Starflake" image and the image created by the model at .10 mm beyond the nominal focal length.

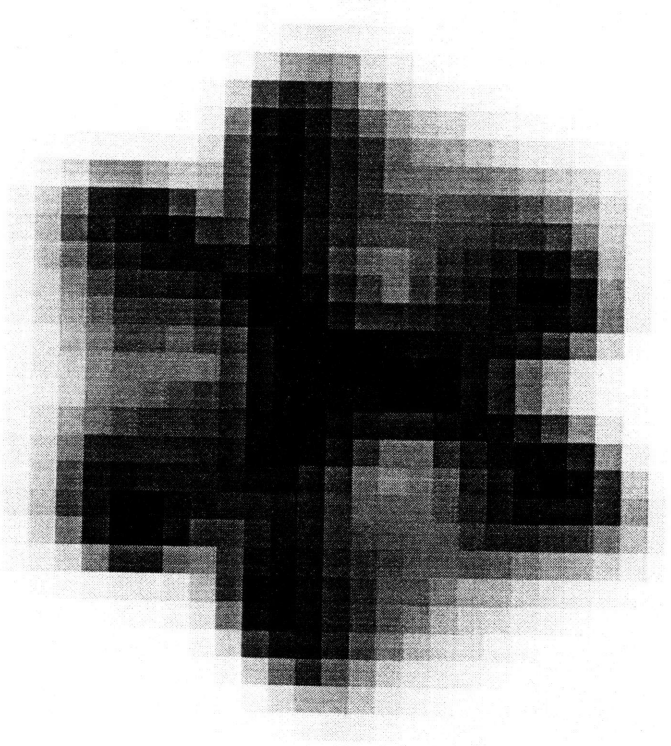

Figure 9.3.4: MDM/Hiltner "Starflake".

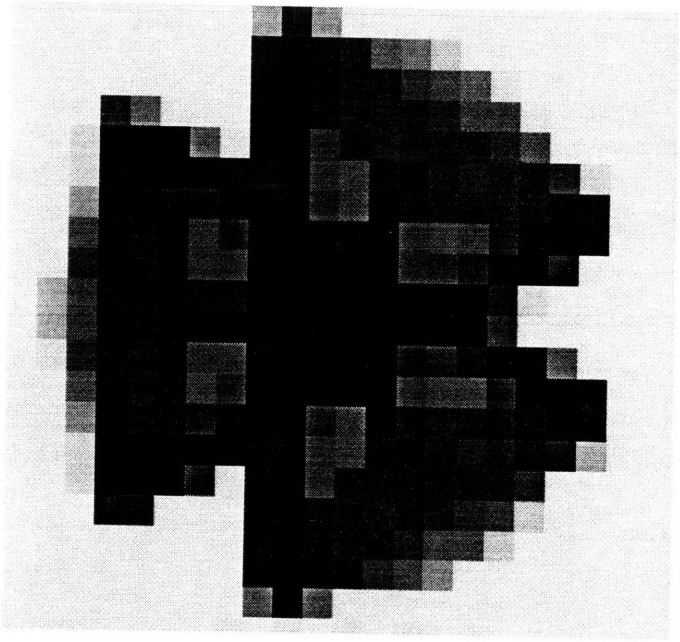

Figure 9.3.5: Finite element version of "Starflake", blurred to match Kitt Peak seeing conditions.

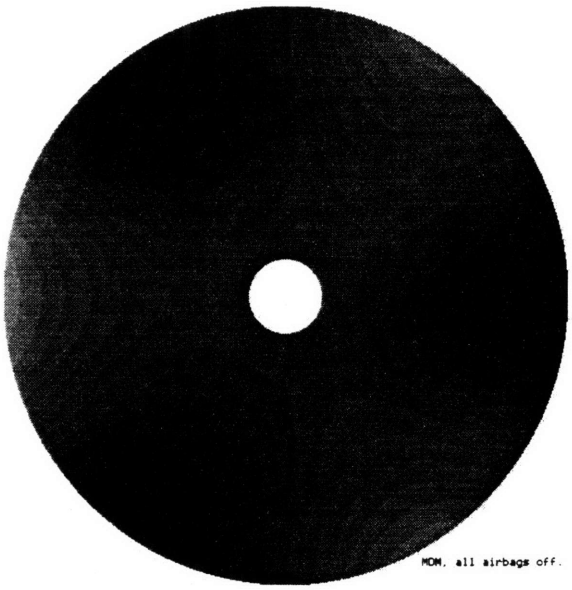

Figure 9.3.6 A: SURFACE contour plot of mirror on hard points.

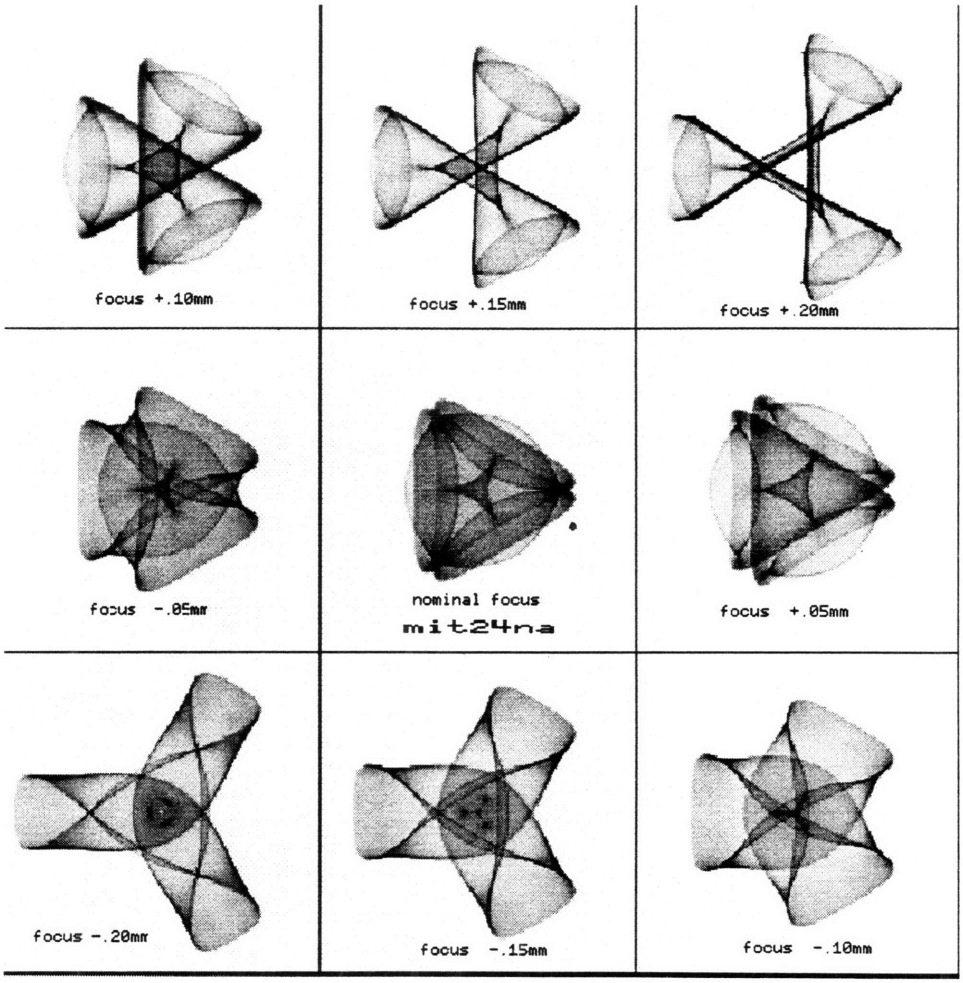

Figure 9.3.6 B: Spot diagrams from mirror on hard points.

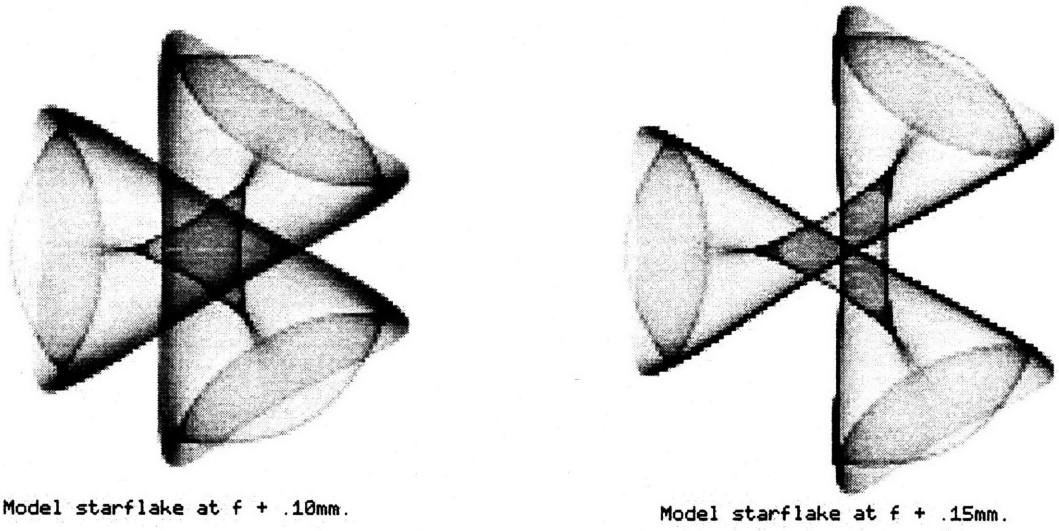

Figure 9.3.7: Enlargements of spot images at .10 mm and .15 mm beyond nominal focus for the model resting on the hard points.

Table 9.3 presents optical results for the "Starflake" image and the model's rendition of the "Starflake". The 50% and 100% energy columns are measures of angular width, in arc seconds, for encircled energy. The RMS is an average ray displacement from center spot measured in arc seconds.

Focal Plane vs. Nominal	RMS	50% Energy: Arc seconds	100% Energy: Arc seconds
Nominal - .20 mm	2.22	2.05	3.62
Nominal - .15 mm	1.98	1.85	3.165
Nominal - .10 mm	1.78	1.70	2.75
Nominal- .05 mm	1.65	1.60	2.59
Nominal Focus	1.59	1.55	2.485
Nominal + .05 mm	1.61	1.55	2.53
Nominal + .10 mm	1.72	1.67	2.75
Nominal + .15 mm	1.90	1.85	3.05
Nominal + .20 mm	2.12	2.06	3.395
"Starflake"			2.85

Table 9.3: The model's best representation of the "starflake" image is at approximately at .10 mm beyond nominal focal length.

Chapter 10

Structural and Optical Analysis of the MDM/Hiltner Primary Mirror

This chapter presents the results of a finite element and optical analysis of the 2.4 meter primary mirror of the Michigan Dartmouth MIT/Hiltner Telescope. The structural analysis is accomplished using the NASTRAN finite element code and the finite element model described in Chapter 9. The optical analysis uses NASTRAN supplied data processed by the PCFRINGE and SURFACE optical test codes.

The analysis examines the MDM primary mirror and its support systems. The case study which verifies the finite element model is also analyzed. This verification relieves all air pressure from the mirror's axial support air bags, causing the mirror to deform as it rests on its hard points. Other scenarios investigate the mirror's structural and optical sensitivity to externally applied point forces. Point loads of 20, 40, 60, 80 and 100 pounds are applied to nodes that define the interface between the mercury belt radial support and the mirror's side wall. There are three basic cases: application of a single spike force in the negative "z" direction, application of a pair of spike forces pointed in the negative "z" direction, and simultaneous application of two pair of spike forces, one pair oriented in the positive "z" direction and the other pointed in the negative "z" direction.

10.1 Analysis of the MDM Primary Mirror

This section analyzes the mirror in its nominal state. The mirror's optical axis is oriented in the pure vertical, so that gravity is applied in the negative "z" direction of the mirror's reference frame. The axial and radial support systems are set to function normally. Figure 10.1.1 below presents a conceptual cross section of the mirror and its axial and radial support systems.

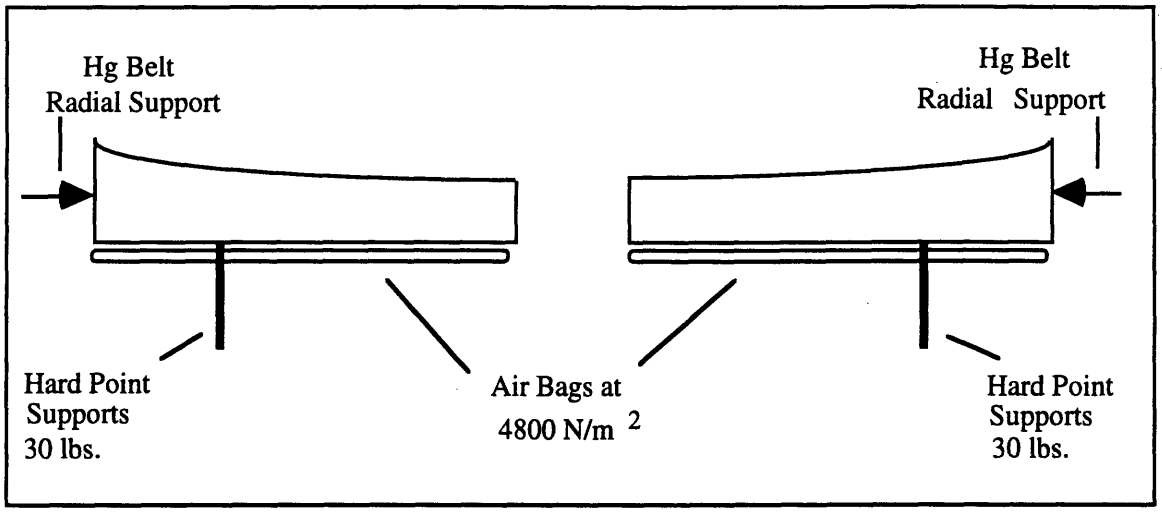

Figure 10.1.1: The 1995 kg mirror sitting on its nominal support configuration.

10.1.1 Mirror Structural Response

The mirror body is characterized by a flat back surface and a hyperbolic front reflecting surface. The mirror material is continuous and homogeneous. This combination of mirror shape and continuous composition creates a non-uniform mass distribution throughout the body of the mirror.

When positioned with the optical axis oriented in the vertical, the mirror's full weight rests on the axial support air bags and the three hard points. The axial air bags exert a uniform pressure across the back of the mirror, while the hard points experience a small z-axis reaction load.

The combination of uniform axial pressure across the back of the mirror with the mirror body's non-uniform mass distribution creates a stress field and bending moment that pushes the center of the mirror upward while

causing the mirror's exterior rim to droop. This axial-pressure induced bending moment serves to put the surface of the mirror under tension and the back of the mirror under compression. The back surface compression draws the exterior rim of the back surface inward. The surface tension is responsible for the bulging of the mirror center.

The mirror surface around the inner radius is forced up by $\approx .402\ \mu m$. The greatest z-direction sag is in the outer rim area between each of the hard point radials, and is $\approx .388\ \mu m$.

The second major deformation mode is a readily discernible triangulation of the mirror surface. This trefoil shape is created by the action of the hard points' thirty pound reaction loads, the mirror's variable thickness, and the uniform axial support pressures. The stress field that causes a bulging of the mirror center and drooping of the mirror rim is interrupted by the constraining action of the hard point supports. This constrains mirror surface deformation, as seen in the fact that the smallest z-axis deformations appear on the outer edge of the mirror's surface and are located on the hard point radials. The greatest z-axis deformations are located along the outer edge between the hard point radials. The hard points act to locally prop-up the radial to which they are attached, while causing a slight valley to form in the interregnum.

Figure 10.1.2 on the next page is a juxtaposition of two PCFRINGE representations of the wavefront behavior as it leaves the mirror. Figure 10.1.2 A plots exit pupil wavefront variations in contour intervals of .2 λ (λ = .633 μm). Figure 10.1.2B is an attempt at a three dimensional representation of wavefront variations. The graphics depict differences from a perfect reference wavefront. A perfect, converging spherical wavefront would be presented in Figure 10.1.2A as a circle with zero contours, and in Figure 10.1.2B as a flat surface.

NASTRAN z-axis surface deflections can be seen in Figure 10.1.3 on the following page. The scale on the right hand side of the mirror depiction in Figure 10.1.3 is in millimeters.

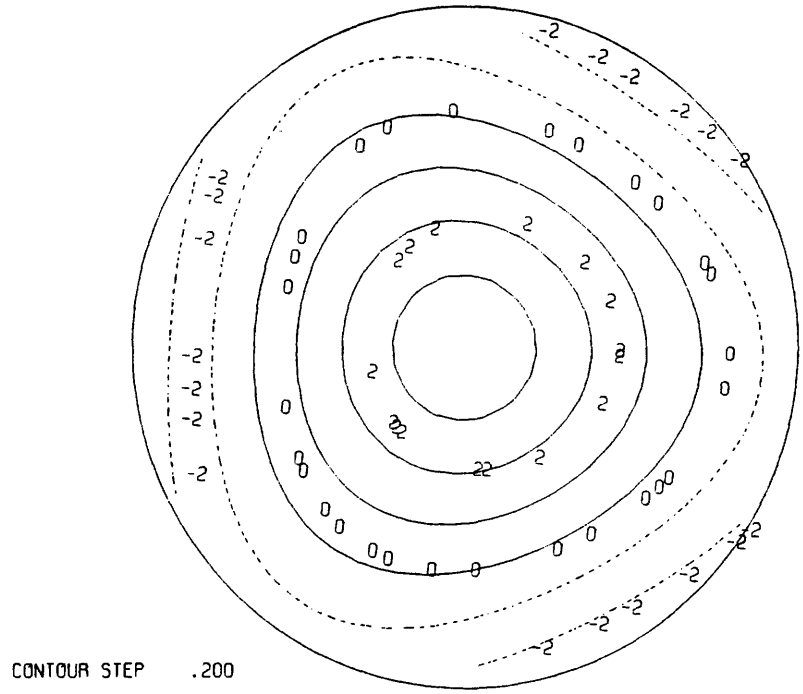

Figure 10.1.2A: Wavefront contour diagram at the exit pupil. MDM primary mirror in the vertical orientation, nominal axial and radial support.

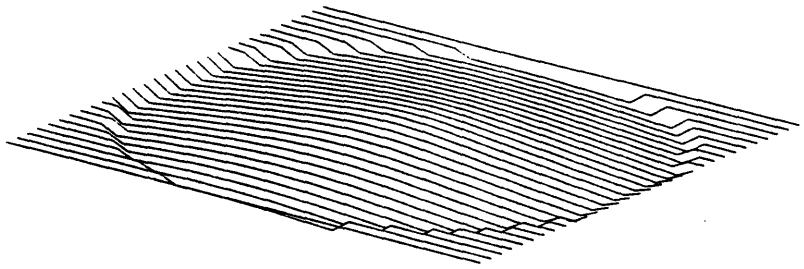

Figure 10.1.2B: Wavefront 3D graphic. Exit pupil, MDM primary mirror, in the vertical orientation, nominal axial and radial support.

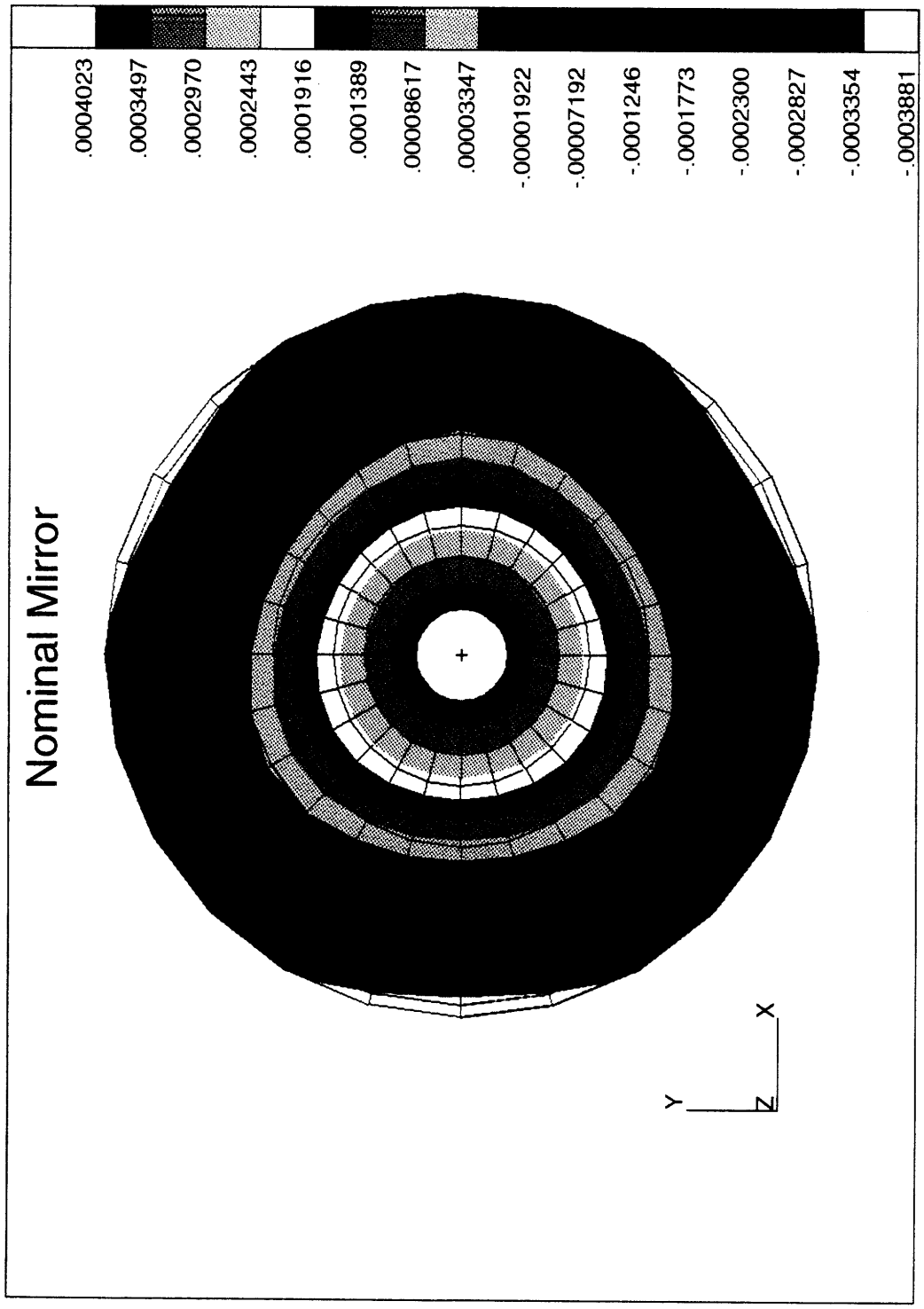
Nominal Mirror
.0004023
.0003497
.0002970
.0002443
.0001916
.0001389
.00008617
.00003347
-.00001922
-.00007192
-.0001246
-.0001773
-.0002300
-.0002827
-.0003354
-.0003881
Y
X
Z

Hard Point Reaction Forces

Table 10.1.1 (below) presents the reaction forces experiences by the three hard point supports under nominal support conditions when the mirror's optical axis is oriented in the vertical.

Hard Point	X-Axis RF (N)	Y-Axis RF (N)	Z-Axis RF (N)
SPC 1	302	0	129
SPC 2	-151	262	129
SPC 3	-151	-262	129

Table 10.1.1: Reaction forces at SPC's 1, 2 & 3 for the nominal case.

The reaction forces calculated by NASTRAN at the model's three single point constraints show the compression experienced by the mirror's back surface. The outer rim of the mirror's back side is drawn inward by the uniform axial pressure acting on the mirror's non-uniform mass distribution.

SPC 1 is pushing in the positive x-direction while SPC 2 & 3 push in the negative x-direction in opposition to the inward movement of the mirror rim. The same story is seen in the y-direction, as SPC's 2 & 3 oppose the compressive stress experienced by the mirror's back. The SPC's exhibit uniform z-axis residual loads of 129 Newtons as required by programmed boundary conditions.

RMS and Peak-Valley

Table 10.1.2 presents a measure of wavefront behavior in the exit pupil. Peak-Valley measures the difference between maximum and minimum z-axis displacements. The RMS is the average surface displacement in microns.

	RMS (μm)	P-V (μm)	P-V (λ)
Wavefront	0.385	1.572	2.483
Mirror Surface	0.1925	0.786	1.242

Table 10.1.2: Nominal MDM mirror surface with air bags and Hg belt on, z-axis gravity

10.1.2 Optical Results For the Nominal Mirror

The structural deformations degrade the mirror's optical performance. The triangular symmetry in the mirror surface is reflected by the shape of the spot images formed at various focal planes. The drooping of the mirror's outer rim and the bulging of the center area act to create a defocus condition, as well as to introduce almost three quarters of a wavelength of spherical aberration.

Figure 10.1.3 B (on the next page) is a series of 9 spot diagrams taken at intervals of .05 mm along the optical axis. Spot diagram #1 is made at the nominal focal length minus .20 mm. Spot #5 is made at the mirror's nominal focal length, and Spot #9 is at nominal focus plus .20 mm. These spots show a distinct trefoil that grows more acute in the region near the actual focus. The spot series shows quite clearly that the mirror does not focus at its designed focal length of 4.82 meters when resting on the designed support system.

Table 10.1.3 is an aggregation of data on the series of 9 spots centered on the design focal length. The 50% and 100% Energy columns are measures of angular width, in arc seconds, for encircled energy. The RMS is the average ray displacement from center spot measured in arc seconds.

Spot Location vs. Nominal Focus	RMS (Arc seconds)	50% Energy (Arc seconds)	100% Energy (Arc seconds)
Nominal Focus - .20 mm	1.76	1.76	2.45
Nominal Focus - .15 mm	1.39	1.39	1.94
Nominal Focus - .10 mm	1.02	1.02	1.41
Nominal Focus - .05 mm	0.66	0.65	0.92
Nominal Focus	0.30	0.28	0.40
Nominal Focus + .05 mm	0.15	0.10	0.29
Nominal Focus + .10 mm	0.48	0.43	0.81
Nominal Focus + .15 mm	0.84	0.79	1.38
Nominal Focus + .20 mm	1.21	1.17	1.88

Table 10.1.3: Data for spot series around the design focus.
Columns 2, 3 and 4 are in units of arc seconds.

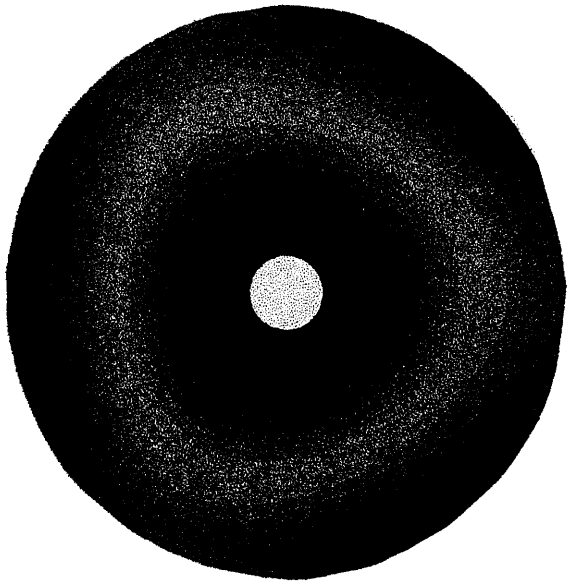

Figure 10.1.3 A: SURFACE contour plot of the nominal mirror.

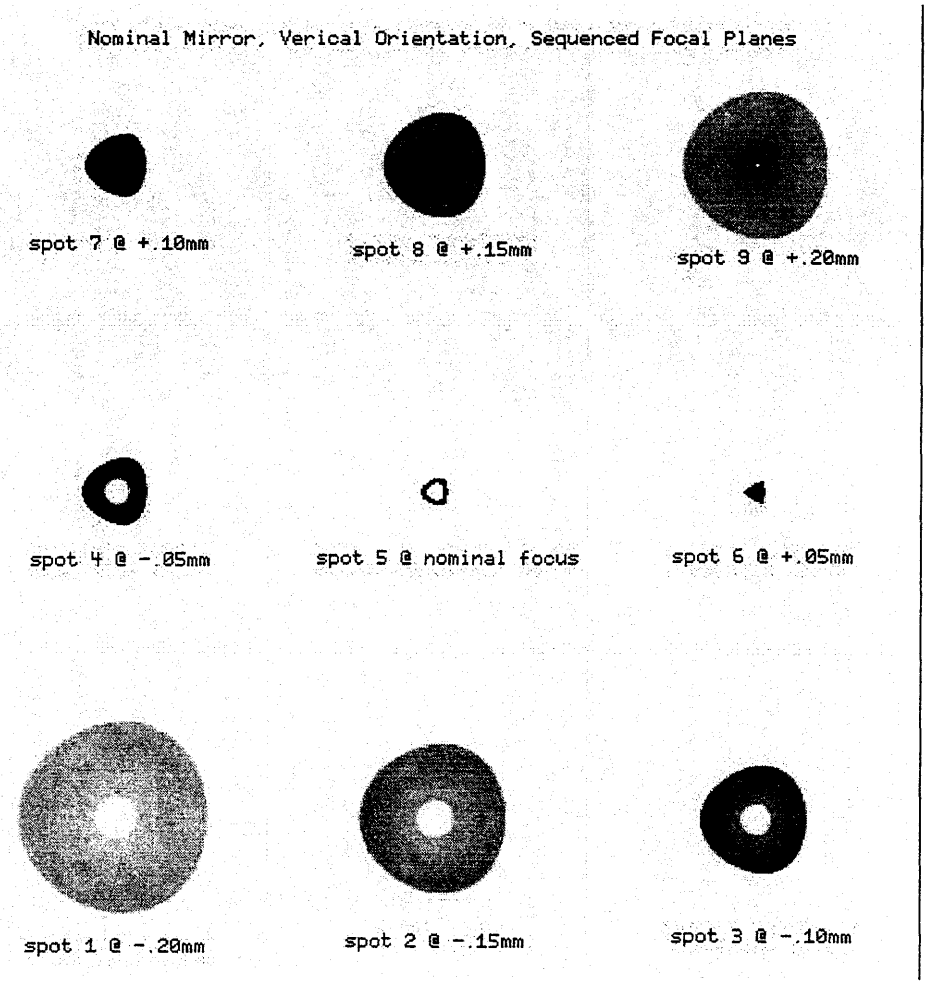

Figure 10.1.3 B: Spot diagrams for nominal mirror.

Third Order Aberrations

Table 10.1.4 presents third order optical aberration generated by PCFRINGE. PCFRINGE fits Zernike polynomials to NASTRAN surface deflection and then projects the result to the mirror's nominal focal point. Both the spherical aberration and the defocus can be attributed to the bulging of the center and drooping of the surface rim that is caused by uniform axial pressure acting on the mirror's non-uniform mass distribution.

Nominal MDM	Tilt	Defocus	Astigmatism	Coma	SA
Waves	0	-1.103	0	0	.776

Table 10.1.4: Third order aberrations for the MDM primary mirror under nominal support conditions, optical axis in the vertical.

Actual Focus

Figure 10.1.3 B shows that the mirror focuses somewhere between the nominal focus and a point .10 mm beyond nominal focus. Figure 10.1.4 on the following page is a series of spot diagrams taken at intervals of .01 mm, starting from nominal focus minus .10 mm and running to .10 mm beyond the nominal focus. Significant data for the set of 15 spot diagrams depicted in Figure 10.1.4 is listed below. The 50% and 100% energy columns are measures of radius in arc seconds for encircled energy. RMS is an average ray displacement from center spot measured in arc seconds. The data suggest that the actual focal plane for the mirror under nominal conditions is at approximately .04 mm beyond the design focal length.

Spot	RMS	50% Energy	100% Energy
Nominal + .02 mm	0.17	0.15	0.295
Nominal + .03 mm	0.12	0.09	0.25
Nominal + .04 mm	0.11	0.09	0.225
Nominal + .05 mm	0.15	0.10	0.24
Nominal + .06 mm	0.20	0.14	0.325

Table 10.1.4: Spot diagrams in increments of .01 mm around the nominal focal plane. Columns 2, 3 and 4 are in units of arc seconds.

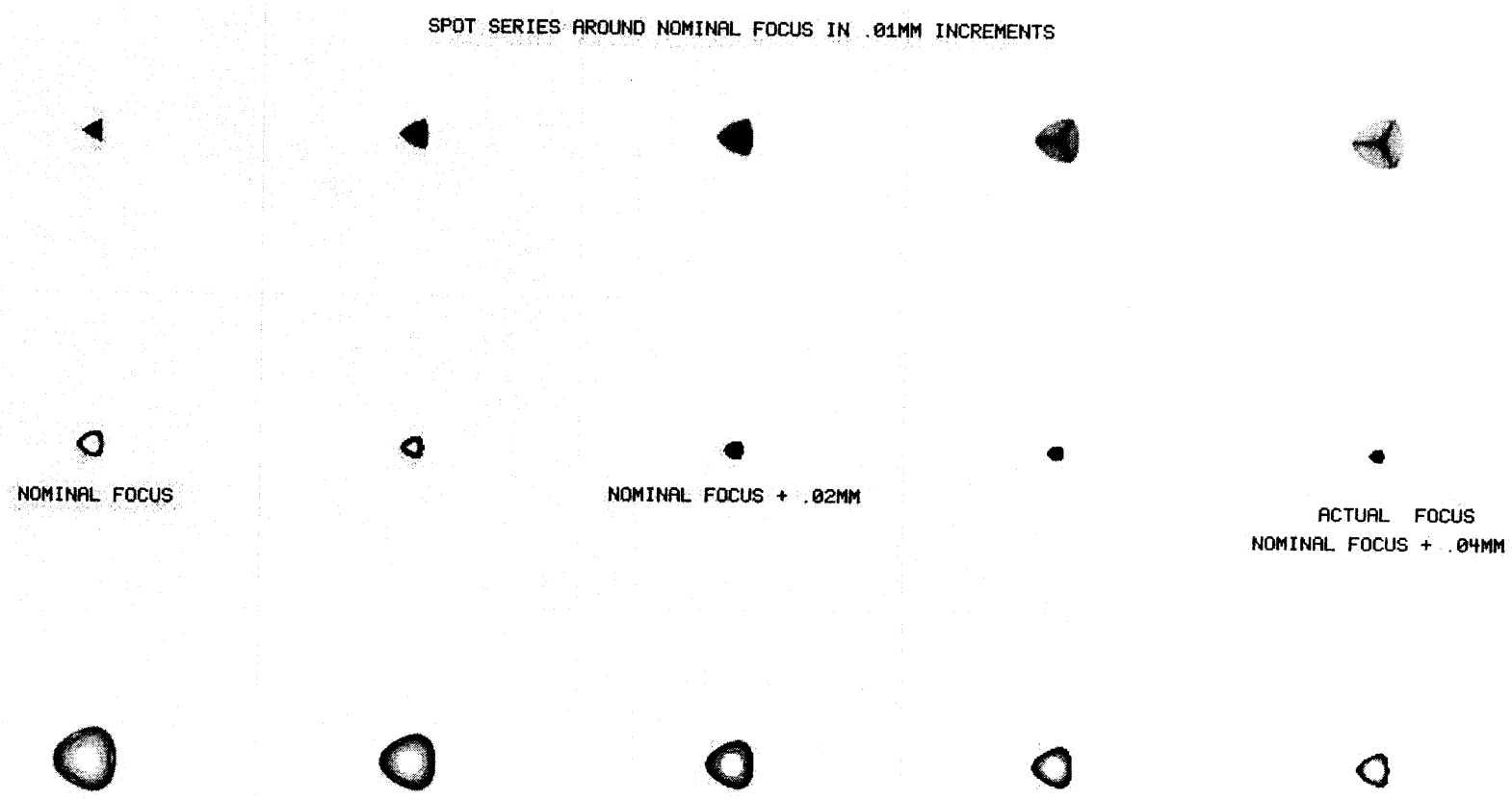

Figure 10.1.4: Spot images around the nomial focus at .01 mm intervals. In search of the actual focus.....

Comparison of Actual vs. Nominal Spot Images

Images at both the actual focus and the nominal focus exhibit a well defined trefoil. This triangular symmetry is the result of the 30 pound (133N) reaction forces at the hard point supports. The outer edges in the regions between hard point radials are massive, and respond to their unsupported gravity condition by deflecting downward. This forces the material that lies along the hard point radials to create small, very stiff ridges. The result is a reflecting surface with a triangular symmetry that throws light off in a distinctive pattern.

Figure 10.1.5: Spot diagrams taken at the design and actual focus for the MDM primary mirror under nominal support conditions, optical axis vertical. The actual focus occurs at .04 mm beyond the nominal focus.

The next section will detail the structural results obtained from placing the model under the conditions of the verification experiment at MDM; all air is relieved from the axial support air bags. The resulting triangulation is extreme, but the cause and effect are essentially the same as exhibited in the nominal mirror.

10.2 Mirror Resting on Hard Points

The action of the three hard points pushing against the mirror's mass creates a series of ridges and valleys in the mirror, as seen in Figures 10.2.1 and 10.2.2. The ridges are created along the radials on which the SPC's are located. The valleys form between the SPC radials. The ridge-valley surface shape can be explained by Rayleigh Ritz theory: it is the lowest order mode that reaches a minimum total potential energy.

Each ridge line can be interpreted as a longitudinal axis around which the mirror material bends. These ridge lines are very stiff in the longitudinal direction, as any solid material becomes much stiffer in one direction after having experienced bending in a perpendicular direction. The highest deflection points are at the outer radius along these ridge lines, and measure +.032 μm (microns) above the reference (unaberrated) position. The lowest position are in the valleys between SPC radials at the outer radius and measure -4.646 μm. This gives a wave front Peak-Valley (twice the structural P-V) of 9.322 μm. The RMS surface displacement is 2.083 μm.

RMS (μm)	P-V (μm)	P-V (λ)
2.083	9.322	14.7267

Table 10.2.1: Mirror surface RMS and P-V measures for the case of the mirror resting on three hard points.

The model correctly locates the hard points (SPC's) at the radial and vertical center mass, as can be seen by examining the action of deflections in Figure 10.2.1. The dark green contours in the NASTRAN z-axis contour plot indicate a mean deflection of approximately 2.307 μm. This is half of the difference between the peak value of +.0038 μm and the minimum value of -.4646 μm. The outer radius is deformed into a sine wave pattern, the peaks and valleys of the sine wave being separated by the uniform and symmetric dark green band of the mean contour. It can be seen that there exists an overall balance in the mass distribution on either side of the hard points.

Hard Point Reaction Forces

Table 10.2.2 (below) presents a comparison of the reaction forces experienced by the three hard points in the nominal case and in the current scenario where they support all the mirror's mass.

Hard Point	X-Axis RF (N)	Y-Axis RF (N)	Z-Axis RF (N)
SPC 1	302 / -1238	0 / -3	129 / 6506
SPC 2	-151 / 619	262 / -1071	129 / 6506
SPC 3	-151 / 619	-262 / 1071	129 / 6506

Table 10.2.2: Reaction forces at SPC's 1, 2 & 3 for the nominal case and the "air bags off" case wherein the SPC's support the full weight of the mirror.

The z-axis reaction force component shows the three SPC's supporting the full weight of the mirror.

The reaction forces calculated by NASTRAN at the model's three single point constraints show force orientations that are the opposite of those found in the nominal configuration. Here, the x-axis component of the reaction force on SPC 1 is pulling on the mirror in the negative x-direction. Conversely, SPC 2 & 3 are pulling the back of the mirror in the positive x-direction. Tension is also seen in the y-direction reaction forces on SPC's 2 & 3. The stress field induced by resting the mirror on the three hard points puts the bottom surface of the mirror under tension in the horizontal plane and draws the outer rim of the mirror's back side outward.

Figure 10.2.1 shows the NASTRAN plot of z-axis surface deflections. The contours of the NASTRAN plot are measures of the z-axis difference between the actual surface node position and a reference, or unaberrated node position. Figure 10.2.2A is a PCFRINGE wave front diagram showing the wavefront as it exits the mirror pupil. The contour lines are measures of difference from a perfectly spherical wave front, and can also be construed as measures of surface displacement in the mirror face. The contour lines are drawn at intervals of .4 λ (wavelengths), where $\lambda = .633\ \mu m$.

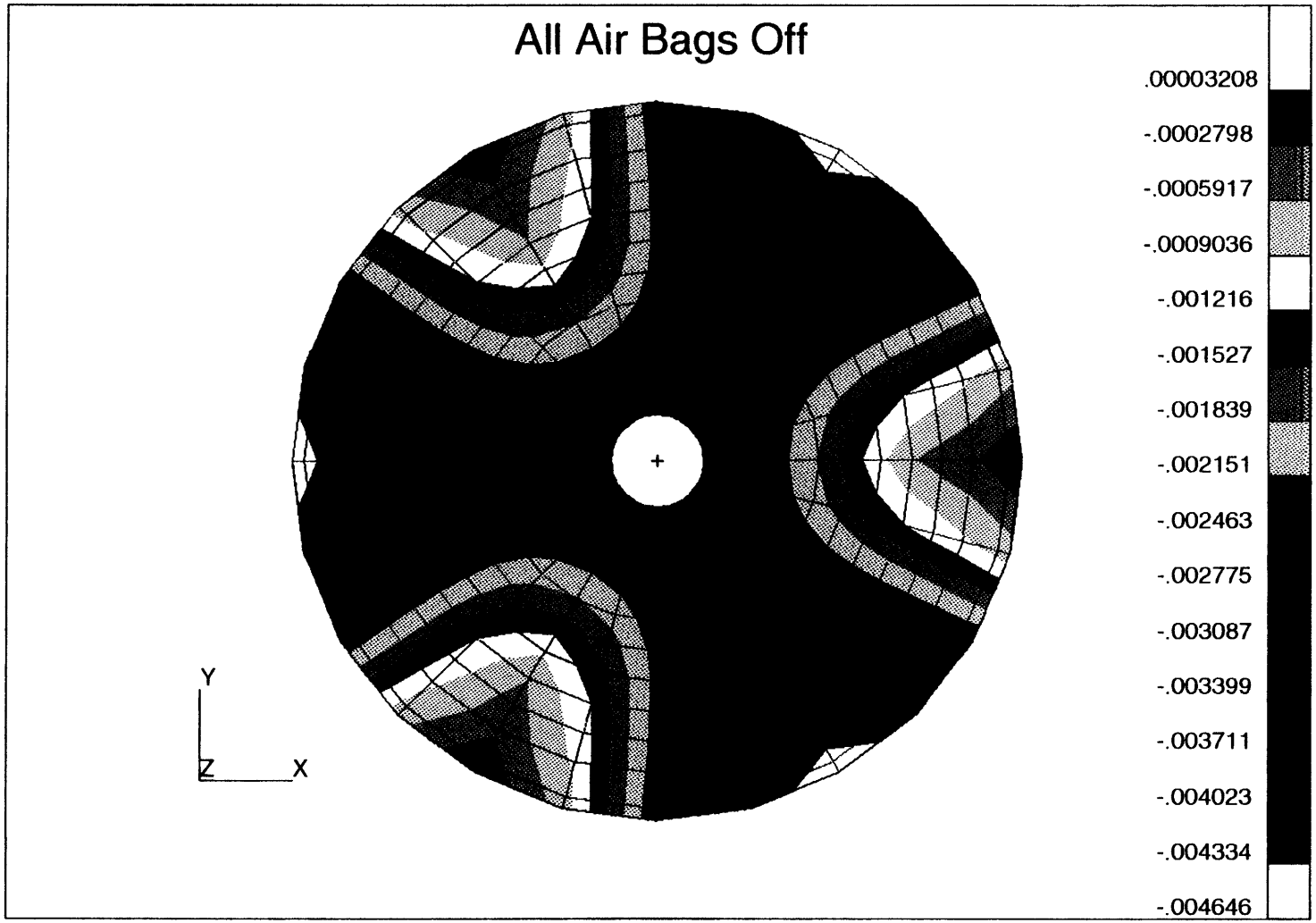

Figure 10.2.1: NASTRAN z-axis contour diagram of surface deflections showing the deformed model as it sits on the three hard points.

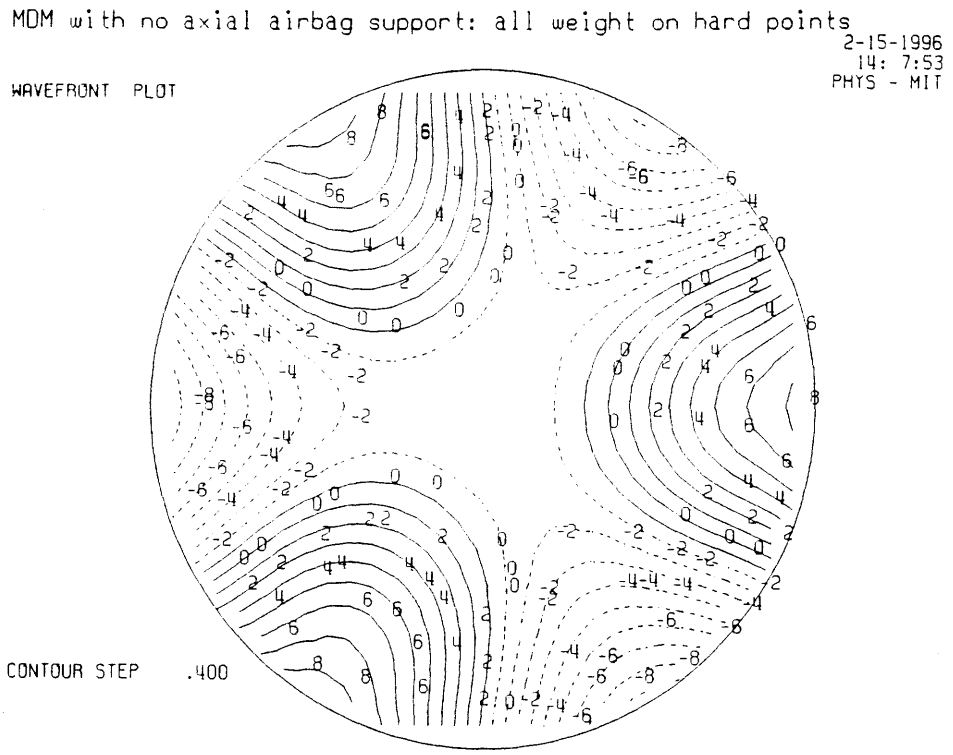

Figure 10.2.2A: Wavefront contour diagram at the exit pupil. MDM primary mirror in the vertical orientation, mirror resting on hard points.

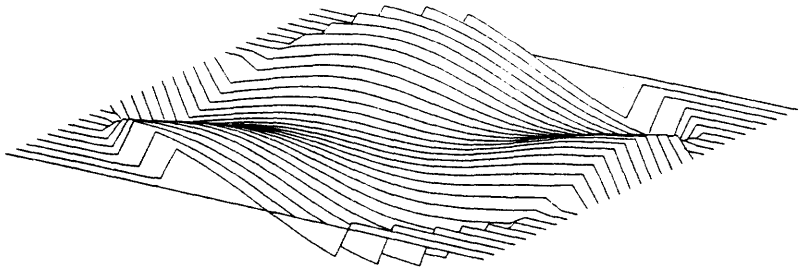

Figure 10.2.2B: Wavefront 3D graphic. Exit pupil, MDM primary mirror, in the vertical orientation, mirror resting on hard points.

Optical Results, Mirror Resting on Hard Points

The wavefront that results from the extreme mirror deformation exhibits a six fold symmetry, showing a three fold line astigmatism. The picture below shows the starflake image that forms at a point .10 mm beyond the mirror's nominal focus. Table 10.2.3 shows RMS and encircled energy data for the series of 9 spot diagrams on the following page.

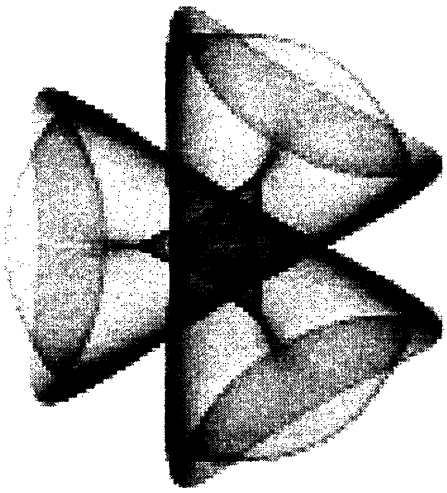

Figure 10.2.3: Starflake image: MDM/Hiltner model with all air bag axial support turned off. Note the six fold symmetry, and the three line astigmatism

Focal Plane vs. Nominal	RMS Arc seconds	50% Energy: Arc seconds	100% Energy: Arc seconds
Nominal - .20 mm	2.22	2.05	3.62
Nominal - .15 mm	1.98	1.85	3.165
Nominal - .10 mm	1.78	1.70	2.75
Nominal- .05 mm	1.65	1.60	2.59
Nominal Focus	1.59	1.55	2.485
Nominal + .05 mm	1.61	1.55	2.53
Nominal + .10 mm	1.72	1.67	2.75
Nominal + .15 mm	1.90	1.85	3.05
Nominal + .20 mm	2.12	2.06	3.395

Table 10.2.3: RMS and encircled energy of 9 spot images resulting from the extreme "air bags off" mirror deformation.

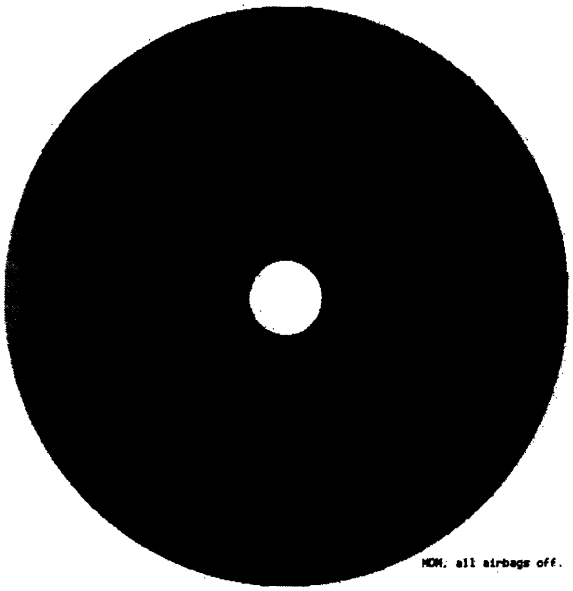

Figure 10.2.3 A: SURFACE contour plot of mirror on hard points.

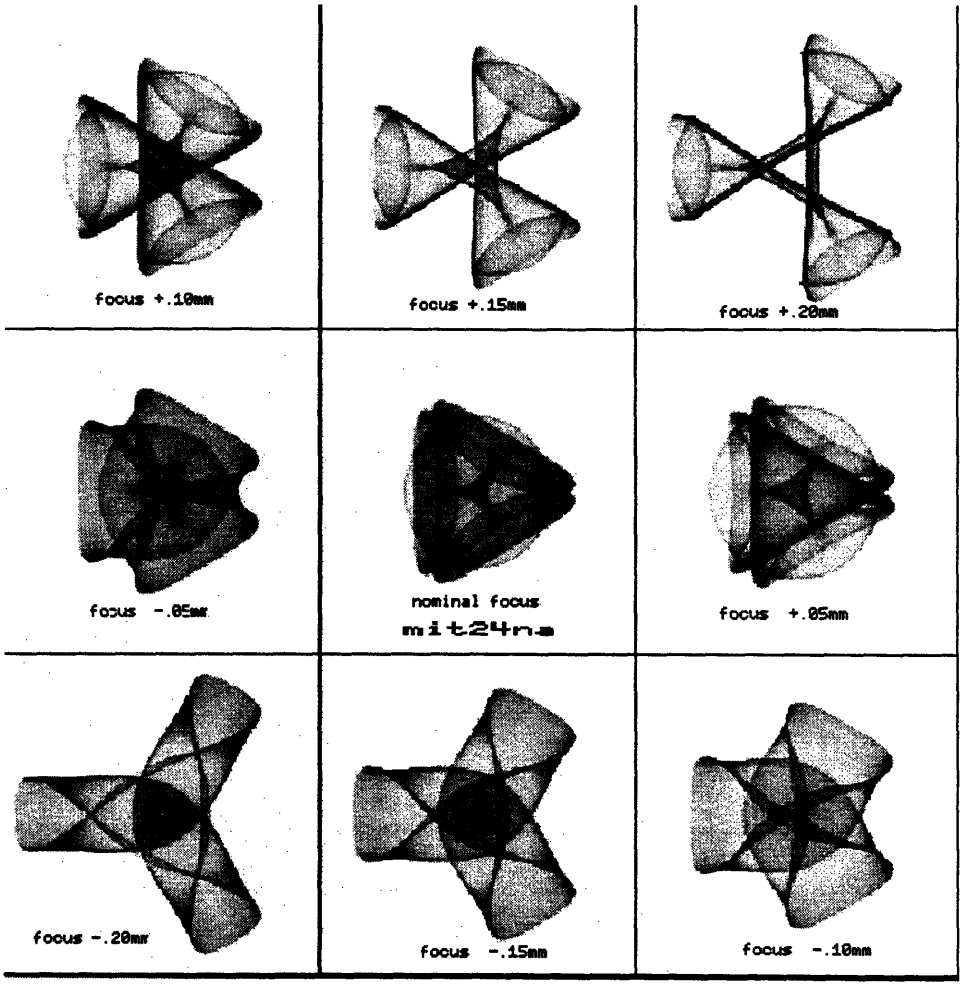

Figure 10.2.3 B: Spot diagrams from mirror on hard points.

10.3 Single Point Load Perturbations

A series of point loads are applied to the mirror in order to investigate the mirror's sensitivity to applied force. Point loads of magnitude 20, 40, 60, 80, and 100 pounds are applied in the negative z-direction to a node at the position (r = 1.143 m, $\theta = \pi$, z = .082 m). This node is part of the mercury belt radial support, is located on the negative x-axis, and is an equal distance from SPC 2 and SPC 3., as shown in Figure 10.3.1.

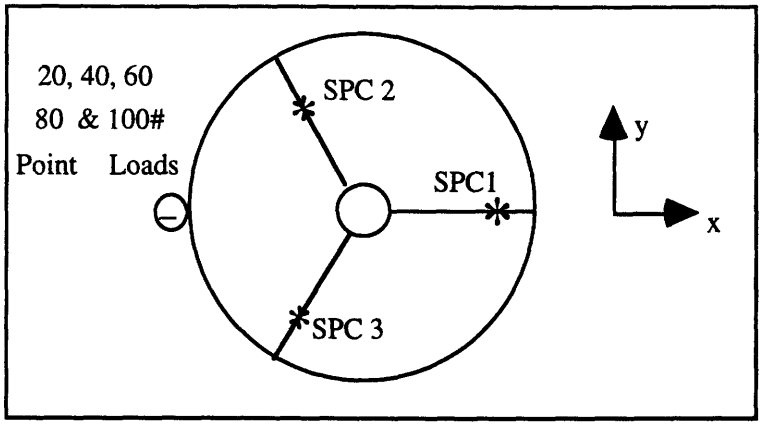

Figure 10.3.1: Location of a series of "spike" forces at (r = 1.143 m, $\theta = \pi$, z = .082 m).

10.3.1 Structural Response to A Point Load

The application of a downward spike force creates a torque which rotates the mirror about the three hard points. This rotation pushes the center of the mirror up, putting the surface material under tension. The material on the back of the mirror is compressed as the outer rim of the mirror's backside is forced inward. This inward motion is opposed in the x-direction by all three hard points, as can be seen in Table 10.3.1 on the next page. (Please see Figures 10.3.2 A, B, C and D for plots of mirror surface z-direction deflections.)

The 20 pound point load initially exaggerates the triangulation effect seen in the nominal mirror in Section 10.1, Figure ?.?. The center of the mirror reaches a maximum positive deflection of .4181 μm above the design position. The surface area in the vicinity of the point load application shows the greatest negative deflection at -.8938 μm.

The 60 pound spike force noticeably squeezes the center of the mirror, changing the triangulation pattern into something that resembles an ellipse. The load on SPC 1 has gone negative, meaning that tension exists and the SPC is now holding the mirror down. At 80 pounds of spike force the surface triangulation pattern is completely removed. The mirror surface bulges into a highly eccentric ellipse centered to the east of the central hole. The 100 pound spike-force pushes the mirror surface beyond the elliptical shape into a series of contour ridges that run north-south, parallel to the mirror surface's y-axis. A steep gradient has formed along the negative x-axis.

SPC Reaction Forces

Table 10.3.1 below shows hard point reaction forces. Charts 10.3.1 X, Y, Z on the next page show the linearity of reaction forces. Figures 10.3.2 A, B, C and D on the following four pages show NASTRAN and SURFACE generated contour plots of z-axis spike force induced perturbations.

Case/Reaction Force		X-Axis RF (N's)	Y-Axis RF (N's)	Z-Axis RF (N's)
Nominal:	SPC 1	302	0	129
	SPC 2	-151	261	129
	SPC 3	-151	-261	129
20 lb's:	SPC 1	387	0	76
	SPC 2	-194	196	200
	SPC 3	-194	-196	200
60 lb's:	SPC 1	558	0	-30
	SPC 2	-278	66	343
	SPC 3	-278	-66	343
80 lb's:	SPC 1	642	0	-82
	SPC 2	-321	1	414
	SPC 3	-321	-1	414
100 lb's:	SPC 1	728	0	-135
	SPC 2	-364	-65	485
	SPC 3	-364	65	485

Table 10.3.1: SPC reaction forces for spike loads. RF's in Newtons.

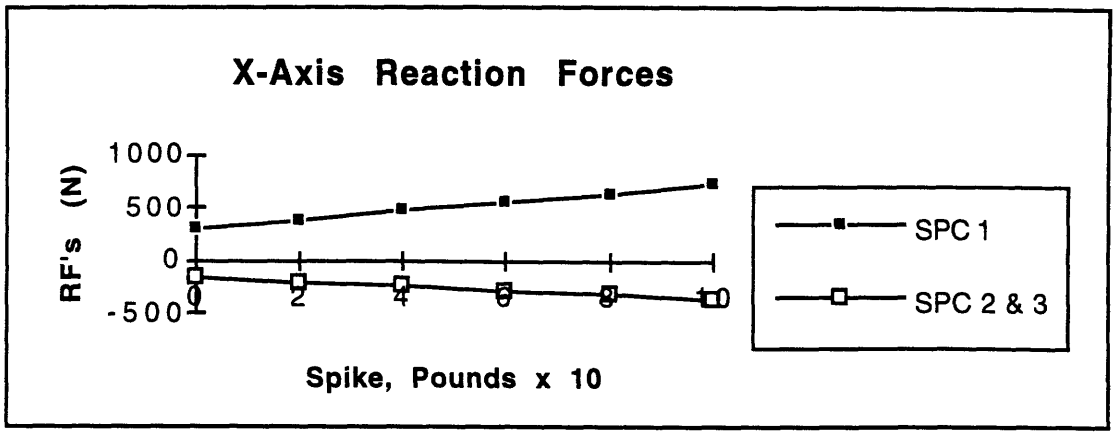

Chart 10.3.1 X: X-Axis reaction forces for the spike load series.

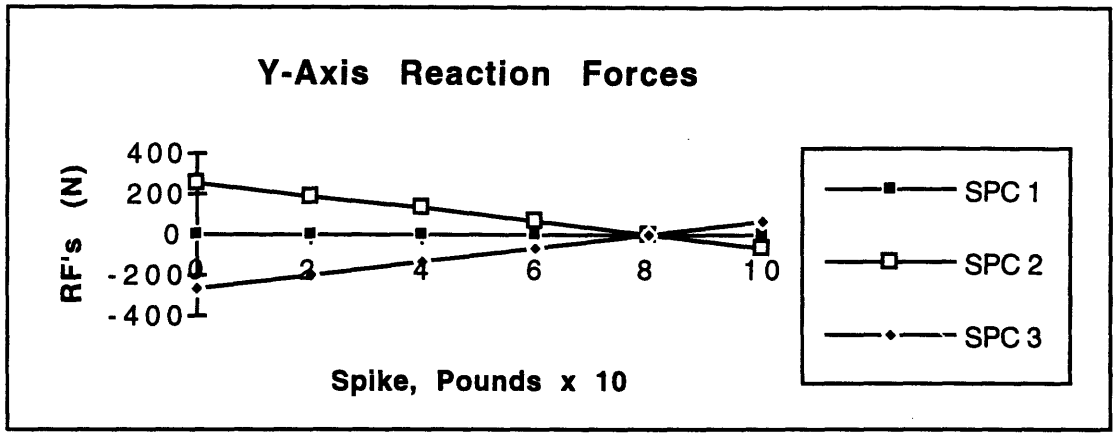

Chart 10.3.1 Y: Y-Axis reaction forces for the spike load series.

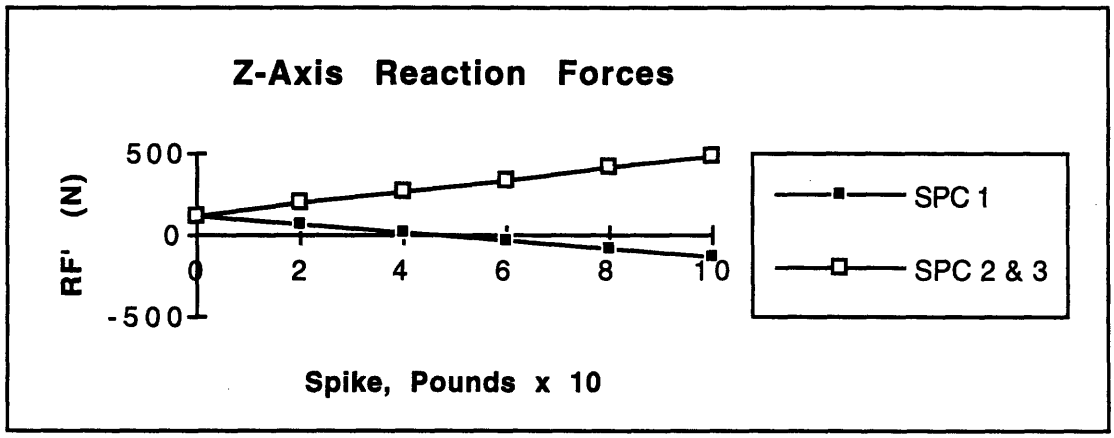

Chart 10.3.1 Z: Z-Axis reaction forces for the spike load series.

Z-Axis Surface Displacements

NASTRAN and SURFACE z-axis surface displacement contour plots follow.

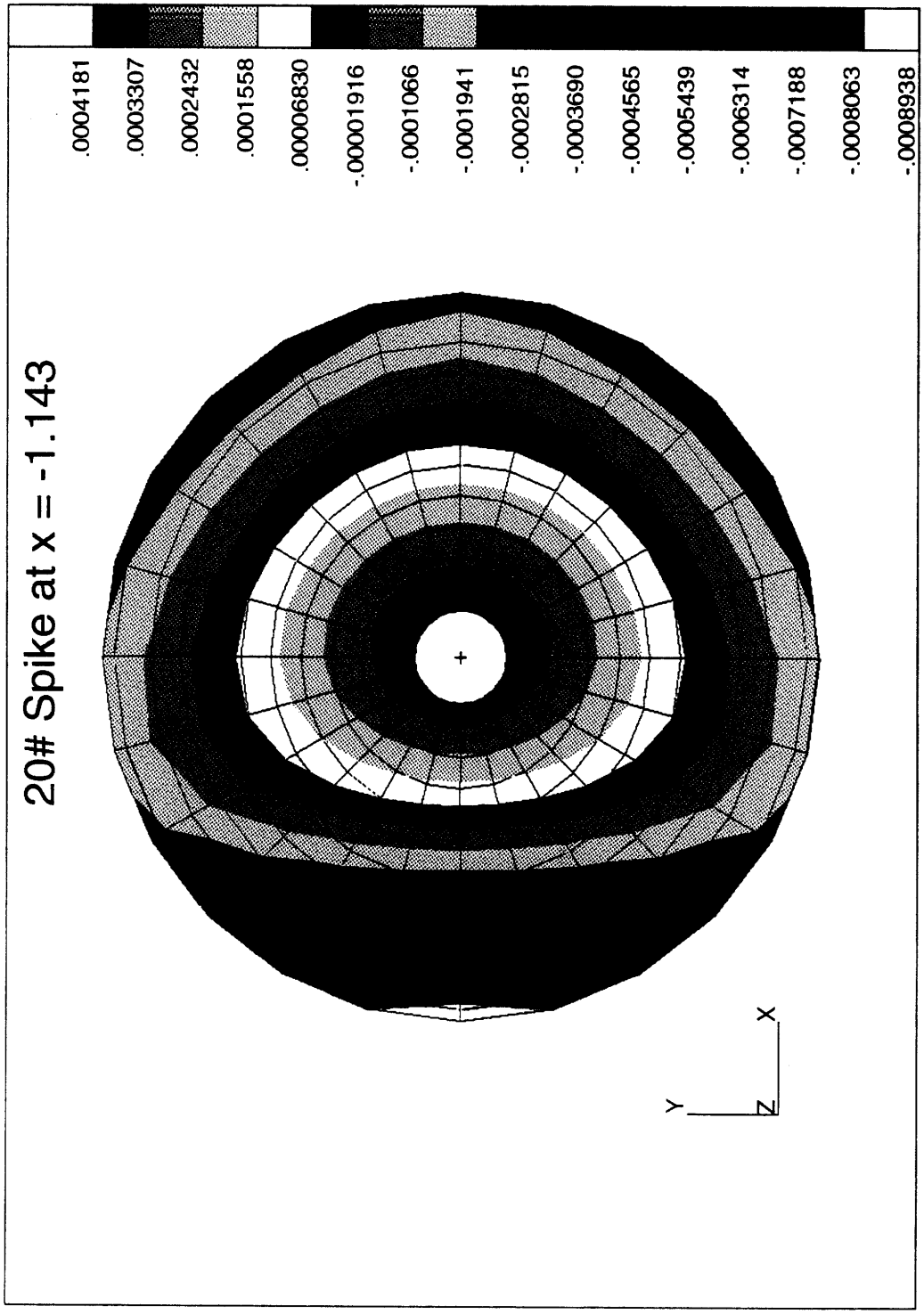
20# Spike at x = -1.143
.0004181
.0003307
.0002432
.0001558
.00006830
-.00001916
-.0001066
-.0001941
-.0002815
-.0003690
-.0004565
-.0005439
-.0006314
-.0007188
-.0008063
-.0008938
Y
Z
X

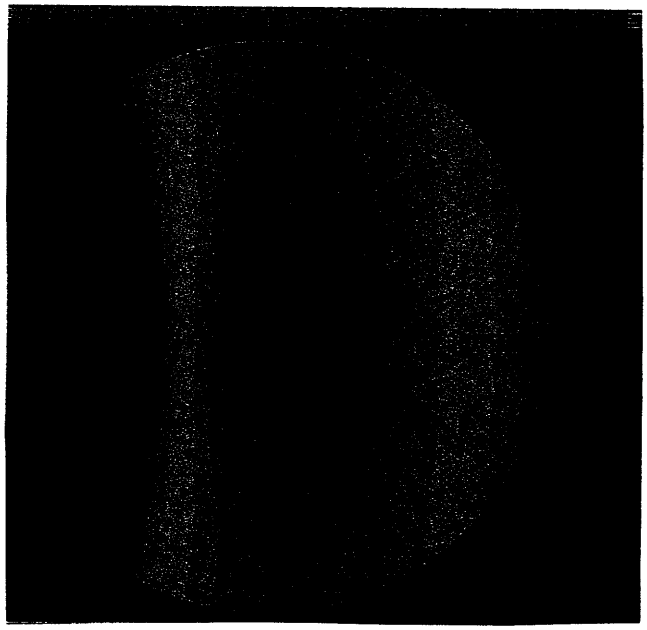

Figure 10.3.2 B: Surface contour plot of 60 pound spike perturbation.

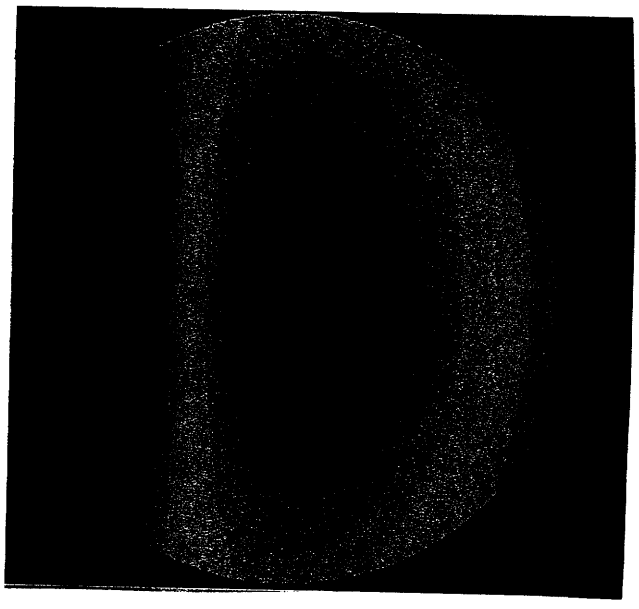

Figure 10.3.2 C: Surface contour plot of 80 pound spike perturbation.

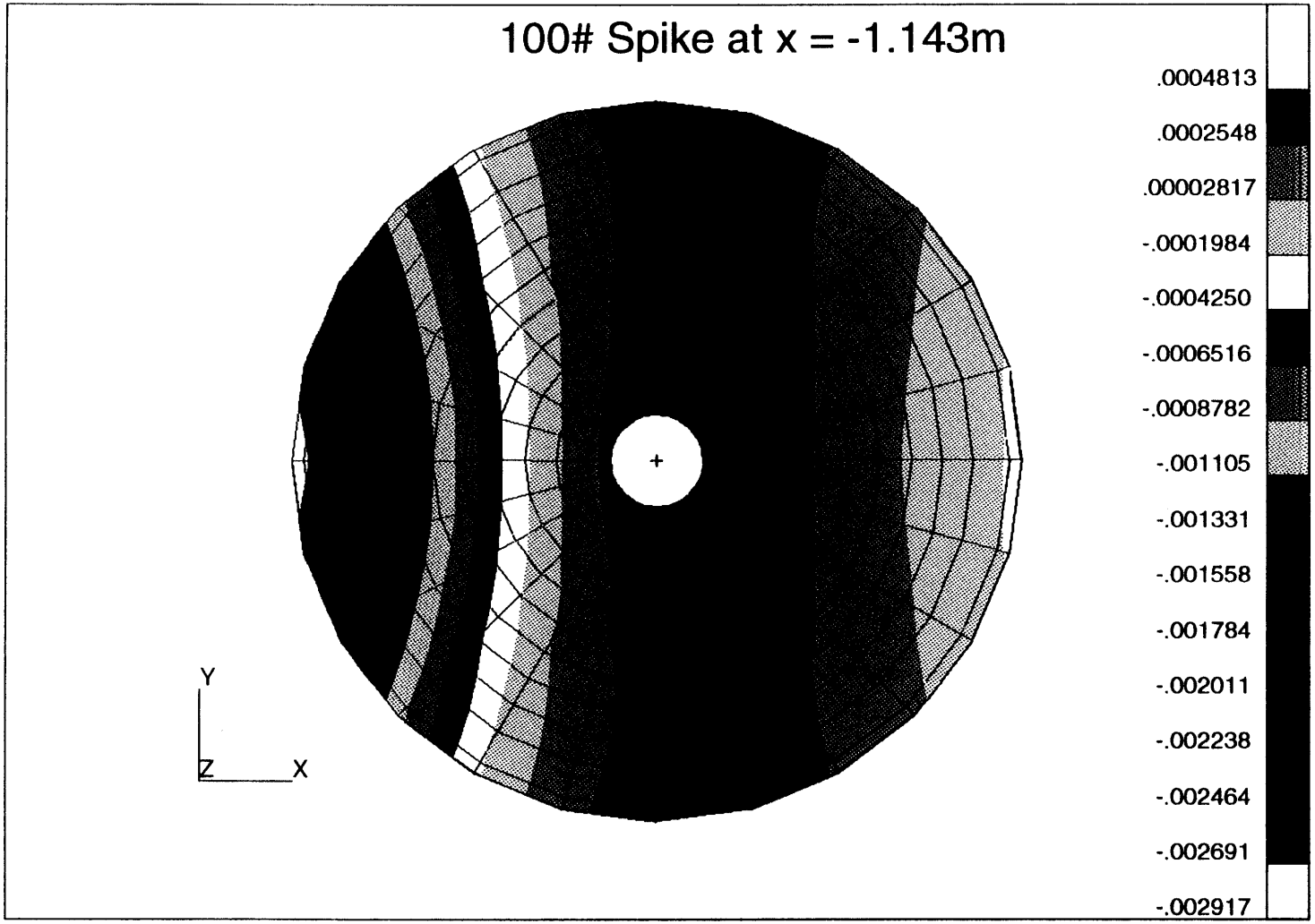
100# Spike at x = -1.143m
.0004813
.0002548
.00002817
-.0001984
-.0004250
-.0006516
-.0008782
-.001105
-.001331
-.001558
-.001784
-.002011
-.002238
-.002464
-.002691
-.002917
Y
Z
X

Mirror Surface RMS and P-V

The RMS kink in Chart 10.3.2 is due to the linear action of two distinct modes. The primary deflection mode is due to gravity. The mode that results from the point load adds linearly to the gravity mode. P-V is also linear.

Case	Nominal	20 lb Spike	60 lb Spike	80 lb Spike	100 lb Spike
RMS	.385 μm	.486 μm	.898 μm	1.133 μm	1.378 μm
P-V	1.572 μm	2.602 μm	4.679 μm	5.710 μm	6.752 μm

Table 10.3.2: RMS and P-V data for spike-force series.

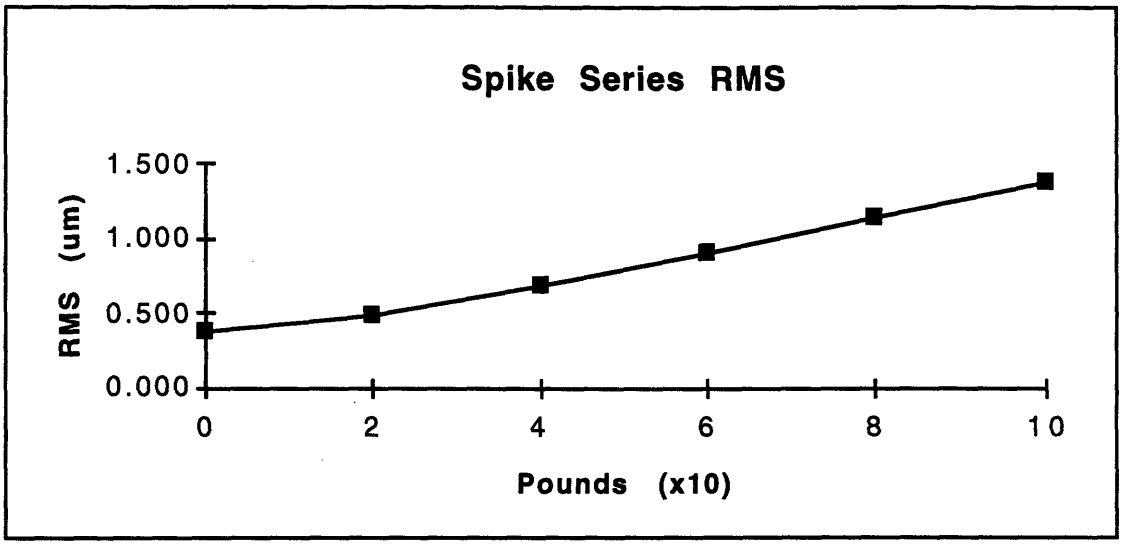

Chart 10.3.2: Mirror surface RMS under the influence of spike loads.

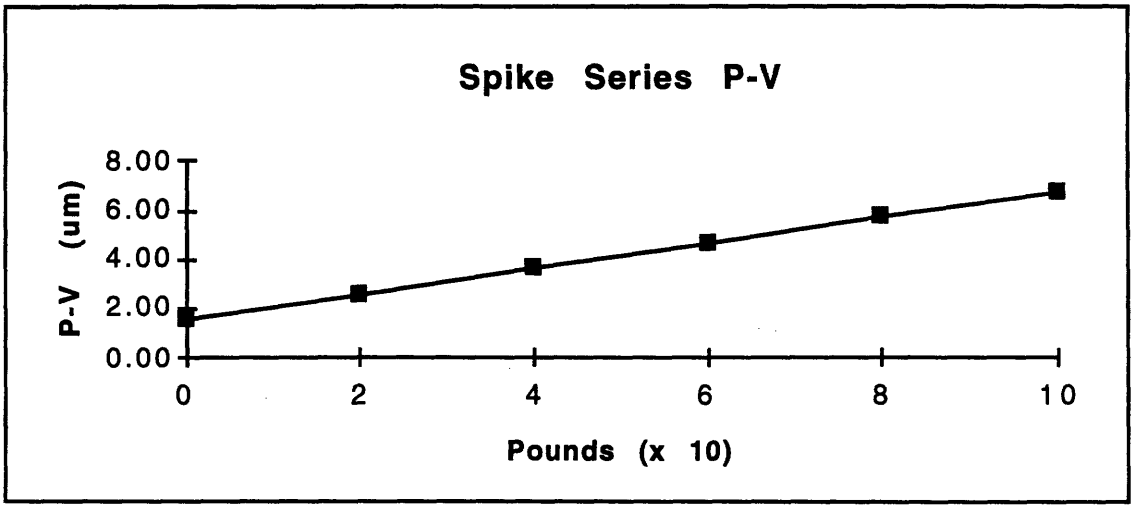

Chart 10.3.3: Peak-Valley for the series of spike loads.

10.3.2 Optical Response to A Point Load

Figures 10.3.3, 10.3.4 and 10.3.5 on the next three pages show the aberrated mirror's contour shape and the associated spot diagrams. The spot diagrams are taken at .05 mm intervals on either side of the mirror's nominal focal point. The spots show that increasingly large spike loads create increasing amounts of tilt, coma and astigmatism.

The spot diagrams for the 20 pound perturbation show that the actual focal point is approximately .04 mm beyond the nominal focal point. The wavefront shape transitions at this point from a shape that resembles a tear drop with a horizontal orientation to a tear drop with a vertical orientation. The vertically oriented tear drop exhibits a noticeable triangulation.

Figures 10.3.4 A and B show the 60 pound perturbation results. The tear drop pattern in the area before nominal focus is elongated. The transition at the actual focus is more abrupt than the 20 lb. case, developing a horizontal definition that transitions to a vertical definition at the actual focus. The wave form in the post-focus phase is reminiscent of a crescent moon.

The 100 pound perturbation result is seen in Figures 10.35 A and B. Pre-nominal focus tear drop shapes are even more elongated. The trefoil shape of the original focal-area aberration gives way to an extreme oblation so that the wavefront in the area of nominal focus is a horizontally elongated blob. The astigmatic change in orientation is more abrupt, and the post focus vertical image more well defined.

This series of convoluted wave forms may be best quantified by RMS. Tables 10.3.3 A, B and C on the page following the last spot diagram present RMS and 50% and 100% encircled energy radii. The 50% and 100% energy columns are measures of angular width, in arc seconds, for encircled energy. The RMS is the average ray displacement from center spot measured in arc seconds. Third order optical aberration data calculated by PCFRINGE for an image taken at the nominal focus is presented in Table 10.3.4 and Charts 10.3.3 and 10.3.4 on the page following the spot diagram data.

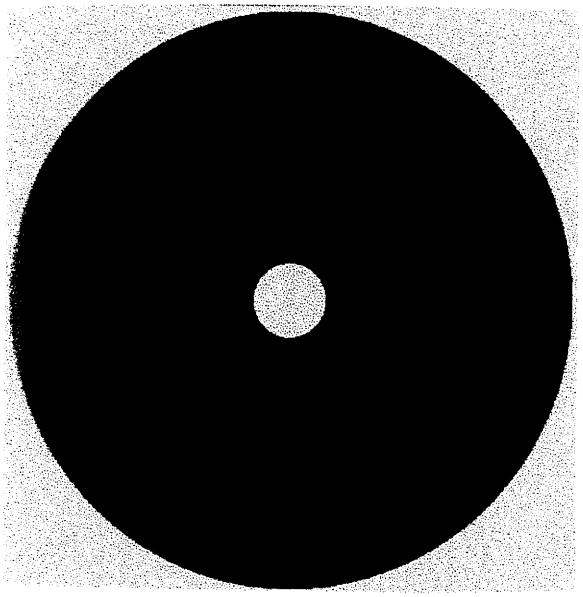

Figure 10.3.3 A: SURFACE contour plot of 20 pound spike perturbations.

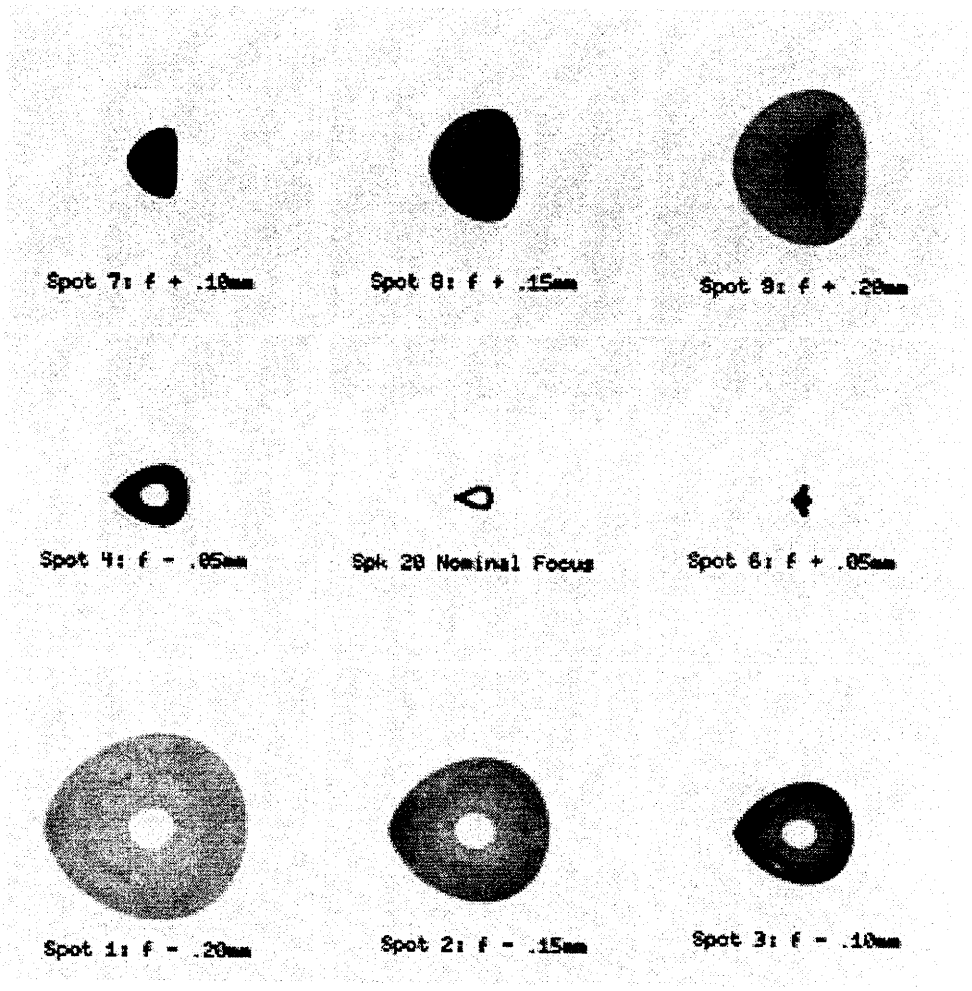

Figure 10.3.3 B: Spot diagrams of 20 pound spike perturbations.

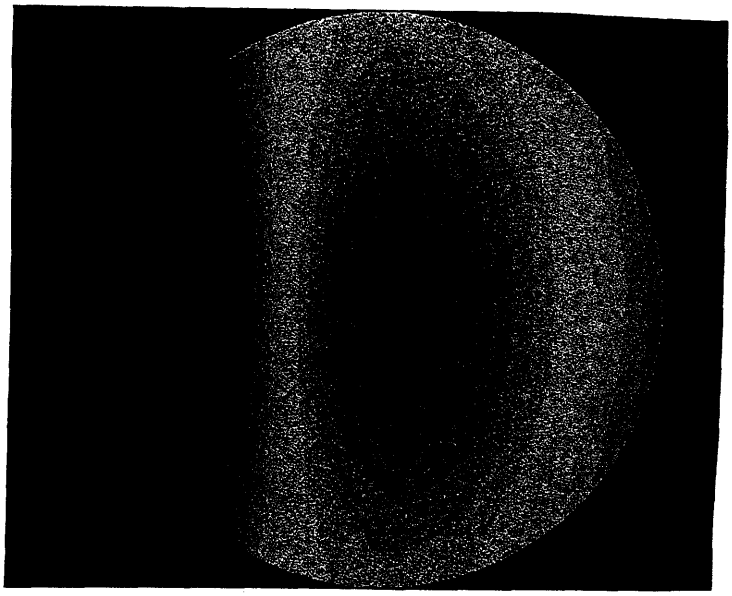

Figure 10.3.4 A: SURFACE contour plot of 60 pound spike perturbations.

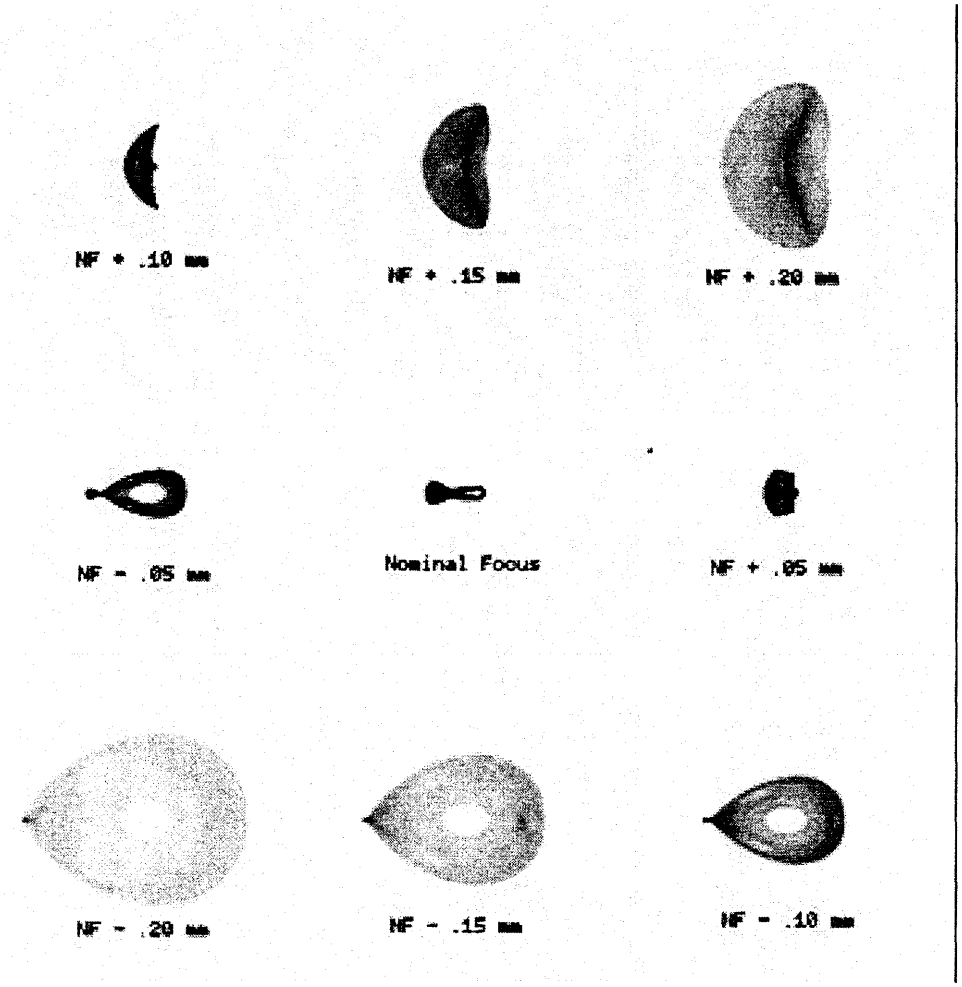

Figure 10.3.4 B: Spot diagrams from 60 pound spike perturbations.

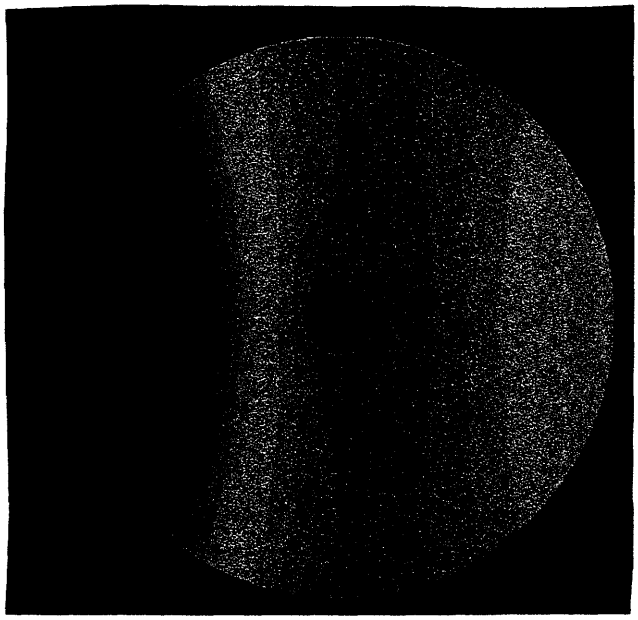

Figure 10.3.5 A: SURFACE contour plot of 100 pound spike perturbations.

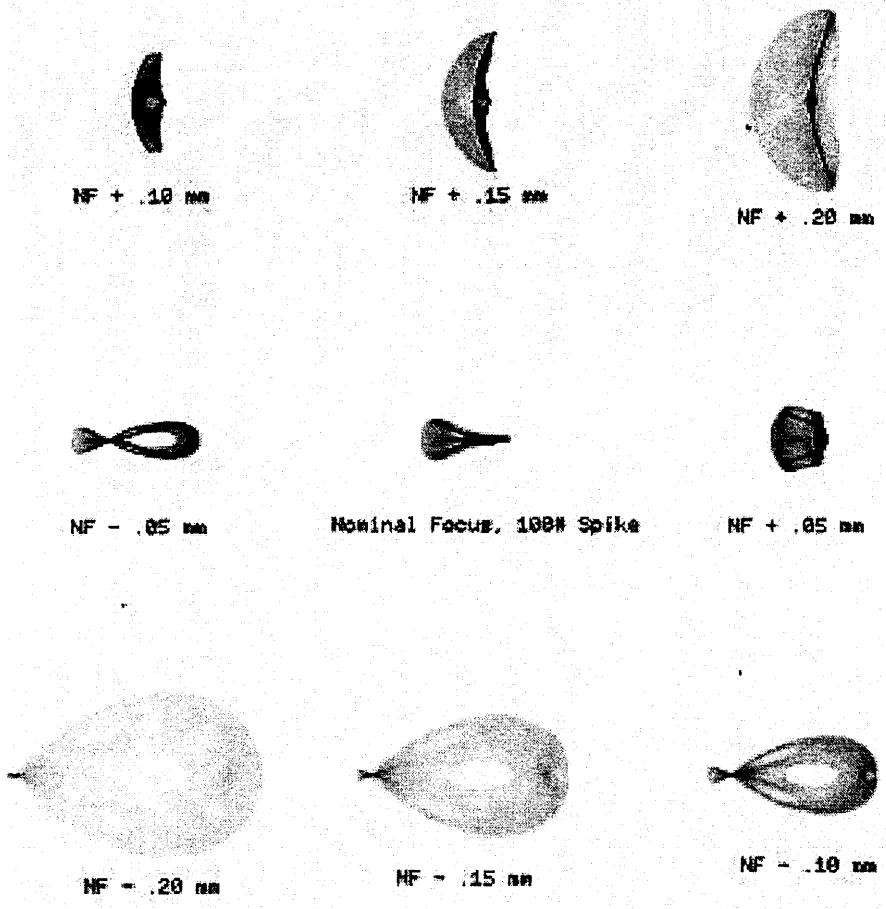

Figure 10.3.5 B: Spot diagrams from 100 pound spike perturbations.

Case: 20 lb Spike	RMS	50% Energy	100% Energy
Nominal - .20 mm	1.79	1.78	2.60
Nominal - .15 mm	1.42	1.41	2.10
Nominal - .10 mm	1.05	1.04	1.60
Nominal - .05 mm	0.69	0.66	1.10
Nominal Focus	0.34	0.31	0.58
Nominal + .05 mm	0.18	0.12	0.38
Nominal + .10 mm	0.47	0.40	0.90
Nominal + .15 mm	0.83	0.77	1.44
Nominal + .20 mm	1.20	1.14	1.92

Case: 60 lb Spike	RMS	50% Energy	100% Energy
Nominal - .20 mm	1.85	1.81	3.10
Nominal - .15 mm	1.49	1.44	2.65
Nominal - .10 mm	1.13	1.05	2.10
Nominal - .05 mm	0.78	0.71	1.60
Nominal Focus	0.47	0.43	0.80
Nominal + .05 mm	0.34	0.29	0.65
Nominal + .10 mm	0.53	0.43	1.13
Nominal + .15 mm	0.85	0.75	1.58
Nominal + .20 mm	1.20	1.10	2.08

Case: 100 lb Spike	RMS	50% Energy	100% Energy
Nominal - .20 mm	1.93	1.83	3.80
Nominal - .15 mm	1.58	1.45	3.15
Nominal - .10 mm	1.24	1.12	2.60
Nominal - .05 mm	0.92	0.82	2.25
Nominal Focus	0.65	0.60	1.35
Nominal + .05 mm	0.53	0.46	1.15
Nominal + .10 mm	0.65	0.53	1.27
Nominal + .15 mm	0.91	0.78	1.74
Nominal + .20 mm	1.23	1.10	2.23

Tables 10.3.3 A, B & C: RMS and encircled energy, in arc seconds.

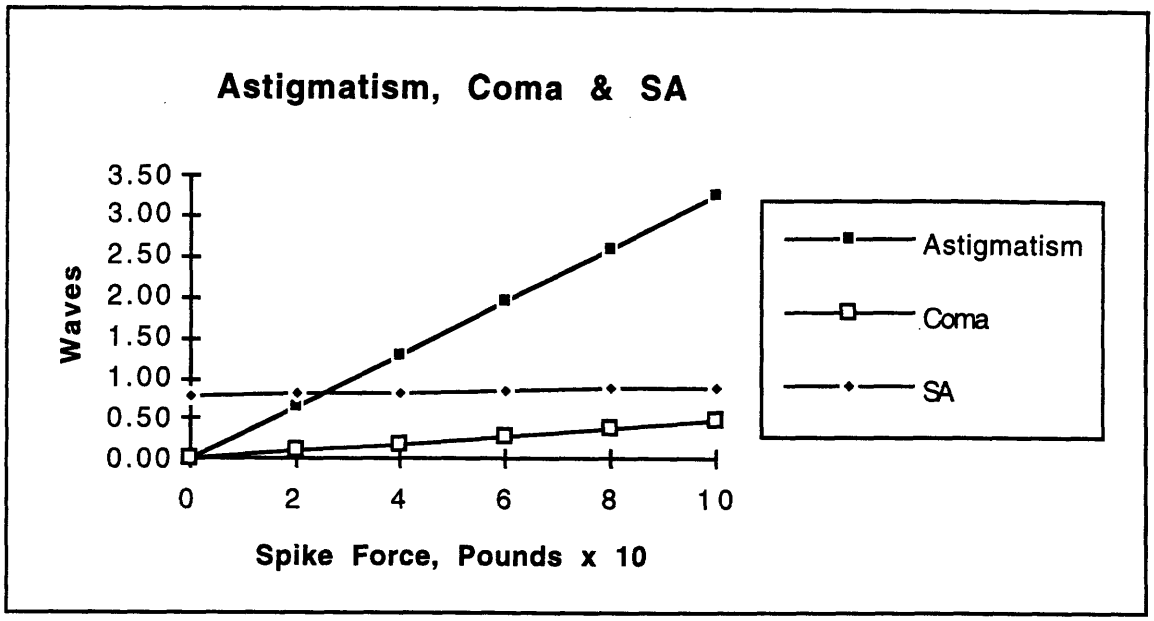

Chart 10.3.3: Astigmatism, Coma and Spherical Aberration at the nominal focal point as functions of force.

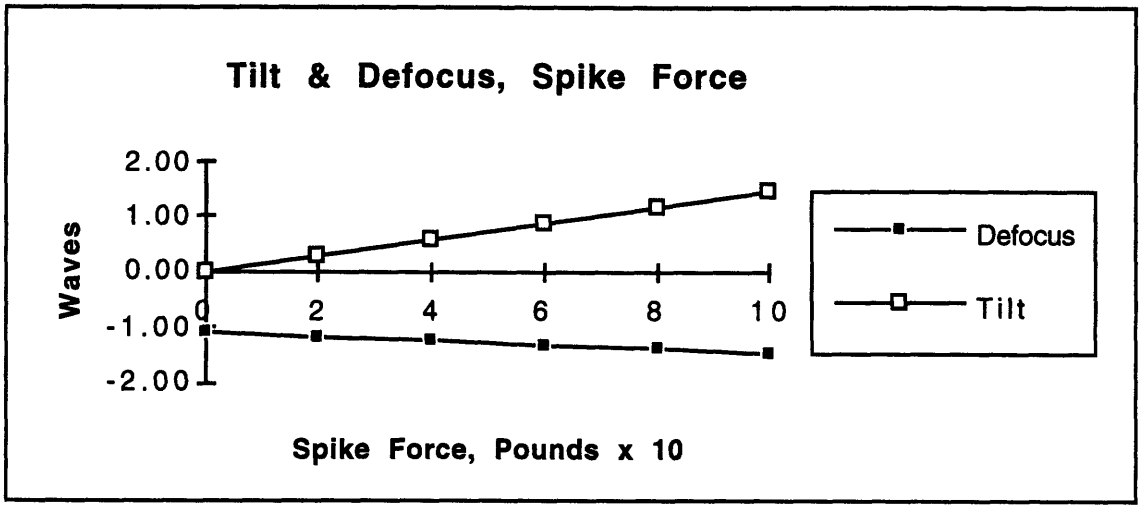

Chart 10.3.4: Tilt and Defocus at the nominal focal point as functions of force.

Case	Tilt (λ)	Defocus (λ)	Astigmatism (λ)	Coma (λ)	SA (λ)
Nominal	0	-1.103	0	0	.776
Spike 20 lb	.296	-1.172	.653	.097	.799
Spike 60 lb	.887	-1.312	1.961	.292	.845
Spike 80 lb	1.181	-1.382	2.610	.389	.868
Spike 100 lb	1.478	-1.452	3.267	.486	.891

Table 10.3.4: 3rd Order aberrations at nominal focal point, in wavelengths.

Actual Focus

Table 10.3.5 (below) shows image RMS and 50% encircled energy radius measured in arc seconds as functions of the amount of perturbing force that is applied to the mirror. Chart 10.3.5 presents the encircled energy data for the actual focus in graphic form.

Case: Actual Focus	RMS (Arc Seconds)	50% Energy (Arc Seconds)
Nominal	.11	.09
Spike 20 lb.	.16	.12
Spike 60 lb.	.34	.29
Spike 80 lb.	.44	.37
Spike 100 lb.	.54	.46

Table 10.3.5: Encircled energy as a function of applied force at the actual focus for single spike perturbations.

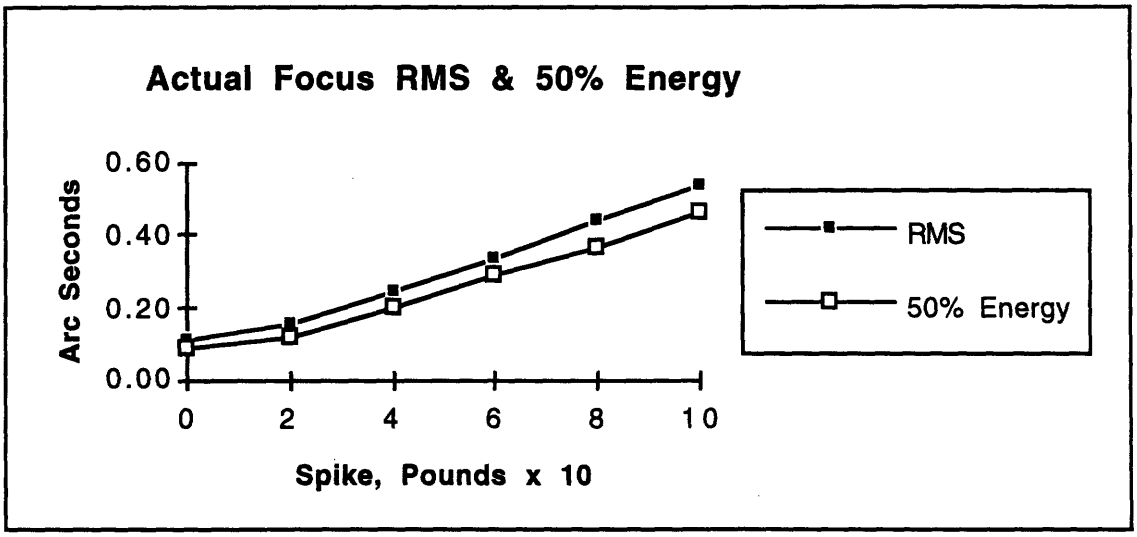

Chart 10.3.5: Image RMS and 50 % encircled energy radius calculated at the reflected wavefront's actual focus for the series of spot diagrams generated in the single point load analysis.

10.4 Perturbations From Two Point Loads

In a further investigation of the mirror's sensitivity to applied force, a series of paired or "coupled" point loads are applied to nodal components of the mercury belt radial support. Pairs of point loads of magnitude 20, 40, 60, 80, and 100 pounds are applied in the negative z-direction to nodes at the position ($r = 1.143$ m, $\theta = \pi/2$ & $\theta = 3\pi/2$, $z = .082$ m). Both nodes are part of the mercury belt radial support. One is located on the positive y-axis, the other is on the negative y-axis. This arrangement creates a two-fold symmetry with respect to the SPC's, as shown in Figure 10.4.1.

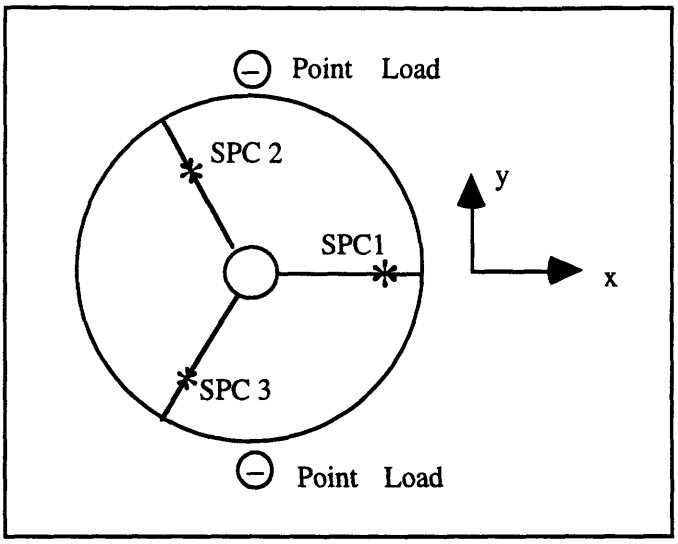

Figure 10.4.1: Location of two paired "spike" forces, oriented in negative "z" direction: ($r = 1.143$ m, $\theta = \pi/2$, $z = .082$ m), ($r = 1.143$ m, $\theta = 3\pi/2$, $z = .082$ m).

10.4.1 Structural Response to A Pair of Point Loads

The application of simultaneous point loads along the y-axis squeezes the mirror into a wedge pattern. The leading edge of the wedge is defined along the positive x-axis. The trailing edge of this wedge pattern forms along the mirror's outer surface in an orientation perpendicular to the x-axis. The wedge grows more acute as the magnitude of the point loads increases. Points of greatest positive deflection are found along the negative x-axis. Points of greatest negative deflection are found along the surface's periphery in the first and fourth quadrants.

The wedge pattern can be explained as the result of the interplay between the point loads and the hard point supports. The hard point supports form a natural triangle that contribute to mirror surface behavior under a variety of load conditions. In this case, mirror surface deflections can be plotted in relation to an imaginary set of lines that join the hard points. The greatest negative deflections occur in areas that lie along lines perpendicular to the imaginary connections between SPC 1 and SPC 2, and between SPC 1 and SPC 3. The greatest positive deflections lie along the negative x-axis, which bifurcates the right triangle created by connecting the SPC's. This pattern is depicted in Figure 10.4.2, below.

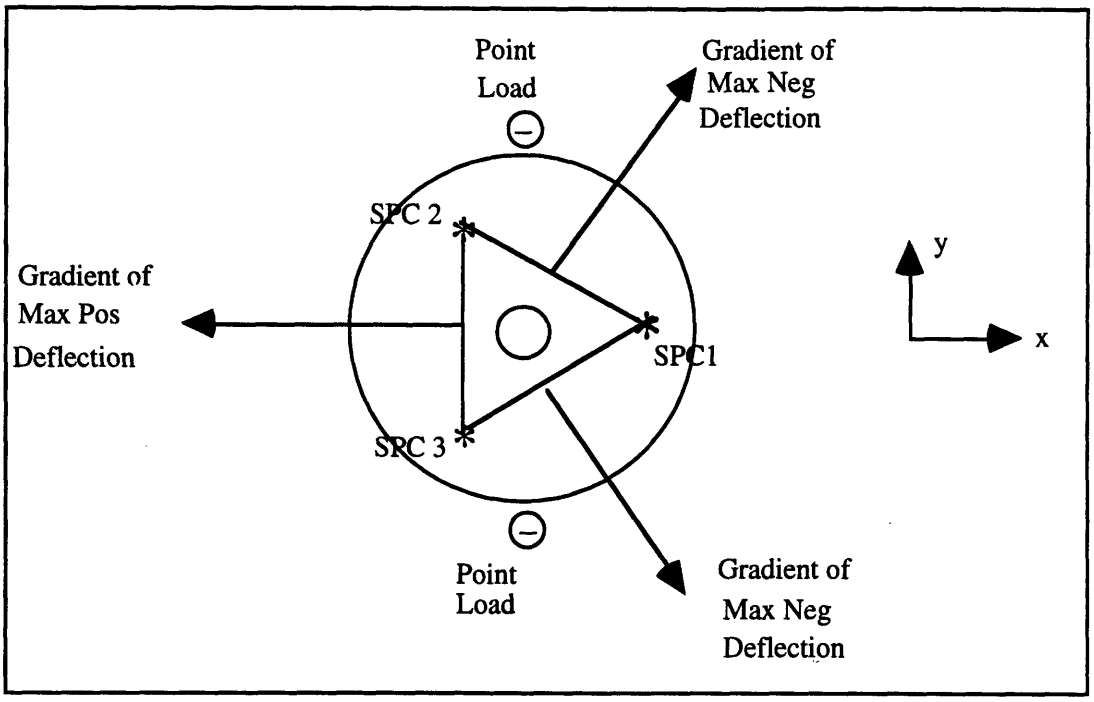

Figure 10.4.2: Triangulation formed by the interplay of coupled point loads, and the three hard points and the gradients of maximum positive and negative displacements.

Contour plots of the mirror surface deflecting under the combined action of the paired point loads and the reaction forces of the SPC's are shown in Figures 10.4.3A - 10.4.3F, on the next five pages. The plots are made by SURFACE. Following the contour plots are charts of mirror surface deflections and mirror surface RMS.

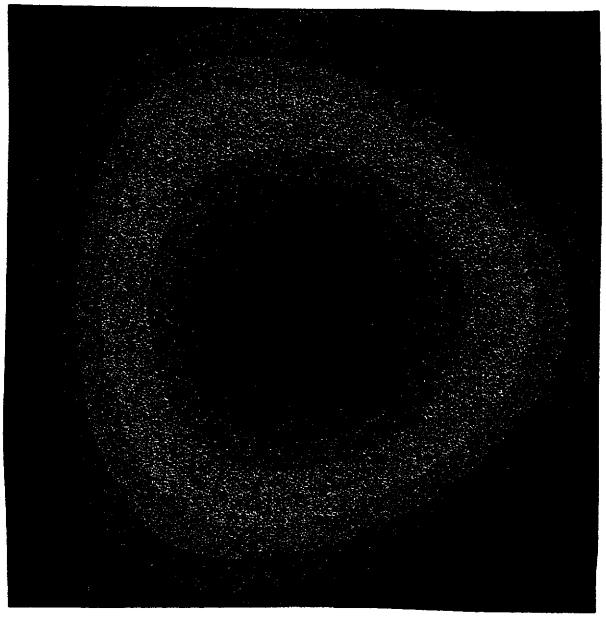

Figure 10.4.3 A: Surface contour plot of nominal mirror.

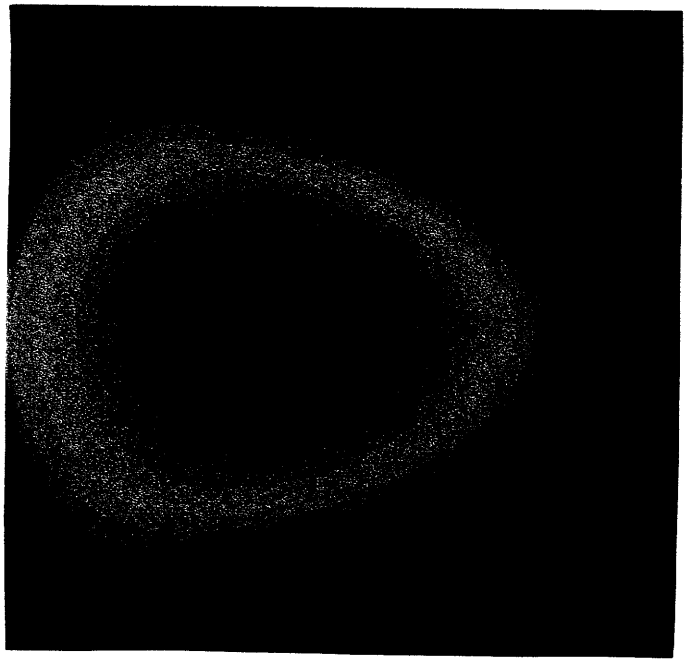

Figure 10.4.3 B: Surface contour plot of two 20 pound spike perturbations.

Figure 10.4.3 B: Surface contour plot of two 40 pound spike perturbations.

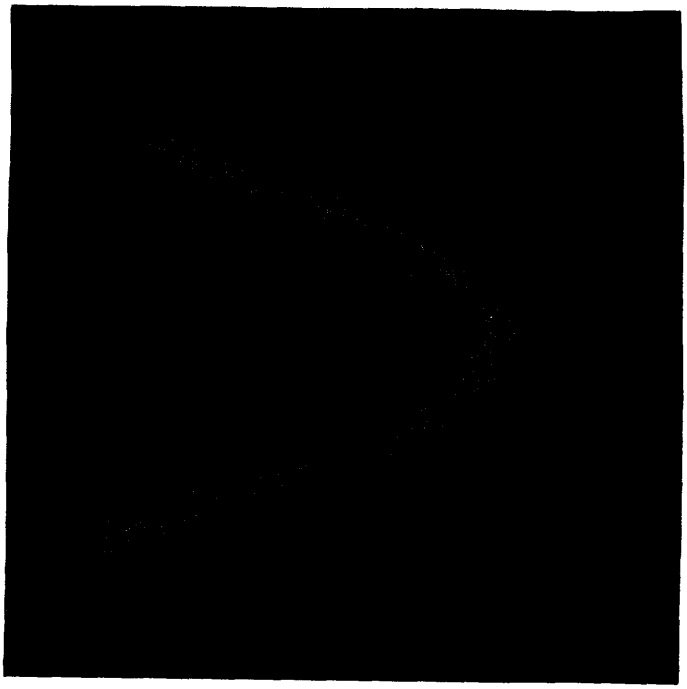

Figure 10.4.3 B: Surface contour plot of two 60 pound spike perturbations.

Figure 10.4.3 B: Surface contour plot of two 80 pound spike perturbations.

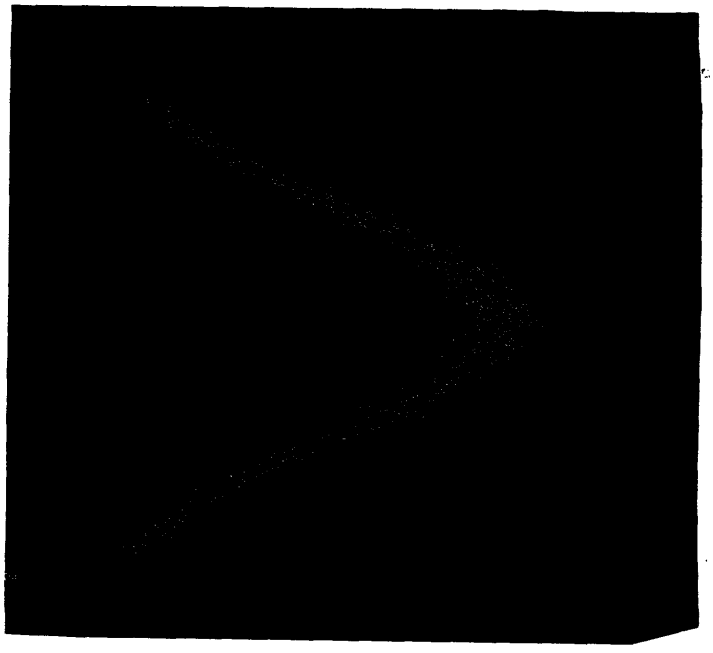

Figure 10.4.3 B: Surface contour plot of two 100 pound spike perturbations.

Surface Deflections and RMS

Chart 10.4.1 compare deflections at certain points on the mirror surface with the eflected wavefront RMS as mesured at the exit pupil.the gradients of maximum positive and negative deflection in the mirror surface. Figure 10.4.4 is a graphic of the locations of the surface points chosen for display.

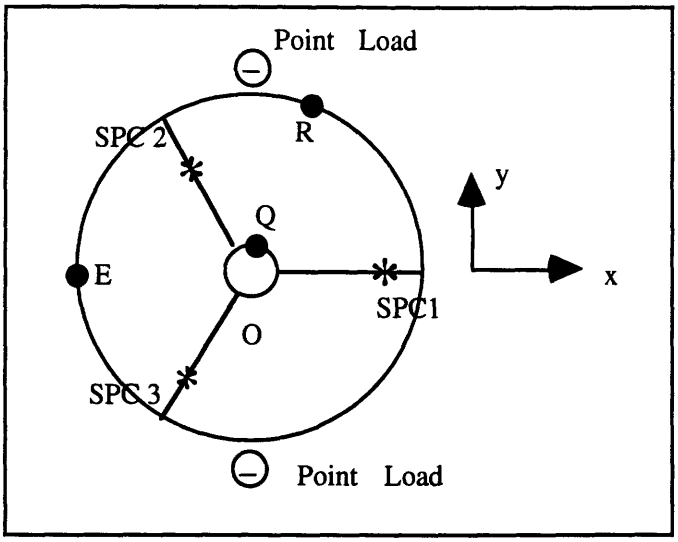

Figure 10.4.4: Selected displacement points for the series of two paired point loads. Points Q and R are on the radial of maximum negative gradient.

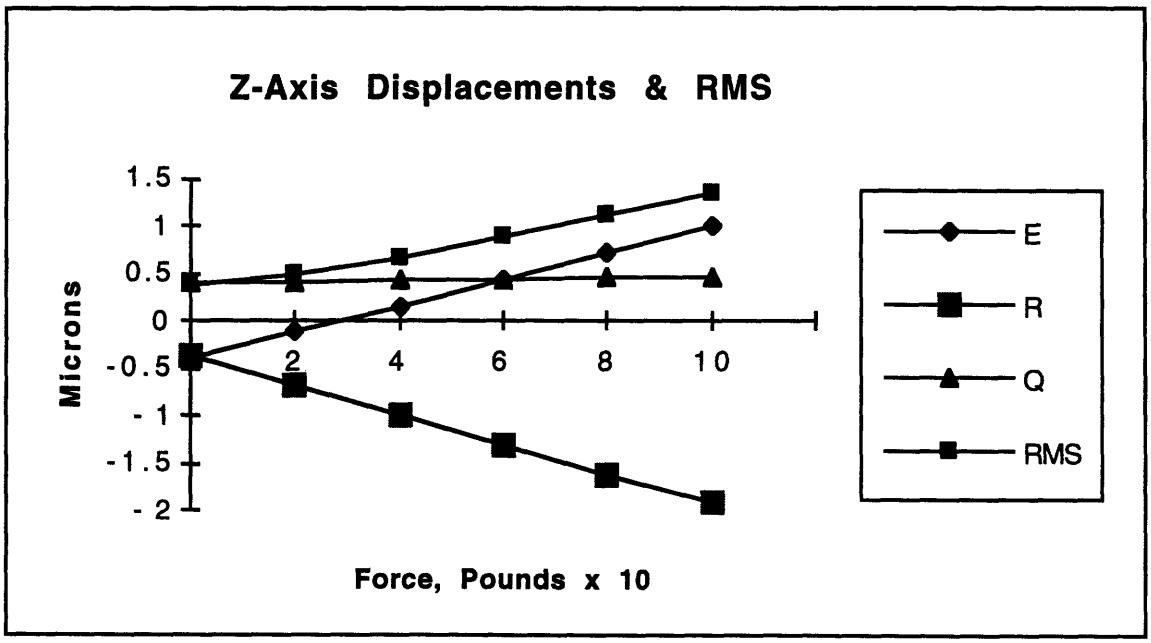

Chart 10.4.1: Z-axis displacements for selected points, and RMS, for the two paired point load case.

Reaction Force Trends

The application of two simultaneous downward spike forces at the extremes of the y-axis is opposed by the hard points. A bending moment is created which pushes the y-axis rim of the mirror down, and the center of the mirror up. This puts the surface material under tension and the material on the back of the mirror under compression. The outer rim of the mirror's backside is forced inward. This inward motion is opposed in the y-direction by all three hard points. The y-axis stress acts to relieve the x-axis stress that is found in the nominal support case. The paired spike forces apply a symmetric z-axis load, which is reflected in the uniform and linear distribution of z-axis reaction forces. Table 10.4.1 below and Charts 10.4.2 X, Y and Z on the next page present the reaction forces for each of the two point load cases.

Case/Reaction Force	X-Axis RF (N's)	Y-Axis RF (N's)	Z-Axis RF (N's)
Nominal: SPC 1	302	0	129
SPC 2	-151	261	129
SPC 3	-151	-261	129
20 lb.'s: SPC 1	232	0	189
SPC 2	-161	377	189
SPC 3	-161	-377	189
40 lb.'s: SPC 1	163	0	248
SPC 2	-81.5	492	248
SPC 3	-81.5	-492	248
60 lb.'s: SPC 1	93	0	308
SPC 2	-46.5	608	308
SPC 3	-46.5	-608	308
80 lb.'s: SPC 1	23	0	368
SPC 2	-11.5	723	368
SPC 3	-11.5	-723	368
100 lb.'s: SPC 1	-47	0	428
SPC 2	23.5	839	428
SPC 3	23.5	-839	428

Table 10.4.1: SPC reaction forces for a pair of spike loads. RF's in Newtons.

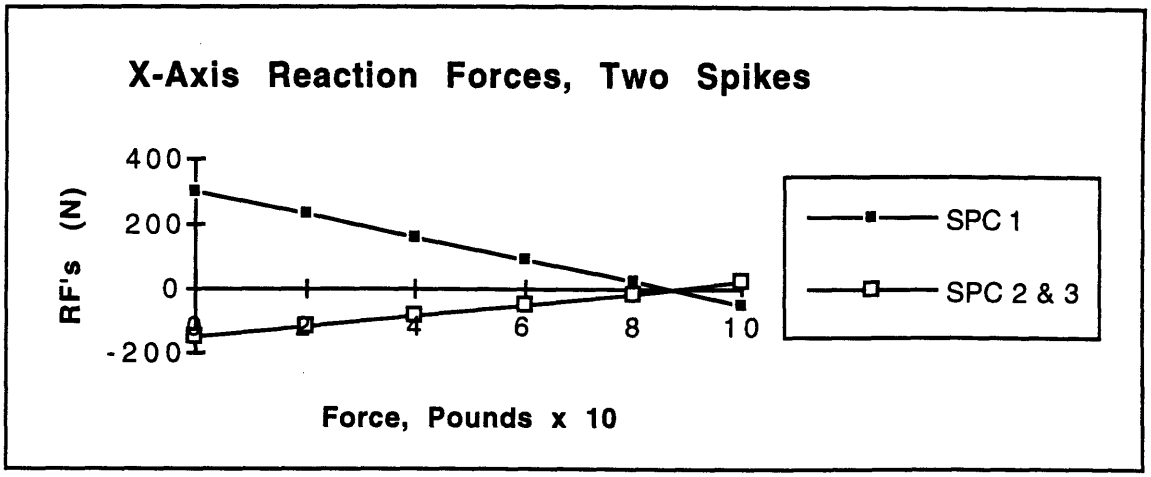

Chart 10.4.2 X: X-axis reaction loads for the two-point-load series.

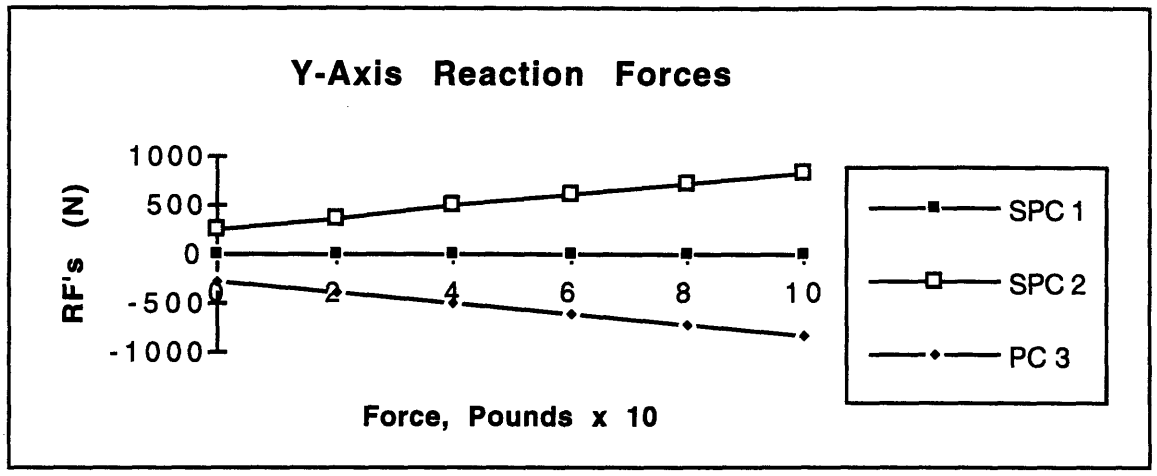

Chart 10.4.2 Y: Y-axis reaction loads for the two-point-load series.

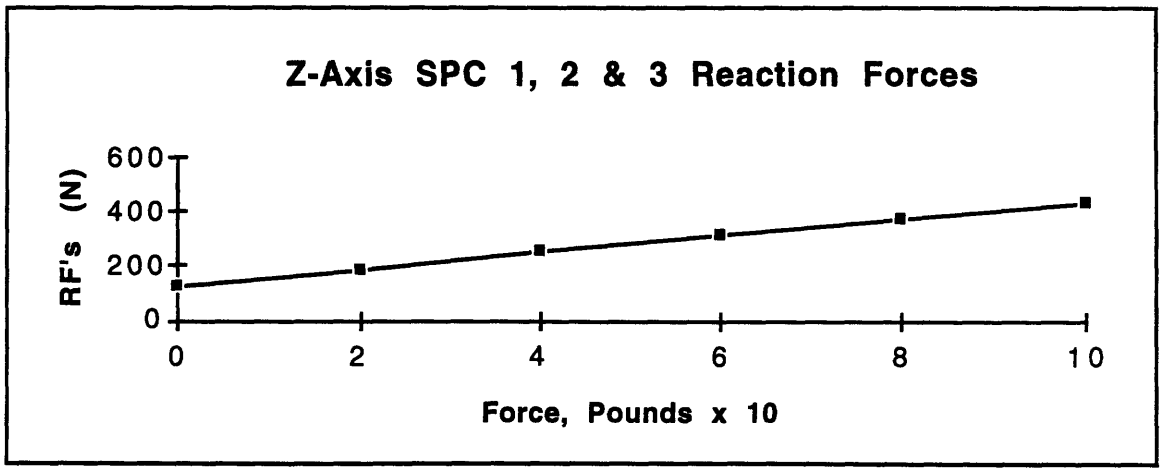

Chart 10.4.2 Z: Z-axis reaction loads for the two-point-load series.

10.4.2 Optical Response, Pair of Point Loads

Spot diagrams taken at .05 mm intervals on either side of the mirror's nominal focal point show the astigmatism produced by the simultaneous application of point loads to the mirror's edge along the y-axis. Figures 10.4.5, 10.4.6 and 10.4.7 on the next three pages show the aberrated mirror's contour shape and associated spot diagrams for the 20, 60 and 100 lb. load cases.

The shapes of the spot diagrams that result from the two point load application to the y-axis are the opposite of the results from the single point load application to the x-axis. In the case of the single spike force, a distinct horizontal astigmatism appeared in the area before nominal focus. That astigmatism reverses itself into a vertical orientation at the actual focus.

In the current case of applying point loads to each extreme of the mirror's y-axis, the initial astigmatic orientation is in the vertical. This orientation reverses to a horizontal orientation at the actual focus. That the two waveforms resulting from the single point load case and the paired load case would have opposite orientations is to be expected. Both load applications squeeze the mirror into astigmatic shapes - one warps the mirror around the y-axis and the other around the x-axis. The magnitudes of the comparative astigmatisms do not show a linear relation because of the differences in orientation between hard point support and location of load application.

Coma is less prevalent in this two point series than in the single spike series. Spherical aberration is enhanced by the two point loads. This, too, is expected - the action of the point loads pushes portions of the mirror's surface away from a parabolic figure and into a more spherical shape. Please see Table 10.4.3 and Charts 10.4.3 and 10.4.4 for third order data.

Tables 10.4.2 A, B and C on the page following the spot diagrams present spot diagram data. The 50% and 100% energy columns are measures of angular width, in arc seconds, for encircled energy. The RMS is the average ray displacement from center spot measured in arc seconds.

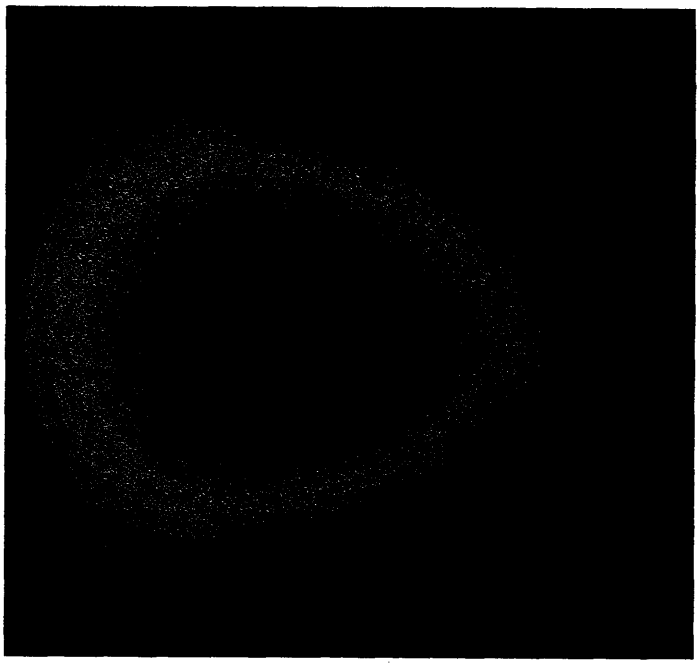

Figure 10.4.5A: SURFACE contour plot of two 20 lb. point loads.

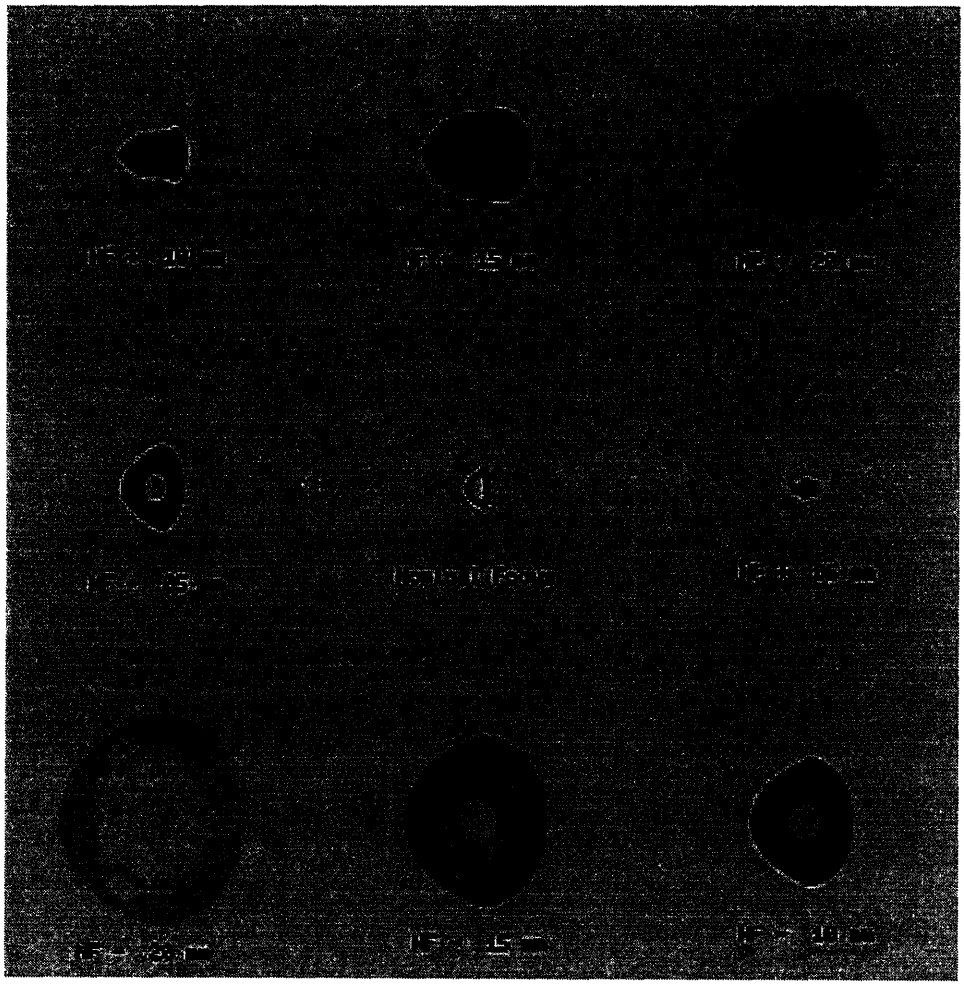

Figure 10.4.5B: Spot diagram from two 20 lb. point loads.

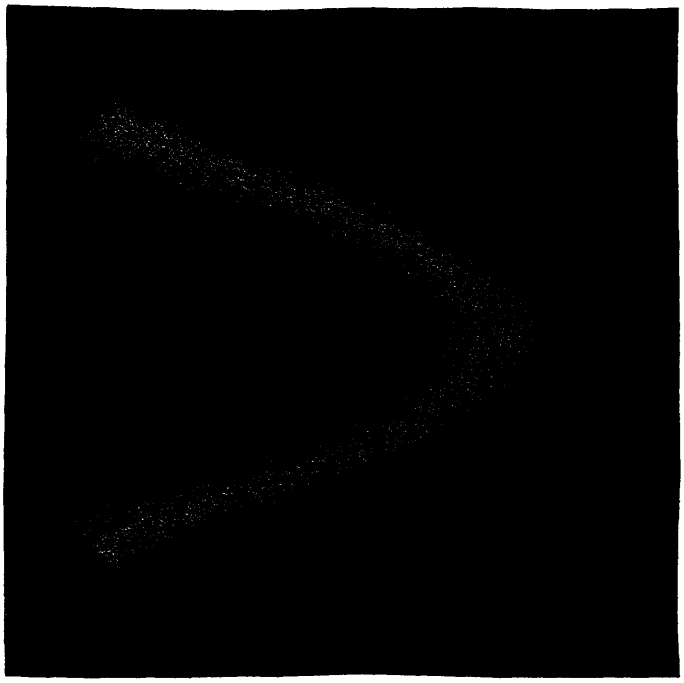

Figure 10.4.6A: SURFACE contour plot with two 60 lb. point loads.

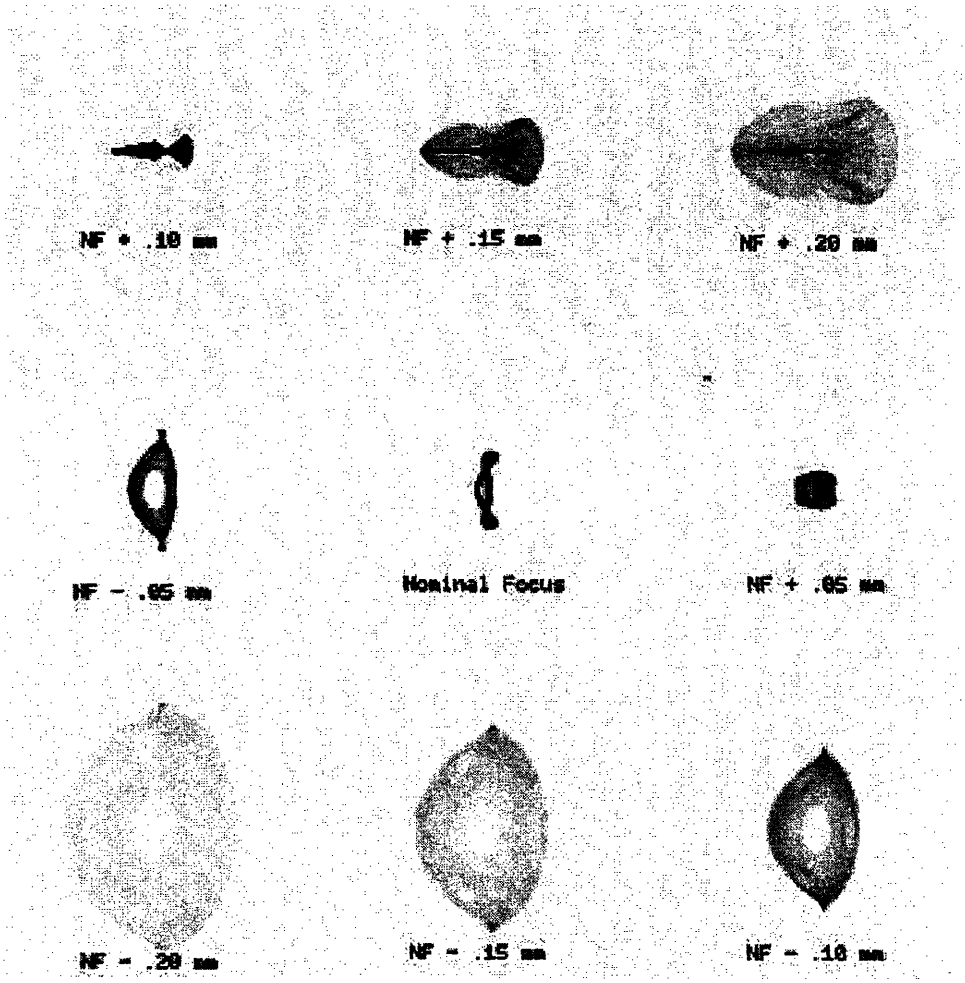

Figure 10.4.6B: Spot diagram from two 60 lb. point loads.

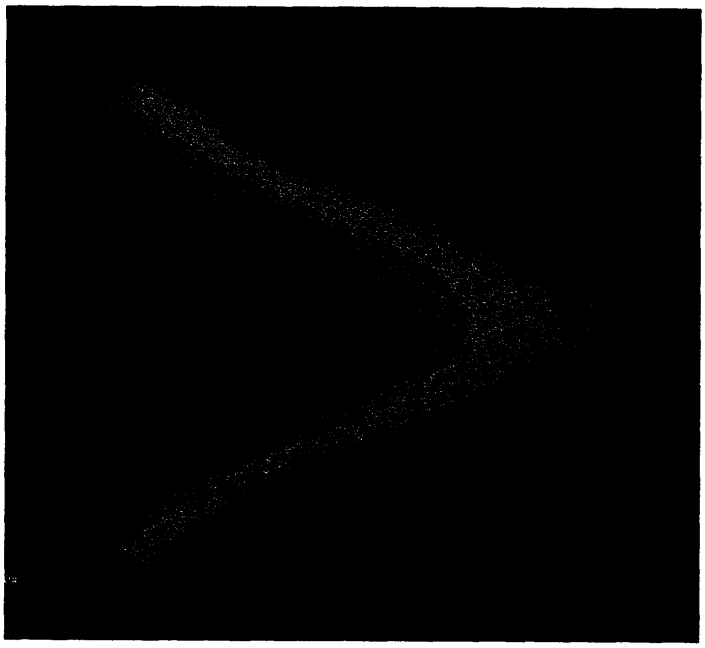

Figure 10.4.7A: SURFACE contour plot from two 100 lb. point loads.

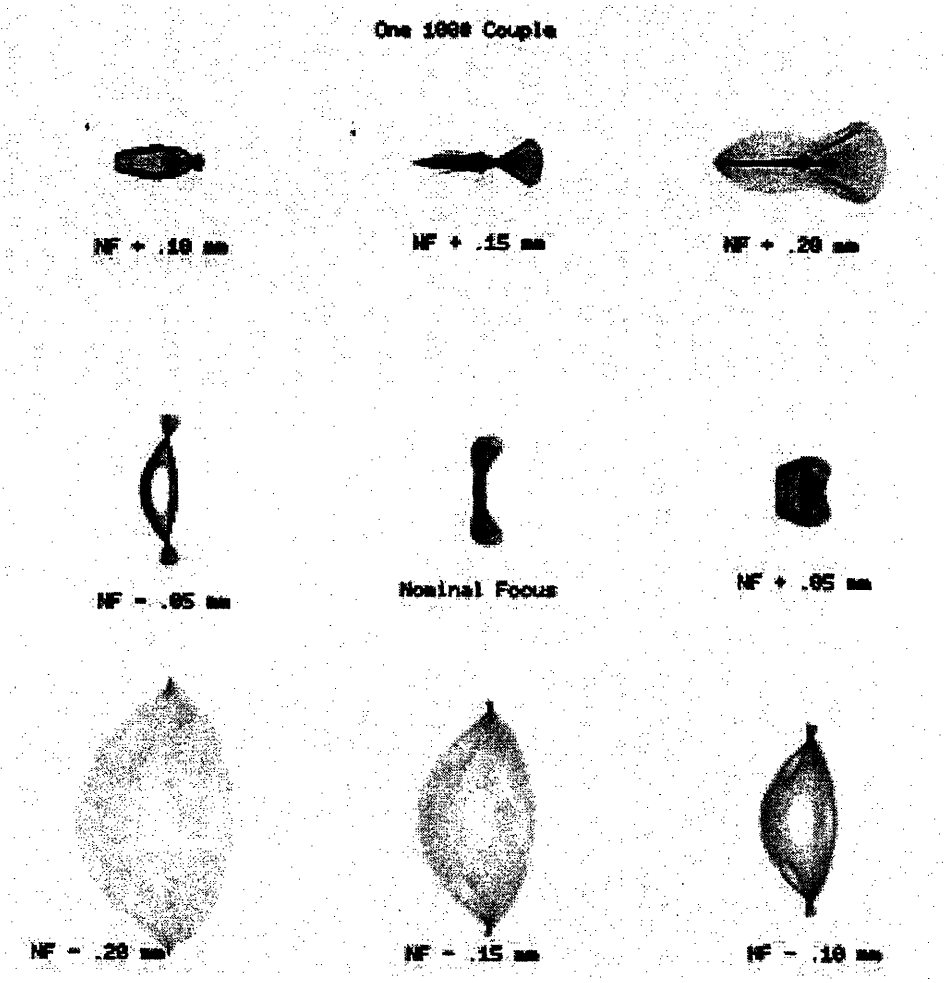

Figure 10.4.7B: Spot diagram from two 100 lb. point loads.

Case: 1-20 lb. Cpl	RMS	50% Energy	100% Energy
Nominal - .20 mm	1.80	1.80	2.71
Nominal - .15 mm	1.43	1.42	2.10
Nominal - .10 mm	1.07	11.05	1.56
Nominal - .05 mm	0.70	0.66	1.10
Nominal Focus	0.35	0.30	0.54
Nominal + .05 mm	0.17	0.13	0.14
Nominal + .10 mm	0.46	0.39	0.90
Nominal + .15 mm	0.82	0.75	1.45
Nominal + .20 mm	1.19	1.12	1.96

Case: 1-60 lb. Cpl	RMS	50% Energy	100% Energy
Nominal - .20 mm	1.90	1.84	3.11
Nominal - .15 mm	1.54	1.46	2.56
Nominal - .10 mm	1.18	1.07	2.01
Nominal - .05 mm	0.83	0.70	1.46
Nominal Focus	0.52	0.44	0.96
Nominal + .05 mm	0.35	0.34	0.69
Nominal + .10 mm	0.51	0.39	1.00
Nominal + .15 mm	0.81	0.69	1.68
Nominal + .20 mm	1.1	1.04	2.00

Case: 1-100 lb. Cpl	RMS	50% Energy	100% Energy
Nominal - .20 mm	2.02	1.87	3.51
Nominal - .15 mm	1.66	1.49	2.95
Nominal - .10 mm	1.32	1.12	2.46
Nominal - .05 mm	1.00	0.82	1.96
Nominal Focus	0.72	0.60	1.45
Nominal + .05 mm	0.57	0.51	1.10
Nominal + .10 mm	0.64	0.53	1.35
Nominal + .15 mm	0.87	0.72	2.00
Nominal + .20 mm	1.18	1.00	2.41

Table 10.4..2 A, B & C: Image RMS and encircled energy, in arc seconds.

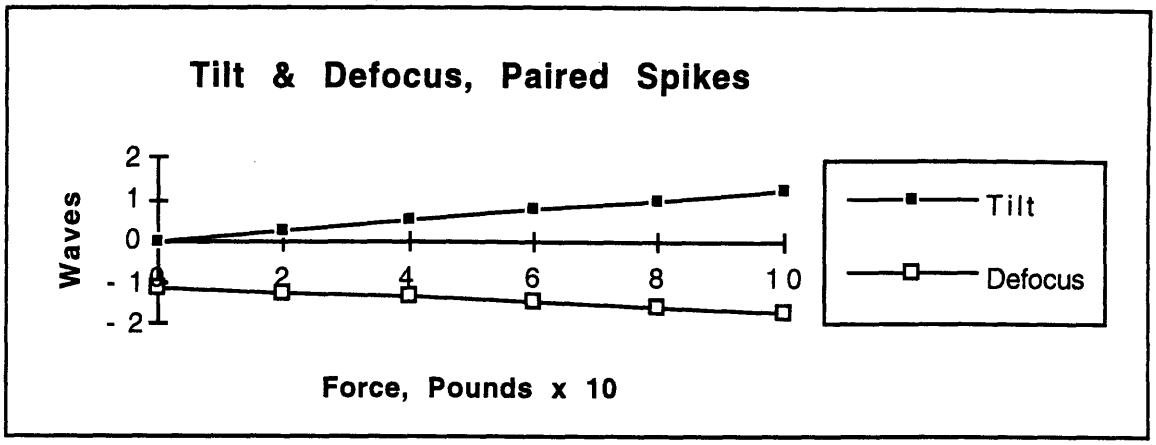

Chart 10.4.3: Tilt and Defocus at the nominal focal point as functions of force.

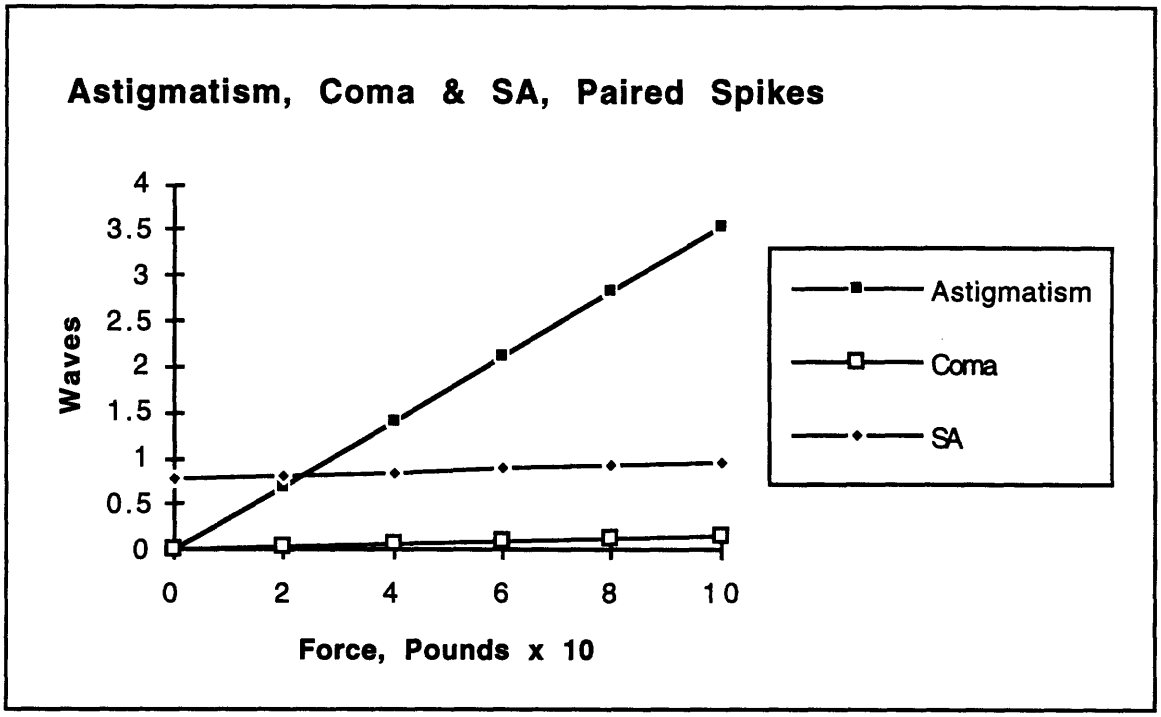

Chart 10.4.4: Astigmatism, Coma and Spherical Aberration at the nominal focal point as functions of force.

Case	Tilt	Defocus	Astigmatism	Coma	SA
Nominal	0	-1.103	0	0	.776
Spike 20 lb.	.296	-1.172	.653	.097	.799
Spike 60 lb.	.887	-1.312	1.961	.292	.845
Spike 80 lb.	1.181	-1.382	2.610	.389	.868
Spike 100 lb.	1.478	-1.452	3.267	.486	.891

Table 10.4.3: 3rd Order aberrations at nominal focal point, in wavelength.

Actual vs. Nominal Focus

Table 10.4.4 (below) shows image RMS and 50% encircled energy radius measured in arc seconds as functions of the amount of perturbing force that is applied to the mirror. Chart 10.4.5 presents the encircled energy data for the actual focus in graphic form. The region of actual focus occurs between .04 mm and .05 mm beyond the nominal focus.

Case: Actual vs. Nominal Focus	RMS (Arc Seconds)	50% Energy (Arc Seconds)
Nominal	.11/	.09/
Two 20 lb. spikes	.16/	.14/
Two 40 lb. spikes	.26/	.23/
Two 60 lb. spikes	.35/	.34/
Two 80 lb. spikes	.46/	.43/
Two 100 lb. spikes	.57/	.51/

Table 10.4.4: Encircled energy as a function of applied force at the actual/nominal focus for two simultaneous point load perturbations.

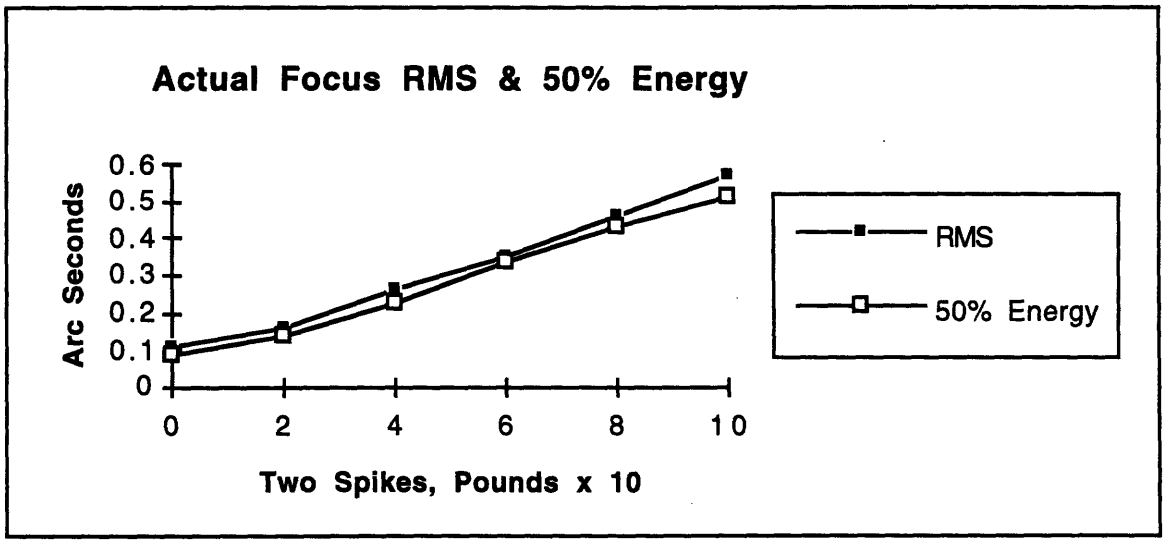

Chart 10.4.5: Encircled energy RMS and 50 % energy radius calculated at the reflected wavefront's actual focus for the series of spot diagrams generated in the pairing of two point loads.

10.5 Perturbations From Two Pair of Anti-Parallel Point Loads

In another investigation of the mirror's sensitivity to applied force, a series of two sets of paired point loads are applied to nodal components of the mercury belt radial support. One pair of forces is oriented in the negative "z" direction, while the other pair is oriented in the positive "z" direction. The point load magnitudes are 20, 40, 60, 80, and 100 pounds. The series is applied to nodes located at the extremes of the x-axis and the y-axis. Figure 10.5.1. illustrates the configuration:

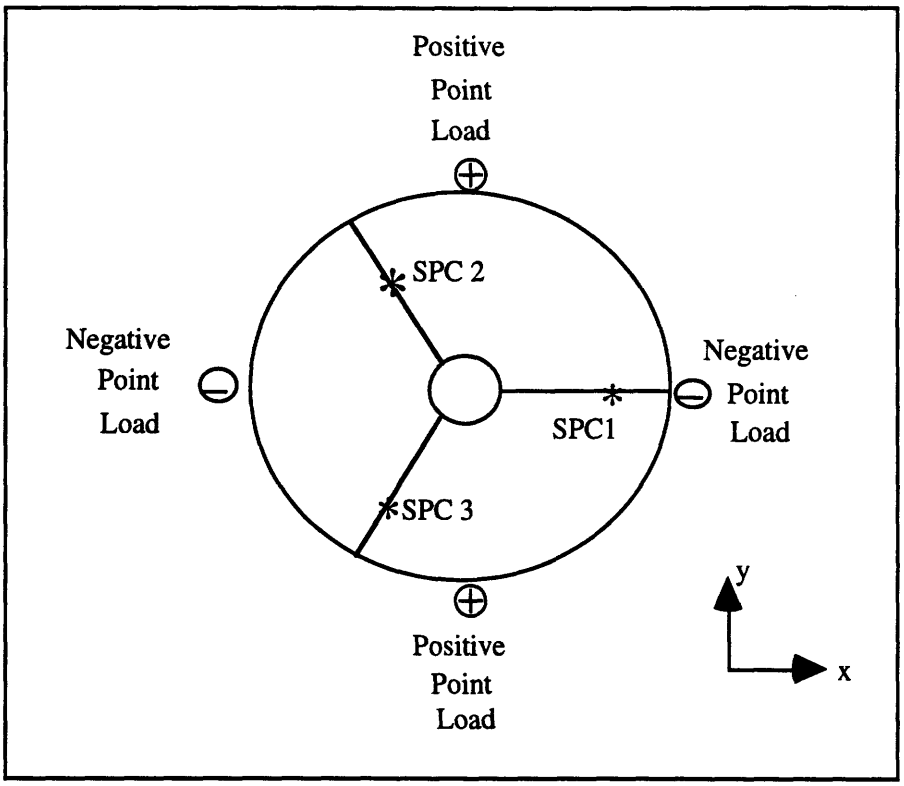

Figure 10.5.1: Positive forces are applied at (r = 1.143 m, $\theta = \pi/2$, z = .082 m) and at (r = 1.143 m, $\theta = 3\pi/2$, z= .082 m). Negative forces are applied at (r = 1.143 m, $\theta = 0$, z= .082 m) and at (r = 1.143 m, $\theta = \pi$, z= .082 m).

10.5.1 Structural Response to Two Anti-Parallel Pair of Point Loads

The effect of applying anti-parallel pairs of point loads is ultimately to warp the mirror into a "potato chip" mode. This "potato chip" shape results from the anticlastic bending of the mirror structure caused by the anti-parallel, off-axis point loads interacting with the hard point supports.

The couple that acts on the x-axis creates negative bending moments about the y-axis. The couple that acts on the y-axis creates positive bending moments around the x-axis. The conflicting moments act to reduce the overall magnitude of deflections that would be possible if only one couple was applied. The configuration exhibits a two fold deflection symmetry about the x-axis.

The low point on the face of the deformed mirror is found through out the series directly above the x-axis negative point load. The high points on the mirror surface migrate from their initial position in an area surrounding the central hole to points at the outer rim that are located slightly to the positive x side of the y-axis. This migration is a function of increasing point load force, the anticlastic bending moment, and the relative locations of point loads and SPC's. Surface shapes and deflection magnitudes can be seen in Figures 10.5.2, 10.5.3, and 10.5.4, which are NASTRAN and SURFACE z-axis contour plots.

Reaction Force Trends and Surface Shape Migration

At 20 lbs. per point load, the hard points interact with the two negative point loads applied along the x-axis to force the center of the mirror to bulge upwards. This x-axis negative point load dominance is gradually overcome by the positively oriented y-axis point loads. At approximately 30.5 lbs. of force per point load, the y-axis SPC reaction forces reach zero. Beyond 30.5 lbs. per point load, the y-axis SPC reaction forces show that the hard point-mirror interface in the y-direction is under tension rather than compression. This means that the upward vector applied by the two y-axis point loads is finally forcing the mirror surface rim upwards, transitioning the surface shape from that of a y-axis ridge into a shape that closely resembles a potato chip.

The x-axis reaction forces act to oppose the bending that is induced by the negative point loads applied at x = +/- 1.143 m. As the point loads push down along the x-axis, the mirror bends around the y-axis The resulting tension in the mirror surface pushes the mirror center into a bulge. The back of the mirror is compressed, and the x-axis reaction forces reveal the work done by the hard points in resisting this compression.

Throughout the series, the z-axis SPC reaction forces remain a constant 129 N. The combination of z-axis point loads applied to the mirror always sums to zero, hence the z-axis reaction force is unchanged at 129 N.

Case/Reaction Force	X-Axis RF (N's)	Y-Axis RF (N's)	Z-Axis RF (N's)
Nominal: SPC 1	302	0	129
SPC 2	-151	261	129
SPC 3	-151	-261	129
20 lb.'s: SPC 1	510	0	129
SPC 2	-255	91	129
SPC 3	-255	-91	129
40 lb.'s: SPC 1	716	0	129
SPC 2	-358	-80	129
SPC 3	-358	80	129
60 lb.'s: SPC 1	924	0	129
SPC 2	-462	-250	129
SPC 3	-462	250	129
80 lb.'s: SPC 1	1130	0	129
SPC 2	-565	-422	129
SPC 3	-565	422	129
100 lb.'s: SPC 1	1338	0	129
SPC 2	-669	-594	129
SPC 3	-669	594	129

Table 10.5.1: SPC reaction forces for two pair of spike loads.

The following two charts present SPC reaction forces graphically. Note the y-axis reaction force point of transition from compression to tension.

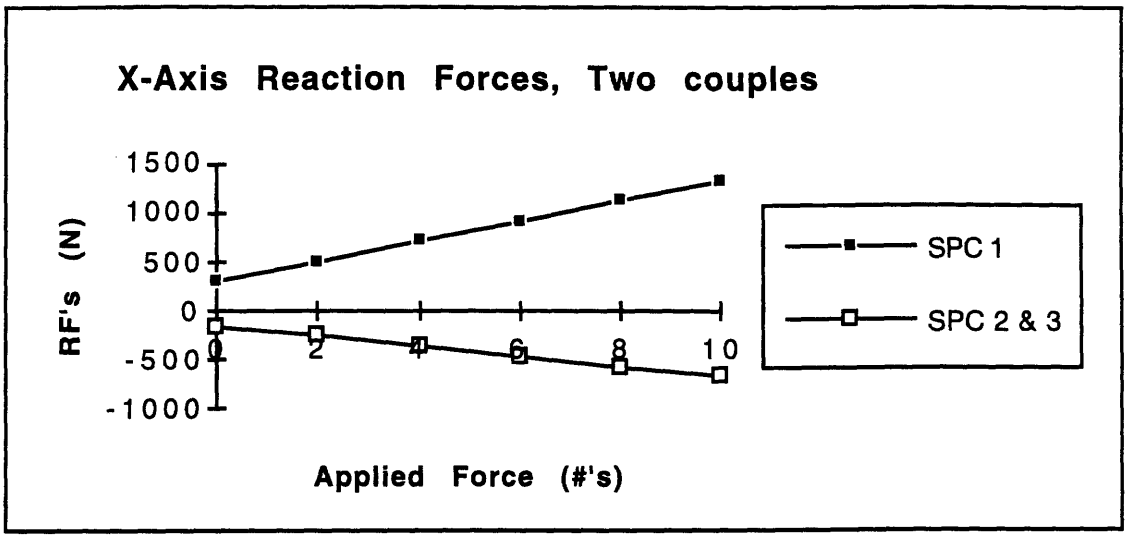

Chart 10.5.1 X: X-axis reaction forces for two sets of anti-parallel point loads.

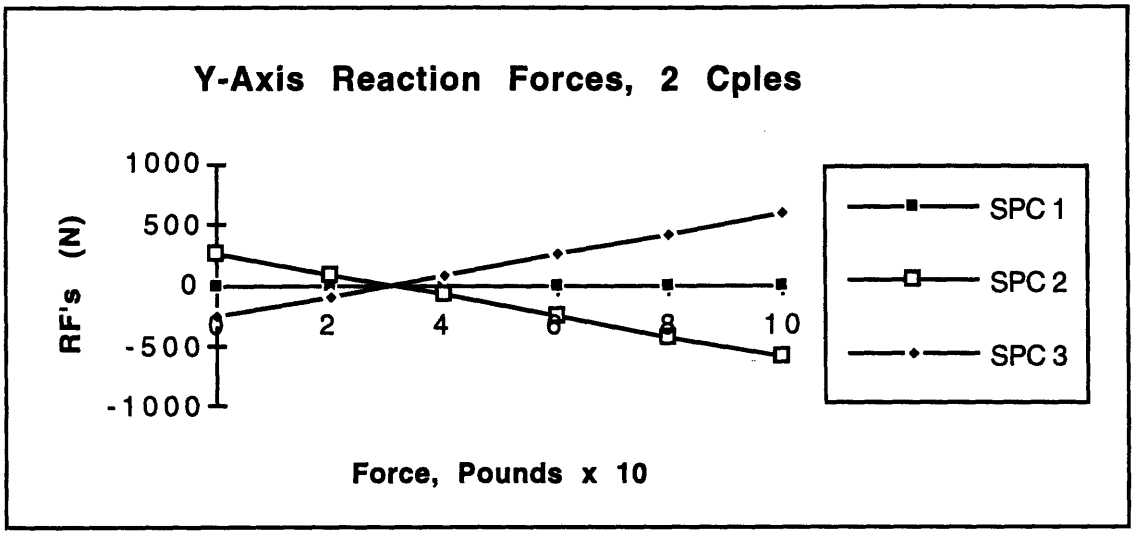

Chart 10.5.1 Y: Y-axis reaction forces for two sets of anti-parallel point loads.

Surface Contour Plots

On the following pages Figures 10.5.2 and 10.5.4 show NASTRAN z-axis surface deflection results. The scale shown on the NASTRAN plots is in millimeters. Figures 10.5.3A-10.5.3B are SURFACE contour plots showing z-axis surface deflections that display the migration trend in deformed mirror surface shapes.

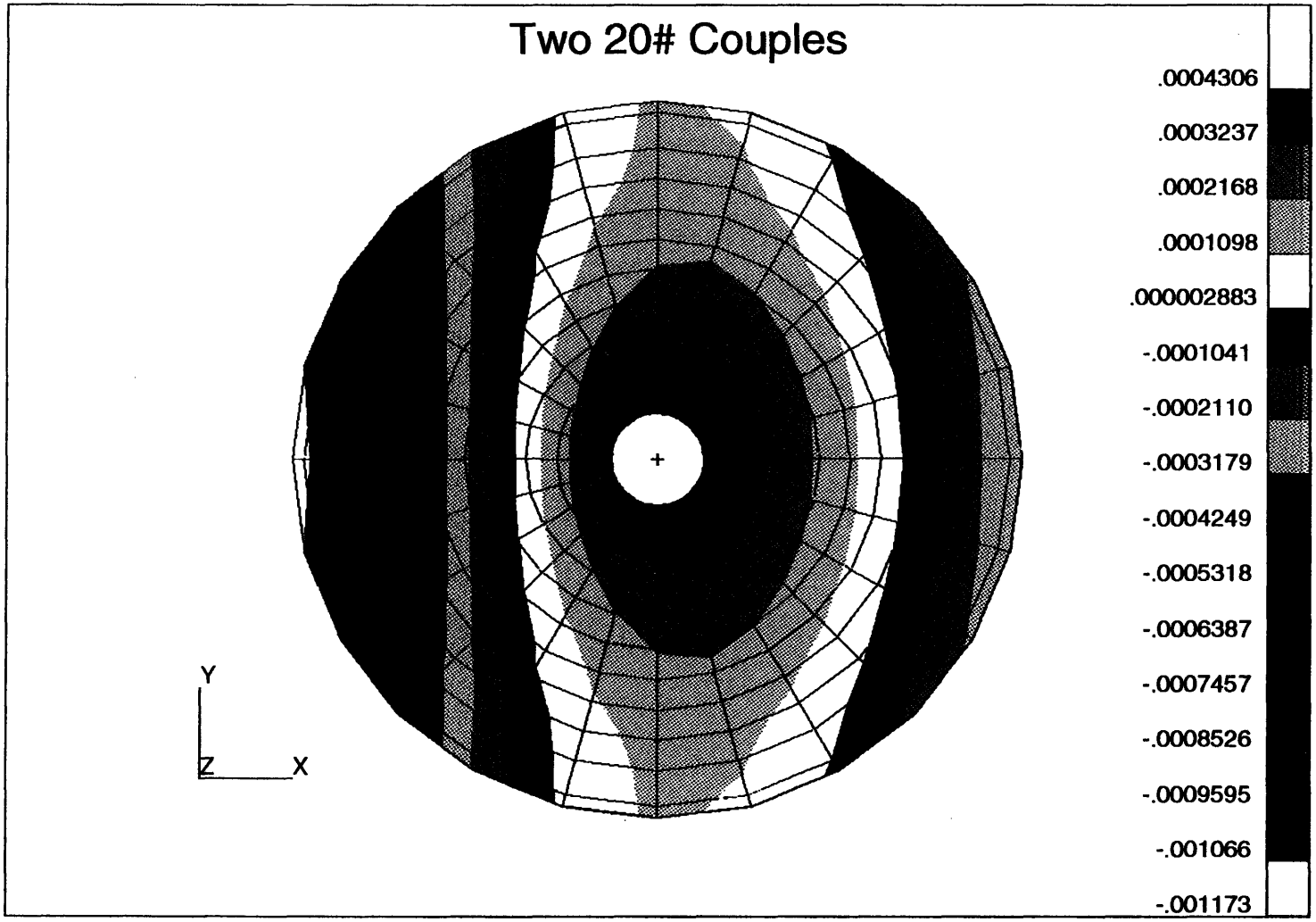
Two 20# Couples
.0004306
.0003237
.0002168
.0001098
.000002883
-.0001041
-.0002110
-.0003179
-.0004249
-.0005318
-.0006387
-.0007457
-.0008526
-.0009595
-.001066
-.001173
Y
Z
X

Figure 10.5.3A: Surface contour plot of four anti-parallel 40 lb. spikes.

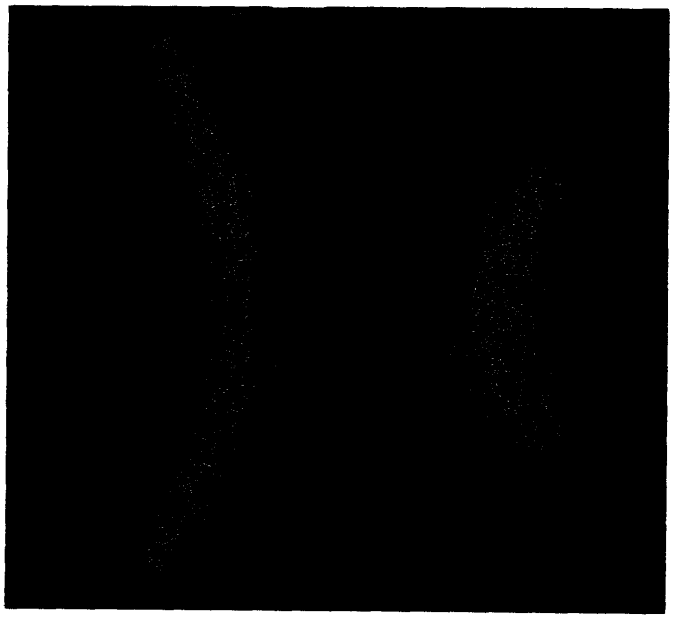

Figure 10.5.3B: Surface contour plot of four anti-parallel 80 lb. spikes.

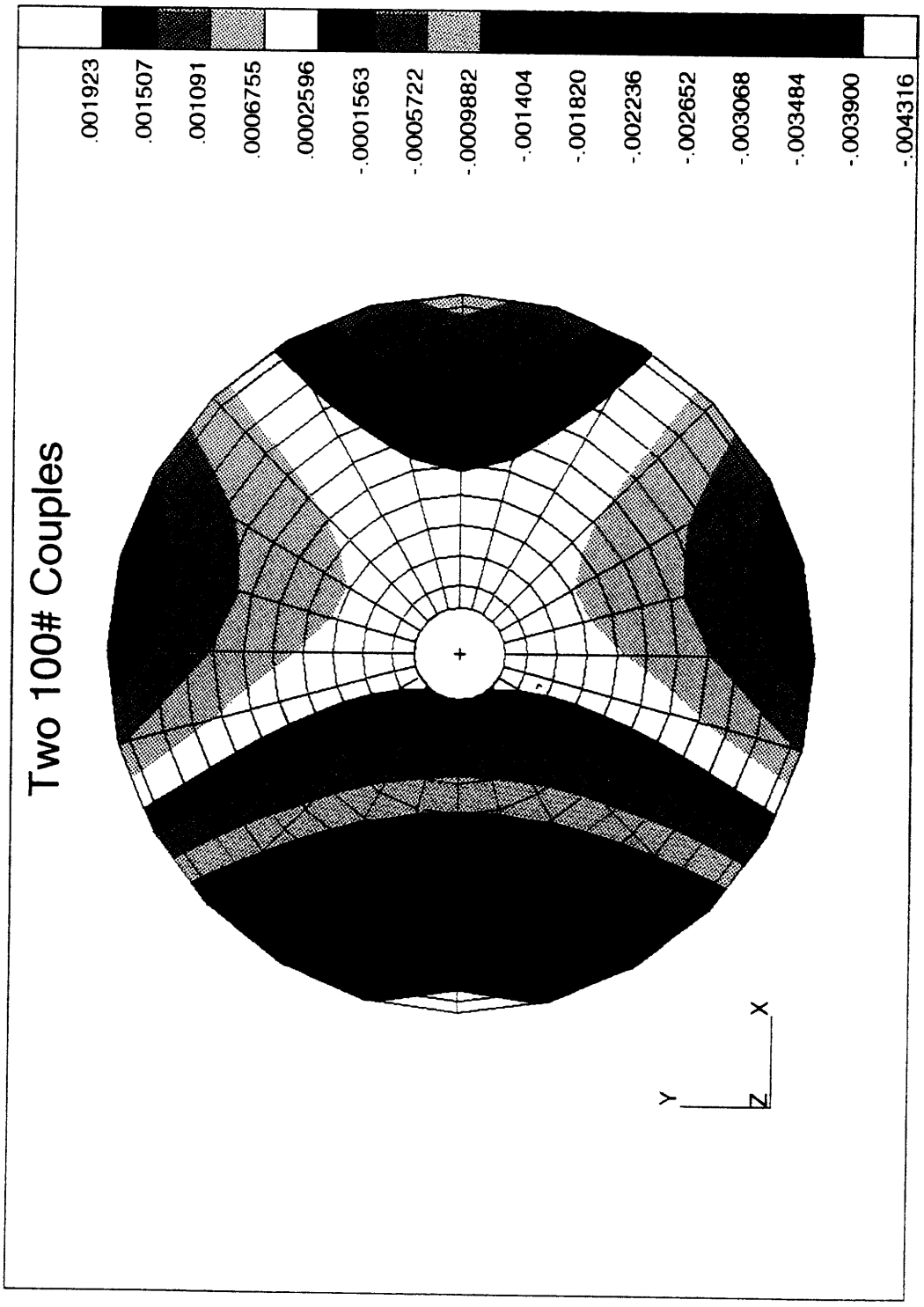
Two 100# Couples
.001923
.001507
.001091
.0006755
.0002596
-.0001563
-.0005722
-.0009882
-.001404
-.001820
-.002236
-.002652
-.003068
-.003484
-.003900
-.004316
Y
Z
X

RMS, P-V, and Specific Deflections

The slight RMS kink in Chart 10.5.2 is due to the linear action of two distinct modes. The primary deflection mode is due to gravity. The mode that results from applying anti-parallel sets of point loads adds linearly to the gravity mode. P-V is linear, as are the surface deflections in Chart 10.5.3.

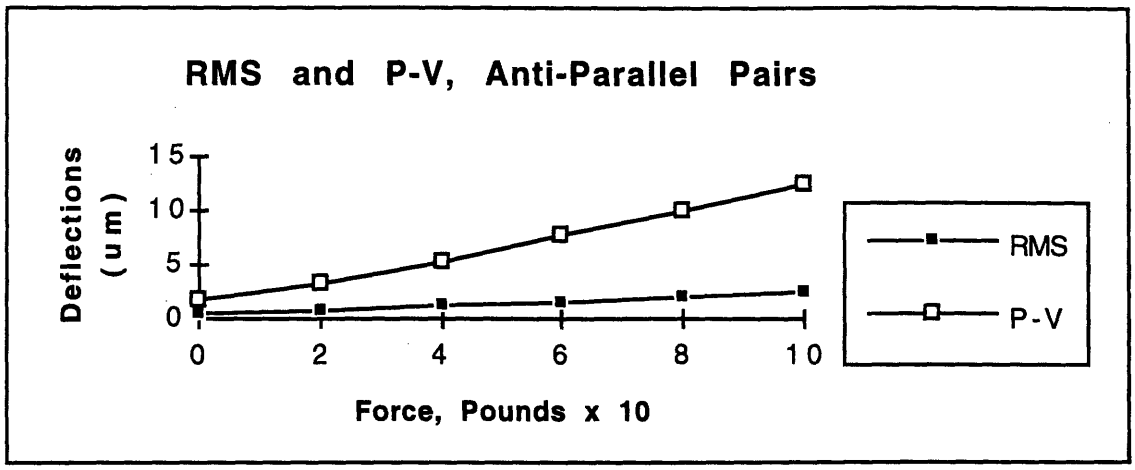

Chart 10.5.2: RMS and P-V for the series of paired, anti-parallel point loads.

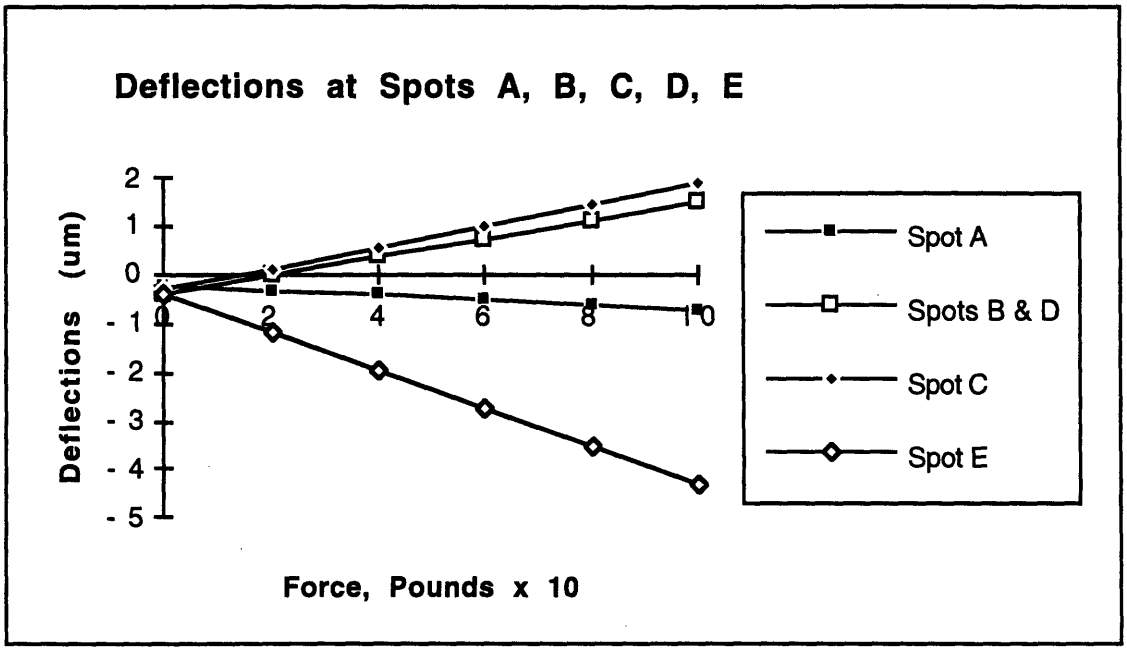

Chart 10.5.3: All spots are on the mirror surface. Polar coordinates are: Spot A = (r = 1.181, θ = 0), Spot B = (r= 1.181, θ= 5π/12), Spot C = (r=1.181, θ = π/2), Spot D = (r = 1.181, θ = 3π/2), Spot E = (r = 1.181, θ = π). Spot E is the series' point of maximum negative deflection, Spot B the point of max positive deflection.

10.5.2 Optical Response to Four Point Loads

Spot diagrams taken at .05 mm intervals on either side of the deformed mirror's nominal focal point show that the optical result of applying anti-parallel sets of point loads in a symmetric configuration is a pure astigmatism. Figures 10.5.5, 10.5.6 and 10.5.7 on the next three pages show the aberrated mirror's contour shape and associated spot diagrams for the 20, 60 and 100 lb. load cases. (Please also see Table 10.3.4 and Charts 10.3.3 and 10.3.4.)

The 20 lb. load case structural result is a ridge of positive deflections that runs along the mirror surface's y-axis. The 20 lb. case spot diagram series is very reminiscent of the spot diagrams of both the single load case (Section 10.3) and two-point-load case (Section 10.4). These show an astigmatic transition from a horizontal to a vertical orientation taking place at the actual focus. The tear-drop shapes hint at the triangulation seen in earlier cases.

The spot diagrams for the 60 and 100 lb. cases are startling different. The 60 lb. and 100 lb. loading creates the "potato chip" shape in the mirror surface. The y-axis SPC reaction forces show tension, and there is real contrast between the positive deflections found to the east of the y-axis along the mirror's rim and the negative deflections found in the vicinity of the x-axis point load applications. Especially in the 100 lb load case, the astigmatism is very well defined. The spots at .10 mm before nominal focus and .20 mm beyond nominal focus show very tightly defined line images. The actual focal point for these two cases, as determined by a spot analysis taken at .01 mm intervals, is at nominal + .05 mm. This means that spot images seen at nominal - .10 mm and at nominal + .20 mm form at equal distances from the actual focus, and represent classic astigmatic line images.

Tables 10.4.2 A, B and C on the page following the spot diagrams present encircled energy data in terms of RMS and 50% and 100% encircled energy radii. The 50% and 100% Energy columns are measures of angular width, in arc seconds, for encircled energy. The RMS is the average ray displacement from center spot measured in arc seconds. The 3rd order aberration data in Table 10.5.3 and Charts 10.4.4 and 10.4.5 is generated by projecting the Zernike polynomial surface fit to the nominal focus.

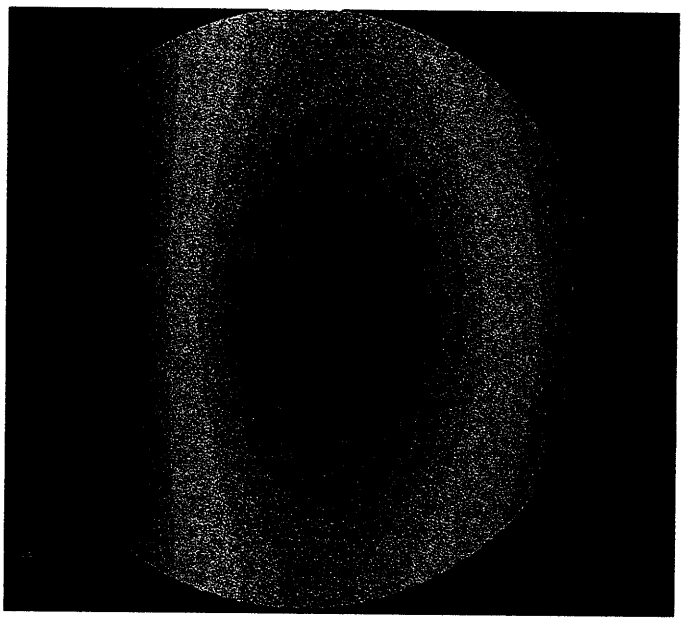

Figure 10.5.5 A: SURFACE contour plot of perturbation of four 20 pound spikes.

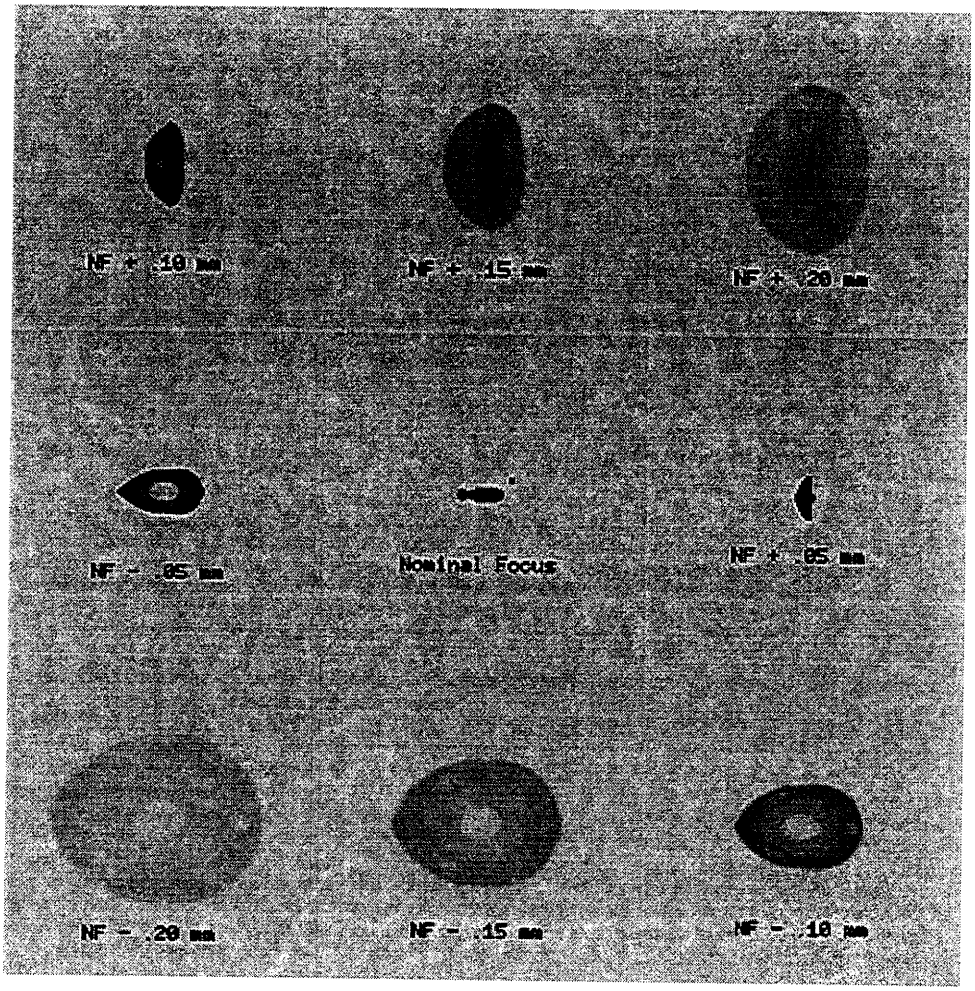

Figure 10.5.5 B: Spot diagrams from perturbation of four 20 pound spikes.

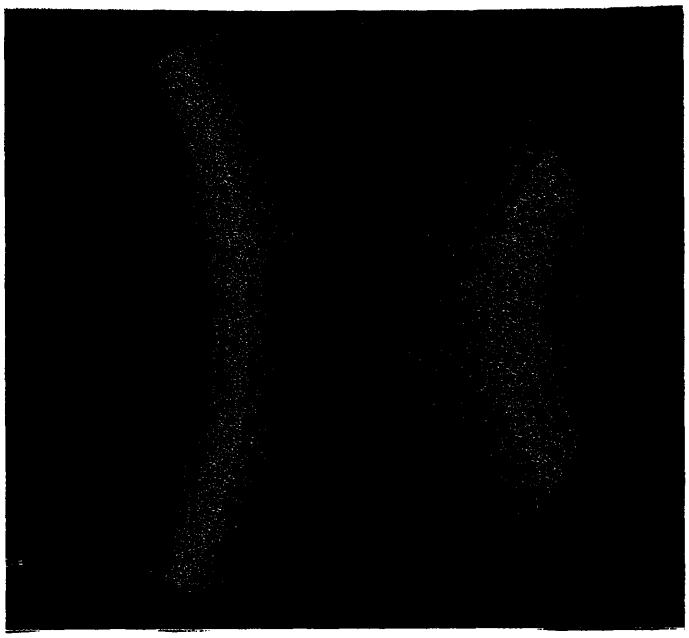

Figure 10.5.6 A: SURFACE contour plot of perturbation of four 60 pound spikes.

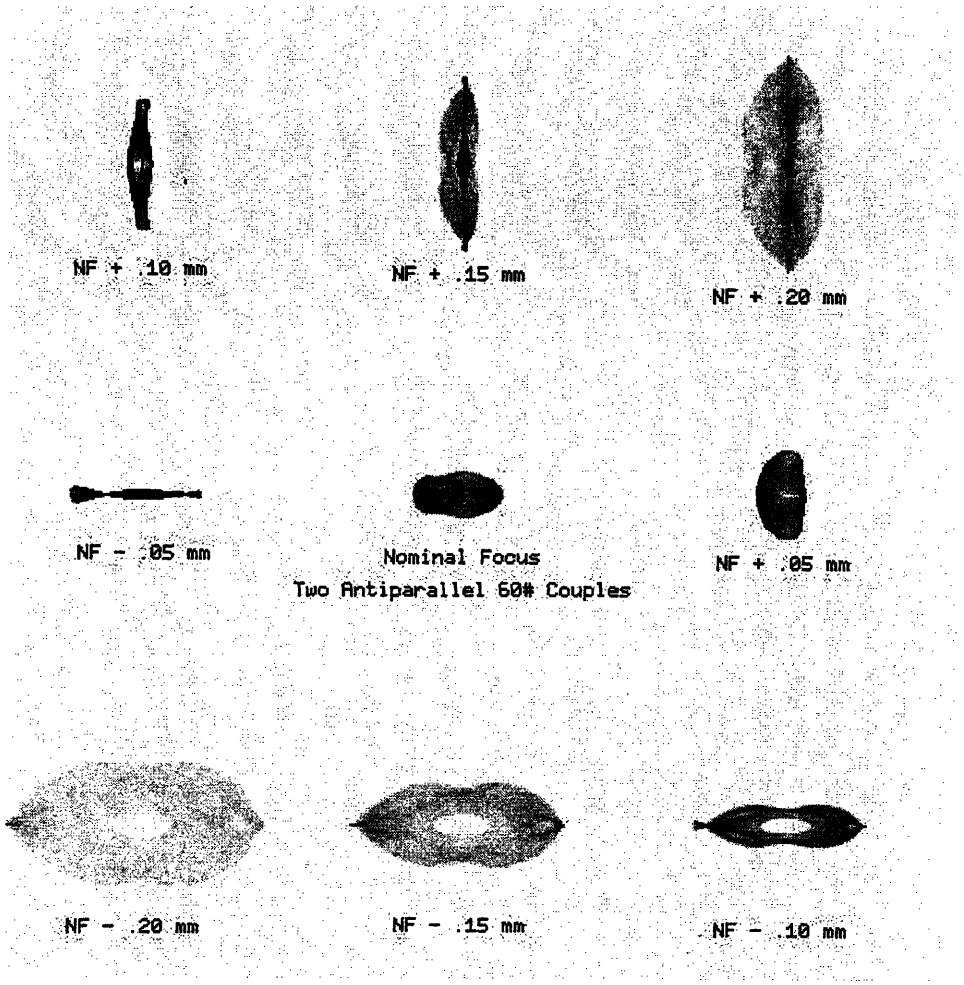

Figure 10.5.6 B: Spot diagrams from perturbation of four 60 pound spikes.

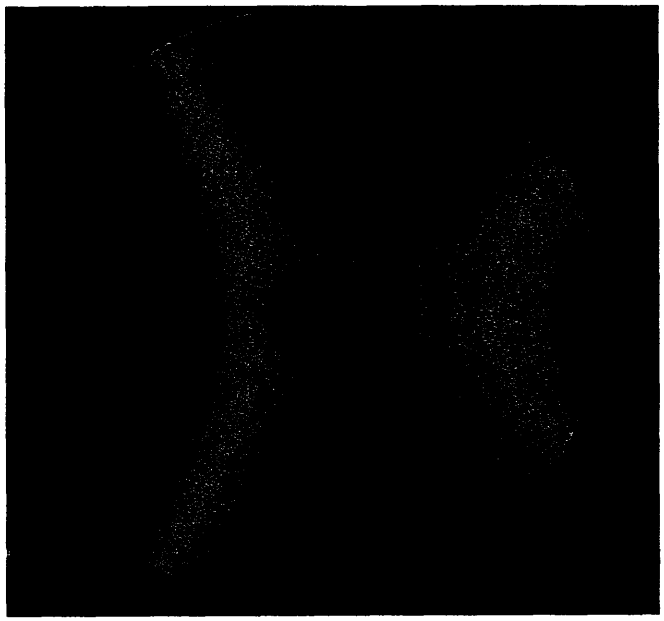

Figure 10.5.7 A: SURFACE contour plot, perturbations of four 100 pound spikes.

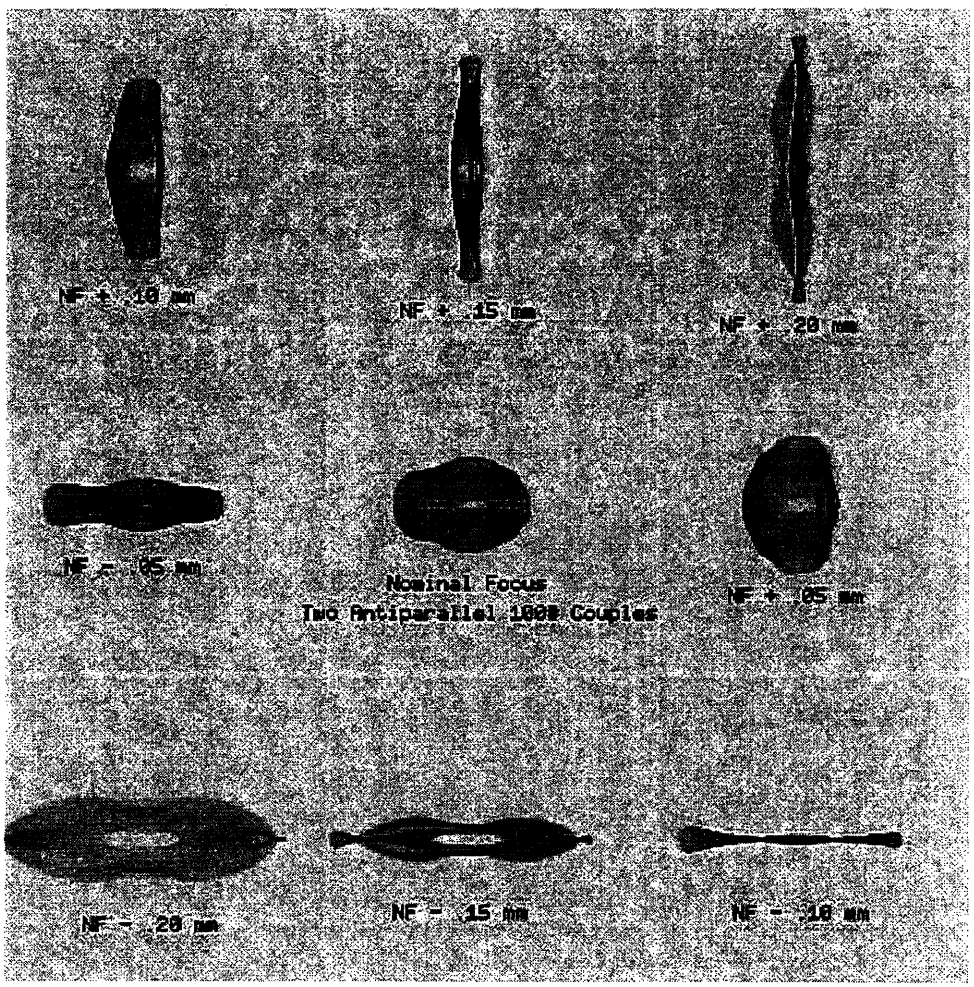

Figure 10.5.7 B: Spot diagrams from perturbation of four 100 pound spikes.

Case: 4-20 lb. Spikes	RMS	50% Energy	100% Energy
Nominal - .20 mm	1.78	1.75	2.70
Nominal - .15 mm	1.41	1.37	2.15
Nominal - .10 mm	1.05	0.99	1.70
Nominal - .05 mm	0.69	0.63	1.15
Nominal Focus	0.36	0.33	0.58
Nominal + .05 mm	0.26	0.19	0.525
Nominal + .10 mm	0.52	0.43	1.105
Nominal + .15 mm	0.87	0.79	1.555
Nominal + .20 mm	1.23	1.16	2.05

Case: 4-60 lb. Spikes	RMS	50% Energy	100% Energy
Nominal - .20 mm	1.81	1.72.	3.05
Nominal - .15 mm	1.46	1.34	2.50
Nominal - .10 mm	1.11	1.00	2.00
Nominal - .05 mm	0.78	0.69	1.75
Nominal Focus	0.52	0.47	1.10
Nominal + .05 mm	0.45	0.38	0.79
Nominal + .10 mm	0.64	0.51	1.35
Nominal + .15 mm	0.95	0.79	1.85
Nominal + .20 mm	1.29	1.14	2.35

Case: 4-100 lb. Spikes	RMS	50% Energy	100% Energy
Nominal - .20 mm	2.05	1.81	3.40
Nominal - .15 mm	1.75	1.54	3.35
Nominal - .10 mm	1.47	1.29	2.80
Nominal - .05 mm	1.25	1.12	2.40
Nominal Focus	1.10	1.07	2.05
Nominal + .05 mm	1.07	1.03	1.675
Nominal + .10 mm	1.17	1.00	2.15
Nominal + .15 mm	1.36	1.14	2.70
Nominal + .20 mm	1.62	1.36	3.20

Table 10.6.2 A, B & C: Spot data for two anti-parallel couples, in arc seconds.

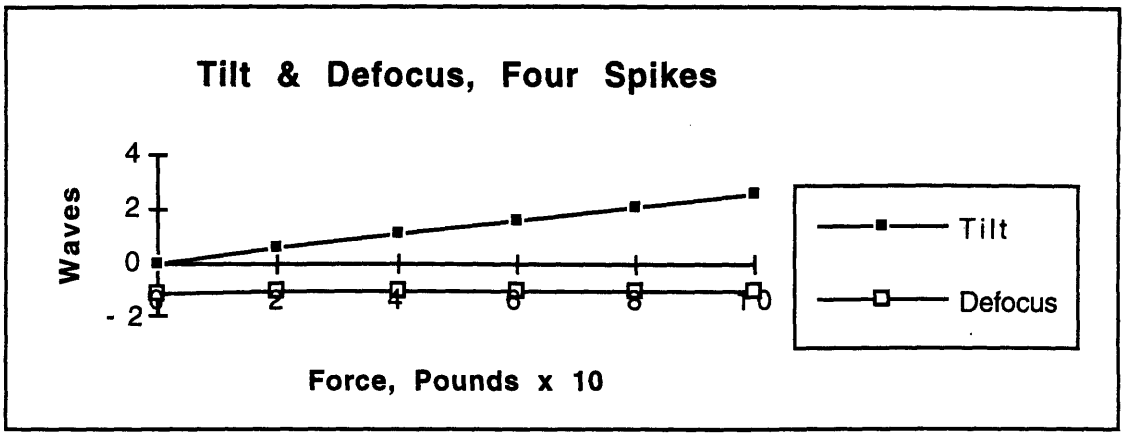

Chart 10.5.4: Tilt and Defocus at the nominal focal point as functions of force.

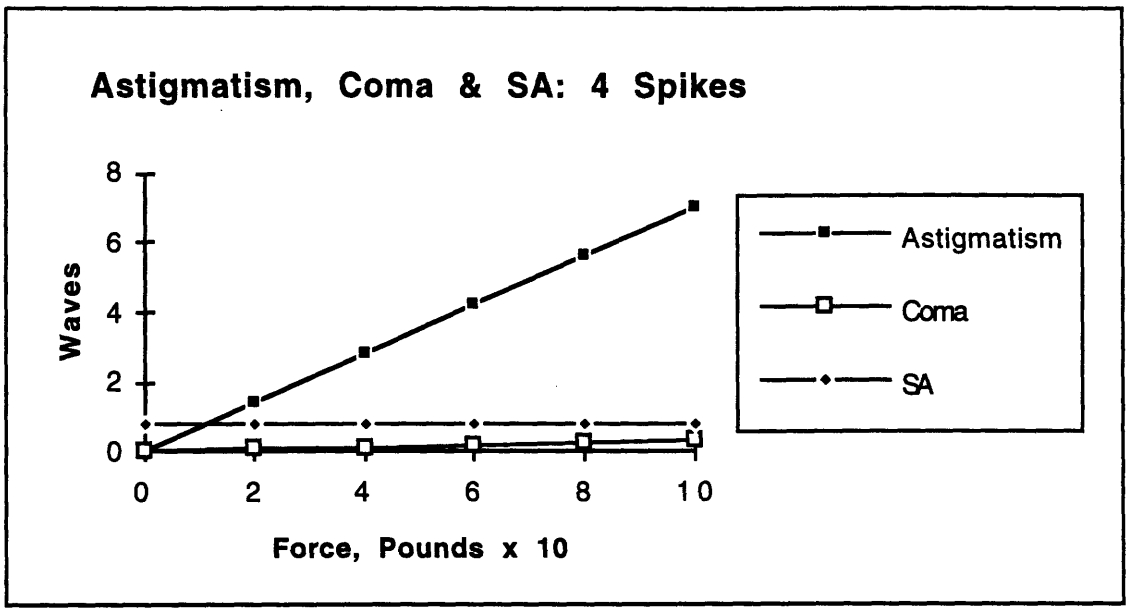

Chart 10.5.5: Astigmatism, Coma and Spherical Aberration at the nominal focal point as functions of force. Note the astigmatic dominance

Case: 4 Spikes	Tilt (λ)	Defocus	Astigmatism	Coma (λ)	SA (λ)
Nominal	0	-1.103	0	0	.776
Spike 20 lbs.	.524	-1.099	1.415	.068	.775
Spike 40 lbs.	1.048	-1.095	2.828	.135	.773
Spike 60 lbs.	1.574	-1.092	4.250	.203	.772
Spike 80 lbs.	2.095	-1.088	5.656	.270	.770
Spike 100 lbs.	2.622	-1.085	7.077	.338	.768

Table 10.5.3: 3rd Order aberrations at nominal focal point, in wavelengths.

Actual vs. Nominal Focus

Table 10.5.4 (below) shows image RMS and 50% encircled energy radius measured in arc seconds as functions of the amount of perturbing force that is applied to the mirror. Chart 10.5.6 presents the encircled energy data for the actual focus in graphic form. The region of actual focus occurs between .04 mm and .05 mm beyond the nominal focus.

Case: Actual vs. Nominal Focus	RMS (Arc Seconds)	50% Energy (Arc Seconds)
Nominal	0.11 / 0.30	0.09 / 0.28
Four 20 lb. spikes	0.24 / 0.36	0.21 / 0.33
Four 40 lb. spikes	0.44 / 0.52	0.40 / 0.47
Four 60 lb. spikes	0.65 / 0.70	0.60 / 0.66
Four 80 lb. spikes	0.86 / 0.90	0.81 / 0.85
Four 100 lb. spikes	1.07 / 1.10	1.03 / 1.07

Table 10.5.4: RMS & encircled energy as functions of applied force at the actual/nominal focus for two simultaneous point load perturbations.

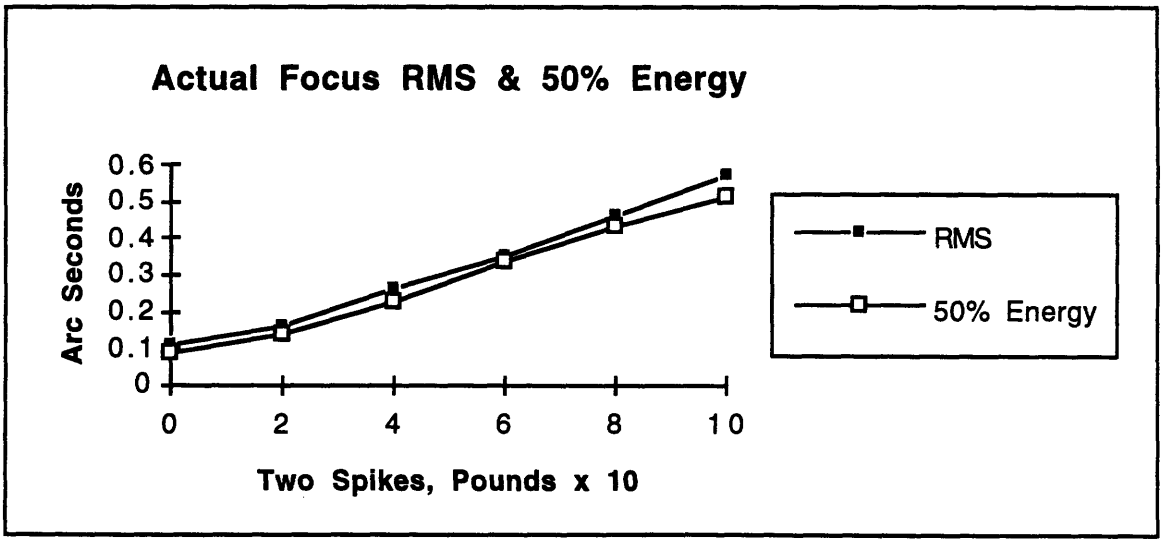

Chart 10.5.6: Encircled energy RMS and 50 % encircled energy radius calculated at the reflected wavefront's actual focus for the series of spot diagrams generated in the pairing of two point loads.

Chapter 11

Active Optics for the MDM/Hiltner 2.4 Meter Mirror

Active optics gives the astronomer the capability to optimize optical image quality by actively managing the telescope mirror's surface. This chapter describes an active optics design for the MDM/Hiltner 2.4 meter primary mirror, and presents the numerical results achieved when using the active optics design to correct mirror deformations induced by the variable loading cases addressed in Chapter 10.

The unique aspect of this project is that it seeks to back-fit active optics to an older, rigid mirror, a mirror which is composed of a relatively dense and stiff homogeneous glass-composite material. The original MDM/Hiltner mirror design philosophy built a mirror that resists gravity-induced deformation by virtue of its own stiffness. This chapter's design philosophy applies a set of actively controlled actuators to the mirror's back surface in order to minimize any gravity induced deformities and thereby recover the mirror's optimal optical performance.

11.1 Active Optics System Theory

The proposed active optics system for the MDM/Hiltner 2.4 meter primary mirror is a set of twelve air bag actuators placed across the back surface of the mirror. These actuators are controlled with information obtained from finite element analysis, a Zernike polynomial optical analysis, and a least squares optimization code. The least squares optimization generates an information set of actuator loads that acts to minimize mirror surface distortions as measured by the Zernike polynomial coefficients.

The first step in setting up the system is to conduct a finite element analysis of the primary mirror and its support structure. This generates two sets of information. For the first information set, the FE analysis calculates the mirror and the mirror support structure's response to gravity. For the second set, the FE analysis calculates the mirror's response to unit force loads as applied by each of the twelve actuators.

The FE information describing both mirror response to gravity and to unit force loads is fitted to Zernike polynomials. The coefficients of the first 36 Zernike terms are calculated for each case and assembled into matrix vectors.

The vectors of Zernike coefficients for the twelve actuator unit loads represent orthogonal displacement basis functions. The optimization code OPTICSMIN superposes these basis functions with the data from the aberrated mirror and runs a least-squares optimization. The optimization calculates the amount of each basis function that is needed to cancel out the mirror's aberrations.

If the desired goal is a diffraction limited image, then the active optics system is given a target of all zero Zernike coefficients. (Perfection in the world of Zernike polynomials means all zero coefficients.) The least squares code then acts to find the exact combination and magnitude of orthogonal displacement modes that, when added to the aberrated mode, yields the desired result.

The wavefront, as represented by Zernike polynomials , is of the form

$$w = \sum_{i=1}^{36} C_i \, Z_i(r, \theta) \tag{11.1}$$

where the C_i's are the Zernike coefficients. The aberrated wavefront that results from a gravity induced deformation of the mirror surface is represented as a Zernike series,

$$w_{aberrated} = \sum_{i=1}^{36} C_i^{aberrated} \, Z_i(r, \theta). \tag{11.2}$$

The goal or "target" wavefront is

$$w_{target} = \sum_{i=1}^{36} C_i^{target} \, Z_i(r, \theta). \tag{11.3}$$

The method superposes the orthogonal basis modes (created with unit actuator loads) with the aberrated wavefront in the least squares optimization code to determine the magnitude of each orthogonal basis modes needed to achieve the desired wavefront. The mode magnitudes are identified by the variable a_i, and the orthogonal basis modes are represented by the $w^{[j]}$'s. The superposition, called the "optimizing" mode, is described by

$$w_{opt} = a_1 w^{[1]} + a_2 w^{[2]} + ... + a_n w^{[n]} + w_{aberrated}. \tag{11.4}$$

The next step is to find the coefficients a_i. This is done by minimizing the difference between the target wavefront and the optimizing mode (the superposition of orthogonal basis modes and the aberrated wavefront):

$$\left[w_{target} - w_{opt}\right]^2 = Minimum \tag{11.5}$$

$$\Rightarrow \frac{d}{da_j}\left[w_{target} - w_{opt}\right]^2 = 0. \tag{11.6}$$

Since W_{target} is not a function of $a_{j,,}$ equation (11-6), when modified with a weighting function R, becomes in matrix form

$$\frac{d}{da_j}\left[-2\mathbf{w}_{tgt}^T\mathbf{R}\mathbf{R}^T\mathbf{w}_{opt}+\mathbf{w}_{opt}^T\mathbf{R}\mathbf{R}^T\mathbf{w}_{opt}\right]=0. \qquad (11\text{-}7)$$

Recall that

$$W_{opt}=\sum_{j=1}^{n}a_jw_j+\sum_{i=1}^{36}C_i^{aberrated}Z_i(r,\theta), \quad \text{where} \quad w_j=\sum_{i}^{36}C_i^{[j]}Z_i(r,\theta),$$

so that the differentiation in equation (11-7) becomes

$$-2\,\mathbf{C}_{tgt}^T\mathbf{Z}_{tgt}^T\mathbf{R}\mathbf{R}^T\mathbf{Z}_{opt}\mathbf{C}_{opt}+\mathbf{C}_{opt}^T\mathbf{Z}_{opt}^T\mathbf{R}\mathbf{R}^T\mathbf{Z}_{opt}\mathbf{C}_{opt}\mathbf{a}=0. \qquad (11\text{-}8)$$

By letting

$$\mathbf{C}_{opt}^T\mathbf{Z}_{opt}^T\mathbf{R}\mathbf{R}^T\mathbf{Z}_{opt}\mathbf{C}_{opt}=\mathbf{A} \quad \text{and} \quad \mathbf{C}_{tgt}^T\mathbf{Z}_{tgt}^T\mathbf{R}\mathbf{R}^T\mathbf{Z}_{opt}\mathbf{C}_{opt}=\mathbf{B},$$

the desired vector quantity can be calculated:

$$\mathbf{a}=[\mathbf{A}]^{-1}[\mathbf{B}]^T. \qquad (11\text{-}9)$$

The vector **a** can be viewed as the magnitude of actuator input required to obtain the target wavefront. In actuality, **a** is a series of coefficients that prescribe how much of each orthogonal actuator basis vector is required to make their superposition with the aberrated wavefront equal to zero.

To be complete, the active optics system (and hence the optimization code) must be designed so that the resulting post-control static equilibrium avoids image shifts due to mirror tilt. This is accomplished by imposing a constraint on the least squares optimization that specifies the sum of the forces applied to the mirror by the active control system.

A text of the least squares optimization code can be found in the thesis appendix.

11.2 Description of the Active Optics System

The active optics system consists of the original finite element model of the mirror and its mercury bladder radial support system modified with a new axial support system. The new axial support system is designed to be completely active. This means that the mirror's weight is almost entirely supported by the active system when the mirror is oriented at or near a vertical position.

The new design uses twelve neoprene air bags configured in two concentric rings of six bags. The three hard points are retained. The least squares optimization code described in Section 11.1 determines axial support pressure loadings. The twelve airbags apply force to the back of the mirror in the axial direction, and can only push against the mirror. (While the optimization code has the capability to generate commands for negative force applications, the air bags can only push.) Applied force is adjusted by changing the individual bag pressures. Commands for pressure changes are generated by an air bag pressure controller. It is assumed that a variation of the MDM/Hiltner telescope's present air bag controller that incorporates this thesis's finite element data and least squares optimization will be sufficient to control air bag pressures.

The use and location of the three axial support hard points of the original MDM/Hiltner design remain unchanged. The introduction of active axial support, however, facilitates the possibility of varying the reaction forces applied to these hard points.

Lateral support is provided by the original mercury bladder system. Because the radial support forces act through the center of mass of the mirror, no overturning moments are created by the radial support system and no active interface with the axial support control system is required.

Figure 11.1 on the next page presents the relative size and location of the twelve air bag actuators. The bags are distributed around the mirror in two concentric circles, with each circle containing six air bags.

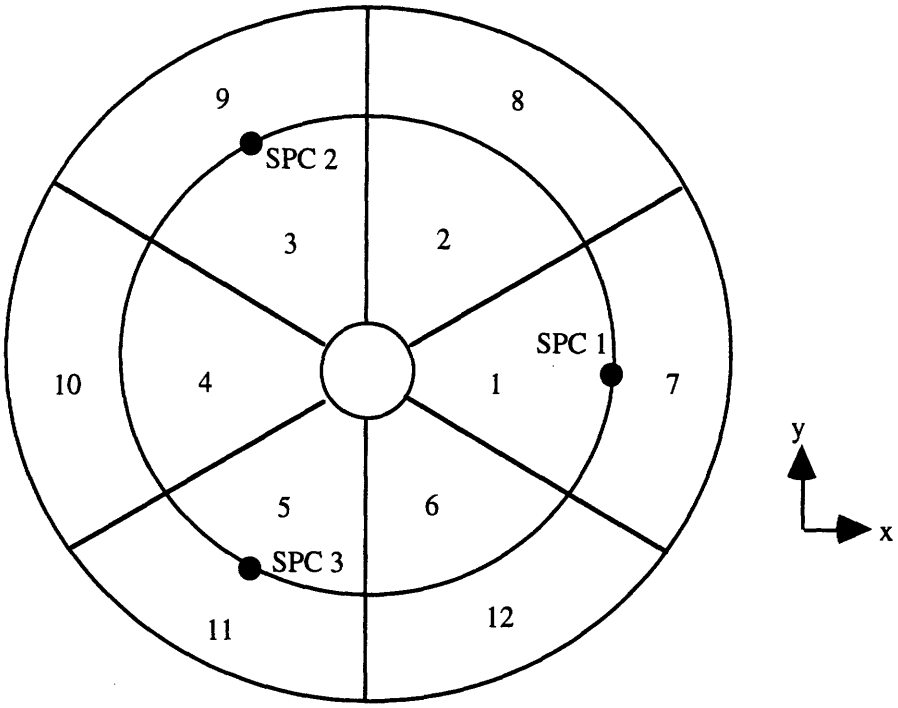

Figure 11.1: Vertical view of the two concentric rings of air bag actuators showing SPC locations and Bag #1 through Bag #12.

The purpose of the air bags is to deform the mirror in such a way as to cancel out surface deflections caused by gravity loading. The control information that determines the amount of actuator force required to achieve this counter-bending is obtained by running finite element and optical analysis of unit load applications. Each air bag is individually turned on while the other bags and gravity are turned off. The finite element analysis then calculates the mirror's response to unit force loads, and the optics analysis calculates the set of Zernike polynomial coefficients that best fit the unit load wavefront.

Since unit load inputs are independent of gravity, the Zernike coefficients that are generated can be used to correct gravity deformations at any mirror orientation. Figures 11.2.1, 11.2.2, 11.2.3 and 11.2.4 on the next four pages show the NASTRAN results of turning on individual bags while turning other bags and gravity off.

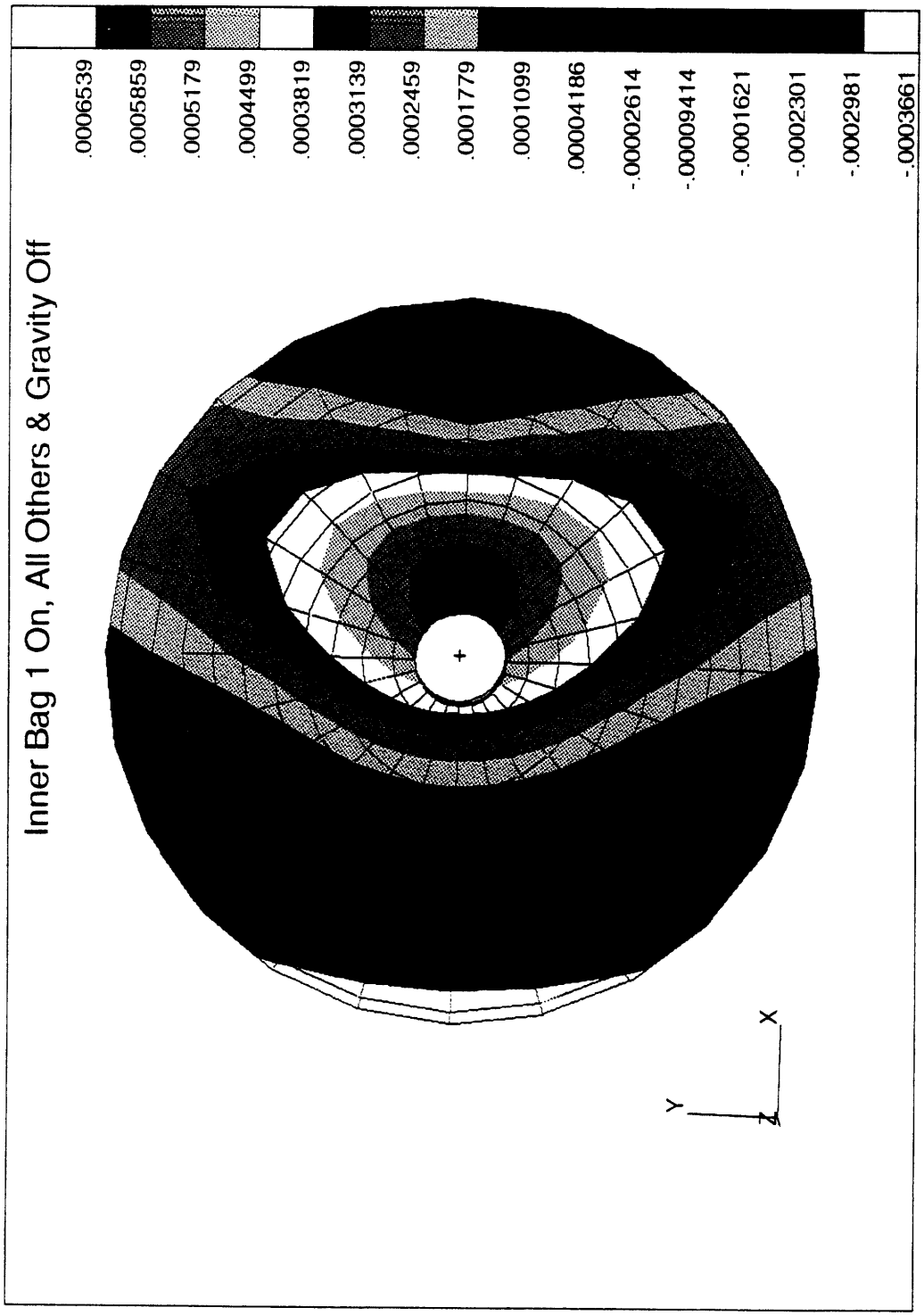
Inner Bag 1 On, All Others & Gravity Off
.0006539
.0005859
.0005179
.0004499
.0003819
.0003139
.0002459
.0001779
.0001099
.00004186
-.00002614
-.00009414
-.0001621
-.0002301
-.0002981
-.0003661
Y
X
Z

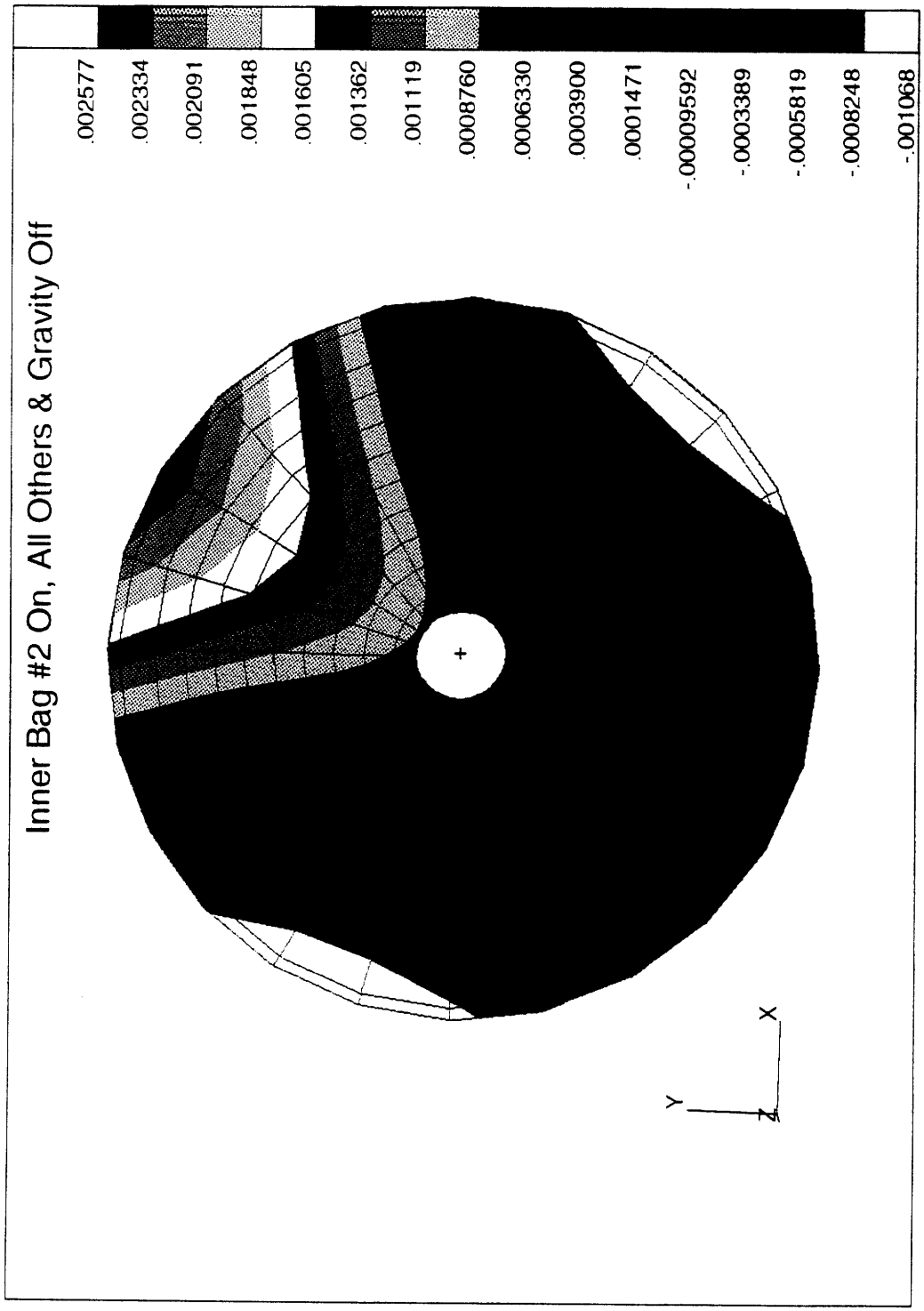
Inner Bag #2 On, All Others & Gravity Off
.002577
.002334
.002091
.001848
.001605
.001362
.001119
.0008760
.0006330
.0003900
.0001471
-.00009592
-.0003389
-.0005819
-.0008248
-.001068
Y
Z
X

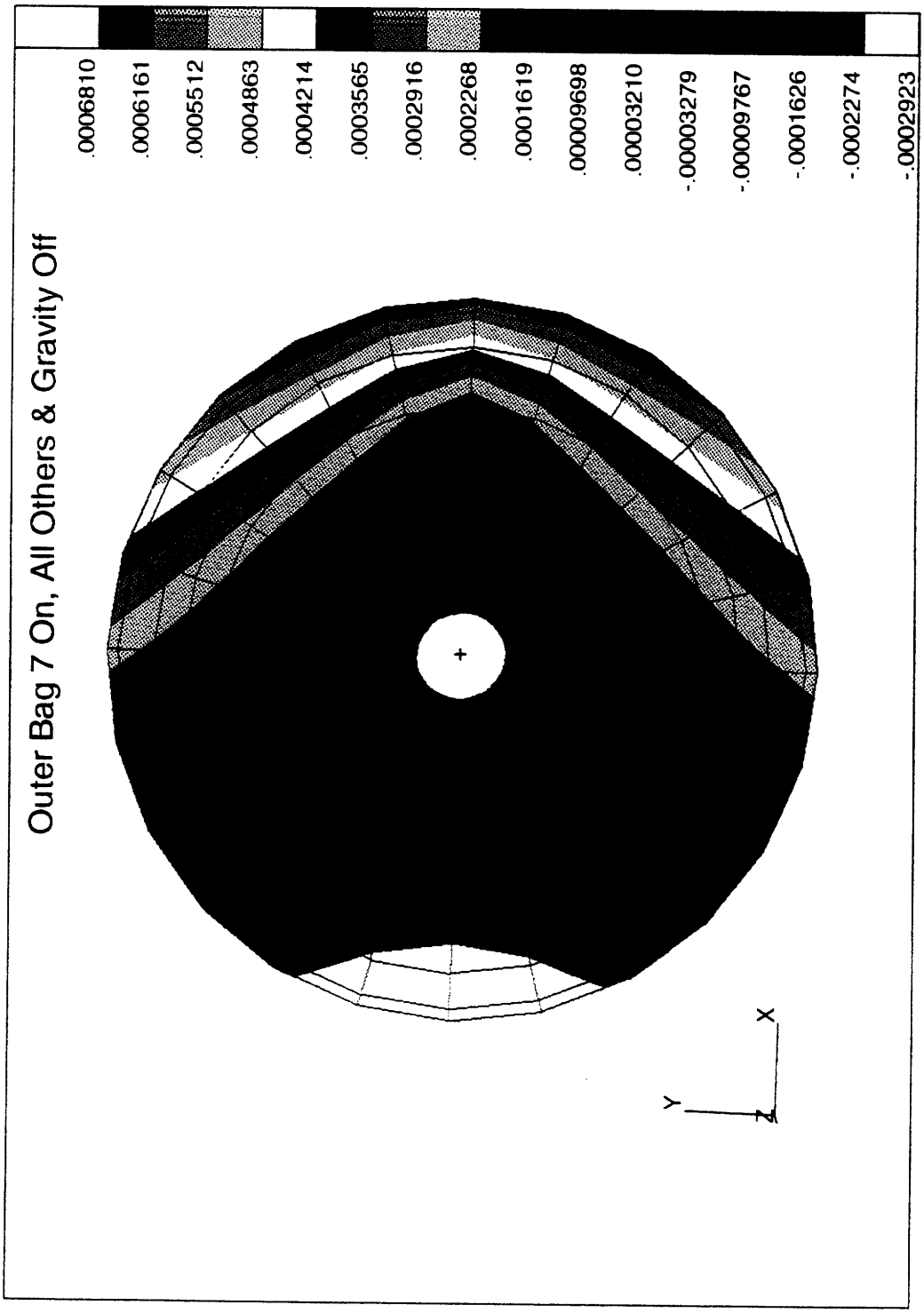
Outer Bag 7 On, All Others & Gravity Off
.0006810
.0006161
.0005512
.0004863
.0004214
.0003565
.0002916
.0002268
.0001619
.00009698
.00003210
-.00003279
-.00009767
-.0001626
-.0002274
-.0002923
Y
X
Z

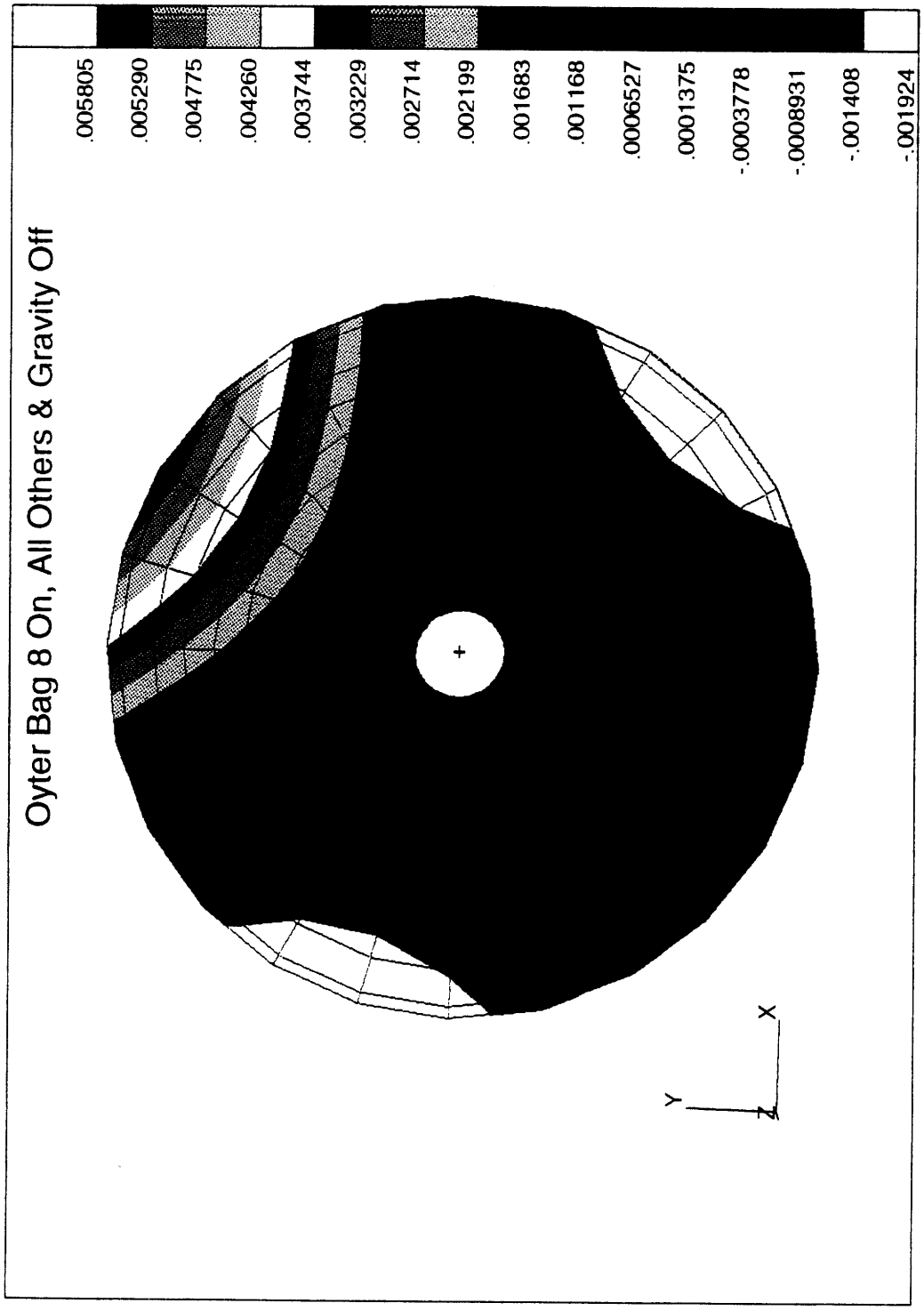
Oyter Bag 8 On, All Others & Gravity Off
.005805
.005290
.004775
.004260
.003744
.003229
.002714
.002199
.001683
.001168
.0006527
.0001375
-.0003778
-.0008931
-.001408
-.001924
Y
X

11.3 Explanation of Design Configuration

The most simple and least expensive approach to installing an active optics system in the MDM/Hiltner telescope is to retain the basics of the existing design and improve the three air bag component of the primary axial support system. It would be uneconomical to redesign the entire interface between the mirror and the mirror cell. Therefore, the decision was taken to keep the three hard points as integral parts of the axial support system.

The reasons for selecting this design configuration are rooted in the decision to keep the three hard points as integral parts of the axial support system, and from the results of Chapter 10's finite element analysis. That analysis shows that under nominal support and load conditions the interior of the mirror bulges up while the exterior sags. This deflection mode is attributed to the combined action of the mirror's non-uniform mass distribution being pushed by a uniform axial supporting pressure. The placement of the hard points at the mirror's radial center of mass serves to add a triangulation effect to the mirror's deflection mode.

To compensate for the natural tendency of the mirror to bulge in the middle and sag along the outside, it was decided to place concentric rings of actuators around the mirror's back surface inside and outside the natural point of reference created by the hard points.

Hard point location also determined the distribution of the air bags within the concentric rings. Section 10.2 presents the finite element analysis of the mirror with all air bags turned off, and the mirror resting on the three hard points. The results show that ridge lines form along the radials that define hard point location. Experimentation showed that centering the actuators along the ridge lines facilitates the optimization and achieves good results with a minimal number of actuators.

The final design arranges the airbags so that six of the bags are centered on hard point radials. This design configuration minimizes the number of actuators (and hence, costs) and facilitates the optimization used in the system's active control.

11.4 Nominal Mirror Active Control

This section applies the twelve air bag active optics system to the finite element model of the MDM/Hiltner telescope. The procedure fits the first thirty six Zernike polynomial terms to the finite element model of the mirror surface. The Zernike coefficients are then supplied to the least squares optimization code (OPTICSMIN, Ref.). OPTICSMIN calculates air bag pressure changes required to bend the mirror in such a way as to minimize the Zernike polynomial coefficients. The code is constrained to recommend pressure changes which maintain 30 pound z-axis reaction loads on each hard point.

Active control results show that it is theoretically possible to correct gravity induced deformations and create a diffraction limited image with the MDM/Hiltner primary mirror.

11.4.1 Active Control of Perturbed Mirror

The nominal case orients the mirror in the pure vertical. All the air bag axial supports are turned on, and each of the three hard points supports a 30 pound z-axis reaction load. Analysis (please see Section 10.1) shows a bulging in the mirror's middle and sagging along the outer radius as a result of the mirror's non-uniform mass distribution reacting to the application of a uniform axial air bag supporting force. Hard point reaction loads contribute a triangulation effect that exaggerates the optical distortion.

Figure 11.4.1 on the next page shows a PCFRINGE contour plot of the uncorrected mirror surface's z-axis deflections. Figure 11.4.2 is a graphic of OPTICSMIN pressure changes. OPTICSMIN recommends reductions in interior bag pressures and increases in outer bag pressures to correct the bulging of the interior surface and the sagging of the outer surface. The exterior air bags show an alternating pattern. Airbags that underlie SPC radials show a smaller positive change than the bags that underlie the area between SPC radials. This compensates for the triangulation caused by the hard points. The interior bags show an alternating pattern that offsets the exterior pattern.

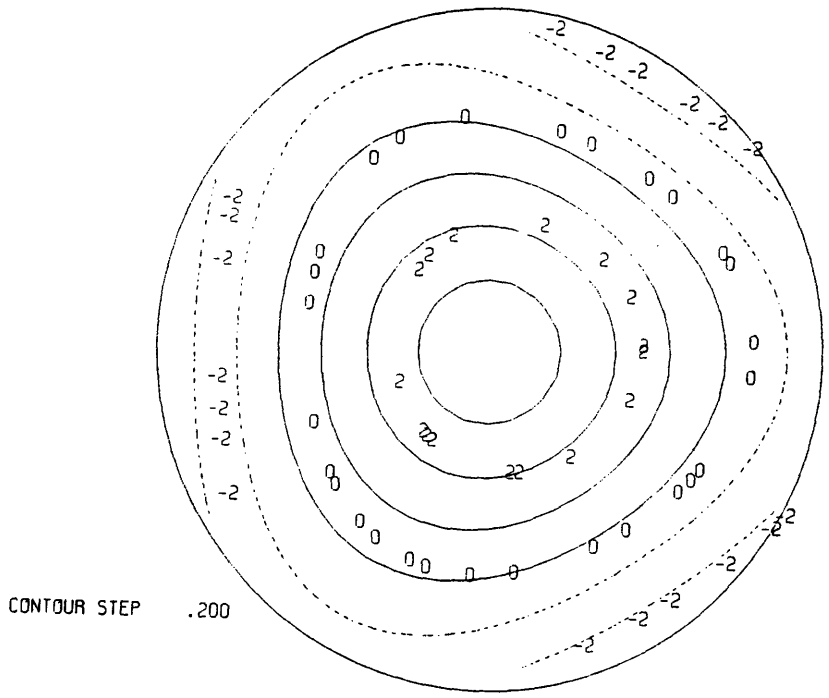

Figure 11.4.1: PCFRINGE contour plot showing z-axis deflections for the uncorrected mirror surface.

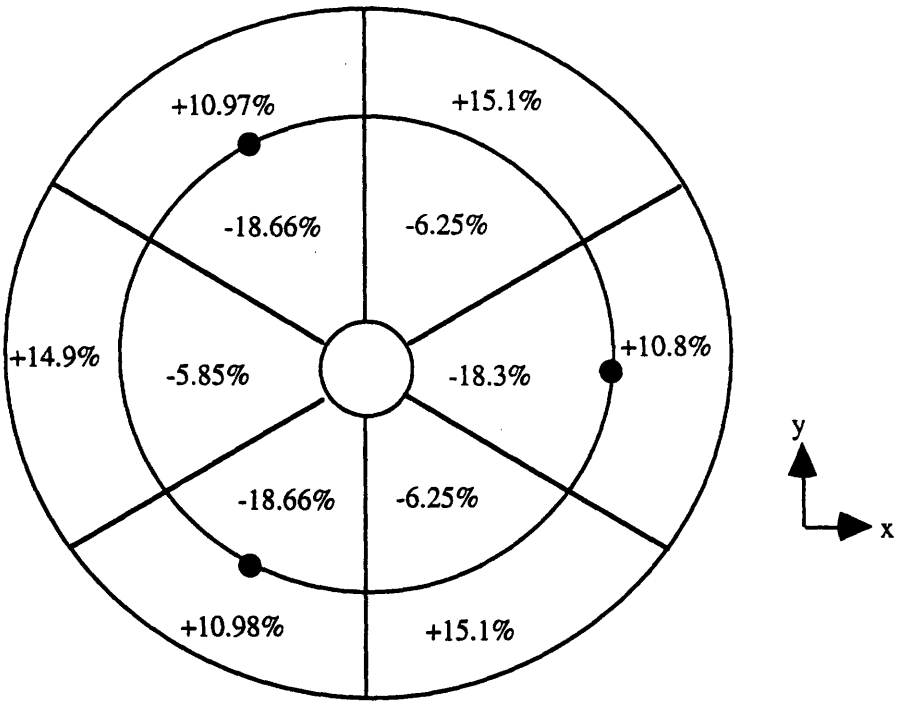

Figure 11.4.2: Changes in axial air bag pressures called for by OPTICSMIN in order to minimize the Zernike coefficients in the reflected wavefront.

Structural Results of Active Control

The active control results are striking. Mirror surface RMS is reduced from .385 μm to .010 μm. Peak to Valley is reduced from 1.572 μm to .032 μm. The PCFRINGE contour plot of Figure 11.4.3 below shows that the largest deflection in the corrected mirror surface is less than .2 λ. .

Figure 11.4.4 on the next page shows the NASTRAN color contour plot of the optimized surface. The scale of the NASTRAN color contour plot, shown on the right-hand side of Figure 11.4.4, is in millimeters. The NASTRAN plot shows a distinctive set of contour shapes in the corrected mirror, but with very small deflections and contour steps. The greatest deflection is approximately .03 μm, or less than 5% of the wavelength of the incident light.

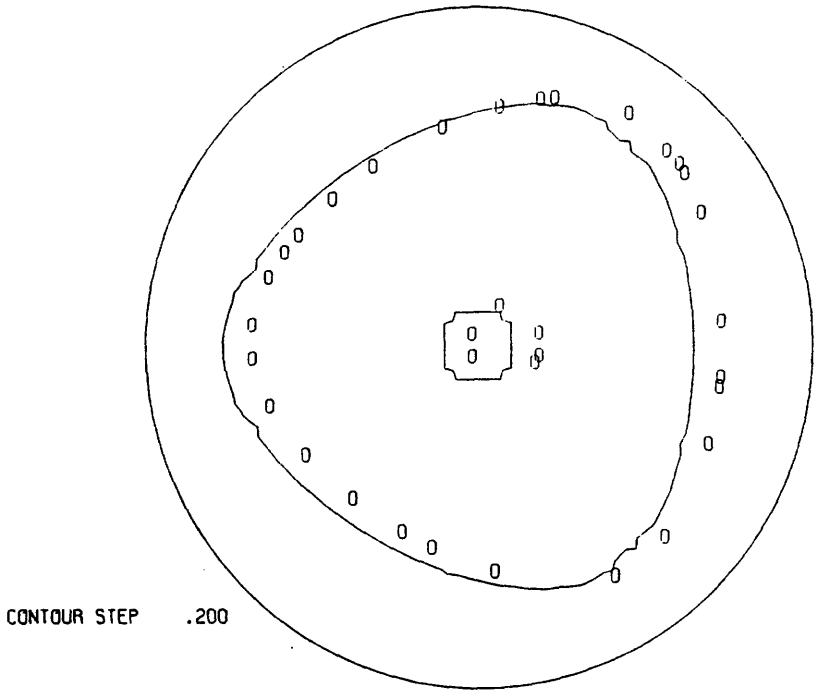

Figure 11.4.3: PCFRINGE z-axis contour plot of the mirror surface corrected with active control. Plot is scaled to show deflections in contour intervals of .2 λ.

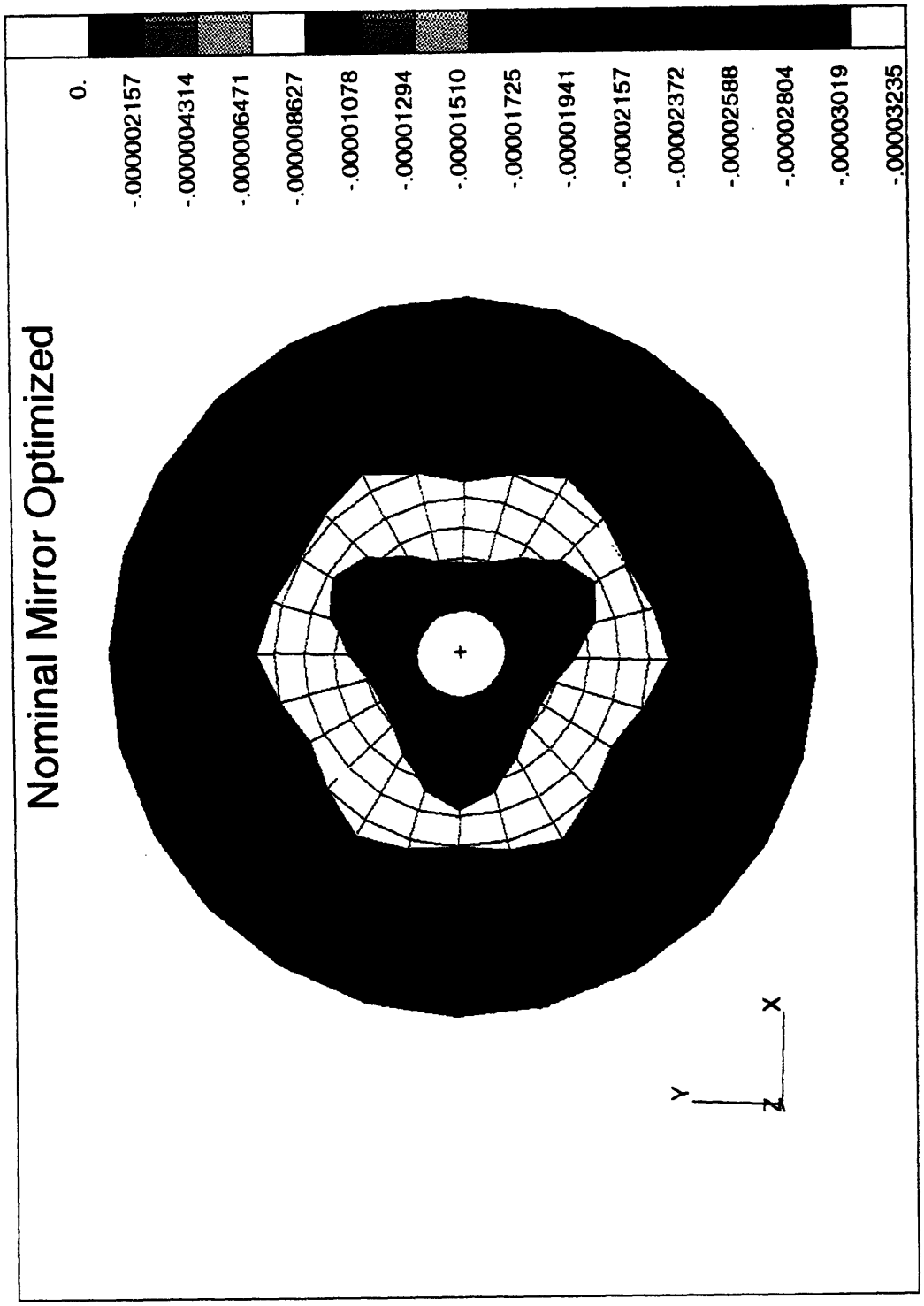

Figure 11.4.4: NASTRAN contour plot showing z-axis deflections for the corrected mirror surface.

Reaction Forces in the Corrected Mirror

Table 11.4.1 below compares SPC reaction forces before and after active control. The optimization maintains the desired 133 N z-axis reaction force at each hard point. The x- and y-direction forces produced at the SPC's show a reversal from compression to tension, as well as smaller magnitudes. X-direction SPC resistance now totals -52 N, as opposed to the +302 N resistance in the uncorrected mirror. Y-axis resistance is reduced from 262 N to -49 N.

Hard Point	X-Axis RF (N)	Y-Axis RF (N)	Z-Axis RF (N)
SPC 1	302 / -52	0 / 0	129 / 133
SPC 2	-151 / 26	262 / -49	129 / 133
SPC 3	-151 / 26	-262 / 49	129 / 133

Table 11.4.1: Reaction forces at SPC's 1, 2 & 3 before/after active control.

Surface Deflections in the Corrected Mirror

The optimization is checked by comparing surface deflections at sample points on the mirror surface.

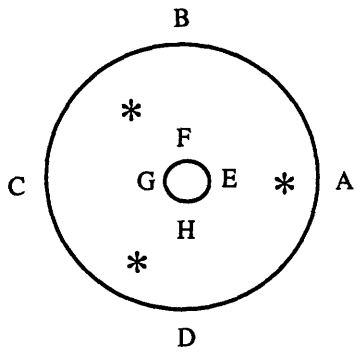

Figure 11.4.5: Sample locations for deflection comparison between the uncorrected and corrected mirror. The *'s are locations of the SPC's.

Sample Point	A	B	C	D	E	F	G	H
No Active	-.230	-.315	-.388	-.335	+.402	+.402	+.402	+.402
With Active	-.019	-.022	-.019	-.022	-.026	-.026	-.026	-.026

Table 11.4.2: Comparison of deflections of the mirror surface before and after active control optimization. All units are μm.

11.4.2 Optical Results

Figure 11.4.4 on the next page shows a series of 9 spot images taken at .05 mm intervals along the optical axis on either side of the nominal focus. These spot diagrams are calculated by a ray tracing code that is not subject to diffraction limits. The radius of 100% encircled energy for the spot image at the optimized nominal focus is .03 μm. The diffraction limit of a telescope mirror that has a focal length of 4.82 meters and a diameter of 2.4 meters is

$$d.l. = 1.22\frac{f\lambda}{D} = .067 \text{ arc seconds}$$

where f is the focal length, D is the mirror's diameter and λ is the wavelength of the incident light (λ = .633 mm). This result shows that the optimized mirror is diffraction limited.

Table 11.4.3 below presents RMS and encircled energy data for the series of 9 spot diagrams in Figure 11.4.6. The table also includes data for the uncorrected mirror, so as to provide the reader with a basis for evaluating the magnitude of improvement gained by the active optics system.

Nominal Focus	RMS	50% Encircled Energy	100% Encircled Energy
NF - .20 mm	1.76 / 1.48	1.76 / 1.45	2.45 / 2.10
NF - .15 mm	1.39 / 1.11	1.39 / 1.08	1.94 / 1.60
NF - .10 mm	1.02 / 0.74	1.02 / 0.71	1.41 / 1.10
NF - .05 mm	0.66 / 0.37	0.65 / 0.34	0.92 / 0.57
Nominal Focus	0.30 / 0.03	0.28 / 0.03	0.40 / 0.03
NF + .05 mm	0.15 / .038	0.10 / 0.36	0.29 / 0.57
NF + .10 mm	0.48 / 0.75	0.43 / 0.74	0.81 / 1.08
NF + .15 mm	0.84 / 1.12	0.79 / 1.11	1.38 / 1.56
NF + .20 mm	1.21 / 1.49	1.17 / 1.47	1.88 / 2.10

Table 11.4.3: Comparison of nominal mirror vs. the same mirror with the active optics system. All data is in arc seconds.

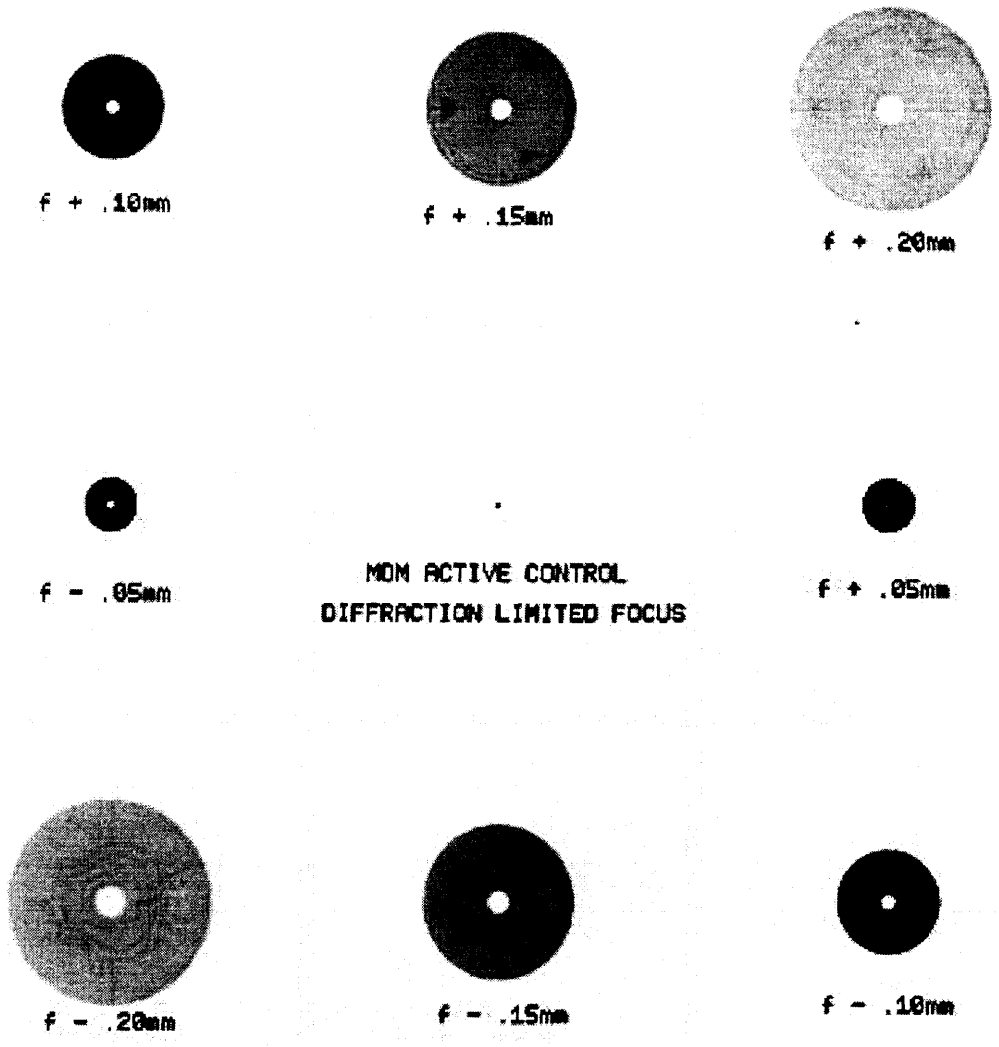

Figure 11.4.6: A series of 9 spot diagrams taken at .05 mm intervals on either side of the nominal focus of the active mirror. The spot diagram at the nominal focus is diffraction limited.

Third Order Aberrations

The following table presents third order aberrations exhibited by the mirror before and the application of after active control.

3rd Order Aberration	Before Active	After Active
Tilt	0.0	0.0
Defocus	-1.103	0.017
Astigmatism	0.0	0.0
Coma	0.0	0.0
Spherical Aberration	0.776	0.015

Table 11.4.5: Third order aberrations before and after active control. Data is given in wavelengths (λ = .633 μm).

Summary

The deformations allowed by the passive support system tend to displace the mirror's actual focus; the outer edge droops and the middle surface bulges upward. Chapter 10 shows that these deformations create defocus and spherical aberration in the reflected wavefront. Best focus for the passively supported mirror is at .04 mm beyond the nominal focus.

The active support system focuses perfectly at the nominal focus, eliminating both the defocus and spherical aberration errors. The symmetry in the spot diagram data for the active mirror demonstrates that the reflected wavefront propagates without distortion. This can be seen by comparing the width of the spot images at equal points before and after the nominal focus. Active control produces identical spot image width at .20 mm beyond nominal focus and at .20 mm before nominal focus.

11.5 Correcting Gravity and Point Load Perturbations With Active Control

The twelve air bag active optics system is used to correct perturbations caused by gravity and the application of a 20 pound point load. The point loads are applied to a node located at (r = 1.143 m, $\theta = \pi$, z = .082 m) that is part of the mercury belt radial support, as shown in Figure 11.5.1 and analyzed in Section 10.3. The load is appled in the negative z-direction. Numerical results show that it is theoretically possible for the twelve air bag active control system to correct the combined gravity and point load induced deformations and, in the 20 pound case, achieve a diffraction limited image.

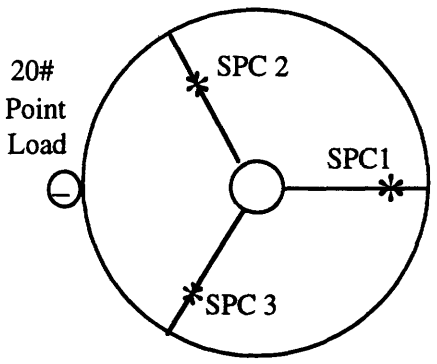

Figure 11.5.1: Vertical view of the location of the 20 and 100 pound point loads: (r = 1.143 m, $\theta = \pi$, z = .082 m).

11.5.1 Active Control of Perturbed Mirror

The 20 pound point load creates a small torque which induces a rotation of the mirror about the three hard points, pinching the middle of the mirror. This action amplifies the triangular surface distortion and general bulging in the middle of the mirror that is created by gravity induced deformation. The point load application also creates a non uniform distribution of reaction loads among the hard points.

The optimization is programmed to minimize the Zernike coefficients and to produce 129 N reaction forces on the hard points. Pressure changes recommended by OPTICSMIN are shown in Figure 11.5.2.

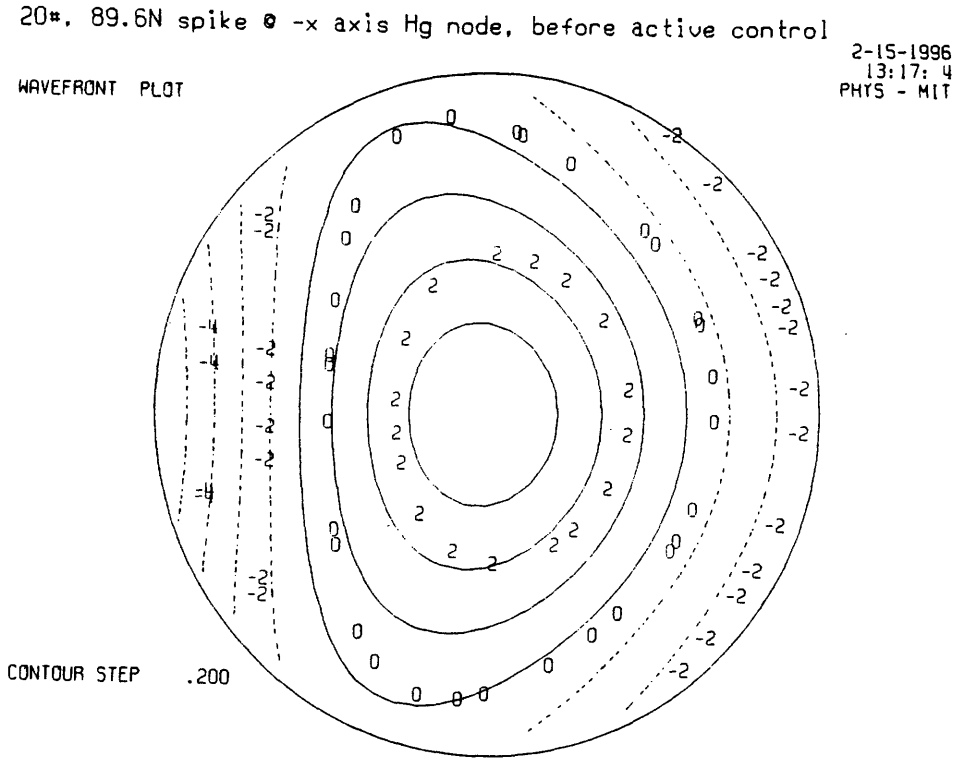

Figure 11.5.2: PCFRINGE z-axis contour plot of surface deflections for a 20 pound load applied to the outside wall of the mirror on the negative x-axis.

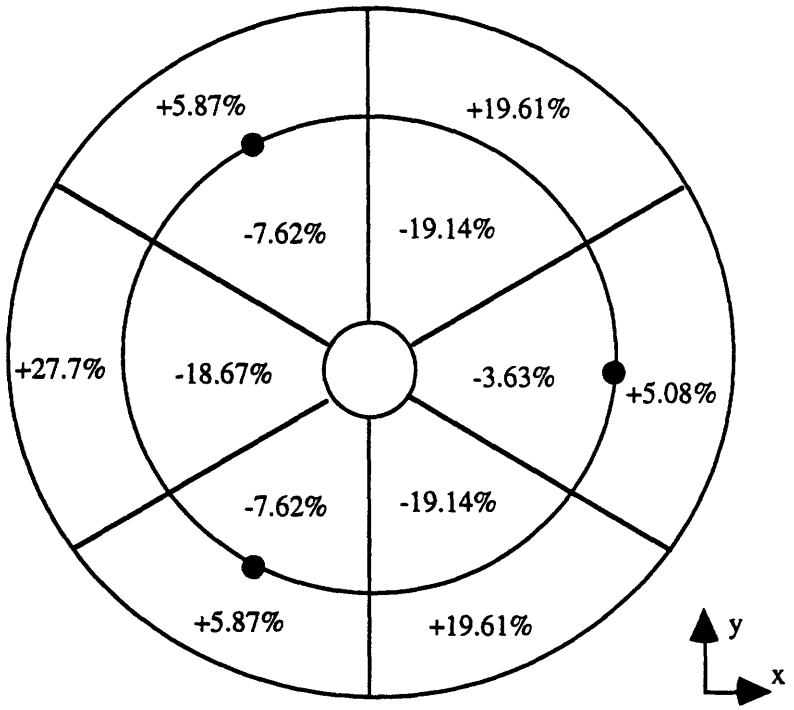

Figure 11.5.3: Pressure changes recommended by OPTICSMIN for the case of a single 20 pound point load perturbation.

The pattern and magnitude of pressure changes are very similar to those of the nominal case, meaning that the active control system is still primarily dealing with gravity induced deformations. The active optics system relieves pressure near the mirror's central hole, allowing the thinner part of the mirror to settle slightly. The largest pressure differential is applied to Bag 10, as Bag 10 is located directly under the point load.

Structural Results of Active Control

Active control achieves a significant improvement in RMS and P-V measures of mirror surface distortion for the 20 pound spike perturbation. These RMS and P-V values nearly match those obtained when optimizing the nominal mirror case. The perturbed mirror surface RMS is reduced from .486 μm to .012 μm. Peak to Valley is reduced from 2.602 μm to .071 μm.

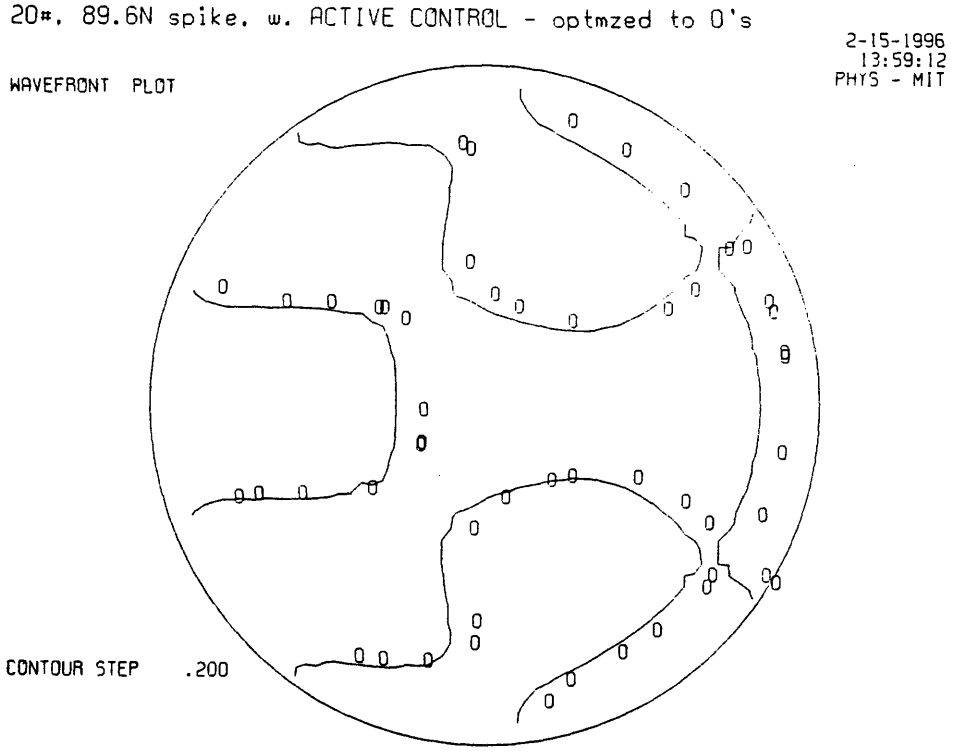

Figure 11.5.4: PCFRINGE z-axis contour plot of the mirror surface corrected with active control. Plot is scaled to show deflections in contour intervals of .2 λ.

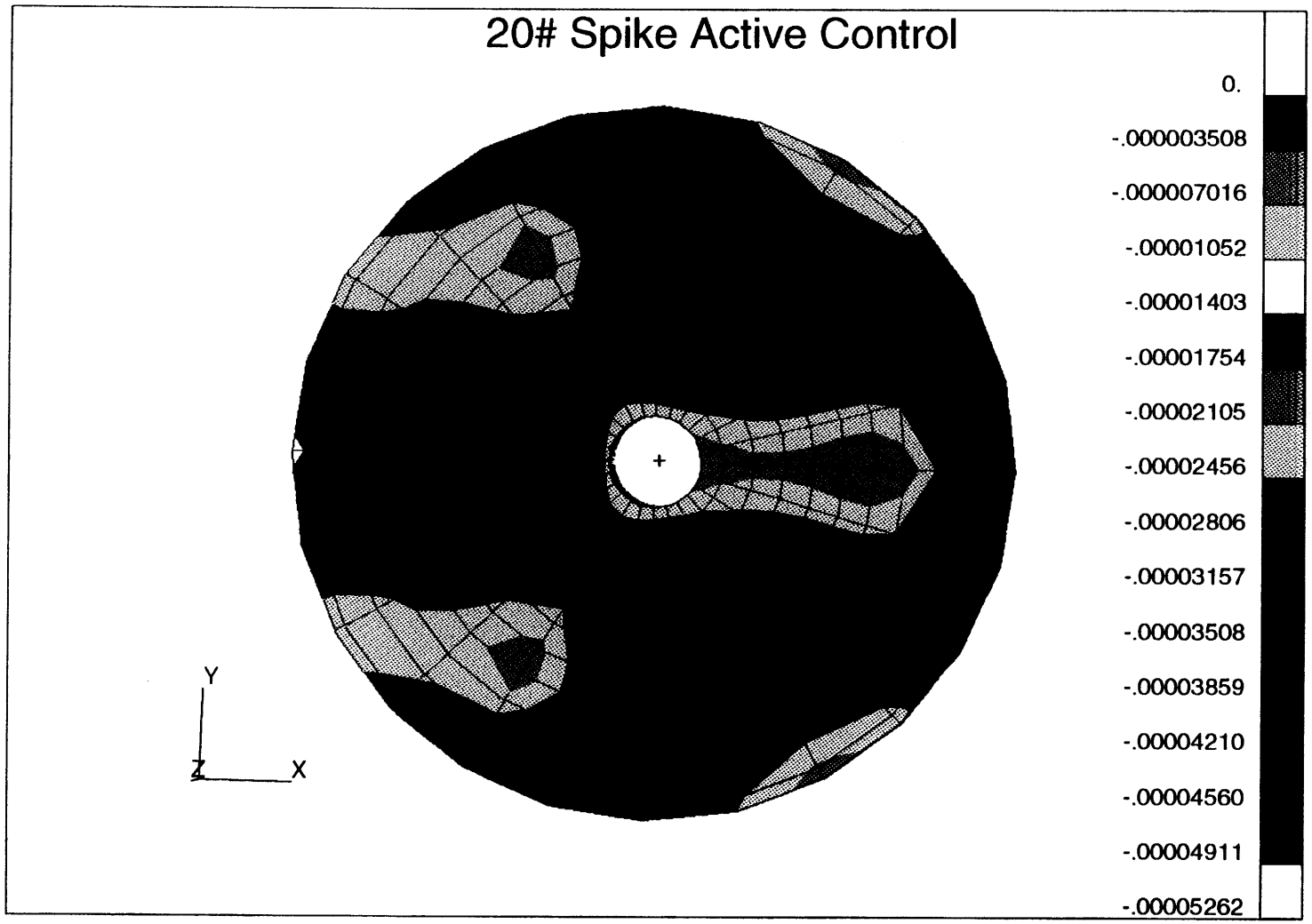

Figure 11.5.5: NASTRAN contour plot showing z-axis deflections for the corrected mirror surface.

Surface Deflections in the Corrected Mirror

The NASTRAN plot shows that the largest surface deflections occur immediately above the node where the point load is applied. The next most severe set of deflections occurs in the valleys between hard points. The surface areas above the hard points produce deflections of median magnitude. Active control adjusts the entire mirror surface downward - there is no point of zero deflection!

A comparison of z-axis deflections at certain points in the mirror before and after optimization demonstrates the overall improvement achieved by active control. Figure 11.5.6 shows the locations of the points selected, and Table 11.5.1 compares z-axis deflections. Point "C" is immediately above the point load application. Note the deflection magnitudes at Point "C" with and without active control.

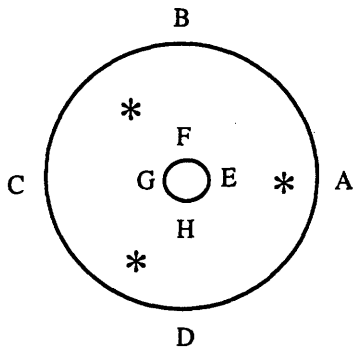

Figure 11.5.6: Sample points for comparing gravity and point load induced deflections with and without active control.
The *'s are the SPC's.

Sample Point	A	B/D	C	E	F/G/H	SPC 1	SPC 2	SPC 3
No Active	-.282	-.194	-.894	+.418	+.418	-.019	-.019	-.019
With Active	-.049	-.0351	-.053	-.021	-.024	-.021	-.021	-.021

Table 11.5.1: Deflections under the influence of gravity and a 20 pound point load, before and after active control. The last three columns show surface deflections above the hard points. All units are μm.

Reaction Forces in the Corrected Mirror

Table 11.5.2 below compares SPC reaction forces before and after active control. The optimization restores the desired z-axis reaction force loading at each hard point. Air bag pressure changes also relieve the x- and y-direction forces produced at the SPC's. X-direction SPC resistance changes from compression to tension, and is reduced from 387 N to -39 N. Y-axis also changes compression to tension, and the magnitude os reduced from 196 N to -34 N.

Hard Point	X-Axis RF (N)	Y-Axis RF (N)	Z-Axis RF (N)
SPC 1	387 / -39	0 / 0	76 / 136
SPC 2	-194 / 19	196 / -34	200 / 140
SPC 3	-194 / 19	-196 / 34	200 / 140

Table 11.5.2: Reaction forces at SPC's 1, 2 & 3 before/after active control.

11.5.2 Optical Results of Active Control

The optical result of active control of the twenty pound point load case is a diffraction limited image. Figure 11.5.7 (next page) shows a series of 9 spot images taken at .05 mm intervals along the optical axis on either side of the nominal focus. The diffraction limit of the mirror is approximately .067 arc seconds. (Please see Section 11.4). The spot taken at the nominal focus in Figure 11.5.4 shows a radius of .03 arc seconds for 50% encircled energy, and .07 arc seconds for 100% encircled energy.

Best focus for the passive, perturbed mirror is at .04 mm beyond the nominal focus. The active support system focuses to a diffraction limit at the nominal focus, but does not produce as tight a grouping as is achieved in the nominal case. The spot diagram data for the perturbed active mirror shows that the reflected wavefront propagates with a very small but still noticeable distortion. The conclusion is that the twelve air bag configuration is sufficient to correct deflections caused by point loads of relatively small magnitude.

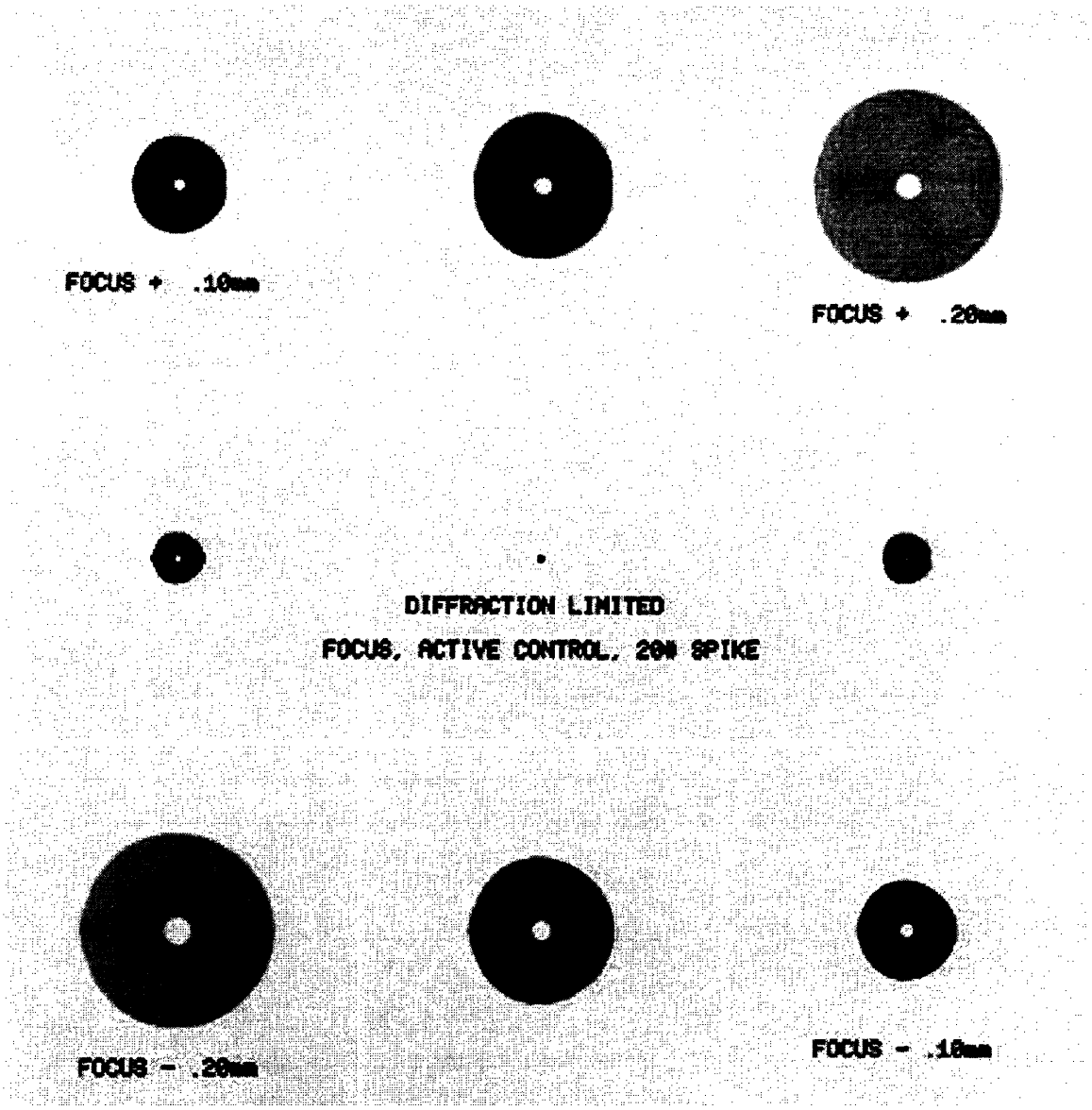

Figure 11.5.7: Series of 9 spot diagrams taken at intervals of .05 mm along the optical axis of the mirror as it experiences gravity and a 20 pound point load.

Table 11.5.3 (below) presents the RMS and encircled energy data for the spot diagrams of Figure 11.5.7. Data from the spot diagrams of the uncorrected 20 pound spike perurbation are also shown for urposes of comparison.

Nominal Focus	RMS	50% Energy Radius	100% Energy Radius
NF - .20 mm	1.79 / 1.49	1.78 / 1.46	2.60 / 2.16
NF - .15 mm	1.42 / 1.12	1.41 / 1.09	2.10 / 1.60
NF - .10 mm	1.05 / 0.74	1.04 / 0.72	1.60 / 1.10
NF - .05 mm	0.69 / 0.37	0.66 / 0.35	1.10 / 0.58
Nominal Focus	0.34 / 0.04	0.31 / 0.03	0.58 / 0.07
NF + .05 mm	0.18 / .037	0.12 / 0.35	0.38 / 0.57
NF + .10 mm	0.47 / 0.74	0.40 / 0.73	0.90 / 1.08
NF + .15 mm	0.83 / 1.11	0.77 / 1.10	1.44 / 1.60
NF + .20 mm	1.20 / 1.48	1.14 / 1.47	1.92 / 2.11

Table 11.5.3: RMS and encircled energy data for the mirror under gravity and a 20 pound point load without / with active control. Data is in arc seconds.

Third Order Aberrations

3rd Order Aberrations	Uncorrected	Active Control
Tilt	0.296 λ	0.001 λ
Defocus	-1.172 λ	-0.007 λ
Astigmatism	0.653 λ	0.003 λ
Coma	0.097 λ	0.005 λ
Spherical Aberration	0.779 λ	0.023 λ

Table 11.5.4: Third order aberrations before and after active control is used to correct gravity and 20 pound spike force induced aberrations. Data is in wavelengths (λ = .633 μm).

Summary

Deformations created by gravity and a point load are almost completely corrected by the pressure changes in the axial air bags. Tilt and astigmatism introduced by the spike load have been removed. The active system is capable of correcting external perturbations of relatively small magnitude.

11.6 Active Control of 100 Pound Point Load / Gravity Perturbation

The twelve air bag active optics system is used to correct perturbations caused by gravity and the application of a 100 pound point load. (Please see Section 10.3.) The point load is applied in the negative z-direction to the mercury belt node on the mirror's negative x-axis at (r = 1.143 m, $\theta = \pi$, z = .082 m).

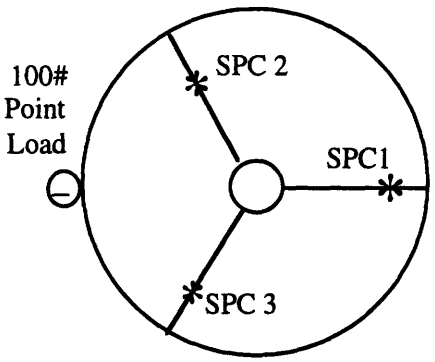

Figure 11.6.1: Vertical view of the location of the 100 pound point load: (r = 1.143 m, $\theta = \pi$, z = .082 m).

11.6.1 The 100 Pound Point Load / Gravity Perturbation

The 100 pound point load induces bending that changes the shape of the mirror surface. A broad positive deflection band is created across the mirror's center. Maximum negative deflection is in the area of the point load. The 100 pound point load causes a non-uniform reaction force distribution.

OPTICSMIN is programmed to minimize the Zernike coefficients and to reproduce 135 N z-axis reaction forces on the hard points. The face of the perturbed mirror is seen in the PCFRINGE z-axis contour plot in Figure 11.6.2 on the next page. Pressure changes are presented in Figure 11.6.3. The active control pattern seen in Figure 11.6.3 can be viewed as a series of adjustments based on the need to use Bag #10 to counter the impact of the spike load.

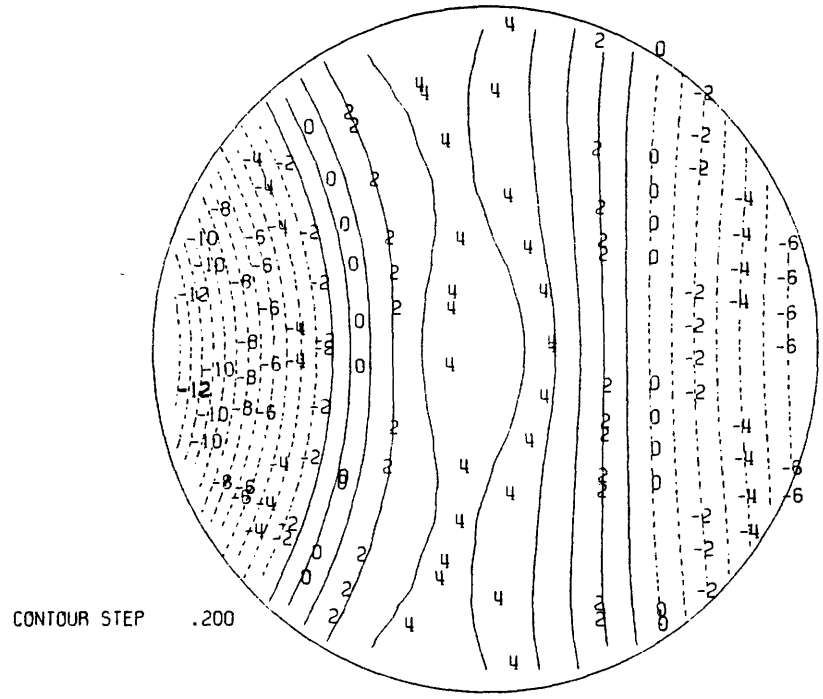

Figure 11.6.2: PCFRINGE z-axis contour plot of surface deflections for a 100 pound load applied to the outside wall of the mirror on the negative x-axis.

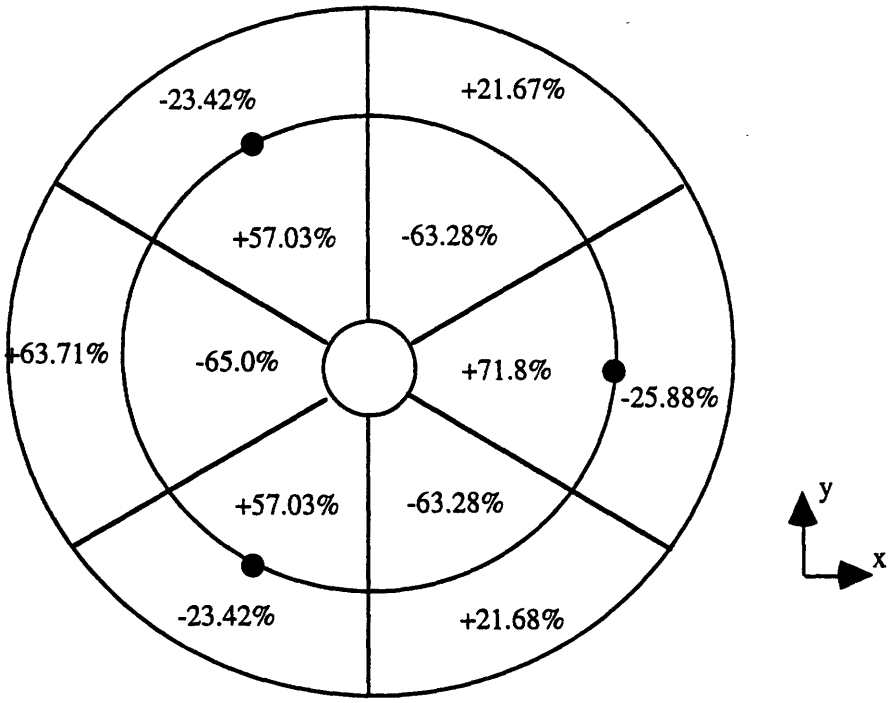

Figure 11.6.3: Pressure changes to optimize the 100 lb point load perturbation.

The pattern of pressure changes indicates that the primary source of deformation is no longer gravity, but the 100 pound point load. Bag #10, located above the point load, compensates for the point load. The adjacent interior bag, Bag #4, is reduced to compensate for the increase in pressure in Bag #10. Bag #1 is increased, and Bag #7 is decreased, showing an alternating pattern from left to right across the x-axis. The alternating pattern of increasing and decreasing pressure continues around both interior and exterior actuator rings.

Structural Results of Active Control

Active control of the 100 pound point load perturbation recovers the shape and the magnitude of deflections displayed by the uncorrected nominal mirror. These less than perfect shapes and deflections result from using only twelve actuators in the active control system to counter a more extreme deflection shape. A significantly higher number of actuators would afford a more flexible and sensitive response. Please see Figure 11.6.4, below.

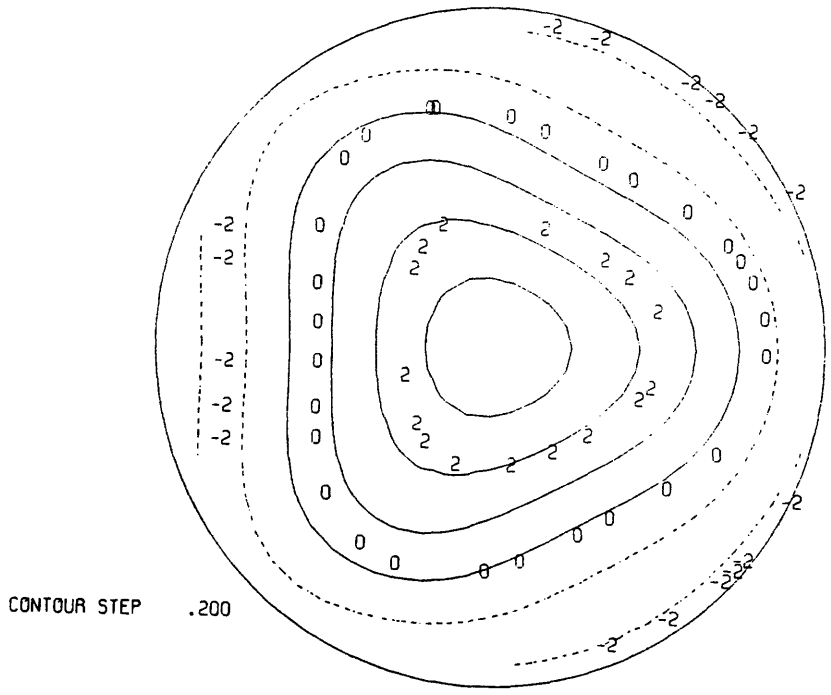

Figure 11.6.4: PCFRINGE z-axis contour plot of the active mirror surface scaled to show deflections in contour intervals of .2 λ.

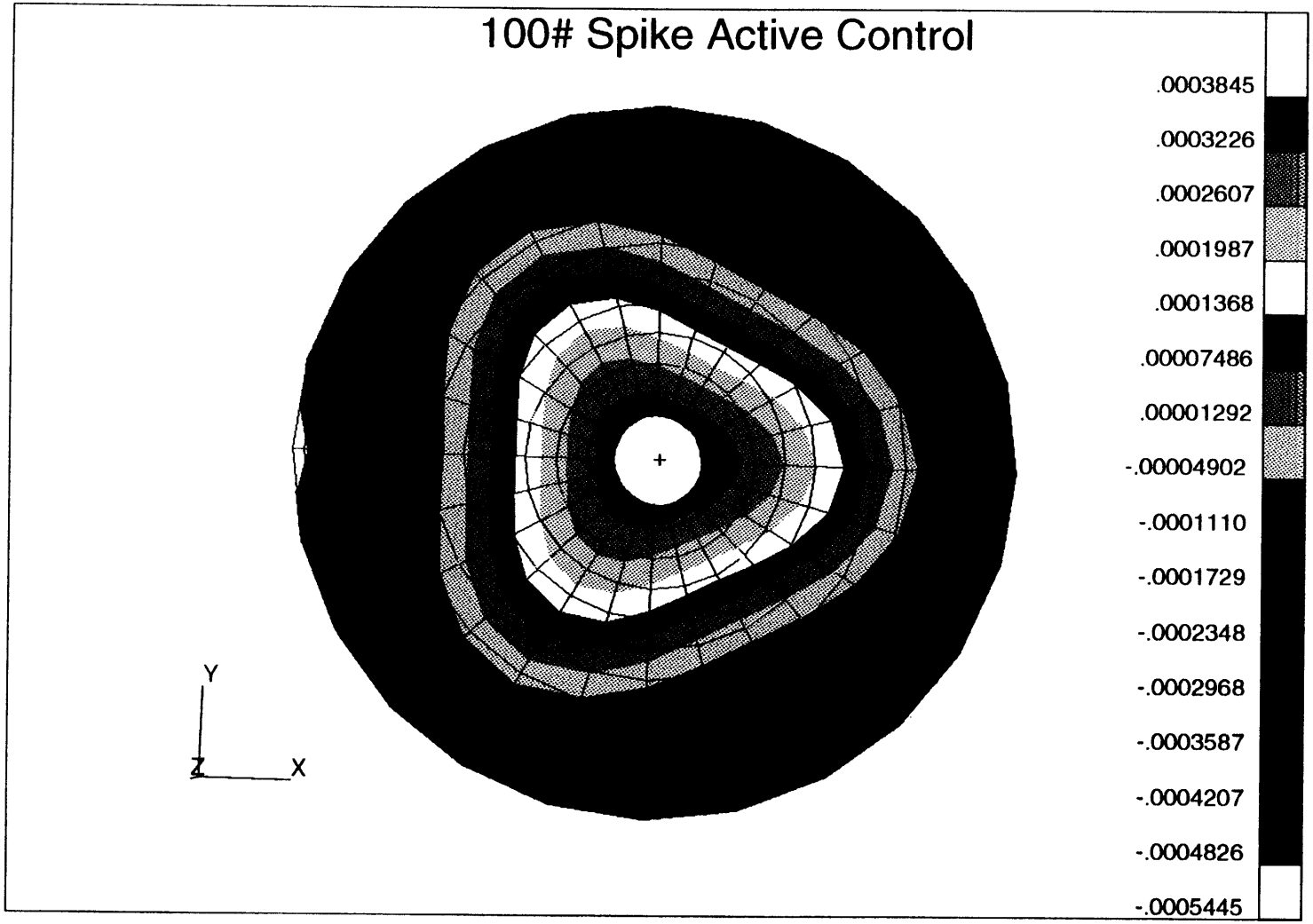

Figure 11.6.5: NASTRAN contour plot showing z-axis deflections for the corrected mirror surface.

Surface Deflections, RMS and P-V in the Corrected Mirror

Table 11.6.1 is a measure of the effectiveness (limitations?) of the twelve air bag active system as it compares z-axis deflections at specific points along the mirror surface before and after optimization. The active control system is able to reduce the magnitude of the deflections, but is incapable of removing them. Figure 11.6.6 shows the locations of the points selected for comparison.

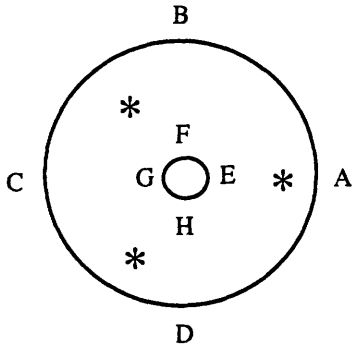

Figure 11.6.6: Sample points for comparing deflections with and without active control. The *'s are the SPC's.

Sample Point	A	B/D	C	E	F/G/H	SPC 1	SPC 2	SPC 3
No Active	-.425	+.4813	-2.917	+.4813	+.4813	+.030	-.198	-.198
With Active	-.359	-.359	-.545	+.385	+.385	-.018	-.018	-.018

Table 11.6.1: Mirror surface deflections under the influence of gravity and a 100 pound point load, before and after active control. All units are μm.

Structural response to active control can be gauged by the improvement in reflected wavefront RMS and P-V measures. These measures are improved, and seem to be very close to those of the pre-optimization nominal mirror case.

Case: 100# Spike	RMS	P-V
No Active Control	1.378 μm	6.752 μm
Active Control	0.390 μm	1.830 μm

Table 11.6.2: RMS and P-V measures in μm for both the uncorrected and the corrected mirror.

Reaction Forces in the Corrected Mirror

The active control system restores the 135 N z-axis reaction forces, and thereby eliminates mirror tilt. The code's pressure changes maintain fairly strong x- and y-axis reaction force components. These reaction forces describe a back surface that is under compression, and reflect both the pressure changes in the outer bags and the presence of the 100 pound spike.

Hard Point	X-Axis RF (N)	Y-Axis RF (N)	Z-Axis RF (N)
SPC 1	+727 / +386	0 / 0	-135 / +135
SPC 2	-363 / -193	-65 / +337	485 / +135
SPC 3	-363 / -193	+65 / -337	485 / +135

Table 11.6.3: SPC reaction forces for the uncorrected and corrected mirrors under the influence of a 100 pound point load.

11.6.2 Optical Results, Correcting 100 Pound Point Load

The series of 9 spot diagrams in Figure 11.6.7 below are taken at .05 mm intervals on either side of the nominal focus. The spot series shows that the 100 pound point load in combination with gravity induced mirror distortions overcomes the twelve air bag system's ability to reform a perfect wavefront. The active mirror remains focused at a point beyond nominal, and the spherical aberration remains at levels seen in the nominal case. Active control significantly improved the astigmatism and coma.

The effect of the point load is seen in the spots taken at .20 mm to .10 mm short of the nominal focus. The severe triangulation effect created by correcting the 100 pound distortion is seen in the spots taken at .10 mm to .20 mm beyond the nominal focus. The point load throws the actual focus in the corrected mirror to approximately 05 mm beyond nominal.

Table 11.6.4 presents spot data in an attempt to isolate the actual focus. Figure 11.6.8 shows a series of six spots taken between the nominal focus and .05 mm beyond nominal. Table 11.6.6 isolates the actual focus.

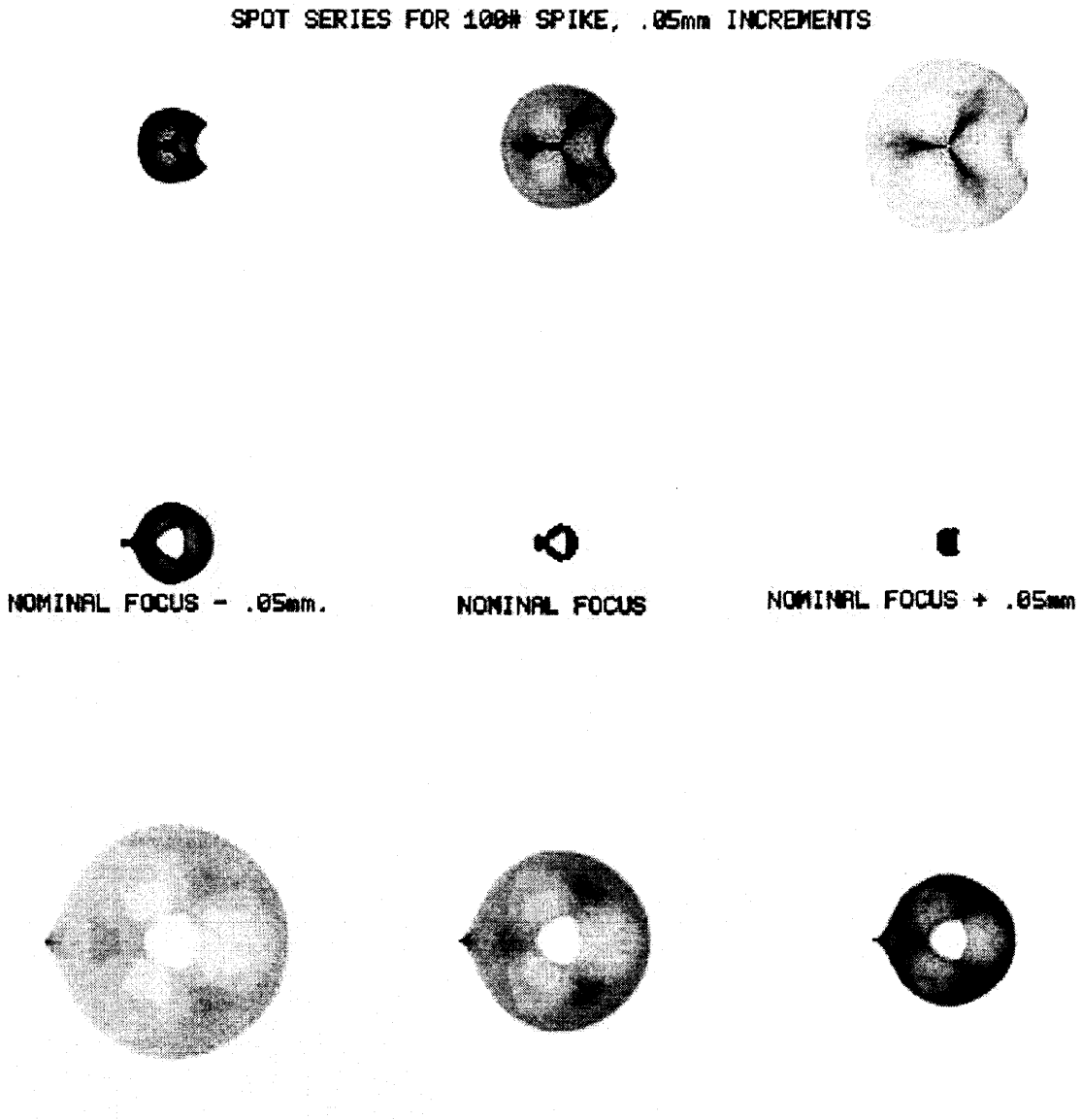

Figure 11.6.7: Spot diagram series at .05 mm intervals about the nominal focus for the case of the mirror under a 100 pound point load with active control.

Nominal Focus	RMS	50% Energy Radius	100% Energy
NF - .20 mm	1.93 / 1.77	1.83 / 1.76	4.35 / 2.60
NF - .15 mm	1.58 / 1.40	1.45 / 1.39	3.70 / 2.05
NF - .10 mm	1.24 / 1.03	1.12 / 1.02	3.00 / 1.55
NF - .05 mm	0.92 / 0.66	0.82 / 0.65	2.30/ 1.00
Nominal Focus	0.65 / 0.31	0.60 / 0.29	1.55 / 0.51
NF + .05 mm	0.53 / 0.16	0.46 / 0.13	0.96 / 0.36
NF + .10 mm	0.65 / 0.48	0.53 / 0.43	1.15 / 0.81
NF + .15 mm	0.91 / 0.84	0.78 / 0.79	1.63 / 1.34
NF + .20 mm	1.23 / 1.21	1.29 / 1.16	2.12 / 1.78

Table 11.6.4: RMS and encircled energy data for the mirror under gravity and a 100 pound point load without / with active control. Data is in arc seconds.

Third Order Aberrations

The 100 pound spike induces a significant amount of astigmatism and coma, and adds to the mirror's inherent spherical aberration. Active control mitigates the astigmatism, tilt and coma induced by the spike force, but is unable to improve the optics beyond that seen in the nominal mirror.

3rd Order Aberrations	Uncorrected	Active Control
Tilt	1.47 λ	.003 λ
Defocus	-1.452 λ	-1.102 λ
Astigmatism	3.267 λ	.016 λ
Coma	.486 λ	.014 λ
Spherical Aberration	.891 λ	.729 λ

Table 11.6.5: Third order aberrations before and after active control is used to correct gravity and 100 pound spike force induced aberrations. Data is in wavelengths (λ = .633 μm).

Finding the Corrected Mirror's Actual Focus

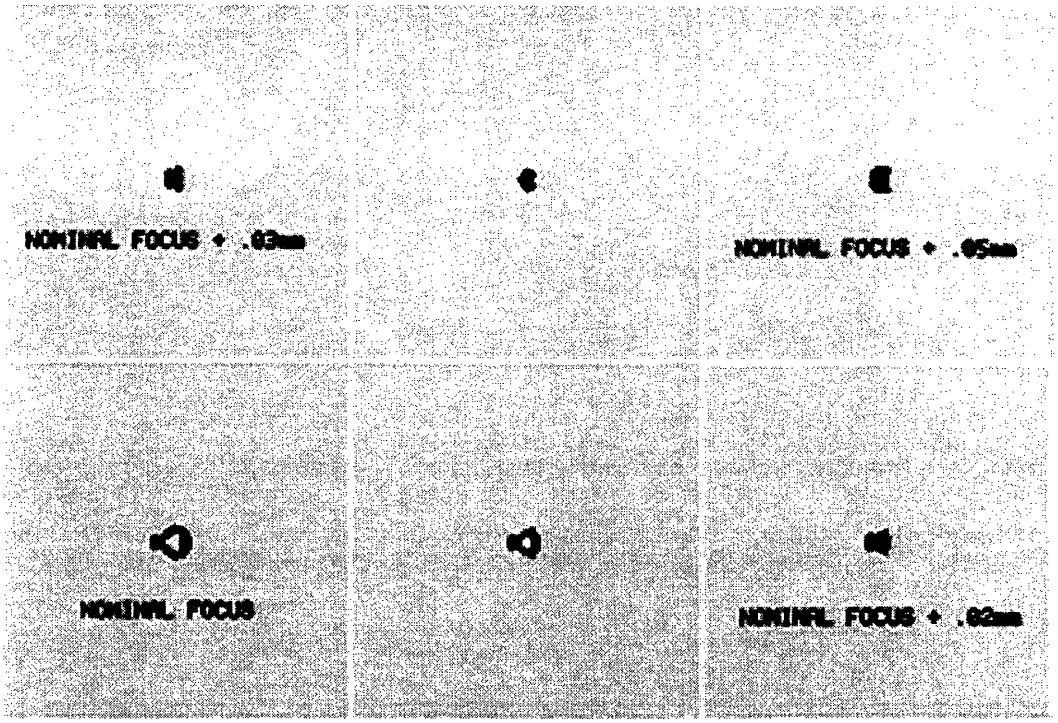

Figure 11.6.8: The reflected wavefront's transition through actual focus for the active mirror under the influence of gravity and a 100 pound point load.

Nominal +	RMS	50% Energy Radius	100% Energy Radius
@ +.03 mm	0.14	0.10	0.32
@ +.04 mm	0.13	0.10	0.28
@ +.05 mm	0.16	0.13	0.36

Table 11.6.6: Spot diagram data for finding the actual focus of the corrected mirror. All data is in arc seconds

Summary

Active control recovers the parameters found in the nominal, uncorrected mirror. The gross astigmatism and coma created by the 100 pound spike force are removed, but the improvement is not diffraction limited. This can be attributed, in part, to the limited capability of an active axial support system comprised of only twelve air bags.

11.7 Correcting Perturbations From Gravity and Four Point Loads With Active Control

The twelve air bag active optics system is used to correct perturbations caused by gravity combined with four simultaneous 20 pound point load applications. The point loads are applied as two sets of paired forces. One set is oriented in the positive z-direction, and is applied to the two mercury belt nodes on the mirror's y-axis (r = 1.143 m, $\theta = \pi/2, 3\pi/2$, z = .082 m). The other set is oriented in the negative z-direction, and is applied to the two mercury belt nodes on the mirror's x-axis at (r = 1.143 m, $\theta = 0, \pi$, z = .082 m).

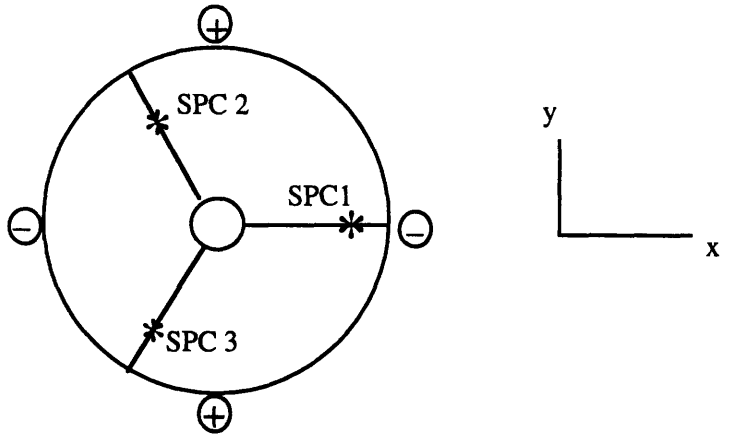

Figure 11.7.1: Two 20 lb. point loads are oriented in the positive Z-direction, and two are oriented in the negative z-direction.

11.7.1 Active Control of Four 20 Pound Point Loads

The point loads, paired so that two loads push up while the other two pull down, produce anticlastic bending moments. The bending is locally constrained by the three hard points to restrict any translational or rotational movement. The deformed mirror surface is defined by an oval shaped ridge of positive deflection that runs along the mirror's y-axis. The ridge is displaced slightly toward the positive x-axis.

The optimization is programmed to minimize the Zernike coefficients and to produce 129 N reaction forces on the hard points. OPTICSMIN recommended pressure changes are shown in Figure 11.7.3.

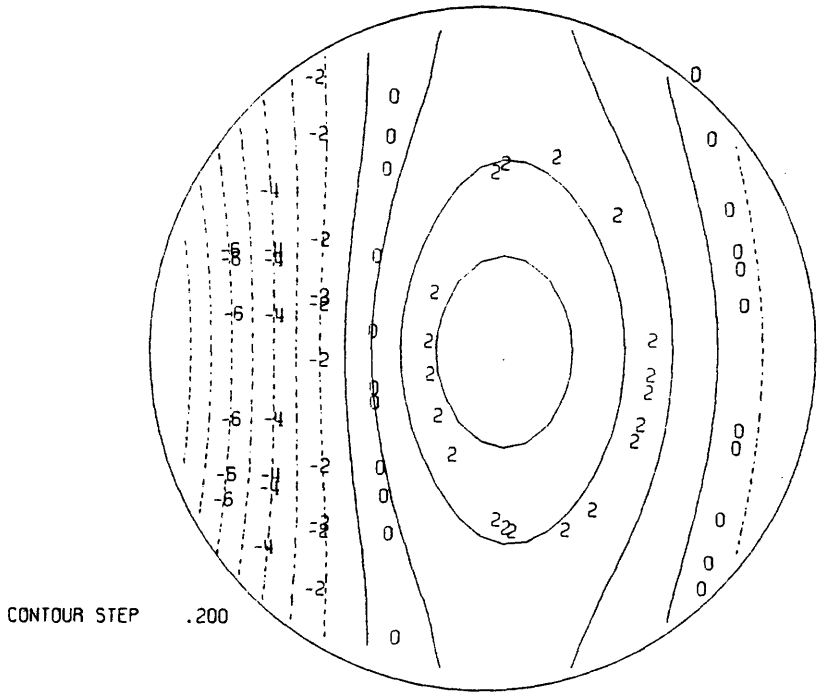

Figure 11.7.2: PCFRINGE plot of deflections from two pairs of antiparallel 20 pound loads applied to the outside wall of the mirror on the negative x-axis.

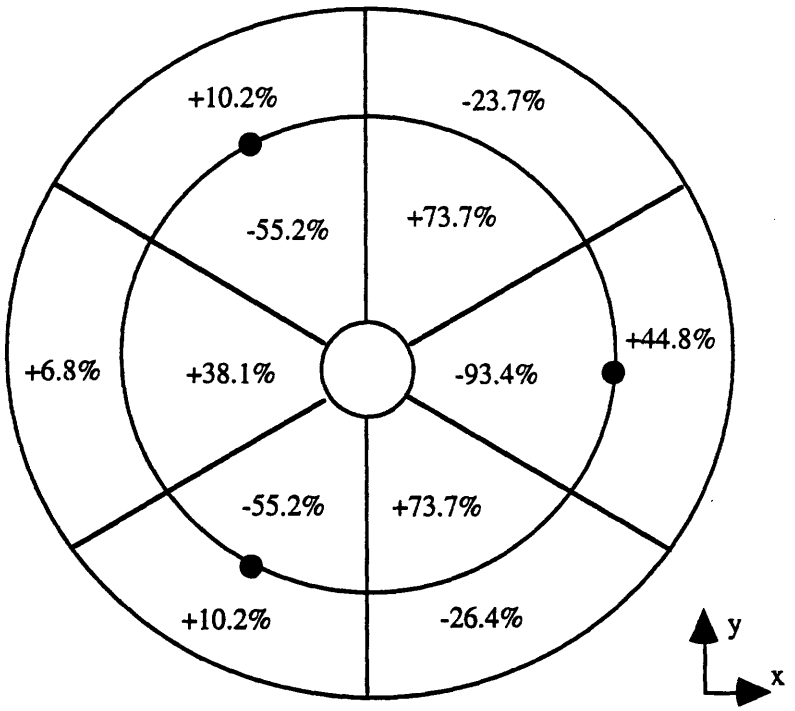

Figure 11.7.3: Pressure changes recommended by OPTICSMIN for the case of two pairs of antiparallel 20 pound point loads.

The pattern and magnitude of pressure changes recommended by OPTICSMIN suggests the severity of the deformation mode introduced by the four paired point loads. The optimization calls for a 93% reduction in pressure for Bag #1, while asking for large increases in Bags #2, #6 and #7. This indicates that the multiple airbag design reaches its limit with these four 20 pound point loads. Active control of larger magnitude anticlastic perturbations requires actuators that can pull as well as push.

Structural Results of Active Control

Active control removes the most deleterious effects of the multiple point loading, and returns the mirror to a shape that is reminiscent of the gravity deformation found in the nominal mirror case (Section 10.4). This case's optimized shape is triangulated, but is the reverse of the shape produced by the nominal mirror case. Active control produces a maximum negative deflection around the mirror surface outer edge, and a maximum positive deflection around the inner radius.

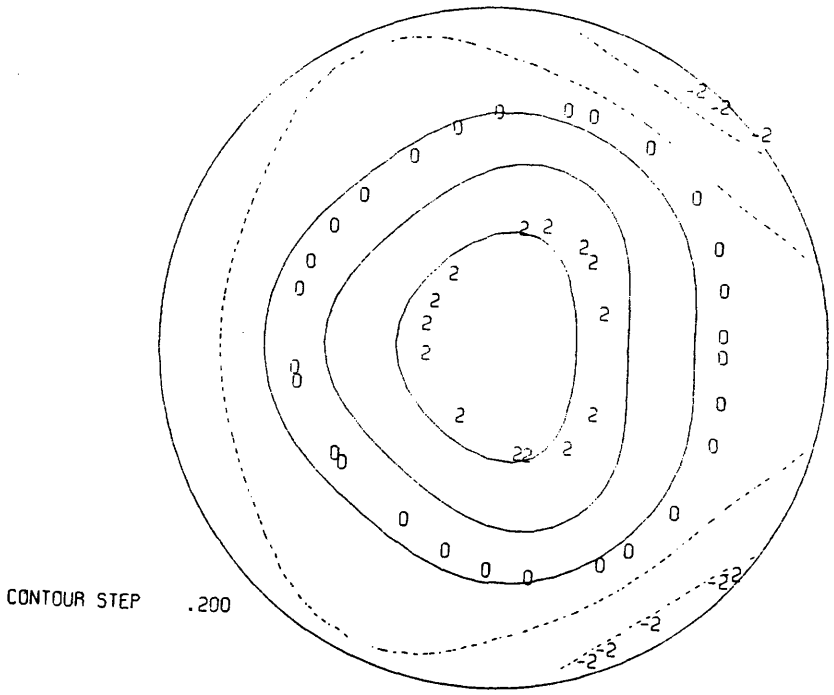

Figure 11.7.4: PCFRINGE z-axis contour plot of the mirror surface corrected with active control. Scale is in contour intervals of .2 λ.

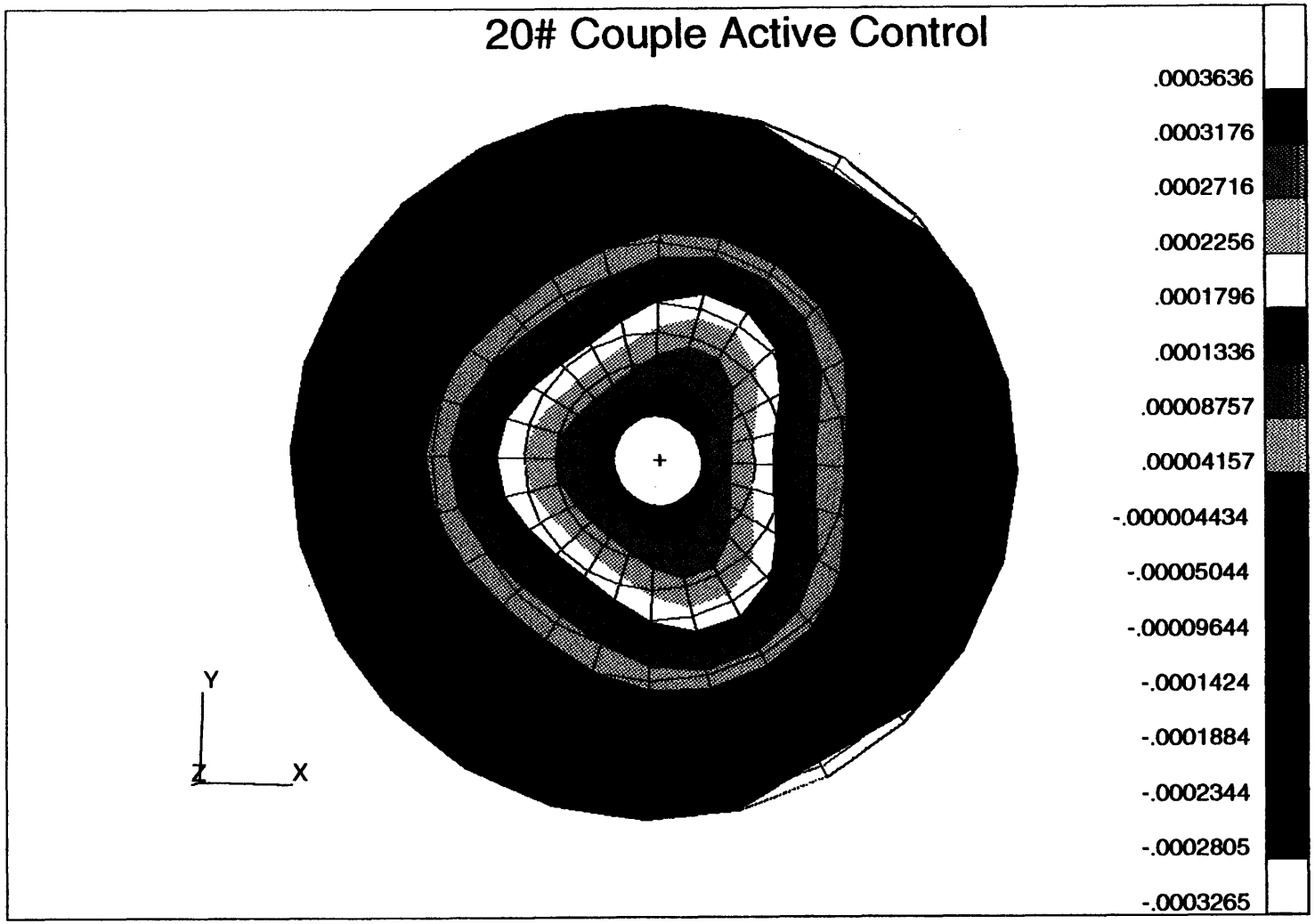

Figure 11.7.5: NASTRAN contour plot showing z-axis deflections for the corrected mirror surface.

RMS, P-V and Surface Deflections in the Corrected Mirror

Table 11.7.1 displays wavefront RMS and P-V at the exit pupil with and without active control. Active control improves wavefront RMS and P-V, though the improvement is not dramatic. (Actual surface deflections are half the wavefront values shown Table 11.7.1.)

Case: 2-20# Pairs	RMS (μm)	P-V (μm)
No Active Control	0.624	3.185
Active Control	0.309	1.367

Table 11.7.1: Mirror with two paired 20 pound point loads and gravity, before and after active control.

Table 11.7.2 compares z-axis deflections at certain points in the mirror before and after optimization Figure 11.7.6 shows the locations of the points selected for comparison in the table.

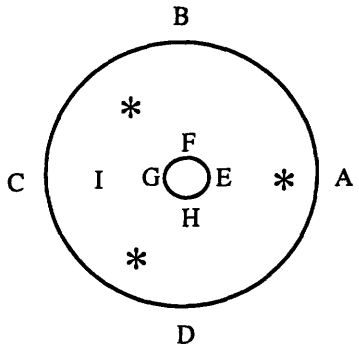

Figure 11.7.6: Sample points for comparing gravity and multiple point load induced deflections with and without active control. The *'s are the SPC's.

Point	A	B/D	C	E/F/G/H	I	SPC 1	SPC 2	SPC 3
No Active	-.318	-.110	-1.173	+.431	-.211	.003	.003	.003
With Active	-.142	-.188	-.281	+.364	-.042	-.025	-.025	-.025

Table 11.7.2: Deflections of the mirror surface under the influence of gravity and multiple 20 pound point loads, before and after active control. Last three columns show surface deflections above the hard points. All units are μm.

Reaction Forces in the Corrected Mirror

Table 11.7.3 (below) compares SPC reaction forces before and after active control. The z-axis reaction forces are undisturbed by the point loading and active control. Air bag pressure changes relieve the x-direction reaction forces, as the differential pressure works against the point loading. Reaction forces in the y-axis change from compression to tension, and increase in absolute magnitude. This is a result of the limited permutations available with the twelve bag configuration, and the optimization's decision to utilize an alternating pressure pattern to minimize the Zernike coefficients.

Hard Point	X-Axis RF (N)	Y-Axis RF (N)	Z-Axis RF (N)
SPC 1	509 / 135	0 / 0	129 / 129
SPC 2	-255 / -67	91 / 148	129 / 129
SPC 3	-255 / -67	-91 / -148	129 / 129

Table 11.7.3: Reaction forces at SPC's 1, 2 & 3 before/after active control.

11.7.2 Optical Results of Active Control

Figures 11.7.7 A & B (please see the next page) show series of 9 spot images taken at .05 mm intervals along the optical axis on either side of the nominal focus for both the corrected and uncorrected mirrors. The corrected wavefront exhibits a consistent, sharp triangulation as it propagates through the area of actual focus, which is a significant improvement over the astigmatic form that propagates from the uncorrected mirror.

Table 11.7.4 on the following page presents spot diagram RMS and encircled energy data for both the corrected and uncorrected mirrors. In the area of nominal and actual focus, active control improves wavefront RMS and 50% encircled energy radius by approximately 33%. The data shows, though, that the corrected wavefront is far from perfect. As in the case of the 100 pound spike perturbation, active control is able to recover a mirror surface quality that is approximately equal to that of the nominal mirror without active control.

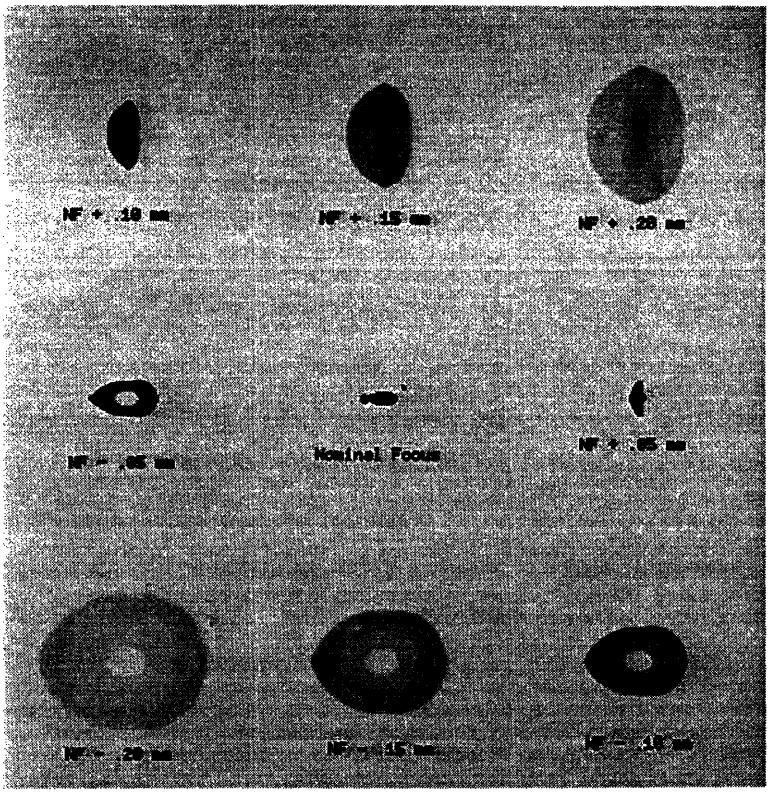

Figure 11.7.7A: Spots of uncorrected mirror, .05 mm intervals.

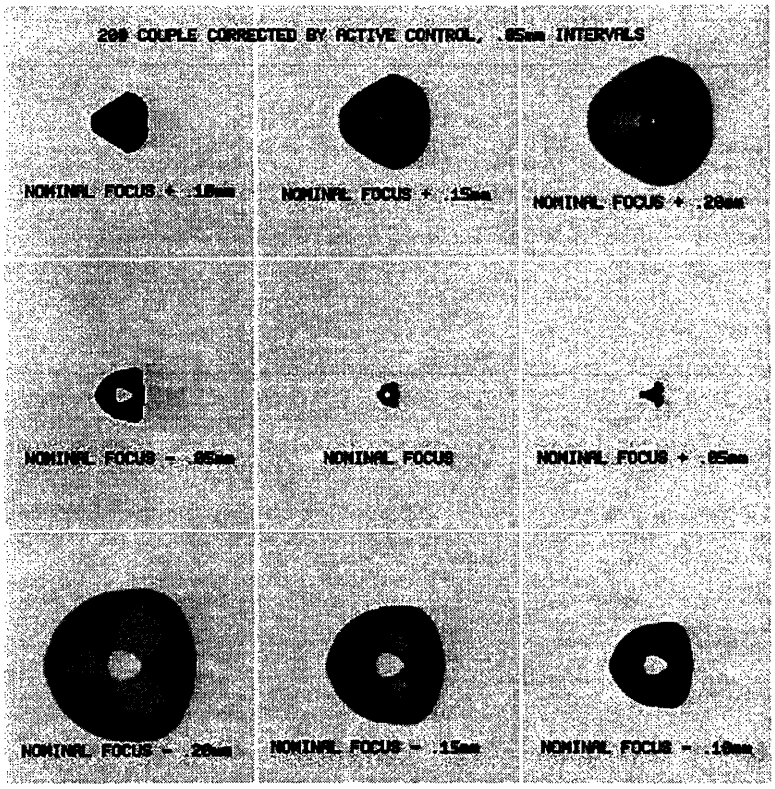

Figure 11.7.7B: Spot diagrams of corrected mirror, also at .05 mm intervals.

Nominal Focus	RMS	50% Encircled Energy	100% Encircled Energy
NF - .20 mm	1.78 / 1.71	1.75 / 1.70	2.70 / 2.40
NF - .15 mm	1.41 / 1.34	1.37 / 1.33	2.15 / 1.95
NF - .10 mm	1.05 / 0.97	0.99 / 0.95	1.70 / 1.39
NF - .05 mm	0.69 / 0.60	0.63 / 0.57	1.15 / 0.90
Nominal Focus	0.36 / 0.25	0.33 / 0.21	0.58 / 0.38
NF + .05 mm	0.26 / .19	0.19 / 0.13	0.53 / 0.46
NF + .10 mm	0.52 / 0.53	0.43 / 0.48	1.11 / 1.93
NF + .15 mm	0.87 / 0.90	0.79 / 1.85	1.56 / 1.45
NF + .20 mm	1.23 / 1.27	1.16 / 1.22	2.05 / 2.00

Table 11.7.4: RMS and encircled energy for the mirror under four 20 pound point loads and gravity, without/with active control. Data in arc seconds.

Third Order Aberrations

The PCFRINGE data in Table 11.7.5 of 3rd order aberrations shows that astigmatism and coma have been largely eliminated, while significant defocus and spherical aberration remain. The magnitude of these aberrations is approximately the same as seen in the nominal mirror case before the application of active control.

3rd Order Aberrations	Uncorrected	Active Control
Tilt	0.521 λ	0.006 λ
Defocus	-1.099 λ	-0.878 λ
Astigmatism	0.406 λ	0.011 λ
Coma	0.067 λ	0.018 λ
Spherical Aberration	0.775 λ	0.613 λ

Table 11.7.5: Third order aberrations with and without active control. Wavelength is .633 μm.

Actual Focus

Spot diagrams taken at .01 mm intervals around the nominal focus (Figure 11.7.8, data in Table 11.7.6) show that the actual focus of the active mirror is at .03 mm beyond nominal focus.

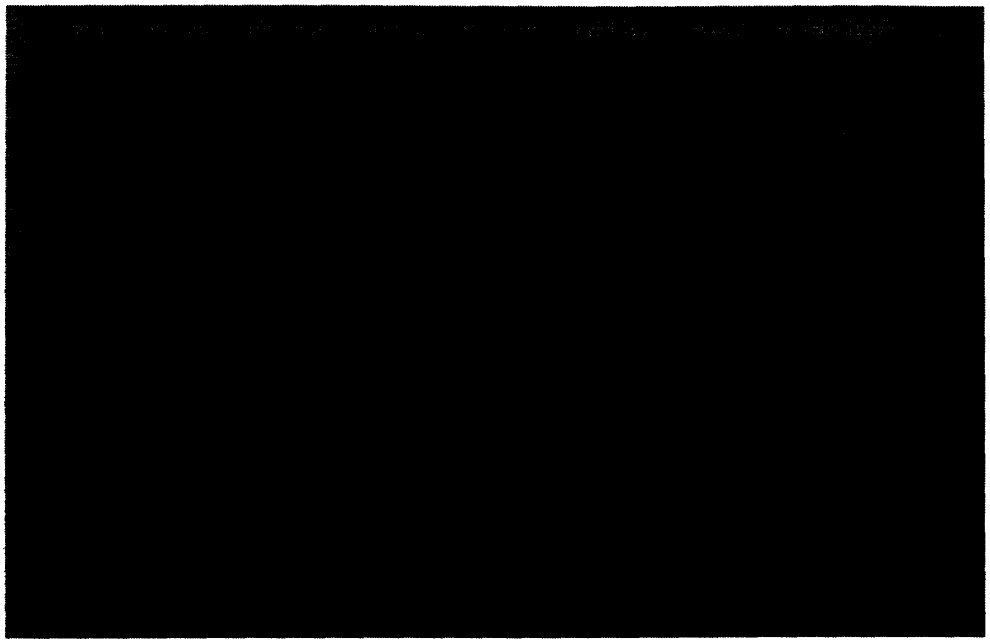

Figure 11.7.8: Actual focus. Spots are at .01 mm intervals.

Nominal +	RMS	50% Energy Radius	100% Energy Radius
@ +.01 mm	0.19	0.15	0.32
@ +.02 mm	0.14	0.10	0.26
@ +.03 mm	0.11	0.09	0.23
@ +.04 mm	0.14	0.09	0.33
@ +.05 mm	0.19	0.13	0.46

Table 11.7.6: RMS and encircled energy, in arc seconds, for Figure 11.6.7.

Summary

The two anti-parallel pairs of 20 pound point loads test the 12 air bag system to the limits of its capability. The small number of actuators limits the system's ability to compensate for the complex wavefront distortion.

11.8 Correcting Two Pair of Anti-Parallel 100 Pound Point Loads

The twelve air bag active optics system is used to correct perturbations caused by gravity and two pair of 100 pound point loads. (Please see Section 10.5.) One pair is oriented in the positive z-direction and is applied to the two mercury belt nodes on the y-axis (r = 1.143 m, $\theta = \pi/2, 3\pi/2$, z = .082 m). The other pair is oriented in the negative z-direction, and is applied to the two mercury belt nodes on the mirror's x-axis (r = 1.143 m, $\theta = 0, \pi$, z = .082 m).

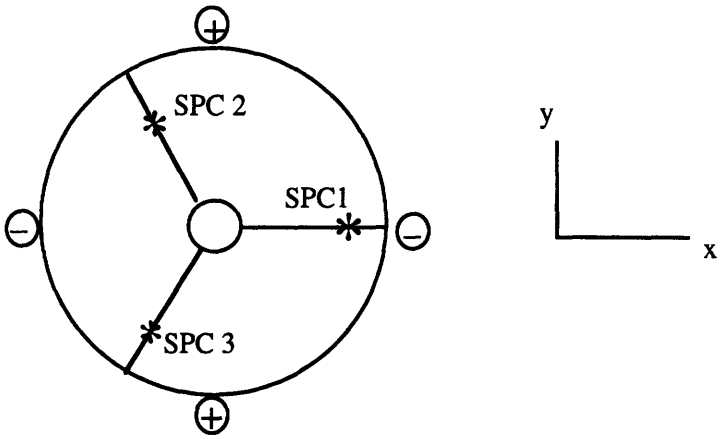

Figure 11.8.1: Two 100 lb. point loads are oriented in the positive Z-direction, and two are oriented in the negative z-direction.

11.8.1 Active Control of Four 100 Pound Point Loads

The bending caused by the 100 pound point loads creates a shape that is completely different than the 20 pound case. The aberrated mirror looks like a horse saddle, pushed down along the x-axis and pulled up along the y axis. The deformations are symmetric about the x-axis, creating a grossly astigmatic surface.

Again, the optimization is programmed to minimize the Zernike coefficients and leave a z-axis reaction force of 129 N on each of the three hard points. A PCFRINGE z-axis contour plot of the deformed mirror and the OPTICSMIN recommended pressure changes are displayed in Figures 11.8.2 and 11.8.3 on the next page.

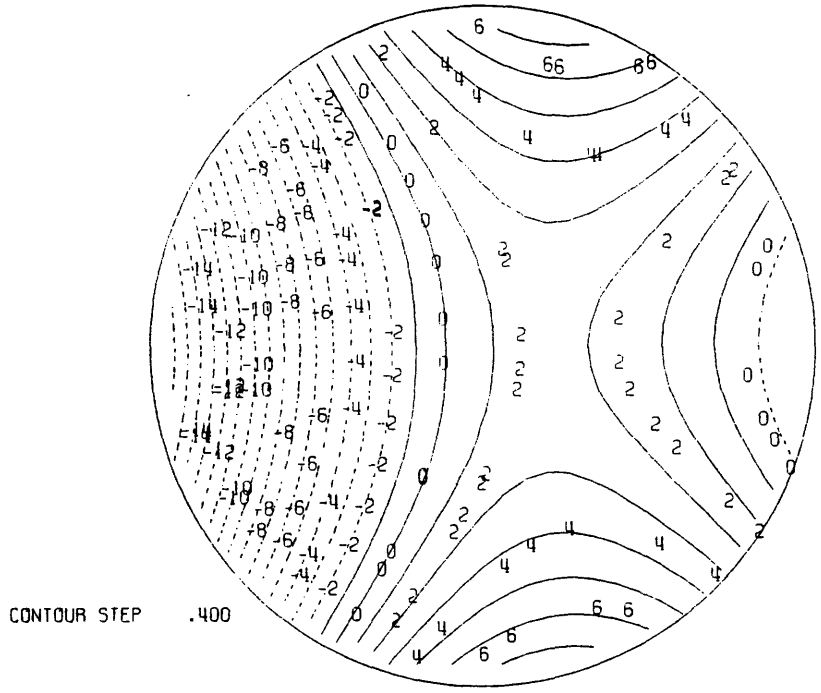

Figure 11.8.2: PCFRINGE plot of deflections from two pairs of antiparallel 100 pound loads applied to the outside wall of the mirror on the negative x-axis.

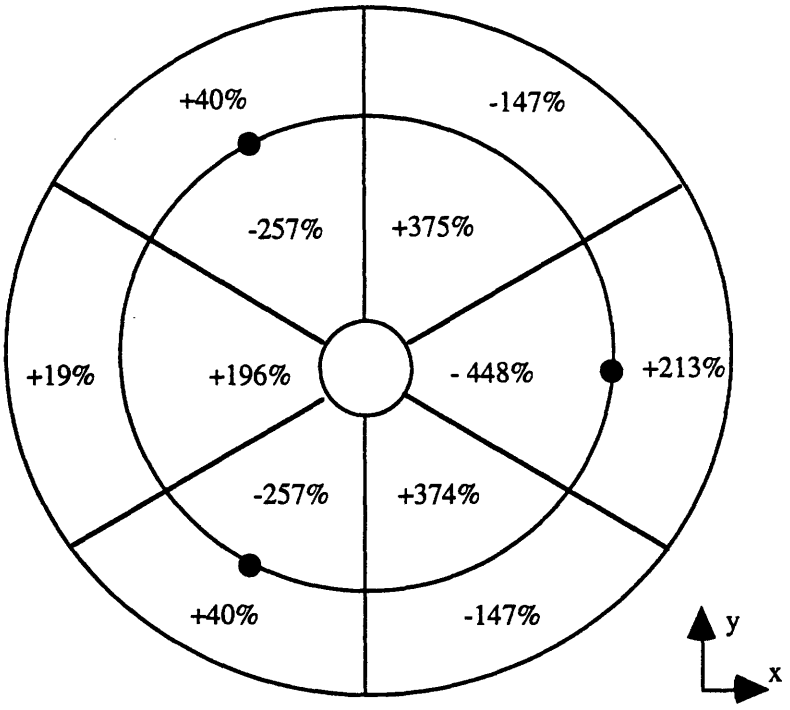

Figure 11.8.3: Pressure changes recommended by OPTICSMIN for the case of two pairs of antiparallel 100 pound point loads.

The alternating pattern of pressure changes is exactly the same as the pattern recommended for the 20 pound anti-parallel pairs case. The magnitudes, however, are a different story. The active control wants to pull on the back of the mirror, as seen in the three digit negative pressure differentials. This case is therefore beyond the capability of the design.

Structural Results of Active Control

The twelve air bag system struggles against the four antiparallel 100 pound point loads. The active mirror surface is a bizarre pattern of peaks and valleys, high points poking up in the area between hard points and low points actually occurring on the surface directly above the hard points. Figure 11.8.4 is a PCFRINGE contour plot of the corrected surface, while the NASTRAN result is Figure 11.8.5 on the next page.

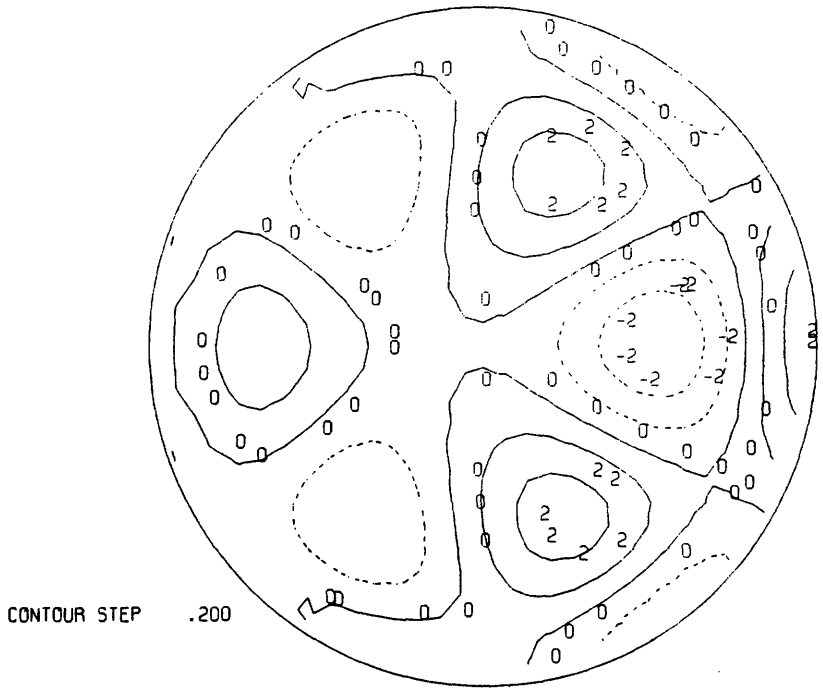

Figure 11.8.4: PCFRINGE z-axis contour plot of the mirror surface corrected with active control. Scale is in contour intervals of .2 λ.

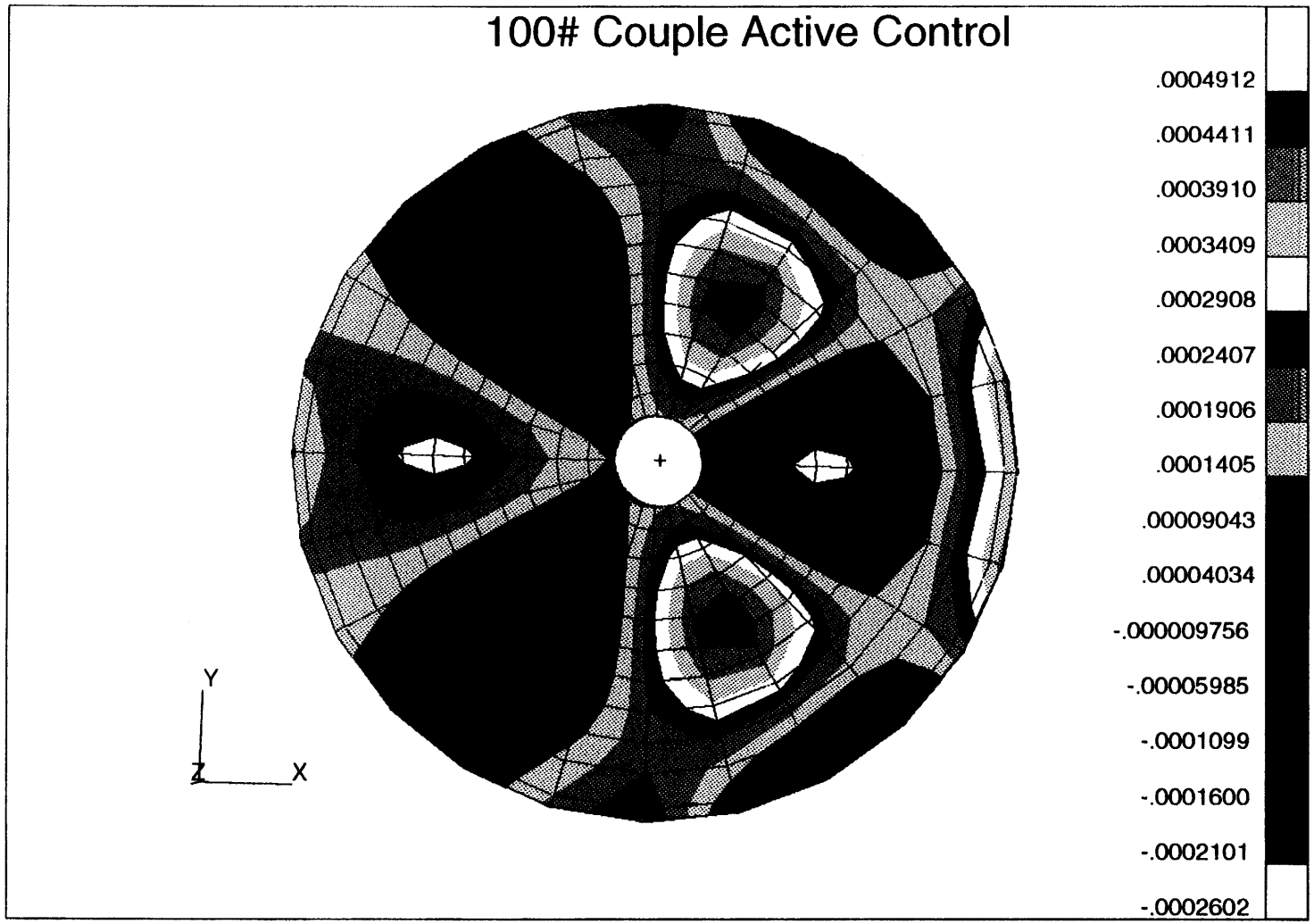

Figure 11.8.5: NASTRAN contour plot showing z-axis deflections for the corrected mirror surface.

RMS, P-V and Surface Deflections in the Corrected Mirror

Despite the odd looking contour pattern, the optimization brings the mirror surface to a quality that surpasses the uncorrected nominal mirror.

Case: 2-100# Pairs	RMS (μm)	P-V (μm)
No Active Control	2.493	12.581
Active Control	0..270	1.469
Nominal Mirror	0.385	1.572

Table 11.8.1: Two paired 100 pound point loads and gravity, before and after active control. Note the order of magnitude improvement.

Reaction Forces in the Corrected Mirror

Table 11.8.3 (below) compares SPC reaction forces before and after active control. The z-axis reaction forces are slightly changed by active control. Pressure changes turn x-direction tension into compression while the y-axis change is only one of magnitude. The system is working hard to compensate for the 100 pound load that points downward at the mirror periphery between hard points #2 and #3. As in the 20 pound anti-parallel pairs, the limited permutations available with the twelve bag configuration.

Hard Point	X-Axis RF (N)	Y-Axis RF (N)	Z-Axis RF (N)
SPC 1	1338 / -528	0 / 0	129 / 132
SPC 2	-669 / 264	-594 / -308	129 / 133
SPC 3	-669 / 264	594 / 308	129 / 133

Table 11.7.3: Reaction forces at SPC's 1, 2 & 3 before/after active control.

11.8.2 Optical Results of Active Control

Figures 11.8.6 and 11.8.7 on the next page compare the spots generated by the uncorrected and corrected mirrors. The extreme line astigmatism is converted into a sort of trefoil that shows no reversal of orientation at the actual focus. The RMS and encircled energy radii show varying improvement.

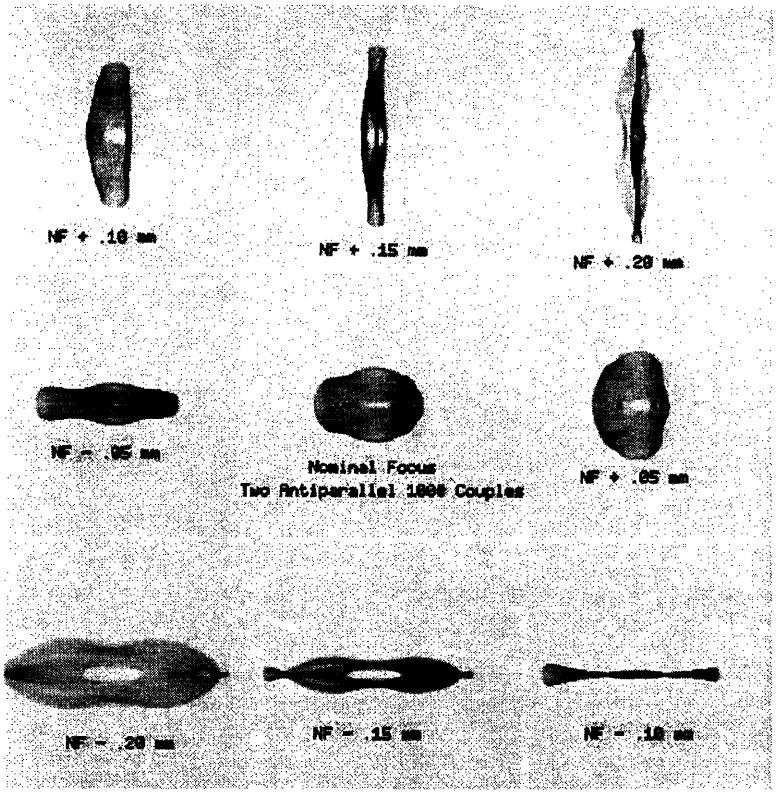

Figure 11.8.6: Uncorrected mirror showing extreme line astigmatism.

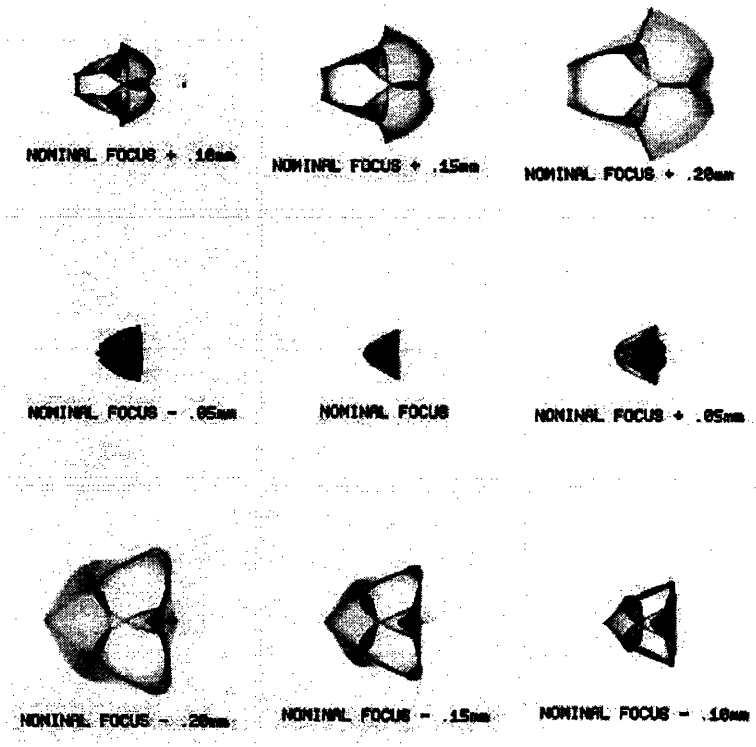

Figure 11.8.7: Corrected mirror showing active results.

Nominal Focus	RMS	50% Encircled Energy
NF - .20 mm	2.53 / 1.52	2.27 / 1.42
NF - .15 mm	2.29 / 1.17	2.01 / 1.06
NF - .10 mm	2.11 / 0.82	1.77 / 0.73
NF - .05 mm	1.97 / 0.51	1.55 / 0.41
Nominal Focus	1.89 / 0.35	1.58 / 0.27
NF + .05 mm	1.89 /0.52	1.59 / 0.48
NF + .10 mm	1.96 / 0.83	1.58 / 0.75
NF + .15 mm	2.09 / 1.17	1.60 / 1.07
NF + .20 mm	2.28 / 1.53	1.77 / 1.44

Table 11.8.4: RMS and encircled energy for the mirror under four 100 pound point loads and gravity, without/with active control. Data in arc seconds.

Third Order Aberrations

Table 11.8.5 shows a uniform level of residual aberration present in the corrected mirror. The most significant change is elimination of astigmatism.

3rd Order Aberrations	Uncorrected	Active Control
Tilt	2.622 λ	0.038 λ
Defocus	-1.085 λ	-0.022 λ
Astigmatism	7.077 λ	0.0356 λ
Coma	.338 λ	0.088 λ
Spherical Aberration	0.768 λ	-.038 λ

Table 11.7.5: Third order aberrations with and without active control. Wavelength is .633 μm.

Summary

It should be noted again that these results are produced by an active control that pulls on the back of the mirror - something which is beyond the capabilities of this active design. The case does show, however, that correction of extreme mirror deformation is possible.

Chapter 12

Conclusions and Recommendations

The results of the verification experiment indicate that the finite element model of the MDM/Hiltner primary mirror and associated support systems accurately describes the mirror's structural response to gravity. The model shows that the combination of uniform axial pressure across the back of the mirror, the mirror body's non-uniform mass distribution, and the effect of the reaction forces exerted on the mirror's back by the three hard point supports causes two distinct deformation modes:

- The center of the mirror bends upward while and the mirror's exterior rim droops outward and down, creating the conditions for a transverse spherical aberration at the mirror's designed focal point.

- The second major deformation mode is a readily discernible triangulation of the mirror surface created by the action of the hard points' thirty pound reaction loads, the mirror's variable thickness, and the uniform axial support pressures.

These two fundamental structural deformations degrade the mirror's optical performance. The triangular symmetry in the mirror surface is seen in the shape of the spot images formed at various focal planes. The drooping of the mirror's outer rim and the bulging of the center area act to create a defocus condition, as well as to introduce almost three quarters of a wavelength of spherical aberration.

The model shows that the mirror's response to external forces is linear, and that a relationship can be established between applied force and mirror surface RMS. The model also shows the linear relationship between externally applied point loads and aberrations in mirror produced imagery.

The model predicts that both structurally induced errors and the effects of artificial point loading can be corrected. The thesis proposes an active optics system for the MDM/Hiltner 2.4 meter primary mirror that would use a set of twelve air bag actuators placed across the back surface of the mirror. These actuators would be controlled with information obtained from this thesis' finite element analysis, the Zernike polynomial optical analysis, and the least squares optimization code. The information generated by the least squares optimization would be used to vary the pressures in the axial air bags so as to minimize mirror surface distortions as measured by the Zernike polynomial coefficients.

Model generated active control results show that it is theoretically possible to correct gravity induced deformations and create a diffraction limited image with the MDM/Hiltner primary mirror.

The author harbored two primary concerns about the efficacy of the finite element model of the MDM/Hiltner mirror and support system. The first concern addressed the use of NASTRAN pressure functions to simulate the action of the axial air bags and radial mercury bags. Results seem to indicate that the pressure functions adequately model the interface between support system and mirror body. In both the axial and radial cases, the effect of the support system is to apply a distributed force to the mirror body. The NASTRAN pressure functions provide an accurate and controllable simulation of this applied force distribution.

The second major area of concern was the use of single point constraints in the finite element model to represent the action of the three hard points. This showed mix success. The verification experiment showed that the real hard point supports suffer a small compression when supporting the full weight of the mirror. Single point constraints do not compress. The translational shift experienced by the actual mirror when all air bag pressure was released had to be accounted for optically, by searching along the optical axis for the actual point of focus. In this way it was determined that the hard points had compressed by approximately .10 mm.

On the other hand, the use of single point constraints as hard points provided a NASTRAN benefit. The NASTRAN code produced measures of reaction forces at the SPC's in all three axis. These reaction force measurements were quite valuable in analyzing the structural behavior of the mirror body.

It is recommended that further study of the MDM/Hiltner telescope be done using this finite element model. The model accurately simulates mirror structural and optical behavior. Given the resources of more time and money, this model could accurately quantify structural and optical deformations through out the full range of optical axis orientations.

When positioned with the optical axis oriented in the vertical, the mirror's full weight rests on the axial support air bags and the three hard point supports. The axial air bags exert a uniform pressure across the back of the mirror, while the hard points experience a small z-axis reaction load. This

References

1. Housner, George W., and Vreeland, Thad Jr., The Analysis of Stress and Deformation, The MacMillan Company, New York, 1966.

2. Timoshenko, Steven, and Goodier, J.N., Theory of Elasticity, McGraw-Hill Book Company, New York, 1951.

3. Thomas, George B., and Finney, Ross L., Calculus and Analytical Geometry, 5th Edition, Addison-Wesley Publishing Company, Reading, MA, 1981.

4. Housner, George W., and Vreeland, Thad Jr., The Analysis of Stress and Deformation, The MacMillan Company, New York, 1966, p. 99.

5. Timoshenko, Steven, and Goodier, J.N., Theory of Elasticity, McGraw-Hill Book Company, New York, 1951.

6. Housner, George W., and Vreeland, Thad Jr., The Analysis of Stress and Deformation, The MacMillan Company, New York, 1966.

7. Cook, Robert D., Concepts and Applications of Finite Element Analysis, John Wiley & Sons, New York, 1981.

8. Cook, Robert D., Concepts and Applications of Finite Element Analysis, John Wiley & Sons, New York, 1981.

9. Cook, Robert D., Concepts and Applications of Finite Element Analysis, John Wiley & Sons, New York, 1981.

10. Cook, Robert D., Concepts and Applications of Finite Element Analysis, John Wiley & Sons, New York, 1981.

11. Thomas, George B., and Finney, Ross L., Calculus and Analytical Geometry, 5th Edition, Addison-Wesley Publishing Company, Reading, MA, 1981.

12. Wyant, James C., and Creath, Katherine, "Basic Wavefront Aberration Theory for Optical Metrology", in Applied Optics and Optical Engineering, Vol. 10, edited by Shannon, Robert R., , and Wyant, James C., Academic Press, Boston, 1992.

13. Wyant, James C., and Creath, Katherine, "Basic Wavefront Aberration Theory for Optical Metrology", in Applied Optics and Optical Engineering, Vol. 10, edited by Shannon, Robert R., , and Wyant, James C., Academic Press, Boston, 1992.

14. Schroeder, Daniel J., Astronomical Optics, Academic Press, New York, 1987.

15. Hecht, Eugene, Optics, Addison-Wesley Publishing Company, Inc., Reading, Massachusetts, 1987.

16. Fowles, Grant R., Introduction to Modern Optics, Dover Publications, New York, 1968.

17. Fowles, Grant R., Introduction to Modern Optics, Dover Publications, New York, 1968.

18. Fowles, Grant R., Introduction to Modern Optics, Dover Publications, New York, 1968.

19. Fowles, Grant R., Introduction to Modern Optics, Dover Publications, New York, 1968.

20. Fowles, Grant R., Introduction to Modern Optics, Dover Publications, New York, 1968.

21. Wyant, James C., and Creath, Katherine, "Basic Wavefront Aberration Theory for Optical Metrology", in Applied Optics and Optical Engineering, Vol. 10, edited by Shannon, Robert R., , & Wyant, James C., Academic Press, Boston, 1992.

22. Wyant, James C., and Creath, Katherine, "Basic Wavefront Aberration Theory for Optical Metrology", in Applied Optics and Optical Engineering, Vol. 10, edited by Shannon, Robert R., , & Wyant, James C., Academic Press, Boston, 1992.

23. Wyant, James C., and Creath, Katherine, "Basic Wavefront Aberration Theory for Optical Metrology", in Applied Optics and Optical Engineering, Vol. 10, edited by Shannon, Robert R., , & Wyant, James C., Academic Press, Boston, 1992.

24. Wyant, James C., and Creath, Katherine, "Basic Wavefront Aberration Theory for Optical Metrology", in Applied Optics and Optical Engineering, Vol. 10, edited by Shannon, Robert R., , & Wyant, James C., Academic Press, Boston, 1992.

25. Wyant, James C., and Creath, Katherine, "Basic Wavefront Aberration Theory for Optical Metrology", in Applied Optics and Optical Engineering, Vol. 10, edited by Shannon, Robert R., , & Wyant, James C., Academic Press, Boston, 1992.

26. Wyant, James C., and Creath, Katherine, "Basic Wavefront Aberration Theory for Optical Metrology", in Applied Optics and Optical Engineering, Vol. 10, edited by Shannon, Robert R., , & Wyant, James C., Academic Press, Boston, 1992.

27. Wyant, James C., and Creath, Katherine, "Basic Wavefront Aberration Theory for Optical Metrology", in Applied Optics and Optical Engineering, Vol. 10, edited by Shannon, Robert R., , & Wyant, James C., Academic Press, Boston, 1992.

28. Wyant, James C., and Creath, Katherine, "Basic Wavefront Aberration Theory for Optical Metrology", in Applied Optics and Optical Engineering, Vol. 10, edited by Shannon, Robert R., , & Wyant, James C., Academic Press, Boston, 1992.

29. Wyant, James C., and Creath, Katherine, "Basic Wavefront Aberration Theory for Optical Metrology", in Applied Optics and Optical Engineering, Vol. 10, edited by Shannon, Robert R., , & Wyant, James C., Academic Press, Boston, 1992.

30. Wyant, James C., and Creath, Katherine, "Basic Wavefront Aberration Theory for Optical Metrology", in Applied Optics and Optical Engineering, Vol. 10, edited by Shannon, Robert R., , & Wyant, James C., Academic Press, Boston, 1992.

31. Optical Telescope Technology, MSFC Workshop, NASA Report A-233, April, 1969

Bibliography

Cho, Myung K., and Richard, Ralph M., PCFRINGE User's Manual Version 4.0,

Cook, Robert D., Concepts and Applications of Finite Element Analysis, John Wiley & Sons, New York, 1981.

Fowles, Grant R., Introduction to Modern Optics, Dover Publications, New York, 1968.

Geary, Joseph M, Introduction to Optical Testing, SPIE Optical Engineering Press, Bellingham, Washington, USA, 1993.

Hecht, Eugene, Optics, Addison-Wesley Publishing, Reading, Mass., 1987.

Housner, George W., and Vreeland, Thad Jr., The Analysis of Stress and Deformation, The MacMillan Company, New York, 1966.

King, H.C., The History of the Telescope, Sky Publishing Corp, 1955.

MSFC Workshop, Optical Telescope Technology, NASA Report A-233, April, 1969

RMR Design Group, Inc., PCFRINGE Manual, Tucson, Arizona, 1995.

Schroeder, Daniel J., Astronomical Optics, Academic Press, New York, 1987.

Thomas, George B., and Finney, Ross L., Calculus and Analytical Geometry, 5th Edition, Addison-Wesley Publishing Company, Reading, MA, 1981.

Timoshenko, Steven, and Goodier, J.N., Theory of Elasticity, McGraw-Hill Book Company, New York, 1951.

Welford, W.T., Aberrations of the Symmetrical Optical Systems, Academic Press, London, 1974.

Wyant, James C., and Creath, Katherine, "Basic Wavefront Aberration Theory for Optical Metrology", in Applied Optics and Optical Engineering, Vol. 10, edited by Shannon, Robert R., , & Wyant, James C., Academic Press, Boston, 1992.